The durability of solder joints under thermo-mechanical loading; application to Sn-37Pb and Sn-3.8Ag-0.7Cu lead-free replacement alloy

Mohammad Ghaleeh

Submitted for the degree of Doctor of Philosophy

Heriot-Watt University

School of Engineering and Physical Sciences/Institute of Mechanical, Process and Energy Engineering

April 2015

ABSTRACT

Solder joints in electronic packages provide mechanical, electrical and thermal connections. Hence, their reliability is also a major concern to the electronic packaging industry. Ball Grid Arrays (BGAs) are a very common type of surface mount technology for electronic packaging. This work primarily addresses the thermo-mechanical durability of BGAs and is applied to the exemplar alloys; traditional leaded solder and a popular lead-free solder.

Isothermal mechanical fatigue tests were carried out on 4-ball test specimens of the lead-free (Sn-3.8Ag-0.7Cu) and leaded (Sn-37Pb) solder under load control at room temperature, 35°C and 75°C. As well as this, a set of combined thermal and mechanical cycling tests were carried out, again under load control with the thermal cycles either at a different frequency from the mechanical cycles (not-in-phase) or at the same frequency (both in phase and out-of-phase).

The microstructural evaluation of both alloys was investigated by carrying out a series of simulated ageing tests, coupled with detailed metallurgical analysis and hardness testing.

The results were treated to produce stress-life, cyclic behaviour and creep curves for each of the test conditions. Careful calibration allowed the effects of substrate and grips to be accounted for and so a set of strain-life curves to be produced. These results were compared with other results from the literature taking into account the observations on microstructure made in the ageing tests.

It is generally concluded that the TMF performance is better for the Sn-Ag-Cu alloy than for the Sn-Pb alloy, when expressed as stress-life curves. There is also a significant effect on temperature and phase for each of the alloys, the Sn-Ag-Cu being less susceptible to these effects. When expressed as strain life, the effects of temperature, phase and alloy type are much diminished. Many of these conclusions coincided with only parts of the literature and reasons for the remaining differences are advanced.

DEDICATION

To my wonderful family; Mum Souheila, Dad Izzaddin, brother, sisters. I love you all so much.

ACKNOWLEDGEMENTS

I would like to express my gratitude to my supervisor Professor R.L. Reuben for his invaluable supervision, guidance, and technical support throughout the period of my research. It has been a great pleasure working under his supervision and learning from his amazing experience.

My thanks will go too to members of staff and postgraduate students in the School of Engineering and Physical Sciences who provided help when I needed it; I would like to give a special thank you to Mr Mark Stewart for his assistance with the design and manufacture of the test rig.

I would like to acknowledge the kind advice and assistance of Dr Hector Steen of Henkel Ltd. for the provision of solder paste and invaluable technical advice.

This research was funded by Aleppo University, Syria, under the Capacity Building Project contracted between the Syrian Ministry of Higher Education and the British Council.

This thesis would never have taken shape without the inspiration of all my family, my father, my mother, my brother, my lovely sisters, and the Leishman family. I would like to express my sincere gratitude to my colleagues especially to Alan Faulkner-Jones, Usama Khalifa and other friends who have supported me through every step of the way.

ACADEMIC REGISTRY
Research Thesis Submission

Name*:*	Mohammad Ghaleeh		
School/PGI:	School of Engineering and Physical Sciences/Institute of Mechanical, Process and Energy Engineering (IMPEE)		
Version: *(i.e. First, Resubmission, Final)*	Final	Degree Sought (Award **and** Subject area)	PhD Mechanical Engineering

Declaration

In accordance with the appropriate regulations I hereby submit my thesis and I declare that:

1) the thesis embodies the results of my own work and has been composed by myself
2) where appropriate, I have made acknowledgement of the work of others and have made reference to work carried out in collaboration with other persons
3) the thesis is the correct version of the thesis for submission and is the same version as any electronic versions submitted*.
4) my thesis for the award referred to, deposited in the Heriot-Watt University Library, should be made available for loan or photocopying and be available via the Institutional Repository, subject to such conditions as the Librarian may require
5) I understand that as a student of the University I am required to abide by the Regulations of the University and to conform to its discipline.

* *Please note that it is the responsibility of the candidate to ensure that the correct version of the thesis is submitted.*

Signature of Candidate*:*		Date:	

Submission

Submitted By *(name in capitals):*	MOHAMMAD GHALEEH
Signature of Individual Submitting:	
Date Submitted:	

For Completion in the Student Service Centre (SSC)

Received in the SSC by *(name in capitals):*			
Method of Submission *(Handed in to SSC; posted through internal/external mail):*			
*E-thesis Submitted (**mandatory for final theses)***			
Signature:		Date:	

TABLE OF CONTENTS

LIST OF TABLES

LIST OF FIGURES

Chapter 1: Background

1.1 Introduction

The reliability of solder joints is a critical issue in the microelectronics industry. The requirement of permanent electrical and thermal connections between solder alloys and the various components of a surface mount device is dependent upon the mechanical integrity of the solder and its interfaces.

Tin-lead based solders have traditionally been used due to their acceptably low melting point and good mechanical properties, eutectic characteristic (good freezing behaviour), fine microstructure (giving good strength), low cost, easy manufacturability, and good wetting of common substrates, such as Cu and Ni. All these characteristics make eutectic or near eutectic Sn-37Pb alloys well suited to electronics applications [1]. However, environmental and health concerns led to the banning of the use of lead in solder alloys from 2006 under the European Commission's (EC) directives, Waste Electrical and Electronic Equipment (WEEE) and Restriction of Hazardous Substances (ROHS). This, and similar initiatives worldwide, make the advent of lead-free electronics inevitable [2].

The ever-growing demand for greater packaging density and high performance is being met with surface mount technologies (SMT) such as flip-chip and ball grid arrays (BGA) [3-7], which involve an increase in the number of solder joints per package and a reduction in joint dimensions, but also lead to the formation of complex heterogeneous microstructures within the solder joints. So understanding the microstructure and mechanical behaviour of solder joints of diminishing size has become critical in determining the overall reliability of interconnections [8].

The natural radius of curvature of molten solder, R, as determined by surface tension (γ), density (ρ) and the acceleration due to gravity, (g), $\left(R = \left({}^{\gamma}/_{\rho g}\right)^{1/2} = 2.2 \text{ mm}\right)$ is already larger than the size of the solder joints in the majority of SMT devices with less than 0.5 mm pitch. This could lead to defective solder joints because of starvation of solder at the pad locations commonly called wicking [8]. This has necessitated new manufacturing cycles with implications for the thermal cycle and hence the microstructure of the joint.

Because of these changes, the development of the understanding of the thermo-mechanical durability of solders has developed in a rather haphazard way, with a plethora of literature on measurements and modelling, mostly made in actual soldered connections and not always published with a view to their general applicability. This thesis aims to carry out a structured series of experiments linking the microstructure and thermo-mechanical properties of two metallurgically different solders in an attempt make some general observations about the challenges involved in minimising the amounts of solder whilst maintaining durability and reliability.

1.2 The development of solder joints and alloys

Soldering can be defined as the metallurgical joining of two surfaces using a molten filler metal, being distinct from adhesive bonding by the formation of metallurgical bonds (intermetallic compounds IMC) between the filler and the other metals in the joint area, usually the copper tracks of the circuit board and component [9, 10]. Five processing variables influence the effective formation of a bond: flux, wetting, temperature, the condition of the surfaces to be joined and time.

Eutectic Sn-37Pb alloy is the traditional choice because of its low melting temperature (183°C) and good wetting properties. It owes its low melting temperature to the presence of a eutectic composition, alloys with higher (or lower) lead contents having appreciably higher melting temperatures, for example 3.5Sn-96.5Pb has a melting temperature of 320°C. Whereas it is necessary to have a range of solder alloys with different melting temperatures for different components and arrangements, the majority of solders used in the electronics industry are soft solders, defined as having a melting temperature below 450°C [11].

Electronics assemblies consist of various components such as microelectronic chips, chip carriers, and printed circuit boards. All are connected by solder joints, and, typically, a solder alloy with a high melting temperature is used between the chip and the chip carrier. When the chip carrier is attached to the printed circuit board, a lower melting temperature solder is used to prevent damage to the printed circuit board and it is this connection, usually made in a mass parallel process, which offers the greatest challenge in terms of mechanical integrity.

1.2.1 Electronic Packaging

Solder provides the electrical, thermal and mechanical connection in electronic assembly and a number of different configurations employ solder.

At a primary level (level 1 packaging) bonding of a silicon die (chip) and the bonding pad (substrate) is achieved using a solder layer, which also serves as a conduction path for the dissipation of the heat generated by the semiconductor.
In the next level of assembly and interconnect, referred to frequently as level 2 packaging the component (essentially the encapsulated silicon die with its substrate) is mounted onto a printed wiring/circuit board (PWB or PCB), where the solder is the primary means of interconnect. Practically all microelectronic devices (packages) are mounted onto PWBs using solders, achieved either using surface mount technology (SMT) or the pin through-hole (PTH) method as illustrated in Figures 1.1 and 1.2, respectively. Surface mounted electronic components can either employ leaded terminations as shown in Figure 1.1, or solder balls that, known as ball grid arrays (BGA), as shown in Figure 1.3.

Pin through hole (PTH) type have been used for many years, but surface mount use has risen steadily to meet the demands of high packaging density, smaller height, lighter weight, better performance, higher signal speed, smaller package size, increased functionality for a given area and lower cost. Ball grid arrays (BGA) have been developed specifically to meet these demands.

From a mechanical point of view, PTH soldering differs significantly from SMT. In PTH a hole needs to be drilled in the PCB to assemble the packages, which leaves a significant area on the back side of the board unutilised. Next, wave soldering is performed to attach the PCB to the PIH components by exposing the back side to a wave of molten solder as shown in Figure 1.4. SMT components are reflow soldered, typically in a forced convection oven. In this process, solder paste (a mixture of solder powder, flux and binder) is applied to the soldering pads of the PCB using a screen printer following which the component is placed onto the solder paste. The assembly is then heated so that the solder in the paste melts and re-solidifies to form the solder joints [12]. Because of the mechanical support offered by the hole, it is clear that the

solder joint is less critical in PTH mounting, so a dependence on solder joint integrity is a consequence of the added efficiency of SMT and particularly BGA technology.

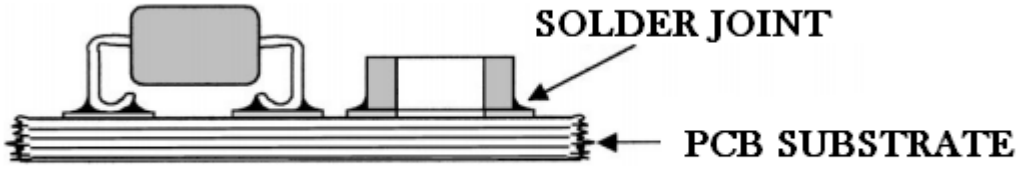

Figure 1.1: Surface mount attachment of PCB assembly [13]

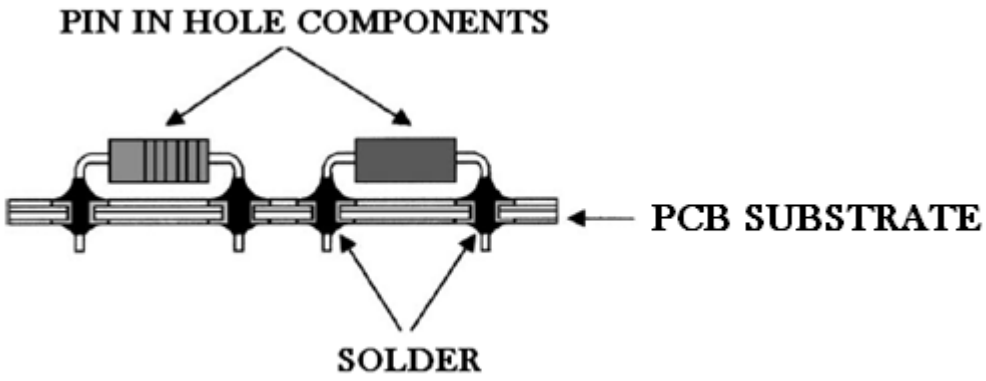

Figure 1.2 Cross section of pin through hole connection of a microelectronics component on a printed wiring board [13]

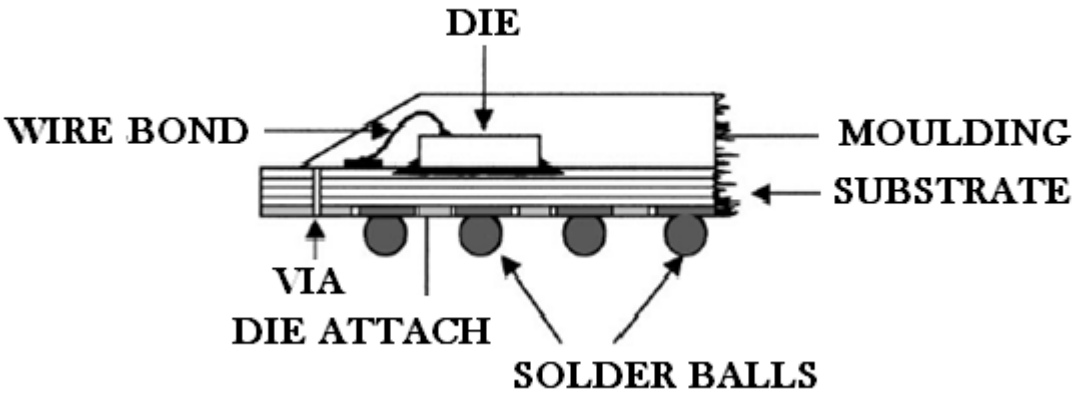

Figure 1.3: Cross section of a ball grid array (BGA) microelectronic component [13]

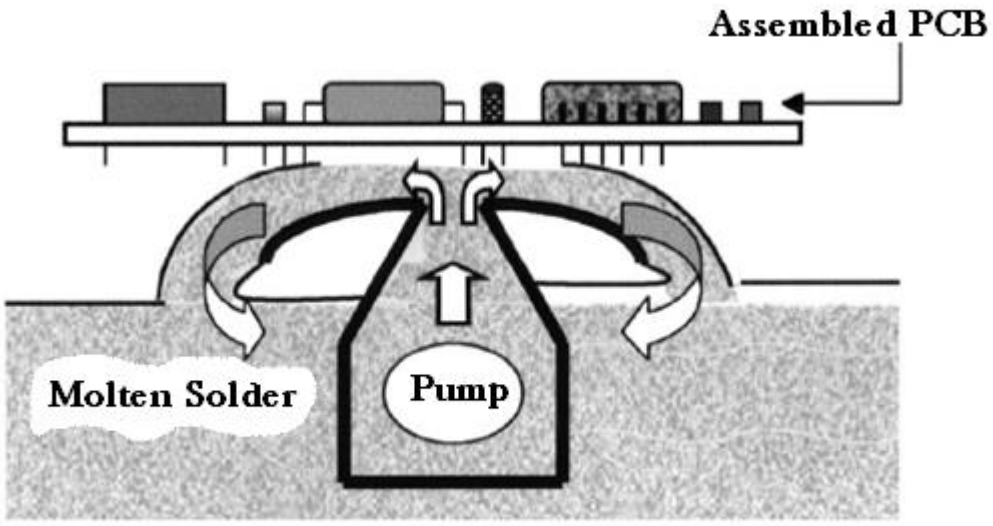

Figure 1.4: wave soldering of a PCB assembly [13]

1.2.2 Solder joint stress and strain in surface mount devices

The entire surface mount assembly, which typically consists of various materials with different properties, is subject to thermal stress and hence low-cycle strain-controlled fatigue, caused by power switching and external factors [14-19], such as warming up and cooling down of adjacent machinery or components. The assembly may also be subject to mechanical forces, for example due to vibration of the assembly and the associated inertial forces. Thus a given assembly may be subject to thermo-mechanical fatigue (TMF) at the frequency (although not necessarily in phase) of the thermal cycling, and mechanical fatigue, which is most likely to be at a higher frequency than the thermal cycling.

TMF is normally due to thermal loading from the environment or internal heating in service, the source being the significant mismatch in the coefficient of thermal expansion (CTE), α, of the component materials of the joint. Both spatial and temporal thermal gradients, coupled with the geometric constraints and thermal mismatch, generate thermally-induced stresses and strains in various parts of a joint. If these change with time, the resulting (generally low cycle, high strain range) fatigue loading can lead to crack initiation, crack propagation, and final failure. Figure 1.5 shows schematically how thermal cycling can result in the generation of a cyclic shear strain due to thermal mismatch in a simplified solder joint.

Table 1.1 shows CTE values for a range of materials used in electronics components and it is clear from the table that the main materials forming the slab-shaped components of Figure 1.5, silicon and glass-epoxy composites (more specifically FR-4 laminate), have widely different CTEs. As the solder joint is the least stiff component in the parallel shear loading system, so solders absorb most of cyclic damage during thermal fluctuations.

Solder joint strain is related to a shear displacement which depends on the thermal expansion of the component materials, the height of the solder joint (thickness), and the temperature excursion of the assembly. As illustrated in Figure 1.5 for the (more likely) case where the CTE of the substrate is greater than the CTE of the die/chip carrier, the substrate expands on heating by and amount $\alpha_s(T_{max} - T_0)$ per unit length, and the board expands by $\alpha_c(T_{max} - T_0)$ per unit length where α_c and α_s are the coefficients of thermal expansion for the component and board, respectively, and T_0, T_{max} are the ambient, and maximum temperatures. The difference between the two expansions will give the net shearing displacement for a given solder joint and can be written as:

$$\frac{1}{2}L(\alpha_s - \alpha_c)(T_{max} - T_0) \tag{1.1}$$

where L is the pitch of the solder balls, if in a BGA.

Similarly, when the temperature is cooled to T_{min}, the substrate contracts more on cooling by $\alpha_s(T_{min} - T_0)$ per unit length, and the board contracts by $\alpha_c(T_{min} - T_0)$ per unit length giving a net shearing displacement of:

$$\frac{1}{2}L(\alpha_s - \alpha_c)(T_{min} - T_0) \tag{1.2}$$

The difference in the displacement between T_{max} and T_{min} is given by

$$\Delta = \frac{L(\alpha_s - \alpha_c)(T_{max} - T_{min})}{2} \tag{1.3}$$

so, the shear strain

$$\gamma = \frac{\Delta}{h} = \frac{L(\alpha_s - \alpha_c)(T_{max} - T_{min})}{2h} \tag{1.4}$$

where *h* is the height of solder joint.

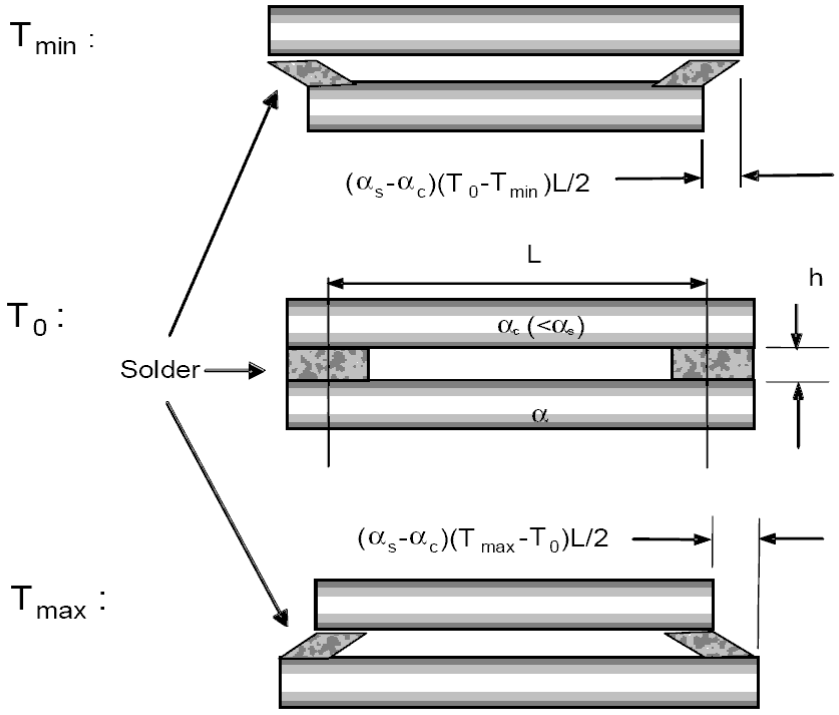

Figure 1.5: Schematic of shear strain due to thermal mismatch in solder joints [20]

Thus, the shear strain range is proportional to the CTE mismatch, the distance between balls and the temperature change, but inversely proportional to the height of the solder joint. This means that solder joints in surface mount technology applications are subject to low-cycle fatigue in shear, although they may also be subject to mechanical fatigue due, for example to vibrations between components and/or inertial vibration of the component.

Table 1.1: Coefficients of thermal expansion at room temperature

Materials	Coefficient of Thermal Expansion (CTE) [10^{-6}/°C]	Reference
Epoxy / Glass	12 / 70	[21]
(FR-4; $T < T_g$) (FR-4; $T > T_g$)	x,y (shear): 15.8 z (direct): 80-90 x,y: 20 z:400	[22]
Silicon	3.2	[23]
Copper	16.9 17 17.3	[22-24]
Tin	22	[25]
Silver	18.9	[26]
Nickel	12.8	[26]
Lead	29.1	[27]
Sn-37Pb	25 21	[28-30]
Sn3.8Ag0.7Cu	17.6 16.7	[31]
Solder mask	19	[28]

1.2.3 Solder alloy development

The main considerations for the selection of a solder alloy have been expressed as [32]:

- low melting temperature
- narrow plastic range
- good solderability (viscosity and wetting properties)
- good mechanical properties (including strength, ductility, creep resistance, fatigue and thermo-mechanical fatigue resistance) appropriate thermal expansion coefficient
- good corrosion resistance
- acceptable and consistent manufacturability
- no toxic problems
- low cost
- acceptable reparability / reworkability

- recyclability
- availability
- appropriate intermetallic compound formation
- joint reliability
- no large pasty range during cooling from liquid
- no commercial limitations, e.g. patents
- no more than three components
- adequate shelf life and performance of paste
- acceptably low dross formation (in wave soldering)

Of course, all of these properties are relative to the existing Pb-Sn eutectic alloy, and a consortium study conducted by the American National Center for Manufacturing Sciences (NCMS) concluded that there is no drop-in replacement for lead-based alloys [32].

A limited number of low-melting point elements can be used to replace lead as the basis metal for solders, a partial list (eliminating the more toxic metals) of whose key properties is as follows [33]:

- Tin (Sn): abundant, very low toxicity, stable in alloy form, easily workable, 231°C melting point, inexpensive.
- Bismuth (Bi): abundant, low toxicity, low ductility and difficult to work, 271°C melting point.
- Antimony (Sb): fairly abundant, very toxic, 419°C melting point.
- Zinc (Zn): abundant, inexpensive, low toxicity, very active chemically (giving corrosion and oxidation issues), 232°C melting point.
- Indium (In): rare and expensive, low toxicity, very ductile, 157°C melting point.

Potential solder alloys have melting points from 139°C to 227°C as seen in Table 1.2. Thus a variety of alternative solder alloys can be chosen for different applications.

Table 1.2: Examples of lead -free solder alloys covering board melting temperature ranges [34]

Category	Alloy composition (wt.%)	Melting range [°C]
Low melting temperature (< 180°C)	Sn-58Bi	138
	Sn-52In	118
Melting temperature (183°C to 200°C) equivalent to Eutectic Sn-37Pb solder	Sn-9Zn	198.5
	Sn-8Zn-3Bi	189-199
	Sn-20Bi-10In	143-193
Mid-range melting temperature (200°C to 230°C)	Sn-3.5Ag	221
	Sn-0.7Cu	227
	Sn-3.8Ag-0.7Cu	217
High melting temperature (230°C to 350°C)	Sn-5Sb	232-240
	Sn-80Au	280

The above list shows tin to be the only reasonable choice as basis metal for lead-free solders and the ability of tin to wet a wide range of substrates adds to its suitability. These solders were compared by the International Electronics Manufacturing Initiative (iNEMI) alloy selection group to determine the relative advantages and disadvantages of each [35, 36]:

- Sn-58Bi eutectic alloy with a melting temperature of 138°C, which is significantly lower than eutectic Sn-37Pb. This alloy shows better performance than Sn-37Pb in the NCMS thermal cycling tests for a range of components [37-40], but has a major disadvantage of the relatively high cost of Bi. The alloy is not compatible with tin-lead-component finishes, because the Sn-58Bi eutectic solder reacts with Pb to form some Sn-Bi-Pb ternary eutectic phases with a eutectic temperature of 96°C, which means the possibility of formation of very large “pasty” range and potentially poor solder joints [41].
- Sn-3.5Ag eutectic alloy with a melting temperature of 221°C considered suitable for wave soldering [42, 43] because its melting point is 4C° lower than Sn-Ag-Cu. The reliability of the alloy is better than Sn-Cu and Sn-Pb particularly in respect of creep resistance [44].
- Sn-0.7Cu eutectic alloy with a melting temperature of 227°C which is 10°C higher than Sn-Ag-Cu ternary eutectic. Because it does not contain Bi or Ag, it is the cheapest available lead free solder alloy. Its high melting temperature

makes it unattractive for reflow application, although the temperature of boards and components in wave soldering applications is much lower than in reflow soldering. In 2000, the IDEALS project [45-48] reported that the reliability of Sn-0.7Cu in early screening trials for plated-through-hole solder joints was poor and Sn-0.7Cu was eliminated as a candidate for wave soldering applications.

A number of ternary alloys have also come into consideration from time to time:

- Sn-8Zn-3Bi alloy has a melting range of 189-199°C which is slightly higher than eutectic Sn-37Pb. The presence of zinc causes many problems [49] such as: easy oxidization, potential corrosion, severe drossing in wave soldering, and very short shelf lives of pastes. The alloy also needs aggressive fluxes. The bismuth confers a number of advantages including, improved wettability, reduction of corrosion and lowered liquidus temperature.
- Sn-Ag-Bi system, with a melting range of 210°C to 217°C for Bi compositions from 3 to 5 wt% and Ag compositions ranging from 2 to 4 wt% [50, 51]. These alloys have shown excellent performance in SMT applications and have good solderability, but have been found to be subject to fillet lifting in through-hole joints with the tendency increasing with increasing Bi concentration in the range of 5-10% Bi [37-40]. When these alloys are used with tin-lead-component finishes, it is possible to form a low melting point Sn-Pb-Bi eutectic [41].
- Sn-Ag-Cu system with a melting range of 217°C to 227°C. These alloys, close to a ternary eutectic composition, show the most promise as lead-free solders. The Sn-3.8Ag-0.7Cu alloy was developed as an improvement on the Sn-Ag binary eutectic, said to have a ternary eutectic at 217°C, although the actual ternary eutectic composition is still a matter of debate. The alloy has been advocated as the best lead-free alloy for reflow based on reliability testing from 20°C to 125°C for up to 3000 cycles and power cycling from 25°C to 110°C for 5000 cycles [45-47], equal to, or better than, eutectic Sn-37Pb and Sn-Pb-Ag. There are three commercially-available Sn-Ag-Cu solders with "melting" temperatures near 217°C; Sn-3.5Ag-0.7Cu, which is available in Japan, and Sn-3.8Ag-0.6Cu and Sn-4Ag-0.5Cu, which are available in North America and Europe. All of these alloys have similar wetting characteristics, mechanical properties, and melting behaviour. The National Electronics Manufacturing Initiative NEMI lead-free group [46] recommends the Sn-3.9Ag-0.6Cu to the industry, a composition in the mid-way between Sn-3.8Ag-0.7Cu and Sn-4Ag-

0.5Cu. Based on the foregoing, many companies have chosen Sn-Ag-Cu as the alloy system to replace Sn-37Pb eutectic, and Table 1.3 shows the major properties recommended by the NCMS [37] as selection criteria. The primary criterion is, of course, the liquidus temperature (below 225°C) and the pasty range (less than 30C°). A drossing test was initially included because some Zn-containing alloys showed considerable oxidation during the wetting balance test. Moreover the selected alloys need to have good wettability and mechanical properties.

Table 1.3: Criteria for down-selection of lead-free alloys [37]

Property	Criterion/definitions	Limits
Liquid Temperature	Temperature at which solder alloy is completely molten.	< 225°C
Pasty Range	Difference between solidus and liquids temperatures. Represents the temperature range where the alloy is part solid and part liquid.	< 30°C
Wettability	Assessed by force required to wet a copper wire is wetted by molten solder. A large force indicates a good wetting, as does a short time to attain a wetting force of zero, and a short time to attain the two-thirds of the maximum wetting force.	F_{max} >300µN t_0 < 0.6s $t_{2/3}$ < 1s
Area of Coverage	Measures coverage of copper test piece by solder.	> 85%
Drossing	Measured by amount of oxide formed in air on the surface of molten solder after a fixed time at soldering temperature.	Qualitative scale
Thermo- mechanical Fatigue (TMF-1)	Cycles to failure for a given percent failed of a test population based on a specific solder joint and board configuration, as compared to eutectic Sn-Pb.	> 75%
Coeff. of Thermal Expansion (CTE)	Differences in coefficients of thermal expansion between alloys might create differences in thermal stresses.	< 29 ppm/°C
Creep	Stress required at room temperature to cause failure in 10,000 minutes is about 167 hours.	> 500 psi
Elongation	Relative elongation of material in uniaxial tension at room temperature.	> 10%

Table 1.4 gives a comparison of Sn-37Pb and Sn3.8Ag0.7Cu with regard to a number of key properties. In comparison with Sn-37Pb solder, the Sn-3.8Ag-0.7Cu alloy has higher melting point, which results in higher process temperatures, but also implies greater temperature resistance of the microstructure and, probably, higher cooling rates resulting in finer microstructures. Sn-3.8Ag-0.7Cu also has higher Young's modulus, homologous temperature (T_h), and lower CTE, all of which have implications for its mechanical performance in solder joints, Most importantly, the ternary alloy has higher

creep resistance and higher tensile strength both of which are attributable not only to the different basis metal, but also to the nature of the strengthening mechanism. Leaded solders rely essentially on a fine (eutectic) mixture of two relatively weak solid solutions, whereas the ternary alloy has a small proportion of second phase, but these are intermetallic compounds which are much more potent strengthens than solid solutions.

Table 1.4: Comparison between eutectic Sn-37Pb and Sn-3.8Ag-0.7Cu

Property	**Sn-37Pb**	**Reference**	**Sn-3.8Ag-0.7Cu**	**Reference**
Melting point [°C]	183	[52, 53]	217	[52, 53]
Reflow temperature [°C]	220	[52]	260	[52]
T_h	0.65	[54]	0.61	[54]
Toxicity	High	[52]	Low	[52]
Density [$^{g}/_{cm^3}$]	8.42	[53]	7.5	[53]
Surface Tension [$^{N}/_{m}$]	0.505	[55]	0.56	[55]
Voiding at microvia (% of Area)	5	[55]	21	[55]
Cost to fill solder pot(760 Kg) of eutectic Sn-Pb (US$)	3.960	[56]	5.742	[56]
CTE	25 21	[28-30]	17.6 16.7	[31]
Vickers Hardness [HV]	16 ± 1 12.9 10.08 12.8	[57],[58],[59], [60]	17 ± 1	[57]
Brinell Hardness [HB]	17	[53]	15	[53]
Yield stress [Mpa]	32	[61]	32.2	[61]
Elastic modulus, E [Gp_a]	46,44.9	[61]	47.1	[61]
Tensile Strength [$^{N}/_{mm^2}$] at strain rate:0.004 s^{-1} (20°C)	40	[53]	48	[53]
Creep Strength [$^{N}/_{mm^2}$]	3.3	[53]	13	[53]

1.3 Thesis objectives

Solder joints have to achieve permanent electrical and thermal connections, but they are also subject to failure resulting from mechanical damage caused by thermo-mechanical fatigue and or vibration. This thesis addresses the holistic implications of changing solder alloys from the mechanical point of view, covering the effects of alloy type, microstructure and mechanical behaviour on solder joint reliability in the face of increasing demands on joint miniaturisation. The study focuses on a comparison

between leaded and lead-free solder over a range of temperatures of interest with the following objectives:

- To design a set of experiments rig to investigate thermal mechanical fatigue (TMF) in leaded and lead- free solders.
- To isolate the behaviour of solder balls experimentally, under shear loading through a commercial glass-reinforced polymer (GRP) laminate substrate with a view to understanding the relative roles of mechanical and thermo-mechanical fatigue and creep.
- To study the effects of combined temperature cycling and vibration loading on plastic ball grid array (PBGA) solder joint fatigue life.
- To determine the influence of thermal exposure (ageing) on microstructure and micro-hardness and hence on the mechanical reliability of solder joints.

Chapter 2: Literature Review

This chapter is divided into four main sections comprising a critical review of the state of knowledge of thermo-mechanical performance of solder joints. The review commences with the constitutive behaviour of solder joints, commencing with elastic modulus measurement, followed by plastic and creep constitutive constants and then cyclic stress-strain behaviour (hardening and softening). This is followed by an examination of what is known about the thermo-mechanical degradation of solder joints under different loading conditions, including isothermal fatigue, thermal fatigue, and, finally, combined thermo-mechanical fatigue. Next, the state of knowledge of the effects of solder microstructure on relevant mechanical properties is reviewed with a view to selecting appropriate alloys and conditions for this study. Finally in this chapter, the experimental techniques that have been used to study fatigue in solders are critically compared in terms of how they contribute to understanding of the phenomena involved in thermo-mechanical degradation of solders.

2.1 Constitutive properties of solder

Solder strain behaviour can be characterised using a linear combination of three components: rate-independent elastic strain (ε_e), rate-independent plastic strain (ε_p), and rate-dependent creep strain (ε_c).

$$\varepsilon_t = \varepsilon_e + \varepsilon_p + \varepsilon_c \tag{2.1}$$

A simple rheological model for solder, shown in Figure 2.1, consists of a spring, a damper and a parallel spring-slider combination to represent the elastic, plastic, and creep portions respectively.

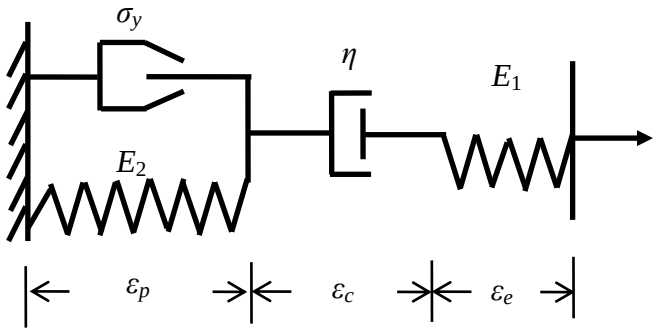

Figure 2.1: Rheological model representing solder behaviour [62]

This rheological model will respond to a stress as shown in Figure 2.2.

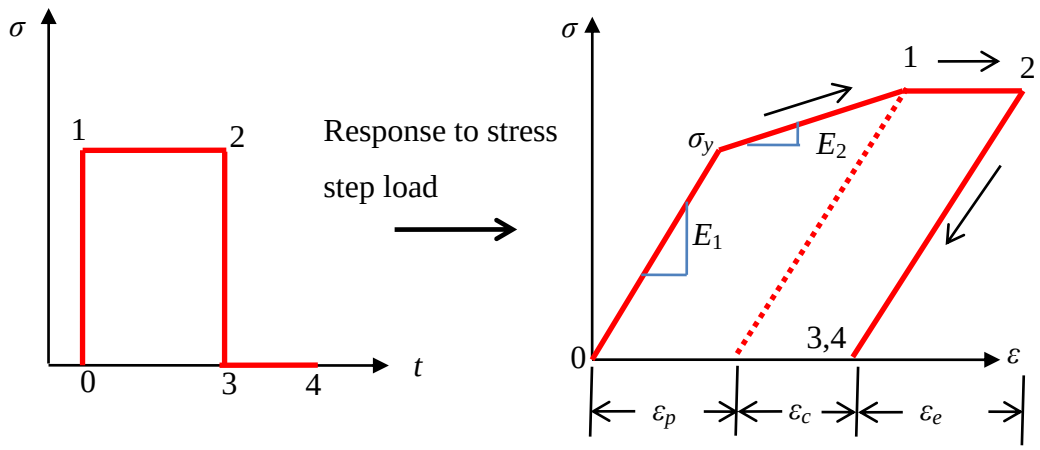

Figure 2.2: Stress-strain response for simple rheological model of solder to a step stress load [62]

This variation in the nature of the mechanical response makes it difficult to directly compare results from experimental and modelling methods. Aside from the constitutive behaviour, there are many other factors that influence the mechanical properties of solder joints, including: strain rate, solder joint geometry, intermetallic layer thickness, temperature, solder joint manufacture, microstructure, alloy composition, substrate material, specimen test methods, solder volume, solder area in contact with substrate, fabrication process and joint quality. The unclear constitutive behaviour and the variation in solder joint quality are probably the two most important factors influencing the wide variation in reported mechanical properties of solders.

2.1.1 Elastic behaviour of solders

Elastic strain is rate-independent recoverable deformation. Considering only uniaxial components, the relationship between applied stress and strain is given by Hooke's law, as shown below:

$$\varepsilon_e = \frac{\sigma}{E} \tag{2.2}$$

where E is the Young's modulus, and σ is the applied stress.

The shear modulus is related to the elastic modulus and Poisson's ratio by the equation:

$$G = \frac{E}{2(1+\nu)} \tag{2.3}$$

where

G = Shear modulus

v = Poisson's ratio which is the ratio of lateral and longitudinal strains

E = Young's modulus

Since some mechanical properties reported in the literature are obtained from shear tests and some from tensile tests, the following standard von Mises relations are employed to compare the results in terms of the effective strains and stresses:

$$\tau = {}^{1}/_{\sqrt{3}}\,\sigma \tag{2.4}$$

$$\gamma = \sqrt{3}\varepsilon \tag{2.5}$$

One of the reasons for the variation in reported elastic modulus in solder joints from different manufacturers could be the cooling rate which determines the grain size and microstructure of the solder joint [63-66], given that the moduli of lead, tin and various intermetallic compounds can vary substantially. Another possible factor is the consistency of actual solder area in contact with the substrate. For example, Basaran *et al*. [67] have suggested that the presence of voids in Sn-37Pb ball grid array packages will lead to an overestimate of the projected contact area and hence an underestimate of Young's modulus. They compared three specimens from three different major USA semiconductor manufacturers and found that specimens with voids had one third the apparent elastic modulus of void-free specimens (E_{void} = 11.79 GPa and $E_{void\text{-}free}$ = 38.64 GPa) and mention that it is very difficult to produce void-free solder joints in microelectronic packaging.

Since elastic deformation is time-independent, the shear modulus should not change with strain rate [68-72]. Tang *et al*. [69] measured the constitutive properties of Sn-37Pb solder in a ball grid array package at a range of temperatures and strain rates. They described the shear modulus by the following equation:

$$G[\mathrm{GPa}] = 19.44 - 0.039 \times T[\mathrm{K}] \tag{2.6}$$

It can be seen from the Figure 2.3 that the value of G = 7.7 GPa fits all of the strain rates at room temperature reasonably well, although it is clear that the yield shear stress and plastic behaviour are influenced considerably by the strain rate.

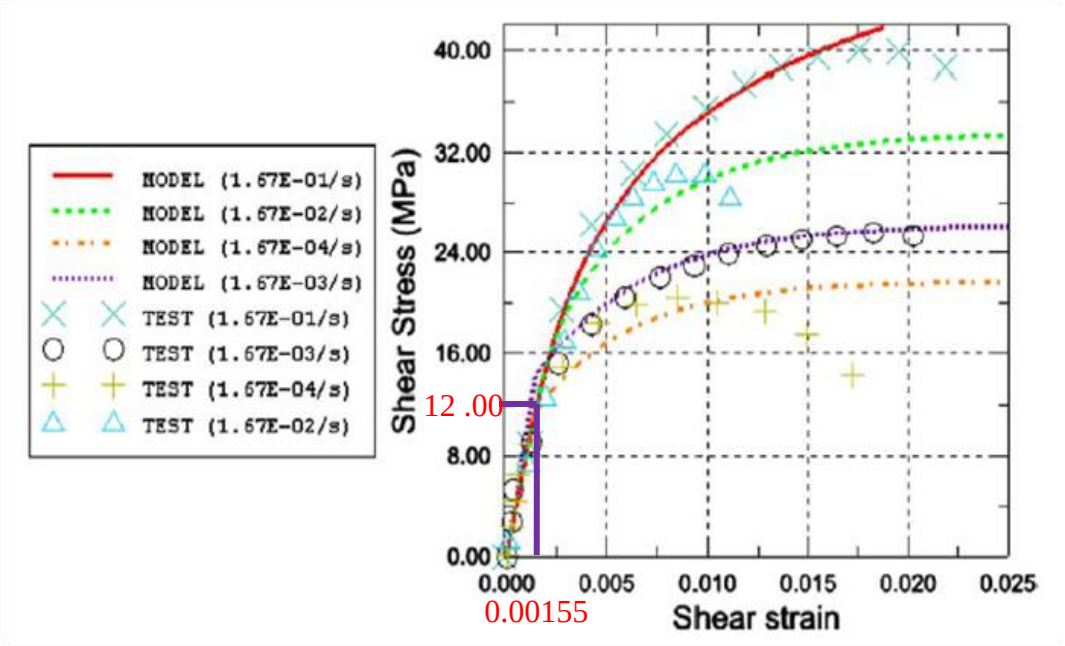

Figure 2.3 Comparison of simulations and experimental results from uniaxial tension tests on Sn-37Pb BGA at room temperature for different strain rates [68]. Elastic region highlighted by author.

Mukai *et al*. [70] performed tension tests on Sn-37Pb thin walled cylindrical specimens and investigated the elastic and creep behaviour of this alloy at room temperature. Young's modulus was found to be E = 20 GPa again not affected by strain rate and this was included in their numerical simulations (Figure 2.4).

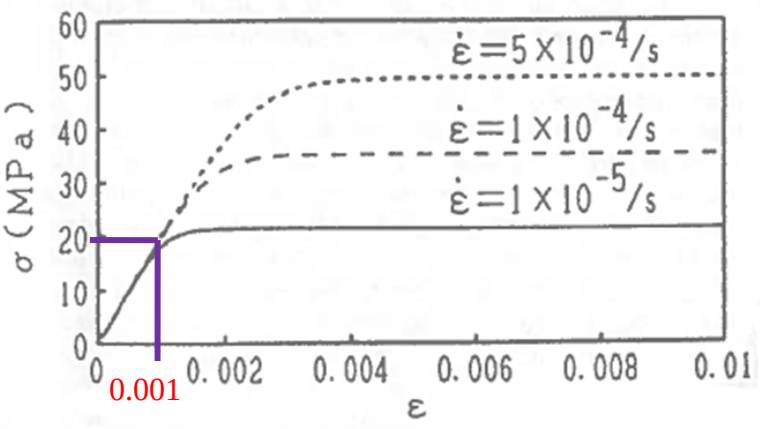

Figure 2.4: Numerical simulation of stress -strain behaviour in Sn-37Pb at room temperature using an elastic- creep model [70]. Elastic region highlighted by author.

Sefton *et al*. [71] studied the effect of strain rate on the deformation of cylindrical Sn-3.5Ag specimens. From Figure 2.5 it is clear that they have assigned a best-fit stress-strain slope independent of strain rate and temperature but that the yield shear stress increases with increasing strain rate and decreases with increasing temperature.

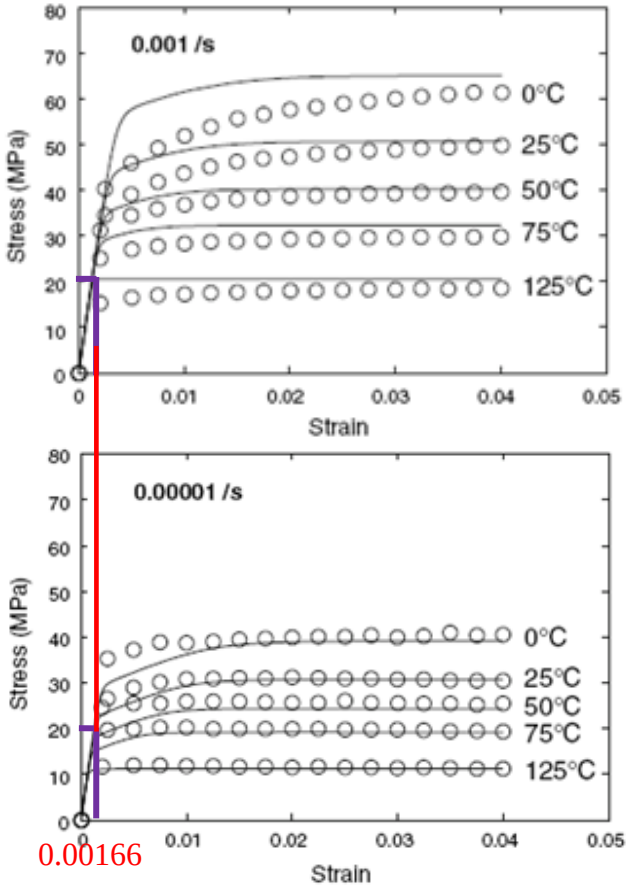

Figure 2.5: Measured stress-strain behaviour during fixed-rate compression testing of Sn-3.5Ag (open circles) compared to model predictions [71]. Elastic region highlighted by author.

Bonnaud *et al*. [72] set up a constitutive model based on measurements under monotonic loading at three strain rates (0.2, 1, 5 sec^{-1}) of Sn-Ag-Cu-Ni lead free solder bulk specimens at room temperature. Figure 2.6 highlights the elastic portion of the measurements and model which used a Young's modulus E = 20 GPa, independent of the strain rate. Again, the yield shear stress increased with increasing strain rate.

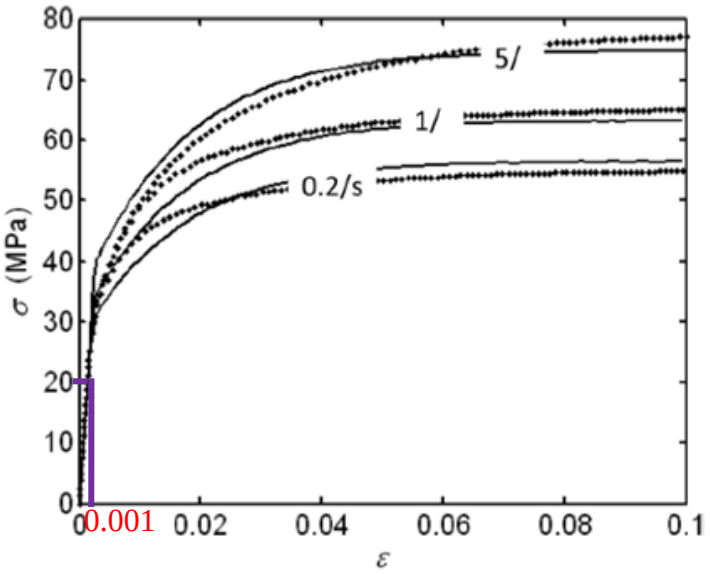

Figure 2.6: True stress vs. true strain for monotonic loading of Sn-Ag-Cu-Ni up to necking at three strain rates (0.2/s, 1/s, 5/s): experiment (dotted lines) and model prediction (solid lines)[72]. Elastic region highlighted by author.

Despite the above, some researchers have suggested that Young's modulus depends on strain rate. For example, Shi *et al*. [73] investigated the effect of temperature and strain rate on the mechanical properties of Sn-37Pb bulk solder specimens. Variations of the modulus as a function of temperature and strain rate are illustrated in Figure 2.7 indicating, for example, that Young's modulus at room temperature increased from 11.7 GPa at 2.78×10^{-5} sec^{-1} to 30.5 GPa at 2.78×10^{-1} sec^{-1}. As with Figures 2.3 to 2.6, Shi *et al*.'s published raw stress-strain curves do not reveal a distinguishable variation in modulus, but the authors indicate that magnification of the curves reveals differences.

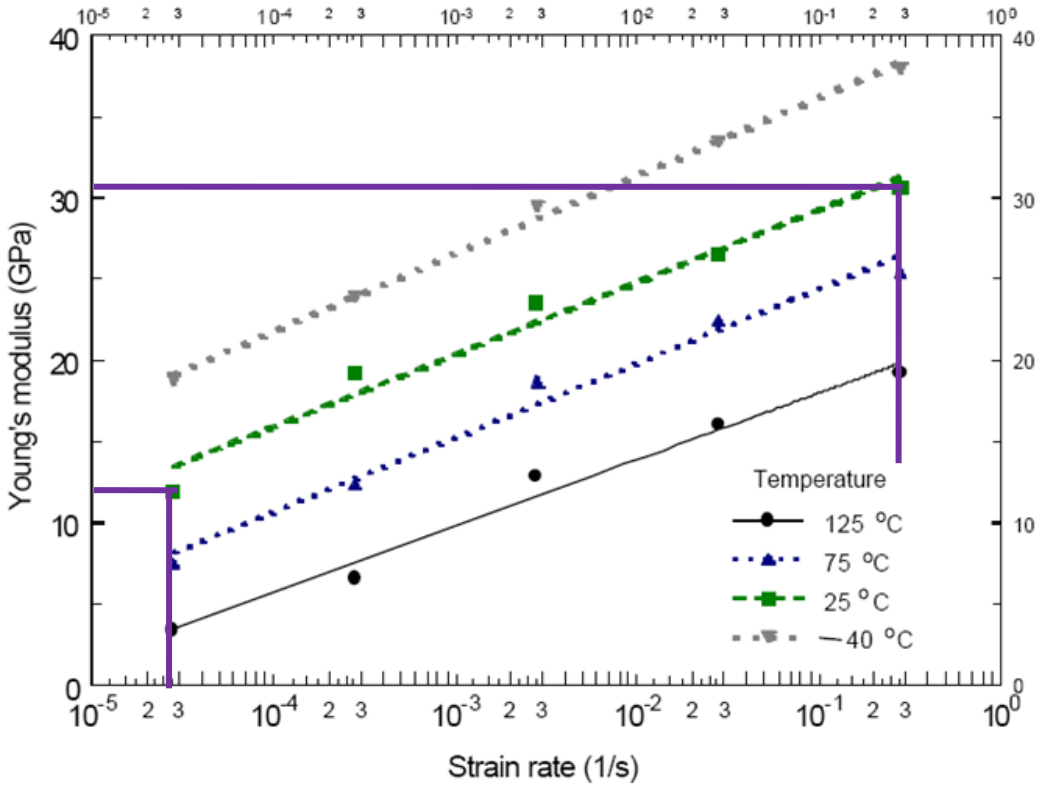

Figure 2.7: Effect of strain rate and temperature on Young's modulus of Sn-37Pb [73]. Highlighted changes for 25°C added by author.

Similarly, Pang *et al.* [74] conducted shear tests on 95.5Sn-3.8Ag-0.7Cu bulk specimens and have published shear stress-strain plots for three different strain rates (2.6×10^{-2}, 2.6×10^{-3} and 2.6×10^{-4} sec^{-1}) indicating values of 0.05, 0.03 and 0.025 GPa, respectively, as can be seen from Figure 2.8. It would appear that there is an error in one or both of the scales, as there values are extremely low. Perhaps more reliable are the summarised moduli based on tensile test results shown in Table 2.1.

Table 2.1: Summary of tensile test results for bulk 95.5Sn-3.8Ag-0.7Cu solder at room temperature [75, 76]

Strain rate [1/s]	***E* [GPa]**
5.6×10^{-4}	44.4
5.6×10^{-3}	50.3
5.6×10^{-2}	58

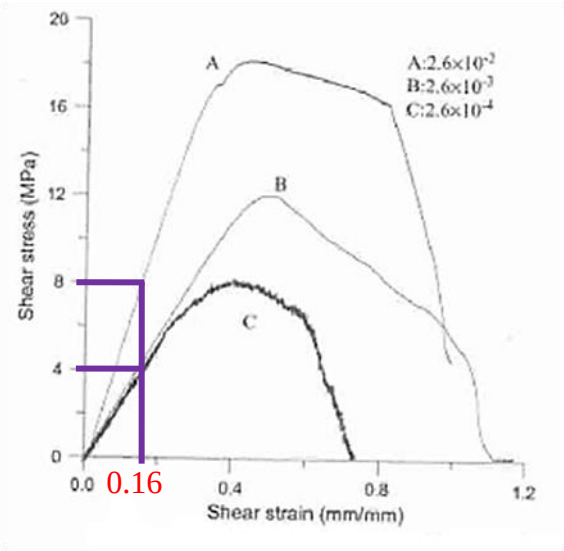

Figure 2.8: Shear stress-strain plot for 95.5Sn-3.8Ag-0.7Cu at 25°C [74]. Highlighted changes with strain rate added by author.

Enns, *et al*. [77, 78] found that the Young's modulus of both Sn-40Pb solders and FR-4 glass/epoxy decreased with increasing strain rate (cyclic frequency) at a given temperature, varying, for example, between 3.32 GPa at 30 Hz to 1.68 GPa at 0.033 Hz. It can be seen from Figure 2.9 and 2.10 that the relationship between modulus and frequency and temperature is quite complex for both the solder and the GRP. Enns, *et al*. obtained Young's moduli as shown in figures 2.9 and 2.10 by performing a bending mechanical test. Some of their data was obtained from an unpublished source and therefore this information cannot be evaluated fully. This data is not used in the rest of this thesis and therefore does not influence the investigation.

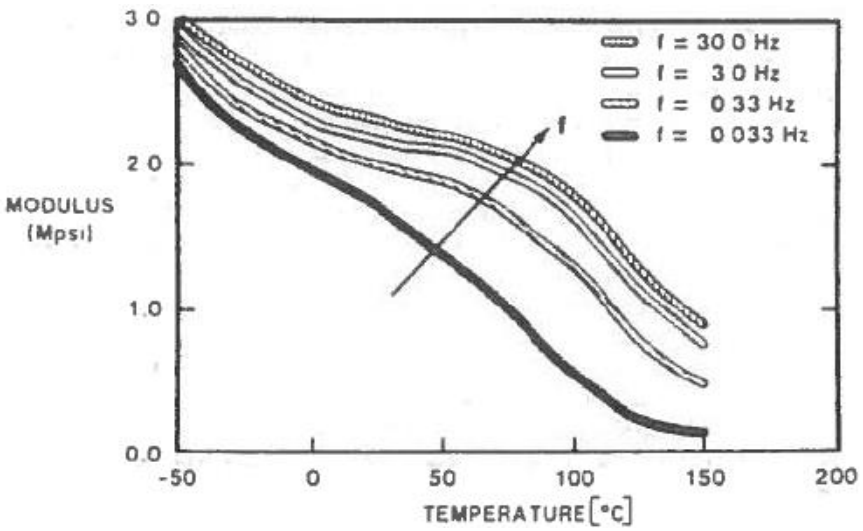

Figure 2.9: Modulus change for Sn-40Pb as a function of temperature and frequency [77, 78]

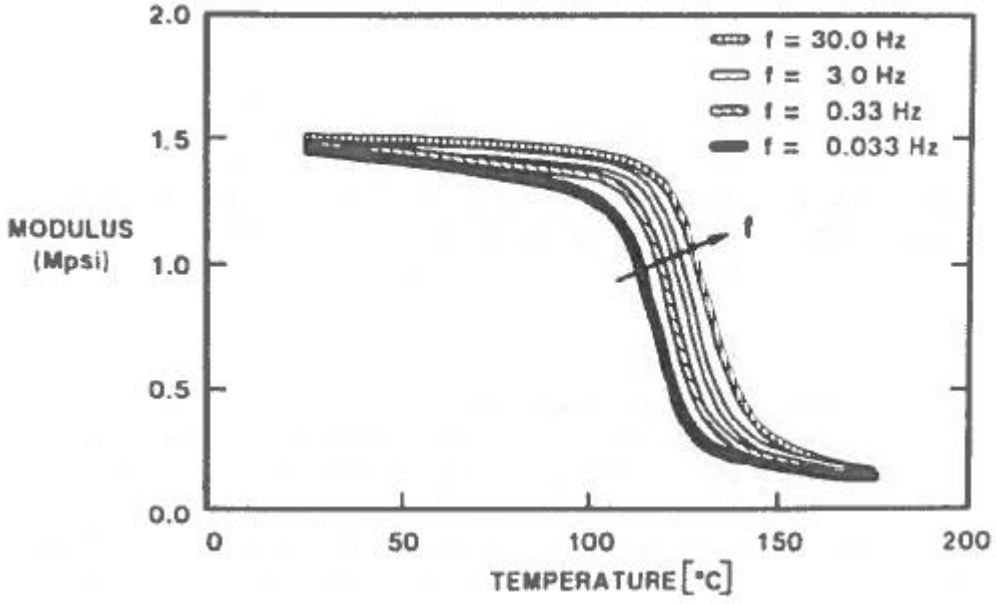

Figure 2.10: Modulus change for FR-4 glass/epoxy as a function of temperature and frequency [77, 78]

Kim *et al*. [66] investigated the effect of cooling rate and strain rate on the mechanical properties of Sn-3.5Ag-0.7Cu, stress-strain curves being shown in Figure 2.11. It was observed that the modulus for the rapidly cooled specimen was lower than the slowly cooled at a strain rate of 10^{-2} sec^{-1} whereas the modulus for rapidly cooled was lower than slowly cooled at a strain rate of 10^{-4} sec^{-1}. Hence, the microstructure affects not only the modulus, but also the strain rate sensitivity of this type of alloy.

Zhang *et al*. [79, 80] investigated the dependence of Young's modulus on temperature for Sn-37Pb and Sn-3.9Ag-0.6Cu solder alloys. The modulus was determined from the unloading slopes of a monotonic test and the first reversing slopes of cyclic loading, and the results are summarised by the following equations:

E [GPa]=18.9 -0.044T [^{o}C] for Sn-37Pb (2.7)

E [GPa] =18.6 -0.021T [^{o}C] for Sn-3.9Ag-0.6Cu (2.8)

A similar experiment was used by Haswell *et al*. [81] for Sn-3.9Ag-0.6 Cu and Sn-37Pb solder joints, the shear modulus being calculated from the unloading slopes of monotonic tests. Their results were again expressed as equations:

G[MPa]=5789 -7.26T [K] for Sn-37Pb (2.9)

G[MPa] =3400 -4.03T [K] for Sn-3.9Ag-0.6Cu (2.10)

from which it can be found that G=3.62 GPa for the leaded solder alloy, and 2.19 GPa for the lead-free solder alloy at room temperature.

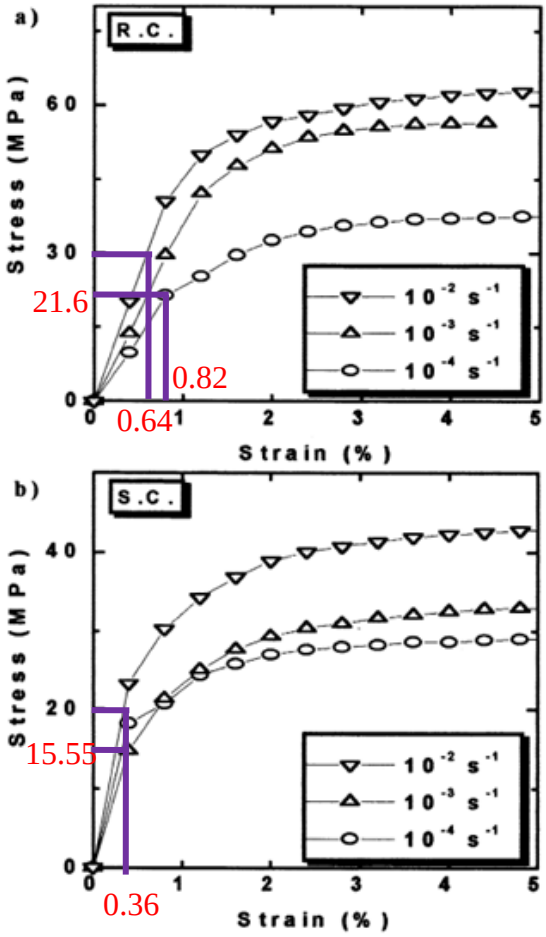

Figure 2.11: Engineering stress-strain curves in tensile tests at different strain rates and cooling speeds(R.C. and S.C. standing for rapidly and slowly cooled) for Sn-3.5Ag-0.7Cu [66]. Elastic region highlighted by author.

Darveaux *et al*. [82] have assumed that the temperature dependent shear modulus for 95.5Sn-3.5Ag is the same as that for pure tin and the temperature dependent shear modulus for 62Sn-36Pb-2Ag is equal to that of Sn-40Pb. Others have estimated Young's modulus form the constituent elements of an alloy, e.g. Enke, et al.[83] for 60Sn-40Pb solder:

$$E_{60/40\ solder} = 0.6 \times E_{tin} + 0.4 \times E_{lead} = 0.6(50) + 0.4(40) = 36\ GPa \qquad (2.11)$$

Enke *et al*. [83] have also summarised the data reported in the literature for Young's modulus of 60Sn-40Pb solder alloy and found that it ranged from 15 to 35 GPa and others [84-86] have described the shear modulus for 63Sn-37Pb by:

$$G = \frac{63.875 - 0.137 \times T[\mathrm{K}]}{2(1+\nu)}\ [GPa] \qquad (2.12)$$

Table 2.2 offers a summary of the published values of shear modulus obtained from mechanical tests on solder alloys at room temperature.

Table 2.2: Summary of published data for shear elastic modulus for lead and lead-free solder alloys at room temperature, , along with strain rate, where given

Materials	Shear modulus [GPa]	Strain rate [sec^{-1}]	Reference
Sn-3.9Ag-0.6Cu	6.45 6.66	1×10^{-1}	[79, 80]
Sn-3.9Ag-0.6Cu	2.19	1×10^{-4} to 1×10^{-1}	[81]
Sn-3.8Ag-0.7Cu	13.2		[87]
Sn-3.5Ag-0.75Cu	2.54		[88]
Lead-free solder	3.9-9.28		[60]
Sn-3.8Ag-0.7Cu	15.8 20.7	5.6×10^{-4} 5.6×10^{-2}	[74, 75]
Sn-3.5Ag	2.4	1×10^{-2}	[89]
Sn-3.5Ag	11.4	1×10^{-2}	[90]
Sn-3.5Ag	4.9		[91]
solder	5.59		[92]
solder	5.35		[93]
solder	7		[94, 95]
Sn-37Pb	6.35 6.25	1×10^{-1}	[79, 80]
Sn-37Pb	3.62	1×10^{-4} to 1×10^{-1}	[81]
Sn-37Pb	5.71		[87]
Sn-37Pb	4.17	2.78×10^{-5}	[73]
Sn-37Pb	10.89	2.78×10^{-1}	[73]
Sn-37Pb	9.6	1×10^{-2}	[90]
Sn-37Pb	7.99	1×10^{-3}	[96]
Sn-37Pb	7.19		[97, 98]
Sn-37Pb	8.2		[84-86]
Sn-37Pb	7.7 7.8	1.67×10^{-4} to 1.67×10^{-1}	[68]

Continued

Table 2.2: Summary of published data for shear elastic modulus for lead and lead-free solder alloys at room temperature, along with strain rate, where given

Materials	Shear modulus [GPa]	Strain rate [sec^{-1}]	Reference
Sn-37Pb	7.9		[99]
Sn-Pb	7.4		[100]
Sn-40Pb	10.89	1×10^{-1}	[101]
Sn-36Pb-2Ag	11.5	1×10^{-1}	[101]
Sn-Pb -2.5Ag	7.6		[102]

It is appears that the varying methods of testing and manufacturing produce a wide range of what might be expected to be a relatively indisputable property. Overall, Young's modulus of lead-free solder alloys vary from 11 GPa to 26 GPa [60] and between 9 and 48 GPa for Sn-Pb [67].

2.1.2 Plastic behaviour of solders

Whereas the elastic properties might be expected to remain constant with basis alloy, this is not the case for yield stress and beyond. Table 2.3 summarises the data reported in the literature for yield shear stress of leaded and lead-free solders at room temperature, exhibiting a huge range between 8 to 87.2 MPa. The primary reason for the observed variations is the strain rate [73, 76, 103, 104], although other possibly contributory factors include joint size [105, 106] solder joint manufacture (cooling rate) [66] and alloy composition [106].

Table 2.3: Summary of yield shear stress of solders from literature, along with strain rate, where given

Solder alloy	Yield shear stress [MPa]	Reference
Sn-0.7Cu	27.5 at 10^{-2} sec^{-1}	[90]
Sn-37Pb	24.9 at 10^{-2} sec^{-1}	[90]
Sn-3.8Ag-0.7Cu	18.35	[107]
Sn-3Ag-0.5Cu	14.14	[108]
Sn-3.8Ag-0.7Cu	20.26 5.6×10^{-4} sec^{-1} 23.5 5.6×10^{-3} sec^{-1} 29.5 5.6×10^{-2} sec^{-1}	[76]
Sn-3Ag-0.5Cu-0.019Ce	36.5 at 0.01 sec^{-1} 53.7 at 0.1 sec^{-1} 87.2 at a strain rate 1 sec^{-1}	[109]
Sn-3.8Ag-0.7Cu	8	[110]
Sn-Ag-Cu	14.1-24.4 depending on micro bump size	[105]
Sn-Ag-Cu-Sb	19	[111]
Sn-37Pb	17.4	[111]
Sn-40Pb	55	[83]

Plastic strain is rate-independent irrecoverable deformation, typically due to dislocation pileups from lattice defects, although other mechanisms, such as twinning may be present in tin. The rate independent plastic strain is usually described by a power law equation as:

$$\tau = C_{pl}\gamma_{pl}^{n} \qquad (2.13)$$

where τ is the shear stress, γ_{pl} is the shear plastic strain and C_{pl}, n are temperature-dependent material constants.

The plastic properties of lead Sn-37Pb and lead-free Sn-3.9Ag-0.6Cu solders were measured at 25°C, 75°C, and 125°C by Zhang *et al*. [80] and their stress-strain plots are shown in Figure 2.12. As can be seen Sn-3.9Ag-0.6Cu exhibits larger plastic deformation than Sn-37Pb for a given stress level at each of the three different temperatures, Haswell *et al*. [81] also measured the plastic properties of the lead Sn-37Pb and lead-free Sn-3.9Ag-0.6Cu solders, and the plastic model parameters from these studies are summarised in Table 2.4.

Table 2.4: Plastic model constants for Sn-37Pb and Sn-3.9Ag-0.6Cu solders

Solder alloy	C_{pl} [MPa]	n	Reference
Sn-37Pb	76.8 -0.28×T [^{o}C]	0.25 -0.00028×T [^{o}C]	[80]
Sn-3.9Ag-0.6Cu	60.1 -0.18×T [^{o}C]	0.29 -0.00046×T [^{o}C]	[80]
Sn-37Pb	106.6 -0.217×T [K]	0.272-0.0007×T [K]	[81]
Sn-3.9Ag-0.6Cu	141.8 -0.307×T [K]	0.651-0.0015×T [K]	[81]

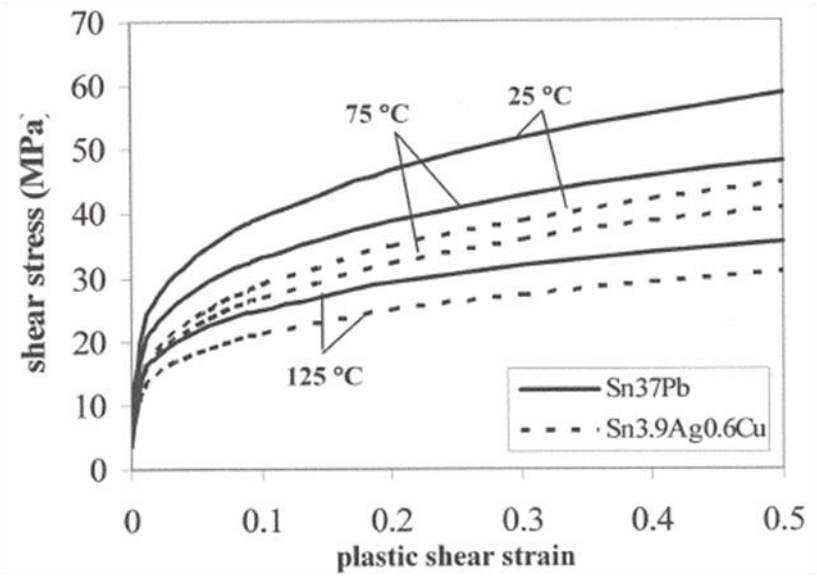

Figure 2.12: Plastic shear-strain stress curves for Sn-37Pb and Sn-3.9Ag-0.6Cu solders

2.1.3 Creep behaviour of solders

Creep is the time dependent deformation of a material when subjected to a constant load or stress and occurs at homologous temperatures greater than $0.4T_m$ (where T_m is the absolute melting temperature) [112]. Creep involves time-dependent deformation mechanisms such as diffusion-controlled dislocation motion or the migration of vacancies, either through the matrix or along grain boundaries, which are thermally activated processes.

To investigate the creep behaviour of metallic materials, the strain is continuously measured at a range of temperature and stresses until fracture. A typical constant stress

creep deformation curve consists of three regions of creep behaviour, namely primary, secondary and tertiary creep as shown in Figure 2.13.

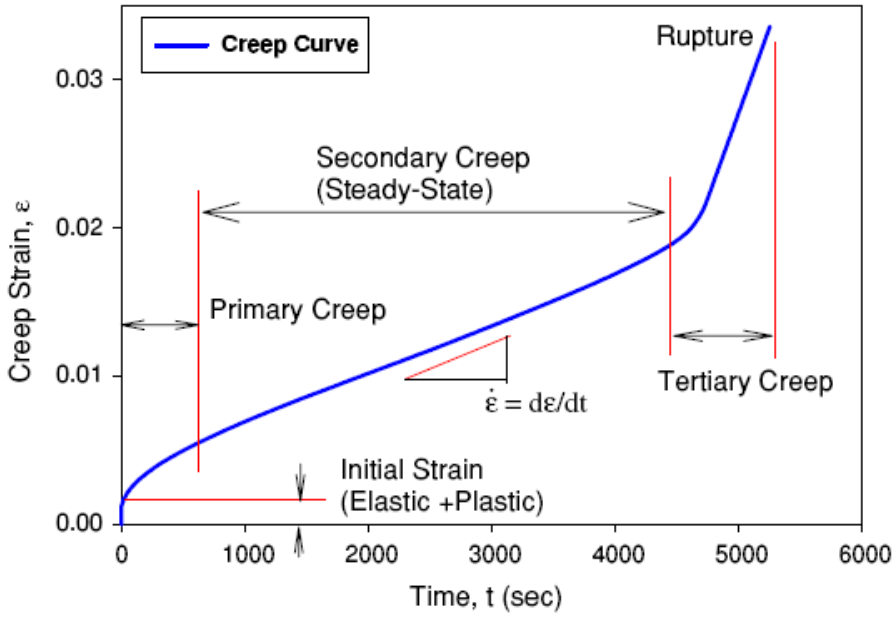

Figure 2.13: Typical creep curve for lead free solders [113-115]

Upon application of the load there is an immediate elastic strain. After this, primary or transient creep occurs at a diminishing creep rate, followed by secondary (or steady-state) creep at a constant rate, and, finally, a tertiary stage, in which the strain rate increases with time until failure.

Steady state creep is of the most engineering significance because it has the simplest and the most reproducible behaviour and is often used for design and characterisation of behaviour. In general, three different models are used to quantify the steady state creep rate [116]:

- The Arrhenius model, most applicable for creep at low stresses:

$$\dot{\varepsilon}_c = A\sigma^n \exp\left(-\frac{Q}{RT}\right) \tag{2.14}$$

or

$$\dot{\varepsilon}_c = A\sigma^n \exp\left(-\frac{C}{T}\right) \tag{2.15}$$

- The Garofalo sinh Law which is most suitable for low to medium stresses.

$$\dot{\varepsilon}_c = A[\sinh(\alpha\sigma)]^n \exp\left(-\frac{Q}{RT}\right) \quad (2.16)$$

or

$$\dot{\varepsilon}_c = A[\sinh(\alpha\sigma)]^n \exp\left(-\frac{C}{T}\right) \quad (2.17)$$

- The double power law, which is based on dislocation glide and is believed to be most applicable at medium and high stresses:

$$\dot{\varepsilon}_c = A_1\sigma^{n_1} \exp\left[-\frac{Q_1}{RT}\right] + A_2\sigma^{n_2} \exp\left[-\frac{Q_2}{RT}\right] \quad (2.18)$$

In all of the above, $\dot{\varepsilon}_c$ is the creep strain, σ is the applied stress, n is the stress exponent, R is the universal gas constant, T is the absolute temperature in k, Q is an activation energy. A_1, A_2, n_1, n_2 are creep constants.

Creep occurs by a number of different mechanisms depending on the applied stress and temperature. Deformation maps (e.g. Figure 2.14) are often used to illustrate the dominant creep mechanism for specific circumstances by plotting stress versus homologous temperature. At higher stress levels (in excesses of the yield stress) the creep deformation involves dislocation glide and climb and generally moving away from barriers. At lower stress levels, lattice diffusion may be the dominant creep mechanism, involving the diffusion and migration of interstitial atoms and lattice vacancies along the grain boundaries under applied tension. Grain boundary sliding can also occur along with the above mechanisms at any stress level. This is a process where grains become displaced with respect to each other but exhibit no significant elongation.

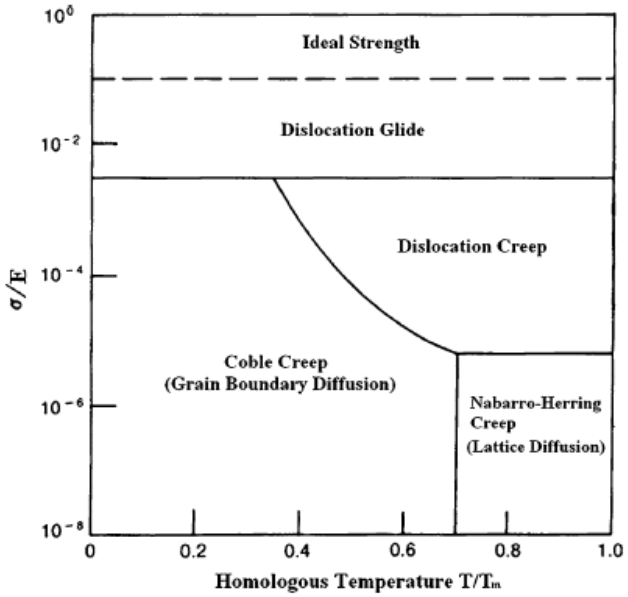

Figure 2.14: A typical creep deformation map [113]

Figure 2.15 illustrates the processes of dislocation glide and dislocation climb. Dislocation glide is the movement of, say, an edge dislocation along a crystal lattice plane and can occur under a shear stress only, whereas climb its movement in a direction normal to its slip plane and requires thermal activation. Once climb has occurred, the dislocation will be free to move. When the free dislocations start to glide, they may become tangled again with other obstacles. The process will then start again. Clearly, the rate of climb depends on the number of vacancies in the lattice, which is proportional to the temperature.

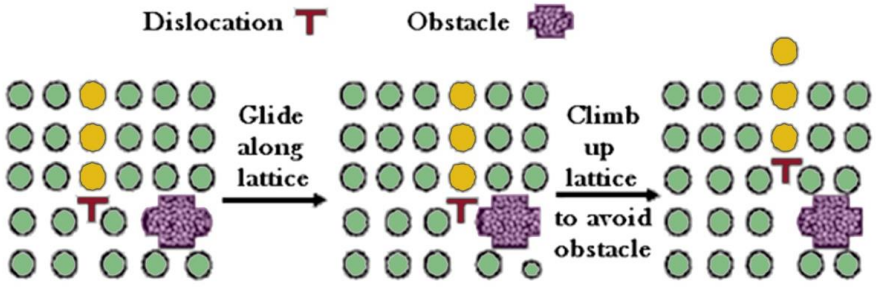

Figure 2.15: Edge dislocation glide and climb mechanism [117]

Diffusional creep involves the stress-directed flow of vacancies that takes place in order to restore an equilibrium condition (Figure 2.16). It can be manifest as lattice or grain

boundary diffusion; Nabarro-Herring and Coble creep respectively. The Nabarro-Herring mechanism dominates the creep process at low stress levels and high temperatures, greater than $\frac{T}{T_m}$ = 0.7. Coble creep is dominant at lower temperatures, but both Nabarro-Herring and Coble mechanisms are favoured by high temperatures and low stress levels.

Diffusion in Coble creep occurs along the grain boundaries rather than in the bulk, so more diffusion paths are available when the grain size is small. Coble and Nabarro-Herring mechanisms are parallel processes and the creep rate due to diffusional flow is considered to be the sum of each, as represented below:

$$\dot{\varepsilon}_t = \dot{\varepsilon}_{NH} + \dot{\varepsilon}_C \qquad (2.19)$$

where ε_{NH} and ε_C are the contributions from Nabarro-Herring and Coble creep respectively.

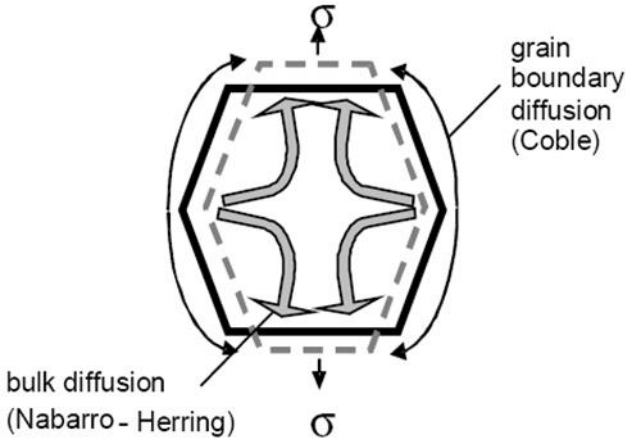

Figure 2.16: Mechanisms of diffusion creep [118]

The values of creep exponent and activation energy are important in the determination of dominant creep mechanisms occurring in particular materials under specific conditions. Table 2.5 summarises the various domains of creep and gives typical values of *n* and *Q* associated with various creep mechanisms, where $Q_{SD,}$ $Q_{core,}$ and Q_{GB} are the activation energies for self-diffusion, core diffusion and grain boundary diffusion respectively.

Table 2.5: Variation of creep exponent and activation energy with stress and temperature [119]

Creep Process	Temperature	Stress	*n*	*Q*
High temperature Dislocation creep	Above $0.7T_m$	Intermediate/High	>3	~ Q_{SD}
Low temperature Dislocation creep	~0.4-$0.7T_m$	Intermediate/High	>3	$Q_{\text{core (pipe)}}$
High temperature Diffusional creep	Above $0.7T_m$	Low	~1	Q_{SD}
Low temperature Diffusional creep	~0.4-$0.7T_m$	Low	~1	Q_{GB}

Extensive research has been performed on the creep properties of tin-lead and lead-free. Available data for solder alloys are summarised in Tables 2.6 to 2.10, according to the parameters in Equations 2.14 to 2.18. Since some creep model constants reported in the literature are obtained from shear tests and some from tensile tests, the following standard von Mises relations are employed to compare the results in terms of the effective strains and stresses:

$$\sigma = \sqrt{3}\tau \tag{2.20}$$

$$\varepsilon = \frac{1}{\sqrt{3}}\gamma \tag{2.21}$$

As with the data for modulus and yield stress, there is considerable variation in parameters, even when the same regimes of stress and temperature and the same moiled are used. Some of this is attributable to varying methods of testing, joint geometry, intermetallic thickness, manufacture and solder volume, but some may well be due to the degree of fit that is achieved over several dimensions of experimental variable, a matter that is taken up later in the discussion.

Table 2.6: Measured parameters for Arrhenius creep model for solder alloys (eq. 2.14)

Solder alloy	Constants			Reference
	A [s^{-1}]	n	Q [KJ/mol]	
Sn-3.5Ag	5×10^{-6}	11	79.8	[120]
Sn-3.5Ag	9.44×10^{-5}	6.05	61.1	[121]
Sn-4.0Ag-0.5Cu	2×10^{-21}	18	83.1	[120]
Sn-Ag-Cu	1.5×10^{-9}	8.2	71	[122]
Sn-Ag-Cu-Ce	6.2×10^{-11}	8.0	80	[122]
80Au-20Sn	8.37×10^{5}	2.07	102	[123]

Table 2.7: Measured parameters for Arrhenius creep model for solder alloys (eq.2.15)

Solder alloy	Constants			Reference
	A [s^{-1}]	n [MPa^{-1}]	C [K]	
Sn-Ag-Cu	1.3037×10^{-5}	6.41	6500	[124]
Sn-3Ag-0.5Cu-0.019Ce	2.2×10^{-3}	3.51	5082.25	[109]

Table 2.8: Measured parameters for Garofalo hyperbolic sinh law creep model for solder alloys (eq. 2.16)

Solder alloy	Constants				Reference
	C	α [MPa^{-1}]	n	Q [KJ/mol]	
Sn-37Pb	0.908	0.105	1.51	35.74	[113]
Sn-37Pb	0.158	0.406	1.38	50.0	[125]
Sn-37Pb	10	0.1	2	44.9	[120]
Sn-37Pb	2.87×10^{-5}	1300	3.3	52.8	[126]
Sn-37Pb	1999.4	0.2	2.1	54.1	[127]
Sn-37Pb	96200	0.086956	3.3	67.39	[2, 128]
Sn-37Pb	12423	0.126	1.89	61.417	[129]
Sn-40Pb	0.1114	751	3.3	53.0	[82, 130]
Sn-3.5Ag	178.5	0.115	4.75	57.1	[120]
Sn-3.5Ag	23.17	0.0509	5.04	41.6	[121]
Sn-3.5Ag	2.46×10^{5}	0.0913	5.5	72.5	[131]
Sn-3.9Ag-0.6Cu	0.184	0.221	2.89	62.0	[125]
Sn-3.9Ag-0.6Cu	3.49×10^{4}	0.005	4.3	43.13	[132]
Sn-3.9Ag-0.6Cu	248.4	0.188	3.79	62.3	[127]
Sn-3.8Ag-0.7Cu	3.2×10^{4}	0.037	5.1	65.3	[133]
Sn-3.8Ag-0.7Cu	2.78×10^{5}	0.0245	6.41	54.2	[124, 134]
Sn-Ag-Cu	7.93×10^{5}	0.0356	5	67.9	[121]
Sn-4.0Ag-0.5Cu	1.77×10^{5}	0.0548	4.89	76.13	[113]
Sn-4.0Ag-0.5Cu	44100	0.005	4.2	44.995	[129]
Sn-1.3Ag-0.5Cu	30000	0.111111	7	66.99	[134]
Sn-2.7Ag-0.4Cu	2×10^{7}	0.1428	5	69.98	[134]
80Au-20Sn	4.62×10^{15}	2×10^{-5}	2.07	102	[123]

Table 2.9: Measured parameters for Garofalo hyperbolic sinh law creep model for solder alloys (eq. 2.16) (eq. 2.17)

Solder alloy	Constants				Reference
	A [s^{-1}]	α [MPa^{-1}]	n	C [K]	
Sn-37Pb	0.158	0.406	1.38	6014	[125]
Sn-37Pb	10	0.20	2	5401.2	[135]
Sn-3.5Ag	178.6	0.115	4.75	6868	[120]
Sn-3.8Ag-0.7Cu	8.09×10^{5}	0.115	5.02	$1.01\text{x}10^{4}$	[136]
Sn-3.8Ag-0.7Cu	2.78×10^{5}	0.02447	6.41	6496	[137]
Sn-3.8Ag-0.7Cu	3.20×10^{4}	0.037	5.1	6524.7	[133]
Sn-3.8Ag-0.7Cu	2.78×10^{5}	0.02447	6.41	6496	[124]
Sn-Ag-Cu	325000	0.05217	5.3	5800	[122]
Sn-3.9Ag-0.6Cu	4.41×10^{5}	0.005	4.2	5412	[76]
Sn-3.9Ag-0.6Cu	143.4	0.188	3.788	7567	[80]
Sn-3.9Ag-0.6Cu	0.184	0.221	2.89	7457	[125]
Sn-Ag-Cu-Ce	284000	0.02432	6.1	6400	[122]
Sn-Ag-Cu-Ce	120	0.072	2.8	5856.02	[109]
Sn-1.0Ag-0.5Cu-0.02Ni	3.94×10^{4}	0.607	6.32	7024.2	[138]

Table 2.10: Measured values of parameters for double power laws creep model for solder alloys (eq. 2.18)

Solder alloy	Constants						Ref.
	A_1	A_2	n_1	n_2	Q_1/R [K]	Q_2/R [K]	
Sn-3.5Ag	7.0×10^{-4}	$2.0\text{x}10^{-4}$	3	11	5639	11198	[139]
Sn-4.0Ag-0.5Cu	1.0×10^{-6}	$1.0\text{x}10^{-12}$	3	12	4162	7349	[139]
Sn-4.0Ag-0.5Cu	1.33×10^{-5}	$3.18\text{x}10^{-10}$	3.2	11.5	2766	7457	[140]
Sn-1.0Ag-0.5Cu-0.02Ni	9.87×10^{-7}	$5.01\text{x}10^{-10}$	7	13	4883.1	8949.2	[138]

As mentioned above, constitutive models distinguish between rate-independent plastic deformation and time-dependent creep deformation, but it is very difficult to separate plastic strain from creep strain in practice. A unified constitutive model proposed by

Anand combines both the rate independent plastic and the rate dependent creep deformation into a rate dependent inelastic deformation [141]:

$$\dot{\varepsilon}_p = A\left[sinh\left(\frac{\xi\sigma}{s}\right)\right]^{1/m} exp\left(-\frac{Q}{RT}\right) \quad (2.22)$$

$$\dot{s} = \left\{h_0(|B|)^a \frac{B}{|B|}\right\}\dot{\varepsilon}_p \quad (2.23)$$

$$B = 1 - \frac{s}{s^*} \quad (2.24)$$

$$s^* = \hat{s}\left[\frac{\dot{\varepsilon}_p}{A}\, exp\left(\frac{Q}{RT}\right)\right]^n \quad (2.25)$$

where $\dot{\varepsilon_p}$ the effective plastic strain, σ is the stress **[**MPa], Q is the activation energy**,** R is the universal gas constant, T is the absolute temperature in [K], A is the pre-exponential factor, ξ is the stress multiplier, m is the strain rate sensitivity of stress, h_0 is the hardening constant (MPa), $\hat{S}$ is the coefficient for deformation resistance saturation value (MPa), n is the strain rate sensitivity of saturation value, and α is strain rate sensitivity of hardening. Table 2.11 provides a summary of measured Anand creep parameters for solders.

Table 2.11: Measured parameters for Anand creep model for solder alloys (eq. 2.22)

Solder alloy	Constants									Ref.
	S_0 [Mpa]	Q/R [K^{-1}]	A [s^{-1}]	ξ	m	$S^\wedge$	n	h_0 [MPa]	a	
63Sn-37Pb	15.1	15600	3.25×10^{4}	7	0.0143	72.7	0.00437	1790	3.73	[142]
Sn-3.5Ag	2.3165	10278.9	177016	7	0.207	52.4	0.0177	27782	1.6	[143, 144]
Sn-3.8Ag-0.7Cu	3.2992	9883	15.773	1.067	0.3686	3.1505	0.0352	1076.9	1.683	[103, 145]
Sn-1.0Ag-0.5Cu	2.3479	8076	3.773	0.995	0.4454	3.5833	0.012	4507.5	2.166	[103, 145]
Sn-3Ag-0.5Cu	45.9	7450	5.87×10^{6}	2.0	0.0942	58.3	0.015	9350	1.5	[142]

Clech [146] provides a thorough review and analysis of the tin-lead, tin- silver and tin-silver-copper solder material creep properties. The lead-free solder material data collated from eight authors, in the Clech review, confirmed the variation in data observed within this thesis review. Clech [146] also suggests that the discrepancies seen among the data sets need to be accounted for before an accurate constitutive model can be developed for small solder joint of electronic packaging.

2.1.4 Cyclic deformation behaviour of solder joints (softening and hardening)

When metals undergo cyclic stresses, the resulting plastic deformation in a given cycle, even if highly localised, causes a change in the material's resistance to further plastic deformation. Both leaded and lead-free solders can exhibit either cyclic hardening or softening, depending on the thermo-mechanical conditions. In a displacement controlled test (i.e. constant displacement range), cyclic hardening is defined as when the peak stress increases with cycling and, conversely, cyclic softening is defined as when the peak stress decreases. In load controlled tests, cyclic hardening is defined as the when the peak displacement decreases with cycling and cyclic softening is when the peak displacement increases.

Wen *et al*. [147] reported that temperature has a strong effect on the hardening/softening behaviour of a 96.5Pb-3.5Sn bulk samples under isothermal fatigue tests. As can be seen from Figure 2.17, cyclic hardening dominates at low temperatures while, at high temperatures, cyclic softening dominates, although Wen reported that temperature is not the only factor affecting hardening or softening, which seemed to be attributable to a combination of loading conditions; temperature, cyclic period, stress level and strain range). Chen et al. [148] reported that 63Sn-37Pb bulk specimens exhibited cyclic softening under uniaxial, torsional loading which they attributed to compliance changes due to nucleation of micro-cracks. Frear *et al*. [149] reported that the cyclic softening behaviour of Sn-40Pb bulk samples was related to the heterogeneous coarsening, although this was not observed in 40Sn-40In-20Pb, which experienced nearly as much cyclic softening. In a study by Hu *et al*. [150] the softening curve of 63Sn-37Pb bulk samples during a fatigue test at 22°C could be divided into three stages; initial rapid softening, a steady-state stage, and a third stage of rapid softening to failure. By way of contrast, in a higher temperature (125°C) fatigue test, the load decreased rapidly over the initial cycles, but the rate of decrease became slower as the test progressed.

Under most test conditions, Sn-rich alloys tend to exhibit cyclic softening, although Sn-Ag-Cu) lead-free solders have been observed to exhibit cyclic hardening during the first few cycles followed by cyclic softening during the fatigue tests [151-153]. Tin has a body centred tetragonal structure which exhibits significant anisotropy so that large local stresses can develop in Sn based solders causing extensive grain boundary sliding and grain boundary decohesion during cyclic loading. Stresses resulting from Sn anisotropy can be much higher than those due to coefficient of thermal expansion mismatches between various components such as solder/substrate and solder/ intermetallics [154].

Liang *et al*. [155] reported that the grain boundaries of tin-rich phases were weak spots for cracking in the low cycle fatigue of 95Sn-5Ag, 99Sn-1Cu, 62.5Sn-36.1Pb-1.4Ag and 97.1Pb-1.5Ag-1.4Sn bulk specimens. They found that the stress peaks gradually decreased with cycling with a sharp drop near the end of the test, corresponding to the initiation and propagation of a major macro-crack. In a study by Pang *et al*. [90] the softening curve of 99.3Sn-0.7Cu bulk samples with an equiaxed grain microstructure was divided into three stages; an initial stage of rapid softening (involving crack initiation and coalescence), a steady-state stage where the stress amplitude decreased linearly with number of cycles (corresponding to stable fatigue crack propagation), and a third stage of rapid softening to failure. Zeng *et al*. [156] also reported that the cyclic softening behaviour of Sn-3.8Ag-0.7Cu bulk specimens was related to the high density of intergranular micro-cracks on the surface of fatigued specimens. The softening of solder alloys, which started at the beginning of the test, was attributed to the progressive development of the micro-cracks which tended to initiate mostly along grain boundaries.

Experiments by Fiedler [69] generally showed cyclic softening of Sn-4Ag-0.5Cu bulk samples during the first few cycles under displacement controlled isothermal mechanical shear fatigue. They also observed that some of the previously temperature cycled specimens had much longer periods of softening due to a previously formed dislocation structure impeding the motion of new dislocations or possibly due to small cracks. The maximum and minimum stresses increased when the isothermal fatigue test was interrupted, and then decreased when the test was resumed. They attributed the decrease in stresses at the beginning of a fatigue test to an increase in mobile dislocation

density in the tin. On resuming fatigue testing, the dislocation density was supposed to increase approximately to the values before the interruption, following a "relaxation" during the interruption, where the internal energy decreases through a reduction in dislocation density by dislocation climb and annihilation. Shang *et al*. [157] reported that Sn-3.8Ag-0.7Cu alloys exhibit cycle-dependence and cyclic softening. A steep rise of the cyclic stress- strain curve at 10% fatigue life was taken to indicate that the alloy has a strong tendency to work-harden under cyclic loading. By contrast, the equiaxed microstructure experienced significant cyclic softening, attributed to a high density of intergranular micro-cracks on the surface of fatigue specimens.

Yang *et al*. [158] reported that the hardness of Sn-Ag-Cu solder joints decreased when they were subjected to shear fatigue tests or thermal ageing. However, precipitate coarsening was not observed in the shear fatigue test, which indicated that coarsening is not the sole factor affecting softening or hardening under vibration at room temperature. Localized slip bands and plastic deformation inside individual Sn dendrites were observed under mild load cycling, but the secondary precipitate sizes and their distribution around the Sn dendrites were not affected by the shear cycling. The angles of the slip bands indicated that all the dendritic arms belonged to a same Sn grain. In harsh cycling, the slip bands were different as those found in mild load, tending to cross the precipitate regions with fracture of some of the Ag_3Sn intermetallic particles.

For fine solder interconnected structures, such as flip-chip solder bumps, individual grain boundaries may extend over the entire bump structure so that the effect of grain boundary cracking becomes an even more serious concern. Therefore, it is necessary to further understand how these intergranular cracks may influence the fatigue behaviour of a solder alloy. Zhu *et al*. [159] reported that the rapid cyclic softening behaviour of Sn-3.8Ag-0.7Cu bulk samples was related to the high density of grain boundary cracking in the equal channel angular pressing (ECAP) microstructure due to the increase in the grain boundary area per unit volume and the reduced resistance of Ag_3Sn to grain boundary sliding. However, Kang *et al*. [160] reported that the presence of large Ag_3Sn plates can actually enhance fatigue life by blocking an advancing crack, although they can also significantly reduce the fatigue life if the Ag_3Sn plates are aligned along the crack path. Experimental results showed the corner joint in thermal cycling to be softer than the others, which is consistent with strain-enhanced coarsening.

This indicates that shear strain contributes to precipitate coarsening and causes more softening.

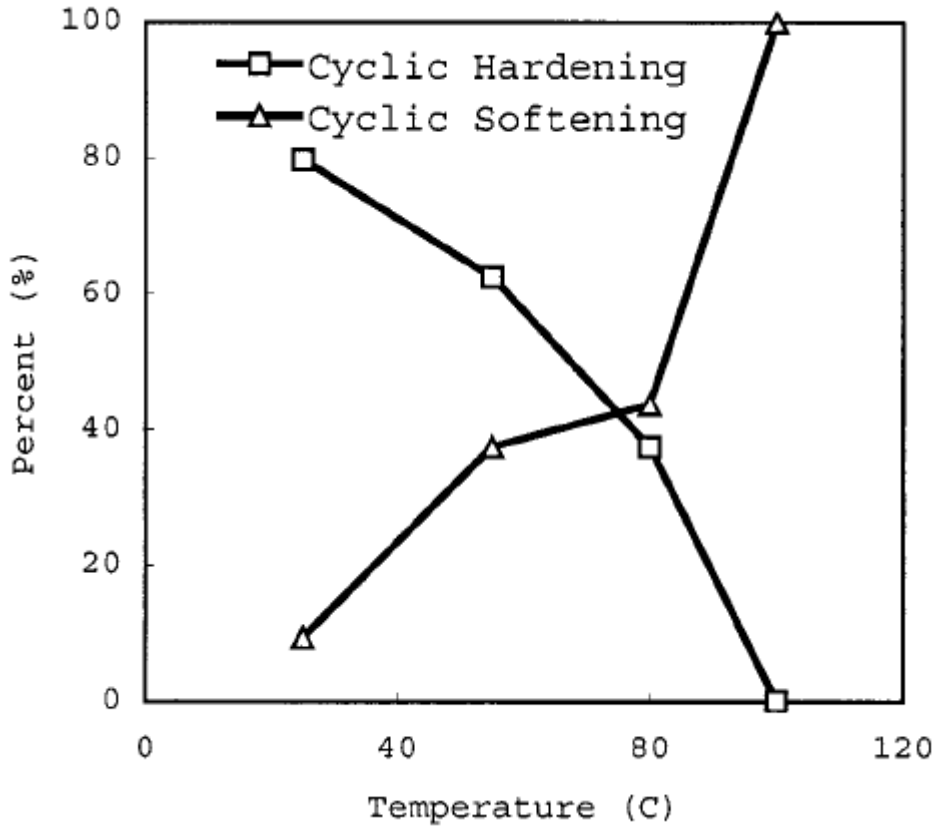

Figure 2.17: Percentage of tests showing cyclic hardening or softening under isothermal fatigue tests at different temperatures [147]

Kanchanomai *et al*. carried out isothermal low cycle fatigue tests on Sn-3.5Ag, Sn-3Ag-0.5Cu, Sn-3Ag-0.5Cu-1Bi and Sn-3Ag-0.5Cu-3Bi bulk samples to study the effects of the additional element on the cyclic deformation behaviour [161, 162]. In the Sn-3.5Ag, Sn-3Ag-0.5Cu and Sn-3Ag-0.5Cu-1Bi solders they observed that the stress amplitude initially showed a rapid decrease with cycling followed by slow rate of softening before instability sets in. The initial rapid decrease followed by a slower rate of decrease of stress amplitude in Sn-3.5Ag was accompanied by the development of extensive surface cracking along β-Sn dendrite boundaries, their linking up and propagation transgranularly through the Sn-Ag eutectic phase and intergranularly along Sn-dendrite and/or sub-grain boundaries. The presence of Cu in Sn-3Ag-0.5Cu-3Bi solder introduces Cu_6Sn_5 precipitates in the eutectic phase and this was thought to be responsible for the higher stress amplitude observed for this material compared to Sn-

3.5Ag. Exceptionally, Sn-3Ag-0.5Cu-3Bi exhibited initial hardening followed by softening at high strain ranges. The initial hardening was considered to arise from the interaction of dislocations with Bi-precipitates formed in dendritic phase.

2.2 Thermo-mechanical degradation of solder

Several variables, such as strain range, environment, temperature, dwell time, and stress range, have been identified as key parameters in characterising the fatigue behaviour of solder material. The reported data can be broadly classified into isothermal, thermal and combined, according to whether the stress or strain cycling is carried out at a single temperature. If the temperature is cycling as well as the stress or strain, the two cycles may or may not be at the same frequency and, if they are, they may or may not be in phase. For real solder joints, purely mechanical fatigue (caused, for example, by vibration) is likely to involve low stress ranges and hence high-cycle fatigue tests are more appropriate, whereas low cycle fatigue testing is more appropriate for thermally-induced fatigue. It is worth noting that thermally induced fatigue may or may not involve temperature cycling of the solder itself, depending on the source of the differential thermal expansions driving the strain range.

The fatigue failure life is considered to be the most important characteristic measured from a fatigue test, although understanding fatigue life involves many of the mechanisms discussed in foregoing sections. The definition of fatigue life is qualified by the type of test and the mechanical behaviour exhibited by the solder alloy. For example, Cutiongco *et al*. defined the cycles to failure (N_f) at which the ratio of the maximum tensile stress to the maximum compressive stress begins to drop significantly [163]. Many others have defined failure as the number of cycles associated with the onset of a load drop, for example a 50% load drop [153, 164-166], a 90% drop [167] a 25% drop [168, 169] or a 30% load drop [170]. Park and Lee denoted cycles to failure by a 20% or 50% or 70% drop in the load [151].
The load drop criterion can generally be defined by [171]:

$$\phi = 1 - \left({}^{\Delta P}/_{\Delta P_m}\right) \tag{2.26}$$

where ϕ is the load drop parameter, ΔP is the load range, ΔP_m is the maximum load range.

The following sections briefly review the range of fatigue measurements that have been reported on solders, divided in to isothermal, thermal and mixed cycling.

2.2.1 Isothermal fatigue of solder joints

Electronic assemblies can be subjected to cyclic mechanical loading from such sources as vibration or bending of structures to which they are mounted. A number of researchers have conducted experiments to study the mechanical cycling and its damage mechanisms in bulk lead-tin [150, 168, 172] and lead-free [165, 173-175] solders and these will be discussed later in conjunction with the results of the current work.

Isothermal fatigue studies have also been conducted on ball grid array solder joints. For example, Wiese *et al*. [176] constructed a micro mechanical fatigue tester and observed the behaviour of 95.5Sn-4Ag-0.5Cu and Sn-37Pb solder joints using an SEM during mechanical cycling experiments at 300Kwith strain ranges was from 0.3% to 4%, at frequencies from 0.0004 Hz to 10 Hz. Power law equations were used to correlate the crack growth rate $\frac{da}{dN}$ with the plastic strain energy ΔW_{p1} or with the accumulated inelastic strain ε_{acc}:

$$\frac{da}{dN} = \alpha.\left(\Delta W_{p1}\right)^{\beta} \tag{2.27}$$

$$\frac{da}{dN} = \alpha.\left(\varepsilon_{acc}\right)^{\beta} \tag{2.28}$$

The crack growth rate was then corrected for temperature and frequency:

$$\frac{da}{dN} = \alpha.\left(\left(\frac{\Delta W_{p1}}{[MPa]}\right)\right)^{\beta}\left(\frac{[Hz]}{f}\right)^{\gamma}.\left(\frac{T}{[K]}\right)^{\delta} \tag{2.29}$$

$$\frac{da}{dN} = \alpha.\left(\varepsilon_{acc}\right)^{\beta}\left(\frac{[Hz]}{f}\right)^{\gamma}.\left(\frac{T}{[K]}\right)^{\delta} \tag{2.30}$$

to give the model parameters summarised in Table 2.12 and Table 2.13:

Table 2.12: Parameters for crack propagation model for leaded and lead free solder joints (eq. 2.29) [114]

ΔW_{p1} ($T = 300K$)	α [m/cycle]	β	γ	δ
Sn-37Pb	8×10^{-7}	1	0.2	-
95.5Sn-4Ag-0.5Cu	2.5×10^{-8}	1.8	-	-

Table 2.13: Parameters for crack propagation model for leaded and lead free solder joints (eq. 2.30) [114]

ε_{acc} ($T = 300K$)	α [m/cycle]	β	γ	δ
Sn-37Pb	2×10^{-7}	1	0.15	-
95.5Sn-4Ag-0.5Cu	5×10^{-8}	2	-	-

Tables 2.12 and 2.13 show that both the exponent and the slope of the crack propagation rate of either model is greater for 95.5Sn-4Ag-0.5Cu solder joints than for Sn-37Pb, at least at room temperature. Stress-strain hysteresis loops were measured for evidence of damage during isothermal fatigue tests. This technique works well for bulk specimens but the calculation of a stress strain hysteresis loop is more complicated in a multi-layer ball grid array specimen.

Park and Lee applied loading conditions varying from tensile to pure shear (Figure 2.18) to Sn-3.5Ag-0.75Cu and Sn-37Pb solder joints. The results showed that the fatigue life increased with increasing angle (i.e. from pure tension to pure shear) as shown in the conventional logarithmic plot of displacement range against number of cycles to failure, Figure 2.19. Figure 2.20 shows the effect of using 20% 50% and 70% load drops as the criterion to determine the fatigue life. Throughout the whole test condition, Sn-3.5Ag-0.75Cu solder joint has longer fatigue life than Sn-37Pb solder joint.

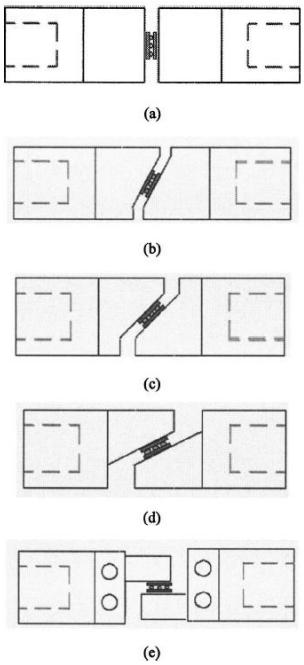

Figure 2.18: Test grip configurations loading angle of each specimen is (a) 0° (pure tension), (b) 27°, (c) 45°, (d) 63°, (e) 90° (pure shear) [151]

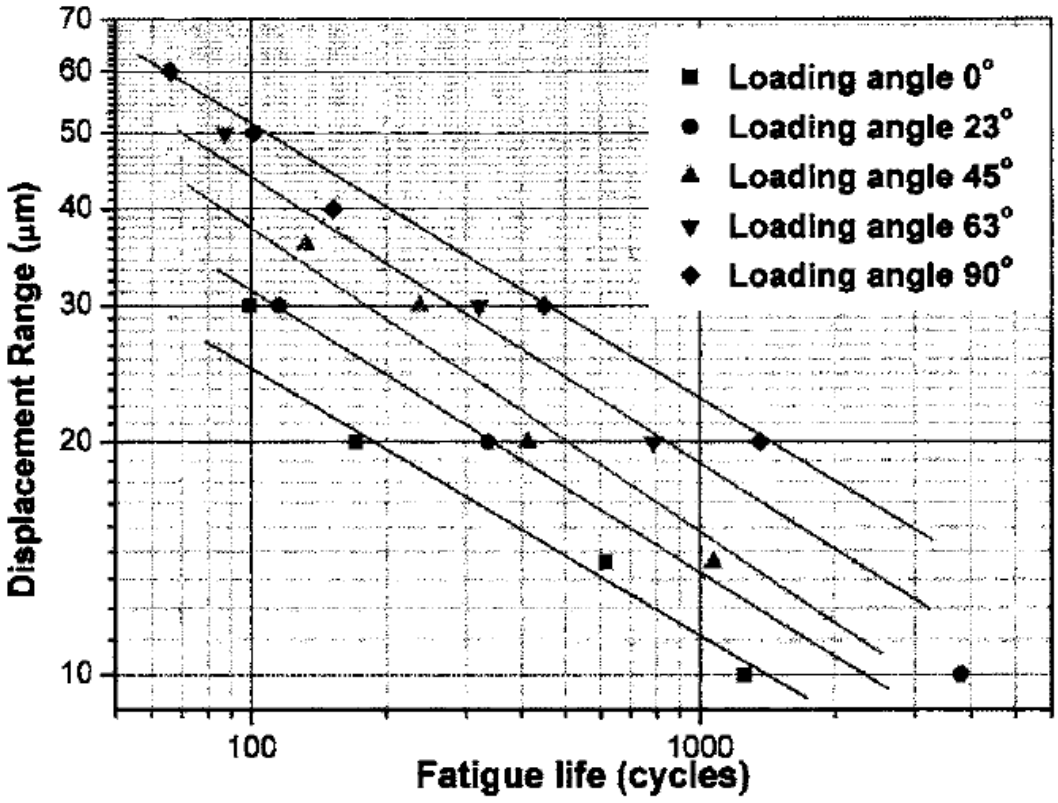

Figure 2.19: Fatigue life versus displacement range for Sn-3.5Ag-0.75Cu using50% load drop criterion [151]

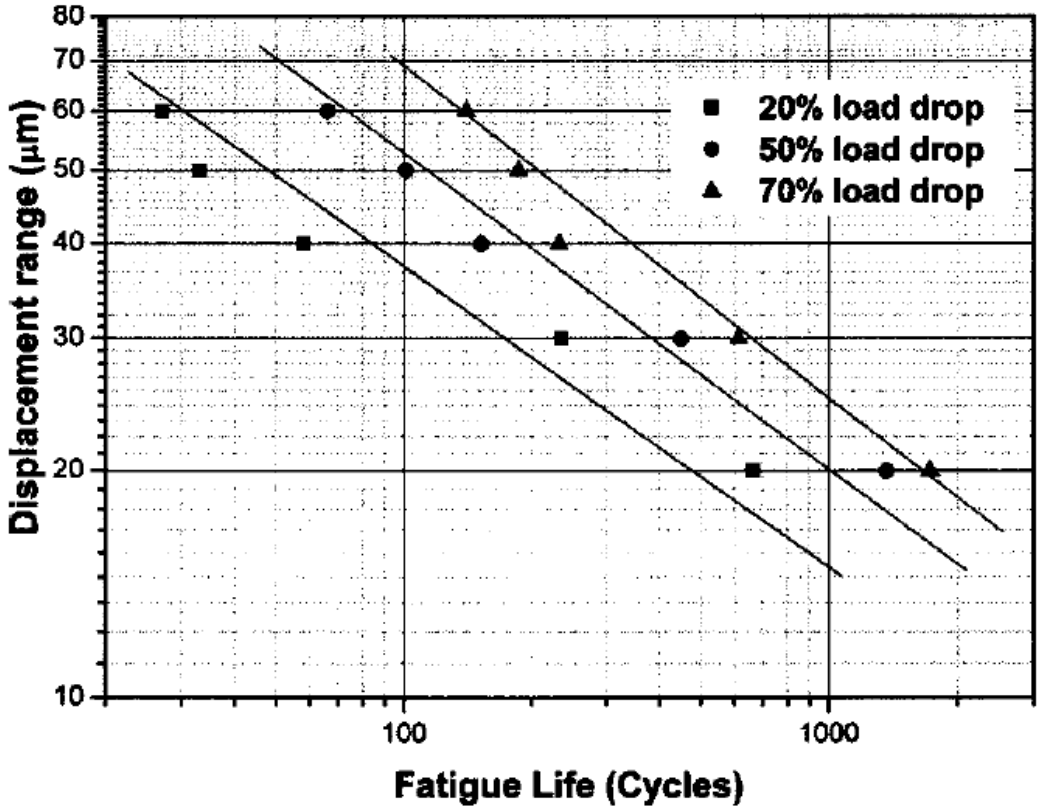

Figure 2.20: Fatigue life versus displacement range for Sn-3.5Ag-0.75Cu, for different load drop criteria loading angle 90 deg (pure shear) [151]

Lee *et al.* have carried out similar low cycle fatigue tests to characterise the fatigue behaviour of Sn-3.5Ag, Sn-3.5Ag-Cu, Sn-3.5Ag-Bi, and Sn-0.7Cu joints at room temperature [177]. They found that the Sn-3.5Ag-Cu solder alloy showed the best mechanical durability of the four alloys tested. Mechanical durability of the remaining alloys were ordered as Sn-3.5Ag, Sn-0.7Cu and Sn-3.5Ag-Bi solder alloys.

Zhang *et al.* [178] used specimens consisting of two copper plates joined in a lap configuration by a thin layer of solder to characterise the isothermal mechanical durability of three lead-free solders (Sn-3.9Ag-0.6Cu, Sn-3.5Ag, and Sn-0.7Cu) and compared with those of the eutectic Sn-37Pb solder at the room temperature and at 135°C. The Sn-3.9Ag-0.6Cu and Sn-3.5Ag had much better durability than the Sn-37Pb, but the Sn-0.7Cu was worse. They used the Morrow energy model which links fatigue life (N_f) with plastic strain energy density ΔW:

$$N_f^m \Delta W = C \tag{2.31}$$

where *m* is the fatigue exponent and *C* is the material ductility coefficient and the results are shown in Figure 2.21 and Figure 2.22.

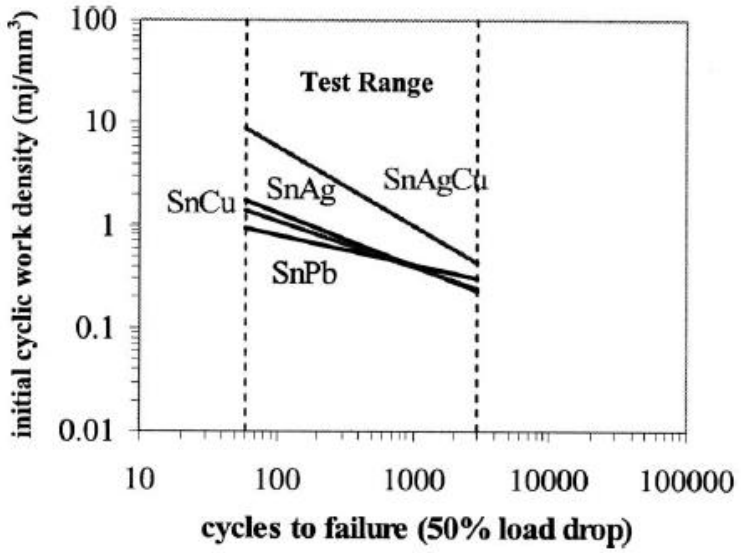

Figure 2.21: Work-based damage relation comparison of four solder alloys at elevated temperature [178]

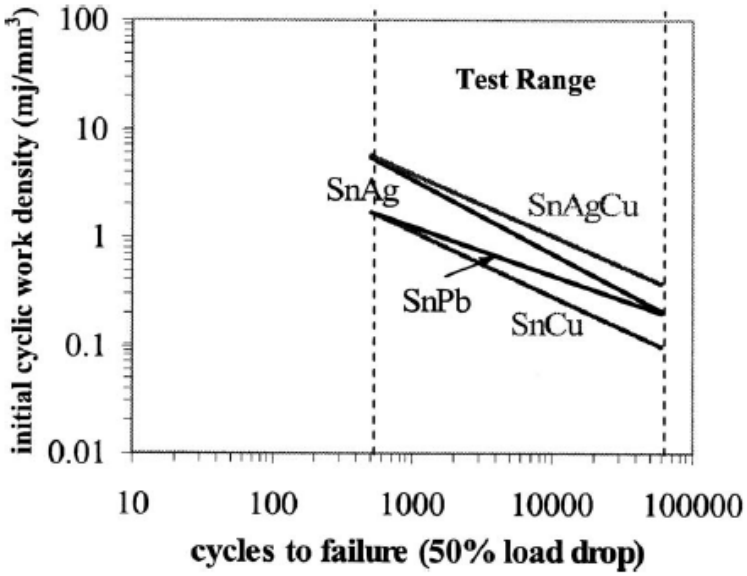

Figure 2.22: Work-based damage relation comparison of four solders alloys at room temperature [178]

A similar tester and specimen design were used by Cuddalorepatta *et al*. to study the effect of cyclic loading damage accumulation on the elastic-plastic properties of lead-free solder joints (Sn-3.0Ag-0.5Cu). They found that initial elastic, plastic and yield properties decreased with increasing damage and that the rate of decrease was proportional to the load severity [179].

Kanda *et al*. [108] investigated the effect of waveform symmetry on the low cycle fatigue of lead-free solder joints (Sn-3.8Ag-0.5Cu) using specimens consisting of two cylindrical copper rods connected with a solder ball. The experiments were carried out at 298K and 398K under displacement control and finite element modelling using elastic-plastic-creep was used to calculate the strain range. They showed that the symmetry of triangular waves had no significant effect on crack initiation life for lead-free micro specimens, in contrast to the reductions observed for large size specimens.

Peng *et al*. [180, 181] determined the Coffin-Manson constants for low cycle fatigue life of Sn-8Zn-3Bi solder joints, using Sn-37Pb eutectic as a reference. Table 2.14 shows the average values of the fatigue life, maximum relative displacement (*ΔL/L*), shear strain ranges and maximum recorded force in the tests.

Table 2.14: Average values of fatigue life, maximum relative displacement (ΔL/L), shear strain ranges and maximum-recorded force in low cycle fatigue testing of leaded and lead-free solder [180, 181]

Displacement loading [μm]	**Maximum $\Delta L/L$ (%)**	**Maximum Force [N]**	**Apparent $\Delta\gamma$**	**Simulation $\Delta\gamma$**	**Lifetime N_f**
			Sn-37Pb		
40	0.127	42.3	0.0508	0.0181	3470
50	0.166	54.3	0.0667	0.0362	657
60	0.204	59.1	0.0844	0.0633	123
			Sn-8Zn-3Bi		
40	0.129	46.4	0.0310	0.0144	4183
50	0.159	56.9	0.0413	0.0283	917
60	0.205	62.8	0.0567	0.0524	113

Duek *et al*. carried out low cycle isothermal fatigue tests on 96.5Sn-3.0Ag-0.5Cu solder joints at 24°C, 30°C, 60°C, 100°C, and 125°C with fixed constant displacement amplitude (±15 μm) [152, 153].

The results as shown in Figure 2.23 revealed that the crack growth is slower at higher temperature with slow mechanical loading and that the fatigue life increased with increasing the temperature as shown in Figure 2.24.

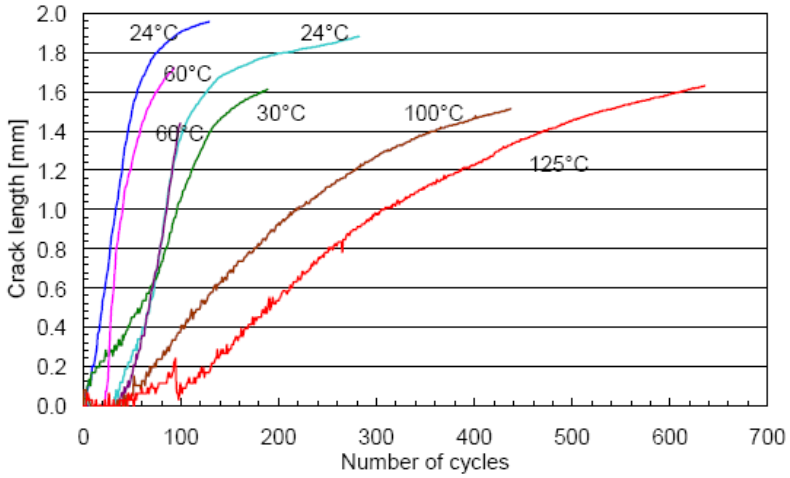

Figure 2.23: Crack length as a function of the number of cycles at various temperatures in lead-free solders [153]

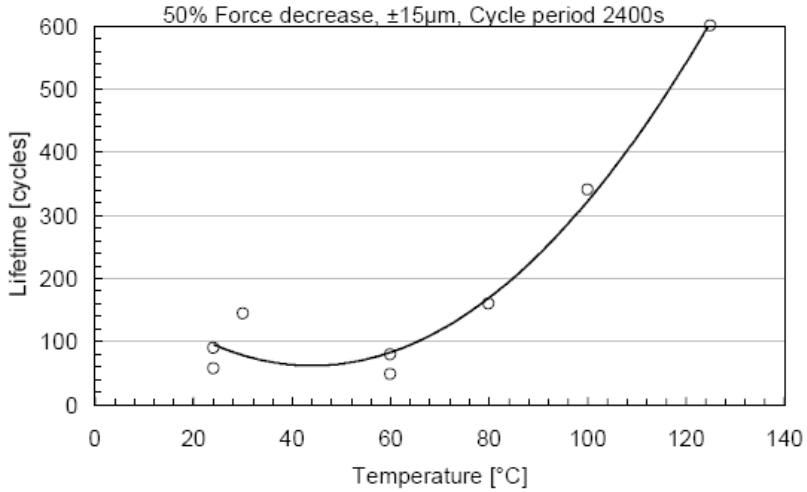

Figure 2.24: Lifetime of lead-free solder joints at various temperatures based on 50 per cent load drop [153]

A similar tester was used by Di Maio *et al*. to characterise the fatigue properties of 96.5Sn-3.0Ag-0.5Cu solder joints. Isothermal tests were carried out at 40°C and 125°C with and without applying a current density of 10^4 $A/_{cm^2}$ with the result that the specimens subjected to high current failed faster than those without [166].

In examining the temperature effect on the low cycle fatigue of cast 96.5Sn-3.5Ag specimens the temperature range (20, 85, and 120°C), Kanchanomai [182] observed that the life decreased with an increase in temperature but that the plastic strain range increased, which mean that the stress range decreased.

A number of investigators have examined the effect of temperature on isothermal low-cycle fatigue. Korhonen *et al*. [183], investigated cast dog-bone lead-free specimens (Sn-3.8Ag-0.7Cu) at several temperatures from -25°C to 125°C and noted that the fatigue failure is dependent on the temperature, the fatigue life of solder decreasing with increasing temperature. By contrast, when comparing the low-cycle fatigue lives of 60Sn-40Pb at -50°C, 35°C, and 125°C, Solomon *et al*. did not find any difference [184]. Vaynman *et al*. similarly found no effect on the fatigue life of bulk cast lead tin solder specimens (96.5Pb-3.5Sn) and (63Sn-37Pb) tested at 25°C to 80°C [185, 186].

Anderson *et al*. [187] tested both bulk and solder joint samples of lead-free solders (Sn-3.5Ag) and (Sn-4.0Ag-0.5Cu) compared with lead tin eutectic (Sn-37Pb) and found that the isothermal fatigue life of lead-free solders was generally better, The fatigue life of the bulk solders decreased slightly with addition of 0.5Cu whereas the opposite was the case in the solder joint sample. Also, the solder joint samples displayed lower fatigue lives (lower slope) than bulk solders, when subjected to higher strain ranges, and the opposite when subjected to lower strain ranges. Based on this Anderson *et al*. has cautioned against using data obtained from bulk materials and directly applying them to electronic solder joints.

Solomon [188, 189] compared the isothermal fatigue behaviour of two simple eutectic solders, Sn-3.5Ag and Sn-40Pb, at 35°C and 150°C using single lap joints under plastic strain control. Using a 50% load drop as the fatigue failure criterion the life of both types of joint decreased with increasing plastic strain range. The life of Sn-3.5Ag solders was longer than that of Sn-40Pb at both temperatures over most plastic strain ranges.

2.2.2 Thermal cycling of solder joints

Whilst they are more realistic than isothermal tests, thermal cycling tests are rather more difficult to compare across the literature due to the effect that configuration (package type and board component finish) have on the response to a given cycle, as well as the effects of heat treatment, temperature cycling amplitude, and solder alloy composition.

Several early work was conducted to investigate the failure mechanism occurring in lead-free interconnects due to temperature cycling. Many of these experiments used temperature ranges of -55°C to 125°C or 150°C, with cycle periods ranging from

several minutes to several hours. Such accelerated tests can result in different failure modes to real operating conditions because of the wider temperature ranges, faster cycle times and reduced isothermal dwell periods which presuppose that no significant time-dependent processes, such as creep and/or microstructural changes, have an effect on life.

One study conducted on Sn-3.8Ag-0.7Cu in Plastic Ball Grid Array (PBGA), Plastic Quad Flat Package (PQFP) and Thin Shrink Small Outline Package (TSSOP) observed cracks initiating between the solder and the intermetallic compounds (IMC) [190]. Two PCB surface finish conditions were investigated for Electroless Nickel/Immersion Gold (ENIG) and organic solderability preservatives (OSP) and the temperature was cycled between - 40°C and 125°C with a period of 60 minutes using a dwell time of 15 minutes at each extreme. It was found that the PBGA assembly was more sensitive to thermal cycling than leaded assemblies such as PQFP and TSSOP, and this was validated using FEA. Assemblies with a Ni/Au surface finish had longer fatigue life than those with OSP surface finishes. A similar experiment on Sn-3.8Ag-0.7Cu and Electroless Nickel/Immersion Gold (ENIG) surface finish on PBGA soldered assembly also observed cracks initiating between the solder and IMC [191]. Another similar temperature cycling experiment was carried out on Sn-Ag-Cu lead-free PBG components on PCBs with a NiAu finish [192], but this time cracks were observed initiating in the Sn-rich bulk solder. The difference between these studies raised questions about the causes of cracks, the damage mechanism(s) and how the IMC affects the failure mode in some test conditions but not others.

Frear *et al*. [193] reported an extensive study on three lead-free solders (Sn-0.7Cu, Sn-3.5Ag, Sn-3.8Ag-0.7Cu) for use as flip-chip assemblies on FR-4 substrates. Two thermal cycling profiles were used: 0-100°C and, -40-125°C both at the frequency of 1 cycle/hour. The thermal strain was calculated based on the the measured bump distance to the neutral point (DNP) and the thermal mismatch ($\Delta\alpha$) between die and substrate. A variety of under-bump metallurgies (UBM) (TiW/Cu, electrolytic nickel, and electroless Ni-P/Au) were also selected to investigate their effects on the durability of the solder bumps. The static shear strengths of the solder joints are shown in Figure 2.25 this being a measure of the ability of the flip-chip interconnects to comply with imposed strain. The shear failure for all joints tested occurred solely through the solder, and, as can be

seen, the Sn-37Pb and Sn-0.7Cu solder bumps have similar values of shear strength while the Sn-3.8Ag-0.7Cu is 20% stronger and the Sn-3.5Ag solder 25% stronger still. The solder joint strength and failure mode were independent of the UBM type.

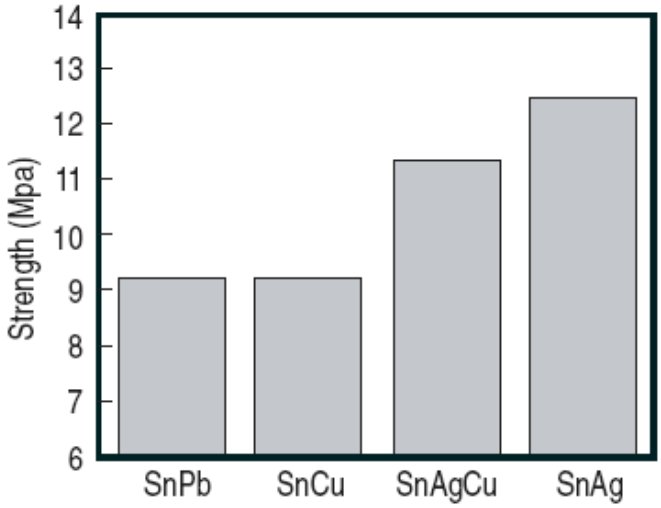

Figure 2.25: Shear strength of the solder flip-chip bumps [193]

The optical micrographs of the failed solder joints following thermal cycling are shown in Figure 2.26. It can be seen that cracks propagate near the solder/intermetallic interface for all the alloys except Sn-0.7Cu, which deforms by grain sliding and fails further in the interior of the joint.

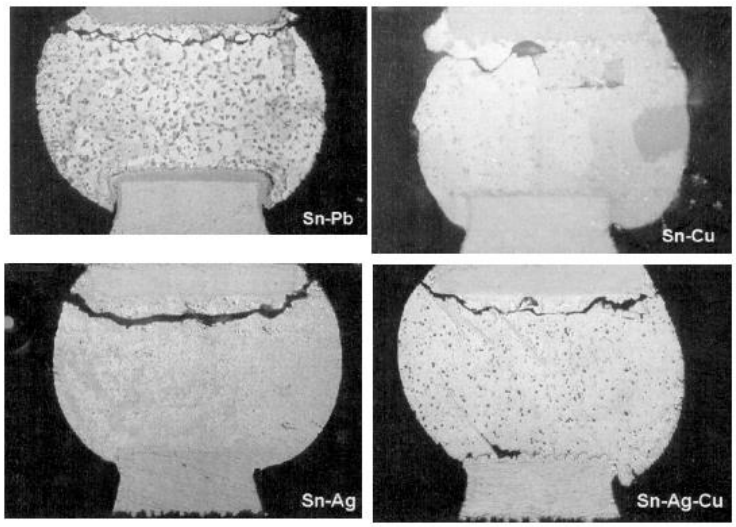

Figure 2.26: Optical micrographs of solder joint cross sections of solder joints on copper UBM/Cu pads on organic substrates after thermal cycling at 0°C -100°C [193]

The thermal fatigue life data, Figure 2.27, shows that Sn-0.7Cu solder is the best performer among Sn-37Pb solder and the lead-free solders, for the selected thermal cycle, due to its ability to sustain large deformations. This deformability occurs because of the relatively low yield strength and relatively high steady state creep rate. The authors also reported that the short fatigue life for Sn-3.8Ag-0.7Cu and Sn-3.5Ag solders was due to the failure mode of crack initiation and propagation at the intermetallics and intermetallic/solder interface.

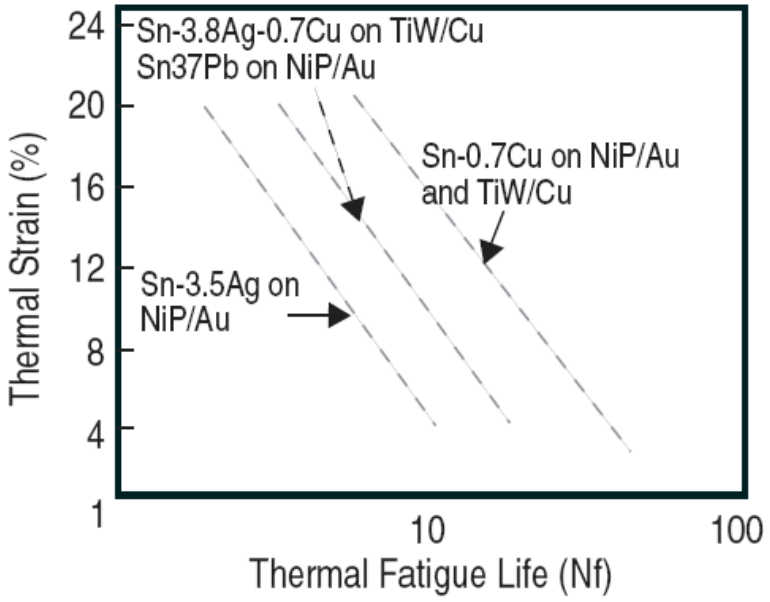

Figure 2.27: Plot of thermal fatigue life as a function of applied thermal strain for Sn-3.5Ag, Sn-37Pb, Sn-3.8Ag-0.7Cu, and Sn-0.7Cu joints [193]

The thermo-mechanical fatigue reliability assessment of lead-free solder joints in flip chip packages was also investigated by Schubert *et al*. [194] who conducted thermal cycling from -55°C to 125°C and -55°C to 150°C (30 min. cycle time, 10 min. dwells) of flip chip packages with Sn-37Pb solder balls, assembled with lead-free solder pastes (Sn96.5-Ag3.5 and Sn95.5-Ag4.0-Cu0.5) with three different underfills. The eutectic Sn-37Pb exhibited the highest fatigue life followed by Sn95.5-Ag4.0-Cu0.5 and finally by Sn96.5-Ag3.5. Another study, by Syed [195, 196], subjected two lead-free solders (Sn4.0-Ag0.5Cu and Sn-3.4Ag-0.7Cu) in three different packages (PBGA, flexBGA, chip array BGA) to three temperature cycle conditions:

- TC1: -40°C to 125°C, 15 minutes ramps and dwells, 1 cycle per hour, single zone chamber cycling.

- TC2: -55°C to 125°C, 2 minute ramps, 13 minutes dwells, 2 cycles per hour, dual zone chamber cycling.
- TC3: 0°C to 100°C, 10 minute ramps, 5 minute dwells, 2 cycles per hour, single zone chamber cycling.

The results indicated generally that the Sn-Ag-Cu alloys have longer thermal fatigue lives than Sn-37Pb under the same test conditions and the ranking is package dependent. The flexBGA interconnects experience higher loading than the PBGA interconnects, because of higher CTE mismatch and this was confirmed by NCMS testing.

In summary, the reliability of most lead-free solder alloys is better than that of Sn-37Pb alloys when the loading levels are not very high, but this difference decreases as the loading level increases. Under extremely high loading (e.g. for severe test conditions and stiff interconnects with large CTE mismatch), Sn-37Pb solder alloys have, however, outperformed some lead-free solder alloys [197, 198].

2.2.3 Combined thermal cycling and mechanical cycling

Solder joint fatigue can be categorized into two basic kinds: low cycle fatigue (LCF) and high cycle fatigue (HCF) the dividing line generally being at 10^4 cycles [199, 200]. The deformation caused by thermal cycling is generally plastic and so results in LCF, whereas the deformation caused by mechanical vibrations is usually elastic and belongs in the HCF regime.

Because of the non-linearity of stress-strain curves and the much lower slope of the plastic portion, strain based equations (and displacement control) are generally used for low cycle fatigue, whereas stress-based approaches are used for HCF. In combined loading which includes LCF and HCF, low cycle fatigue is usually considered the primary cause of failure and a linear superposition methodology (e.g. Miner's rule) has been traditionally used to predict fatigue life [199].

Concurrent vibration and thermal cycling are commonly encountered in solder joint service life. However, although there is extensive research on thermal cycling and mechanical fatigue behaviour of solder joints, as has been seen in the previous two

sections, there has been limited work on the combination of the two. There is work on the high-cycle fatigue comparison between leaded and lead-free alloys [63, 201-207], and the interaction between thermal cycling damage and vibration damage of leaded solder alloys [199, 204, 208-213], but there is very little on combination loading in lead-free alloys.

Barker *et al*. [199] have modified the linear damage superposition approach (Miner's rule) to take in his account the contributions of different frequencies of loading applied to solder joints under combined vibration and thermal cycling, shown schematically in Figure 2.28. The damage was calculated individually for vibration and thermal loads and superposed in a linear fashion taking into account loading frequency. First, the thermal fatigue damage was obtained (assuming a single frequency of loading):

$$D_{th} = \frac{n_{th}}{N_{th}} \tag{2.32}$$

The vibration cycles are generally at a much higher frequency than the thermal cycles, and so the ratio of vibration frequency to thermal frequency was used to determine the vibration damage, again assuming a single frequency of loading.

$$D_v = \frac{n_{th}\left(\frac{f_v}{f_{th}}\right)}{N_v} \tag{2.33}$$

$$D_{total} = D_v + D_{th} = n_{th}\left(\frac{\frac{f_v}{f_{th}}}{N_v} + \frac{1}{N_{th}}\right) \tag{2.34}$$

$$N_f = \frac{1}{D_{total}} \tag{2.35}$$

where

D_{th} : Thermal strain damage

n_{th}: Vibration strain damage

N_{th}: Fatigue life of solder joint under thermal loading

D_v: Vibration strain damage

f_v: Frequency of vibration cycling

f_{th}: Frequency of thermal cycling

D_{total}: Total damage

N_f: Fatigue life of solder joint by combing loading

Barker assumed that there was no interaction between the different loads and that the life data was expressed in terms of strain range for both components. However, there has so far been no experimental validation of this approach.

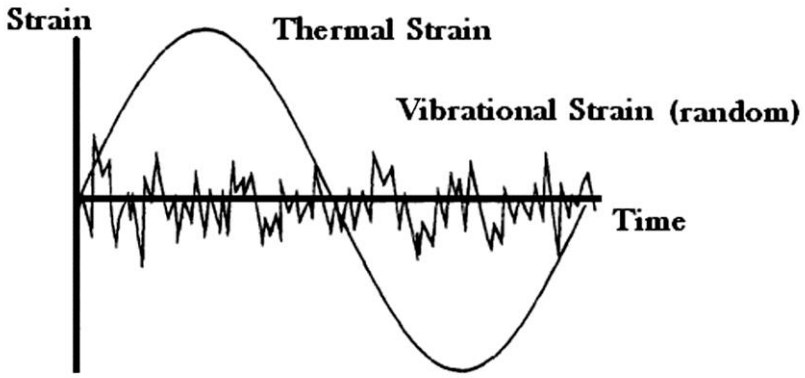

Figure 2.28: Schematic representation of vibrational and thermal strain [199]

Barker *et al*. [200] proposed some modifications to the above superposition approach to calculate the life of PWB solder joints under combined thermal and vibrational loads. The constitutive properties of the solder were described as a function of temperature and characterised by curvature-strain response curves. The approach has so far only been demonstrated on leaded packages (J leaded plastic chip carrier and gullwing quad flat pack).

Equations for cycles to failure for both leadless and with-leads SM attachments have been developed. For leadless attachments:

$$N_f = \frac{1}{2}\left[\frac{F\,L_D \Delta\alpha \Delta T_e}{2\varepsilon_f\, h}\right]^{\frac{1}{c}} \tag{2.36}$$

For with-leads attachments:

$$N_f = \frac{1}{2}\left[\frac{F\,K(L_D \Delta T_e)^2}{2\varepsilon_f 200A\, h}\right]^{\frac{1}{c}} \tag{2.37}$$

The fatigue ductility exponent *c* takes into account the effect of dwell time and creep and is represented by following equation:

$$c = -0.442 - 6 \times 104T_{Sj} + 1.74 \times 10\ln\left[1 + \left({}^{360}/_{t_D}\right)\right] \quad (2.38)$$

$$T_{Sj} = \frac{(T_C + T_S + 2T_0)}{4} \quad (2.39)$$

for near eutectic Pb/Sn solder

In the above:

N_f: Predicted number of operating cycles before failure

F: Empirical non ideal factor indicative of deviations of real solder joints from idealizing assumptions

$2L_D$: Maximum distance between components solders joints

$\Delta\alpha$: Absolute difference in CTEs of component and substrate

ΔT_e: Equivalent temperature range

K: Diagonal lead stiffness

ε_f : Strain fatigue ductility coefficient

A: Solder footprint area

h: Height of the solder joint

c: Coefficient ductility exponent

T_{Sj}: Mean cycle solder joint temperature

T_s, T_c: Steady state operating temperature for substrate, component

T_0: Temperature during half cycle

t_D: Half cycle dwell time

The diagonal lead stiffness (*K*) can be determined either by finite element methods or by strain energy methods and is a function of component aspect ratio, in-lead-plane and out-of-lead-plane flexural spring constants, and lead position on the package. For rectangular packages the diagonal stiffness in the X coordinate system is given by:

$$K_{d1} = \frac{K_x K_z (1 + r^2)}{r^2 K_{x+} K_z} \quad (2.40)$$

and, for the Z coordinate system:

$$K_{d2} = \frac{K_x K_z (1+r^2)}{r^2 K_z + K_x} \tag{2.41}$$

where
K_x , K_z are lead stiffnesses in global X and Z directions
r: The length/width, aspect ratio of the chip carrier

It was noted that stiffer leads will negatively affect the solder joint lives.

Steinberg [214-216] developed an empirical equation for the maximum allowable displacement at the centre of the board, *d*

$$d = \frac{0.00022B}{ct\sqrt{L}} \tag{2.42}$$

in which:
B: The length of the PWB edge parallel to the component located at the centre of the board
L: Length of component
t: Thickness of PWB
c= 1.0 for standard DIP, 1.26 for DIP with side brazed leads, 1.0 for pin-grid array with four rows of pins (one row extending along the perimeter of each =edge), and 2.25 for an LCC

The PWB deformation for the fundamental mode can be expressed in terms of the radii of curvature. This information is obtained from the natural frequency obtained, for example, from finite element analysis. The change in each spring's length is determined as a function of the radii of curvature for a specific component geometry by using the force equilibrium equation for each component:

$$\sum_{i=1}^{m} F_{yi} = 0 = K_{yi}(\delta_i - \delta_0) \tag{2.43}$$

where
δ_0 , δ_i are the spring's initial and deflected length measured from some reference plane and the sum is taken over the number of solder joints for the component.

This procedure can be used for both leaded and leadless components. Once the spring deflections have been determined, the average maximum stress amplitude in each solder joint can be calculated by dividing the force by the nominal cross-sectional area of the solder while accounting for a stress concentration factor. The Basquins high cycle fatigue relation can then be used to determine the fatigue life, and, finally, the generalised Coffin-Mason equation to calculate the combined fatigue life for the thermal and vibration components.

Upadhyayula *et al*. [210] have proposed an incremental damage superposition approach (IDSA) to calculate the damage in surface mount interconnects subject to combined thermal and vibrational stresses. Figure 2.29 shows the discretisation of accelerated loads for the IDSA. They also conducted repetitive shock vibration tests and combined thermal cycling tests on a Plastic Leaded Chip Carrier (PLCC-84), which revealed that the combined thermal cycling and vibration loading can sometimes be less damaging than similar vibration loading at room temperature. They suggested that the reduction in damage was due to the effect of thermo-mechanical mean stresses on vibration induced fatigue. Their approach therefore used a variant of Miner's rule, where by the damage was incrementally considered at each stress level, using FEA, to track nonlinear interactions between different load types of varying frequencies (vibration and thermal cycling).

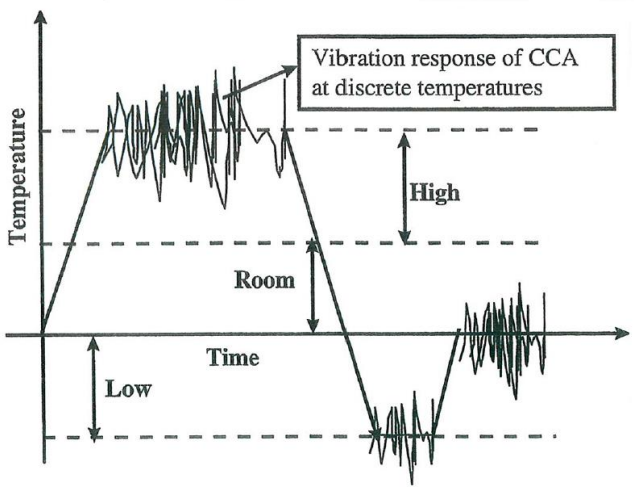

Figure 2.29: Discretization of accelerated test loads for IDSA [210]

A unified damage constitutive model has been developed by Baseman and Chandaroy [217] for Pb40/Sn60 solder joint in leadless ceramic chip carriers (LCCCs). The model uses a thermo-viscoplastic dynamic element procedure coupled with a damage criterion based on the second law of thermodynamics and statistical mechanics. A selection of laboratory test data was simulated, Adams [129], McDowell [218], Busso [219], in order to verify the constitutive model. They concluded that using Miner's rule to calculate cumulative damage using separate dynamic and thermo-mechanical analyses significantly underestimates the actual damage in leaded solder joints.

Qi *et al*. [220] developed a reliability assessment approach, based on accelerated environmental tests combined with computer aided simulation to calculate an acceleration factor, which could then be used to predict the fatigue life of solder joints in plastic ball grid array (PBGA) using Sn-37Pb solder under combined loading conditions. Figure 2.30 shows the flowchart of this approach.

Based on the simulation and test results, it was estimated that PBGA package without underfill under combined loading conditions would not satisfy the long term life expectation. In addition, the experimental results show that the simple application of linear damage superposition for combined multiple stresses loading is overestimate the fatigue life of solder joint of leaded plastic ball grid array package for an avionics application under combined loading conditions due to neglecting the interactions between the loads.

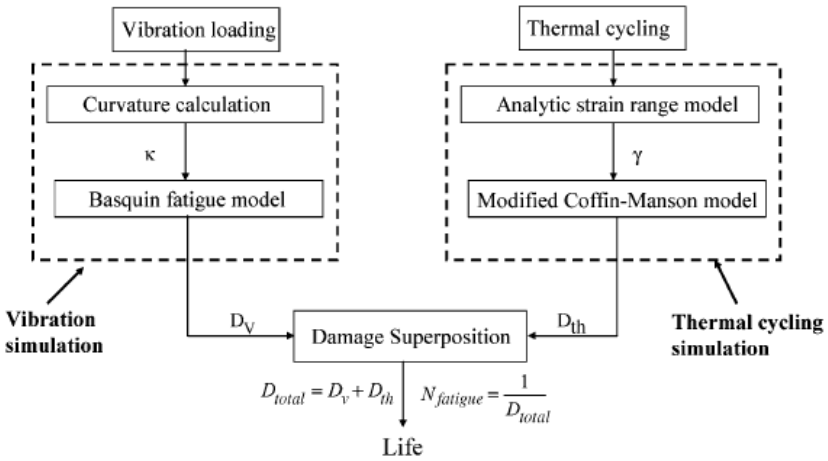

Figure 2.30: Flowchart of the life prediction for PBGA solder joint reliability assessment under combined thermal cycling and vibration loading [220]

The same authors, Qi *et al*. [221] have further developed their approach (Figures 2.30 and 2.31) conducting further experiments including temperature cycles, random vibration, and combined temperature cycling and random vibration loading. Simulation developments included incremental damage superposition (IDSA) and a rapid life prediction approach (RLPA). They showed that IDSA is more accurate for combined temperature cycling and vibration random conditions than LDSA. In these later studies it was noted that the damage to a PBGA under combined loading was 10 times more than that indicated form linear damage approximations using room temperature random vibration and temperature cycling test results.

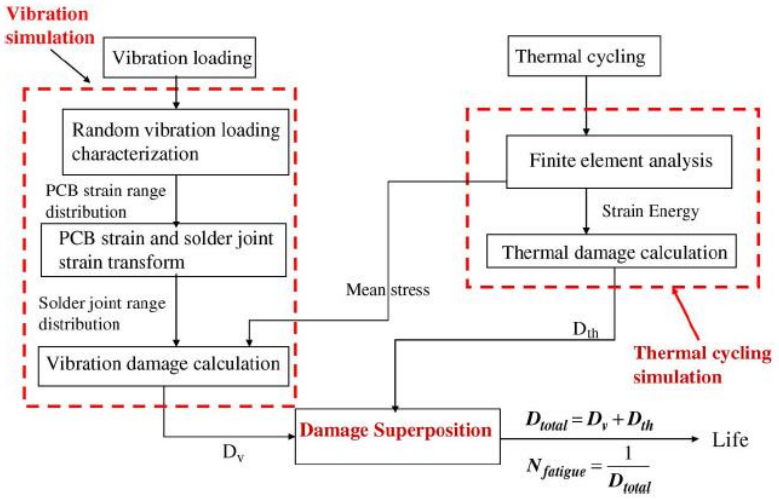

Figure 2.31: Flowchart of the incremental damage superposition approach for PBGA solder joint reliability assessment under combined thermal cycling and vibration loading [221]

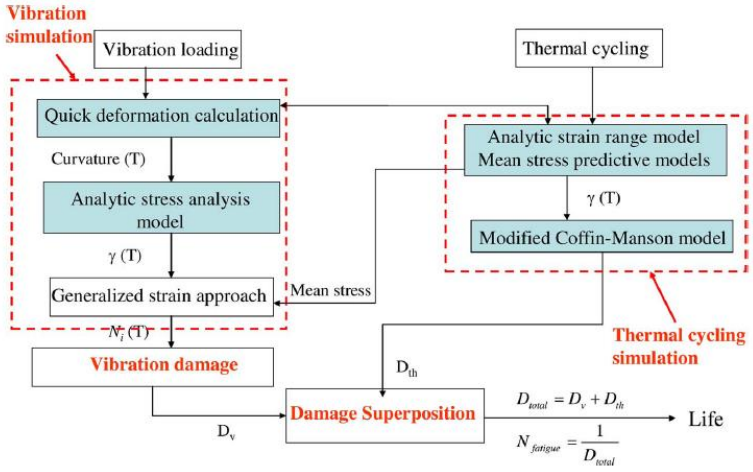

Figure 2.32: Flowchart of the rapid life-prediction approach for PBGA solder joint reliability assessment under combined thermal cycling and vibration loading [222]

Eckert *et al*. [223, 224] investigated the effects of combined vibration and thermal cycling loadings of lead-free solder (Sn-3Ag-0.5Cu), by using of a special flip chip specimen (consisting of solder joint, Fc (Si), and PCB), each chip having three different types of joint. The vibration was imposed by deflection (bending) of the printed circuit board (PCB), clamped on two sides, using an electrodynamic shaker, the vibration being added during the last 15 min of each temperature dwell. Due to the limited testing time, only a few data points from solder joints close to the middle of the board could be collected, and lifetime was taken to be 63% failure. Two modelling techniques, linear and incremental damage superposition, were used and it was shown that neither displayed clear advantage over the other. However, the linear damage superposition approach was recommended for lifetime prediction of combined loads since the incremental damage superposition approach does not use the correct interaction factors. The experimental results showed good agreement with prediction lifetime for high vibration loads but underestimated the damage for the low vibration tests.

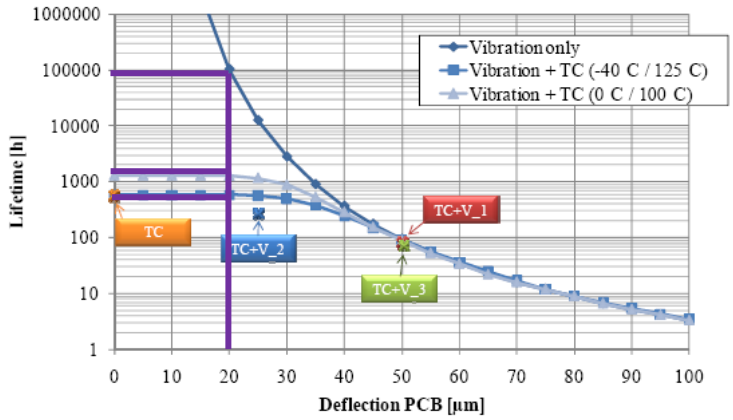

Figure 2.33: Trends for solder joint lifetime in combined load tests [223]. Lifetime highlighted by author.

Eckert *et al*. data tests under vibration alone were performed only at room temperature. It is clear from Figure 2.33 (purple line) for vibration amplitudes resulting in PCB deflections smaller than 20 µm that combining thermal cycling with vibration loading reduces the lifetime of solder joint compared with vibration loading at room temperature.

In order to more fully understand the behaviour of solder joints, vibration tests should be performed at a number of different isothermal temperatures including elevated temperature. Unfortunately, no data at 100°C or 125°C were available in the literature.

2.3 Effect of microstructure on mechanical properties of solder alloys

It is clear from the foregoing that the basic mechanical properties of solders depends on their microstructures and this is relevant when considering replacement alloys for Pb-Sn. It is also evident that an elevated temperature, irrespective whether or not this is cycling, will result in some changes to the microstructure which may, in itself, affect the service life through a change in properties. In this section, the literature on microstructure of solder alloys is briefly reviewed. This is followed by a review of the effect of elevated temperature exposure (ageing) on the microstructure and, ultimately, on the hardness of alloys in solder joints.

2.3.1 As-reflowed microstructures

Upon solidification, different cooling rates are likely to generate different microstructures, thus also affecting the thermo-mechanical fatigue behaviour of solder joint alloys [225]. On solidification, Sn-Ag-Cu solder comprises a pure Sn matrix phase with hard, brittle intermetallic (IMC) particles of Ag_3Sn and Cu_6Sn_5 dispersed in the bulk as shown in Figure 2.34 in which Ag_3Sn assumes a needle shape and Cu_6Sn_5 takes a disk-like morphology. The locations at which the Ag_3Sn plates are formed are random and cannot be predicted. Each Sn "grain" is made up of colonies of β-Sn dendrites and Sn-Ag-Cu eutectic but, because the eutectic mixture contains so little of the non-Sn phases, it is difficult to identify separate colonies. By contrast, the traditionally used Sn-37Pb solder eutectic has approximately equal amounts of the two phases and the microstructure comprises soft islands of Pb embedded in Sn matrix as shown in Figure 2.35. Thus, the strengthening mechanisms are fundamentally different in the two types of alloy, the Sn-Ag-Cu relying on particle hardening, and the Pb-Sn relying on fine grains, each solid-solution hardened (by Pb dissolved in the Sn and Sn dissolved in the Pb).

The melting temperature of Sn-37Pb solder is 182°C, which is lower than that of Sn-Ag-Cu solders. The lower melt temperature combined with the presence of soft Pb islands in Sn3-7Pb (as opposed to hard intermetallics in Sn-Ag-Cu solder) causes higher

fatigue damage in Sn-37Pb compared to the Sn-Ag-Cu solders. In general, the intermetallic compound particles possess much higher strength than the Sn matrix [226, 227]. It has been reported that the fatigue resistance of Sn-Ag-Cu alloys is 3~4 times greater than Sn-37Pb eutectic solder. The higher fatigue resistance is ascribed to the interspersed Ag_3Sn and Cu_6Sn_5 particles, which pin and block the movement of dislocations [54].

The microstructure, fatigue life and thermo-mechanical behaviour of Sn-Ag-Cu solder alloys have also been reported to vary with solder joint size [228]. The term "microstructure" describes the morphology, grain size and configuration, and distribution of phases in a metallic system [229] and the mechanical strength and the long term reliability of solder joints are directly dependent on the microstructure formed when the liquid solder solidifies to form a solder joint [230].

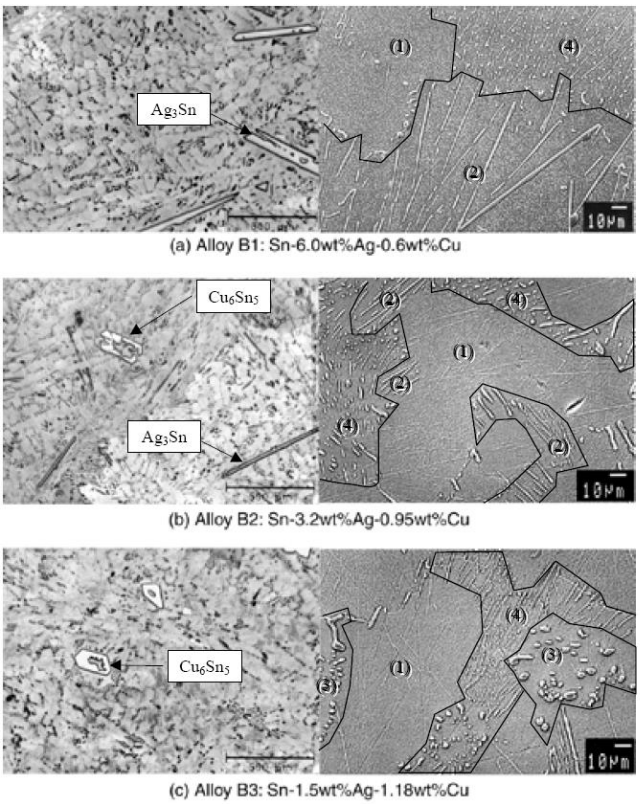

Figure 2.34: Optical micrographs (left hand side) of three alloys showing large intermetallic particles and dendritic (Sn) substructure formed from the remaining supercooled liquid. Photographs on the right hand side are SEM (backscattered) images [231]

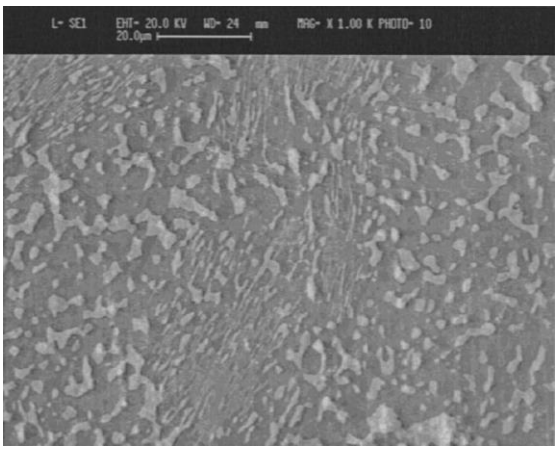

Figure 2.35: SEM micrograph showing the microstructure of a eutectic Sn-37Pb solder. The lead-phase is represented by lighter areas, while the Sn-rich phase is the darker one [126]

Different cooling rates are likely to generate different microstructures that will effect on the durability of solder joints under thermo-mechanical loading. The alloy remains entirely liquid for several degrees below the liquidus temperature. This occurrence is referred to as undercooling. The faster the cooling rate, the greater is the difference between the temperature at which solidification initiates and the liquidus temperature and thus, the greater the deviation of the microstructure away from equilibrium. This nonequilibrium microstructure is retained after solidification because solid-state, mass transport (diffusion) processes are not suitably fast enough to rearrange the elemental atoms into an equilibrium configuration.

De Castro *et al*. [232] reported that the Sn-37Pb eutectic microstructure exhibits anomalous growth morphology with increased undercooling. Similarly Kang *et al*. identified three main microstructural transitions with increasing undercooling; a morphological change of eutectic phase from lamellar to anomalous morphology at lower levels of undercooling, a change of primary α-lead phase from dendritic to equiaxed grains at higher undercooling levels accompanied by a change from eutectic to primary α-lead dendrites plus eutectic [233].

Kinyanjui *et al*. have shown that lead-free (Sn-Ag-Cu) solder ball size can influence solidification temperature upon cooling from the melt. They observed that the Sn dendrite arm width increases monotonically with ball diameter indicating a possible dependence of the mechanical response of such solder balls upon size [228]. Also, Arfaei *et al*. investigated the effect of solder ball size on the undercooling of Sn-3Ag-

0.5Cu lead-solder joints. They found that the diameter of the solder ball has a significant effect on the solidification temperature and microstructure [234].

2.3.2 Solder microstructure evolution

Many studies on the effect of ageing in solder joints have been directed at evaluating the growth of intermetallic layers at the solder substrate interface. In contrast, only limited work has been published on microstructure changes in bulk solder joint alloys during ageing.

Figure 2.36 shows SEM images of the microstructures of aged and un-aged 63Sn-37Pb specimens [235]. It can be seen that the as-cast Sn-37Pb eutectic alloy was consisted of lead-rich phase (white, elongated particles) and β-Sn matrix (grey). After ageing, the microstructure has coarsened and the lead-rich phase remains distributed in the Sn matrix but also contains some Sn particles distributed within it. This phase redistribution was found to affect the deformation behaviour, when observed under the SEM, with the larger grains in the aged specimen permitting much more grain deformation before fracture. In a more practical test, Lampe *et al*. found losses in shear strength and hardness of up 20% in tin lead (Sn-Pb) and tin lead antimony (Sn-Pb-Sb) alloys stored at room temperature for 30 days [236].

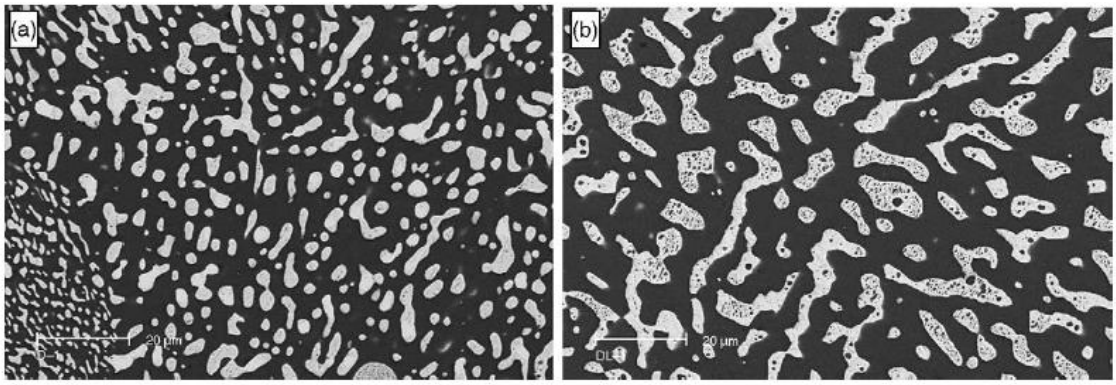

Figure 2.36: Initial microstructures of (a) as-cast and (b) aged specimens [235]

The influence of isothermal ageing on deformation behaviour of 96.5Sn-3.5Ag eutectic solder alloys has been investigated by Ding *et al*. [237]. Optical images of the same field before and after ageing are shown in Figure 2.37 and it can be seen that the macro morphology of the grains has not changed significantly, but the grain and interphase boundaries have become more diffuse. Closer examination revealed many coarsened Ag_3Sn particles along the interphase boundaries between the Sn-dendrites and the Sn-

Ag eutectic structure and the sparse distribution of the eutectic structure with the coarser Ag_3Sn phase had made the boundary indistinct. The overall effect of the ageing was, as one might expect, to increase the tensile ductility and reduce the yield strength and UTS, all by about 30%.

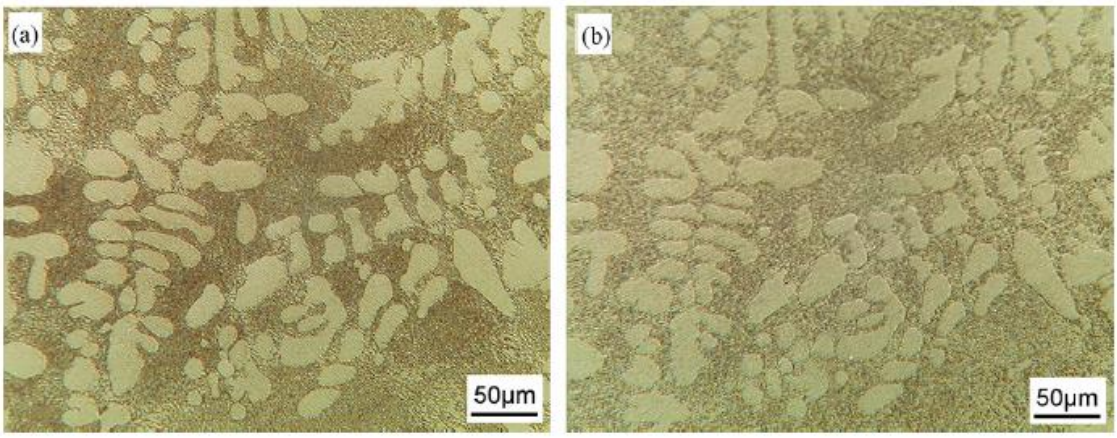

Figure 2.37: Optical image of Sn3.5Ag solder alloys (a) before and (b) after ageing treatment in the same area [237]

A study the effect of thermomechanically induced phase coarsening of Sn-Ag microelectronic solder joint alloys showed that the majority of fine Ag_3Sn particles present in bulk solder after reflow are replaced by a few coarse Ag_3Sn platelets during thermo-mechanical cycling (TMC) [238]. The spacing and size of Ag_3Sn platelets increased in static ageing (500h ageing at 423K), more so in thermo-mechanical cycling (TMC) due to a process of strain-enhanced coarsening. In Sn-4.0Ag-0.5Cu aged at 150°C for 1000 h and Sn-3.8Ag-0.7Cu aged at 35°C at 14 days, 100°C for 14 days or 180°C, considerable microstructural coarsening was found [239]. *Long et al*. investigated the effect of temperature on the microstructure of Sn-3.8Ag-0.7Cu solder under various ageing conditions [241]. They found that the ageing temperature at (100°C and 180°C) has a significant effect on the coarsening microstructure of the Ag_3Sn and Cu_6Sn_5 precipitates in the interdendritic spaces as shown in Figure 2.38.

Pang *et al*. studied the effect of temperature on the microstructure of a Sn-3.8Ag-0.7Cu alloy at a fixed ageing time of 167 hours [240]. They found that the increased ageing temperature made the IMCs become smaller in number, larger in size and rounder in shape, indicating the growth of large IMCs at the expense of the small ones. The effect of time was investigated by using a fixed high ageing temperature 125°C and various

ageing times which revealed, unsurprisingly, that increasing ageing time caused the IMCs to become coarser.

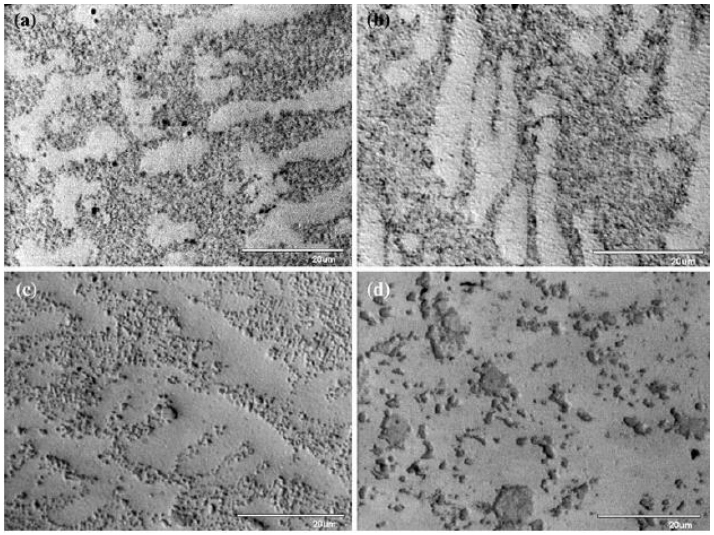

Figure 2.38: Microstructures of the Sn-3.8Ag-0.7Cu samples following (a) reflow and stabilization, (b) aging for 14 days at 35°C, (c) aging for 14 days at 100°C, and (d) ageing for 4 days at 180°C [241]

Snugovsky *et al*. have observed the changes of the Sn-3.8Ag-0.7Cu microstructure during ageing for various times at 150°C [242]. Like others, they found that, with ageing, the Sn dendrite pattern became increasingly less distinct due to the continuous coarsening of the Ag_3Sn and Cu_6Sn_5 phases. They also noted that the Ag_3Sn phase coarsened slowly owing to the slow diffusion rate of Ag in Sn, while coarsening of the Cu_6Sn_5 particles occurred faster because of the much faster diffusion rate of Cu. During thermal cycling, solder joints are subjected to stresses due to CTE mismatches between the package substrate and the PCB. Under these conditions, the Ag_3Sn and Cu_6Sn_5 phases are known to coarsen particularly at the solder-copper pad interface [243, 244].

Several studies have been performed on the degradation of BGA ball shear strength at room temperature [245-248] and elevated temperatures [249-252]. All of these studies have indicated microstructure coarsening and intermetallic layer growth. A number of researchers have also tracked the changes in mechanical properties by measuring the hardness properties as a function of ageing time and temperature. Arfaei *et al*. [234], for example, measured significant hardness losses in Sn-Ag-Cu even after a few hours at temperatures as low as 70°C as shown in Figure 2.39. Arfaei *et al*. also carried shear fatigue tests under load control for samples aged for various times at 125°C and found that the fatigue life and the shear strength both decreased with ageing time. In a slightly

less extensive series of tests Zhang *et al*. [253] found that the Young's modulus and yield stress of the Sn-37Pb and Sn-Ag-Cu alloy decreased with increasing the ageing time at 125°C.

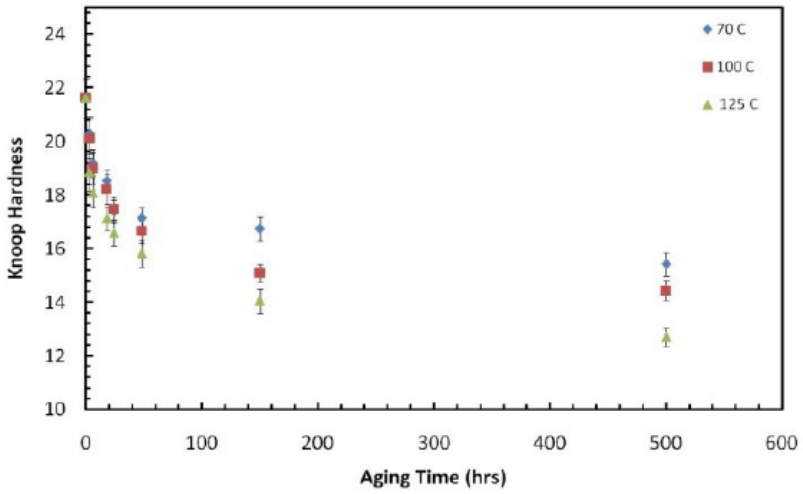

Figure 2.39: The effect of ageing time on hardness of SAC 305 at three different temperatures; 70, 100 and 125°C [234]

2.4 Experimental techniques for solder fatigue

There are considerable challenges involved in making mechanical tests on solder joints which replicate the mechanical situation in service and yet permit appropriate observations and control of the stresses and strains in the solder. Many researchers have simply performed thermal cycling tests for various types of package using thermal chamber to change temperature and hence apply strains to the package [110, 254-256]. However, the approach needs to be backed up by considerable thermo-mechanical analysis for any generic conclusions are to be drawn about the behaviour of the solder, so it is usually restricted to quality control or design assessment.

An alternative approach to loading real electronic components is to carry out the test isothermally and introduce the strain directly. This has the advantage of mechanical control, although the stress distribution between the components can again be difficult to predict. Kim *et al*. [257] assessed the high cycle fatigue strength of leaded and lead-free BGA packages using a new type of vibration fatigue machine to introduce various mixed mode stresses. It was necessary to use FEA to obtain the stress in order to construct an S-N curve for the solder ball. As mentioned earlier Park and Lee [107] have directly loaded BGA in a variety of configurations from pure tension to pure shear. However, the widely varying mechanical properties of the materials involved, Si, glass-

epoxy composite (FR-4) and the solder itself, gives difficulty in finding the displacement (hence the strain) applied to the solder itself [88, 151, 258].

To get round this problem, many workers have developed specific specimens consisting only of copper and solder, which has the advantage that the properties of the copper are guaranteed to be relatively temperature insensitive and linear elastic over the test conditions of interest [178]. Such specimens include lap [259], cylindrical [108] and loading includes using conventional test machines and piezo-actuators [176].

Many researchers have devised their own equipment for carrying out tests on one or several solder balls. For example, Wiese *et al*. [176] constructed a micro mechanical fatigue tester with very precise force and displacement. The test setup consisted of a piezoelectric translator, force sensor and a dual beam laser interferometer (displacement sensor), with each laser beam being reflected at one of two neighbouring edges of the specimen silicon chips. Other devices include a precise micro mechanical fatigue tester using servo hydraulic control [151], although this was limited in terms of speed of operation (frequency). A micro shear tester using a piezoelectric translator, which provides a smooth movement with sub-nanometre resolution for a wide range of velocities with a dual beam laser interferometer to measure the displacement [176] overcame this limitation.

For high cycle fatigue, many researchers have used electrodynamic vibration shakers to apply deflection to various types of package [260-265]. The advantage of using a shaker is that it can drive with high frequency, although it is difficult to control either the load or the displacement.

Laser Moiré interferometry has been used by several researchers to measure the in-plane deformation of cross-sectioned electronic packages that are subjected to mechanical [266-269], thermal [99, 270-275], combined vibration and thermal [213, 276] and electrical power loading [277-280]. The technique can find local deformations and hence the strain contours in the solder material which can be used to validate FEA simulations, but have not been used to estimate the strain range or to estimate fatigue life of solder joints.

2.5 Unresolved research issues

The literature review undertaken by this thesis indicates an improved understanding of the constitutive and thermo-mechanical behaviour and microstructure leaded and lead-free solder joints. However these studies are not as comprehensive as those on Sn-37Pb and there are unresolved areas to be investigated that are critical to understanding the behaviour of these alloys. Given the microstructural sensitivity and the ball grid array (BGA) solder joints, a detailed study of the effect of each of these microstructural parameters on the mechanical behaviour is still lacking within the literature and this experimental study aims to provide a deeper understanding to this subject.

- A point of particular interest is that given the lack of concurrent vibration and thermal loading is commonly encountered in the service life of electronic products. Though extensive research exists in literature for solder joint failures due to thermal cycling, limited research has been conducted on investigating solder joint failures due to a combination of vibration and thermal cycling, and none on a combination of in phase and out phase cycling. In this research, vibration and thermal cycling tests were conducted at various stresses and frequencies under load control on leaded and lead-free BGA assemblies.
- Following this line of investigation, it is also important to assess if the microstructure and micro-hardness changes in bulk solder joint alloys during ageing. Many researchers have investigated the effect of ageing on intermetallic compound layer growth at the solder substrate interface in solder joints. In

contrast, only limited research has been done on microstructure changes in bulk solder joint alloys during ageing.

- Another issue to be examined is to obtain a correlation between the microstructural configuration and mechanical deformation behaviour. While the literature does provide isolated examples of such studies, these however, are not comprehensive enough to cover the entire range of loads and microstructural configurations.

In summary, a comprehensive understanding of the evolution of the constitutive properties, thermo–mechanical fatigue properties and correlation of the microstructure of ball grid array (BGA) solder joints is lacking and needs further investigation.

Chapter 3: Materials, Experimental Apparatus and Methods

This chapter describes all experimental aspects of the thesis. First, the materials tested and sample preparations are covered, followed by the design and commissioning of the load-displacement test rig. Next, the sample characterisation is covered including, metallographic methods, hardness testing and calibration of the load-displacement behaviour of various components of the test rig. Finally, the experimental rationale and procedures are described in preparation for the presentation of the results in the next chapter.

The objective of this research was to examine the thermo-mechanical fatigue behaviour of a lead-free solder in comparison with leaded solder. To this end, vibration and thermal cycling tests were performed at various stresses and frequencies under load control. Also, some supporting quasi-static mechanical tests were necessary, in order to assess the relative effects of creep and plastic deformation under the fatigue test regime.

3.1 Specimens

All of the mechanical testing was carried out on 4-ball arrays of solder joints, produced using similar procedures to commercial ball grid arrays (BGA). The following sections discuss the two solder materials chosen as well as the procedures for fabrication of the 4-ball arrays.

3.1.1 Materials

The compositions of the (Sn-37Pb) and lead-free (Sn-3.8Ag-0.7Cu) alloys as supplied by Multicore Solders, are given in Tables 3.1 and 3.2 and the relevant equilibrium phase diagrams are shown in Figures 3.1 and 3.2, respectively.

Table 3.1: Composition for leaded solder paste

Alloy	**Composition (Weight %)**			
	Tin	**Lead**	**Rosin**	**Modified Rosin**
Sn-37Pb	50-60	30-40	1-5	1-5

Table 3.2: Composition for lead-free solder paste

Alloy	Composition (Weight %)					
	Tin	**Silver**	**Copper**	**Rosin**	**Modified Rosin**	**1,2,5,9,10-Hexabromocyclodecane**
Sn-3.8Ag-0.7Cu	80-90	1-5	0.1-1	1-5	1-5	0.1-1

The compositions quoted on material safety data sheets (MSDS) are often expressed as a range, rather than an exact figure. This is either to protect formulations or, in the case of solder products, because the amount of tin and lead in a solder paste will vary dependant on whether flux is present or not (Sn-37Pb as a solid alloy will be composed of 63% tin and 37% lead, however if you have the alloy in a solder paste at 90% metal content there will be 56.7% tin, 33.3% lead and 10% flux).

Solder pastes consist of the alloy in a powder form combined with a flux which will contain rosin/resin/modified rosin, organic activators (acids and/or halides), solvents and gelling agent.

A modified rosin is essentially a rosin which may have been purified or undergone a reaction to add something extra to the material. Normally modified rosins are paler in colour due to removal of impurities. Often the modified rosin will have a higher softening point.

Table 3.3: Composition for leaded solder alloy obtained by chemical analysis

		Composition (Weight %)										
Sn	**Pb**	**As (max)**	**Bi (max)**	**Fe (max)**	**Cu (max)**	**Al (max)**	**Cd (max)**	**Zn (max)**	**Sb (max)**	**Au (max)**	**Ni (max)**	**Ag (max)**
63-64	Remainder	0.004	0.1	0.02	0.08	0.001	0.005	0.003	0.2	0.005	0.005	0.015

Table 3.4: Composition for lead-free solder alloy obtained by chemical analysis

	Composition (Weight %)											
Sn	**Pb (max)**	**As (max)**	**Bi (max)**	**Fe (max)**	**Cu (max)**	**Al (max)**	**Cd (max)**	**Zn (max)**	**Sb (max)**	**Au (max)**	**Ni (max)**	**Ag (max)**
Remainder	0.05	0.03	0.1	0.02	0.6-0.8	0.001	0.002	0.001	0.1	0.005	0.007	3.6-4.0

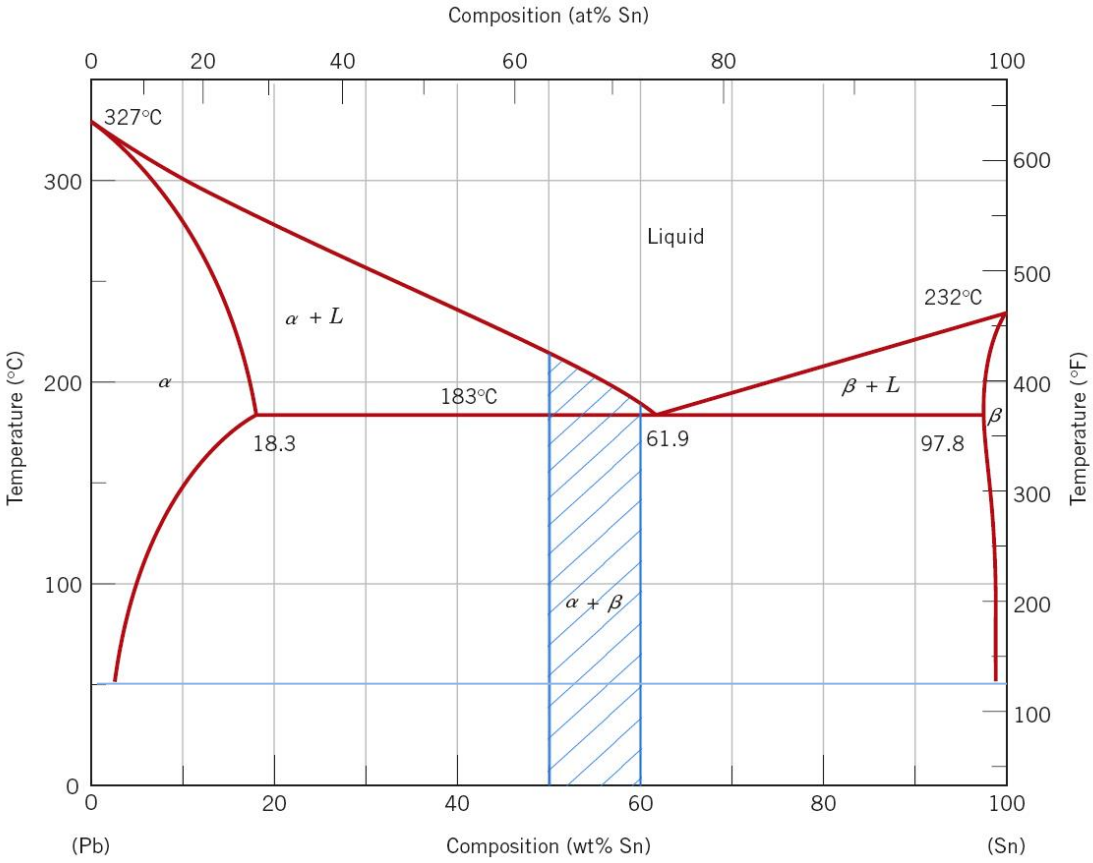

Figure 3.1: Lead-Tin Phase diagram [281]

The lead-tin solder in Table 3.1 is of slightly hypo-eutectic composition and, at equilibrium, will contain a small amount of primary α (Pb) with a two-phase eutectic mixture of α (Pb) and β (Sn), Figure 3.1. The mass fraction of primary α (Pb) at equilibrium at the eutectic temperature will therefore be:

$$W_{1\alpha} = \left(\frac{61.9 - C_{Sn}}{61.9 - 18.3}\right) \tag{3.1}$$

Giving fractions between 0.04 and 0.27 for the composition range cited.

In practice, undercooling of the eutectic mixture in real solder balls means that it is unlikely that primary α (Pb) will be distinguishable from eutectic α (Pb) in the microstructure and therefore it is of more use to determine the mass fractions of the two phases overall at the eutectic temperature:

$$W_{\alpha} = \left(\frac{97.8 - C_{Sn}}{97.8 - 18.3}\right) \tag{3.2}$$

and at lower temperatures where diffusion can still occur (say 50°C, Figure 3.1):

$$W_\alpha = \left(\frac{99 - C_{Sn}}{99 - 3}\right) \tag{3.3}$$

giving a range from 0.47 to 0.60 at eutectic temperature and 0.41 to 0.51 at 50°C.

Thus, the as-solidified solder may contain a weight fraction of between 0.47 and 0.60 of α, assuming that no further changes in microstructure are able to take place after solidification. However, ageing of the alloy (say at 50°C) might be expected to allow the tie line to shift downwards so reducing the weight fraction by about 15% with a concomitant reduction in the amount of dissolved Sn in the α-phase and, to a lesser extent, Pb in the β-phase. This can be shown from the calculation above using lever rules expression for computation of α-phase fraction. Both phase particles might also be expected to coarsen on ageing, and the coarsening, along with the reduced amount of solid-solution strengthening, might both be expected to reduce strength (and hardness).

To calculate volume fractions for comparison with metallographic measurements, it is necessary to estimate the density of each phase. This can be done using the published densities of the pure metals, with a correction for the impurity atom atomic numbers as follows. For the as-solidified composition:

$$\rho_\alpha = \frac{100}{\frac{18.3}{7.24} + \frac{81.7}{11.23}} = 10.20 \ {}^{\mathrm{g}}/_{\mathrm{cm}^3} \tag{3.4}$$

$$\rho_\beta = \frac{100}{\frac{97.8}{7.24} + \frac{2.2}{11.23}} = 7.29 \ {}^{\mathrm{g}}/_{\mathrm{cm}^3} \tag{3.5}$$

For the aged composition:

$$\rho_\alpha = \frac{100}{\frac{3}{7.24} + \frac{97}{11.23}} = 11.05 \ {}^{\mathrm{g}}/_{\mathrm{cm}^3} \tag{3.6}$$

$$\rho_\beta = \frac{100}{\frac{99}{7.24} + \frac{1}{11.23}} = 7.27\ {}^{\mathrm{g}}/_{\mathrm{cm}^3} \tag{3.7}$$

Given the relationship between volume fraction and area fraction:

$$V_\alpha = \frac{\frac{W_\alpha}{\rho_\alpha}}{\frac{W_\alpha}{\rho_\alpha} + \frac{W_\beta}{\rho_\beta}} \tag{3.8}$$

Thus, the range of volume fraction of α-phase that might be expected for the as-solidified structure is $0.39 \leq V_\alpha \leq 0.52$, and, for the aged structure, $0.31 \leq V_\alpha \leq 0.41$.

The Sn-Ag-Cu solder in Table 3.2 is close to the tin rich corner of the phase diagram Figure 3.2, which is where the low liquidus temperature prevails.

As can be seen, there is a ternary eutectic at around 0.8 wt. % Cu and 3.8 wt. % Ag consisting of a (Sn)/ Ag_3Sn/ Cu_6Sn_5 mixture. The range of alloy compositions makes it likely that any solder will contain primary (Sn), although it is possible that alloys may contain primary Cu_6Sn_5 or Ag_3Sn. The eutectic is expected to contain relatively small amounts of the two intermetallics, but a large amount of (Sn).

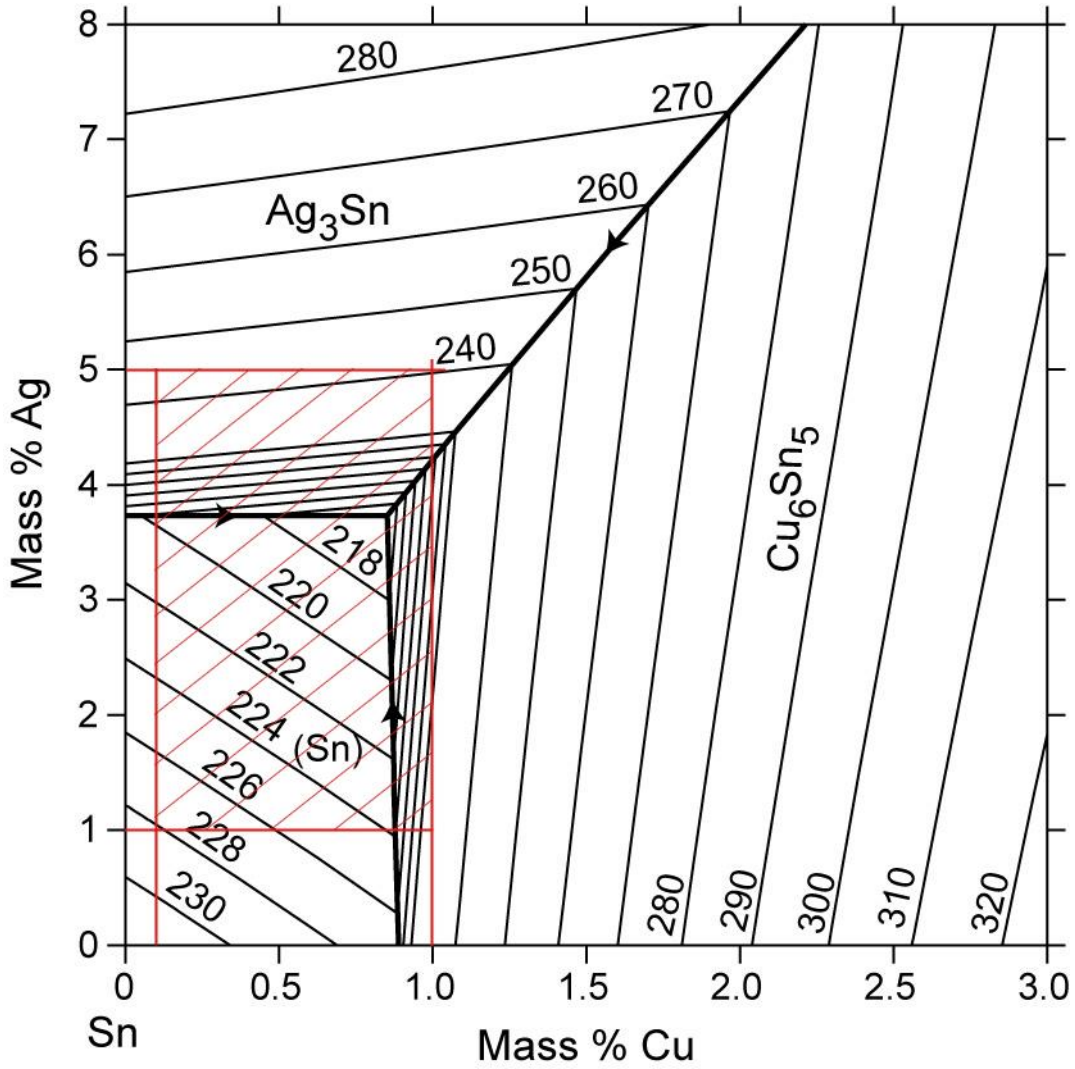

Figure 3.2: Sn-Ag-Cu phase diagram at the Sn-rich corner [282]

3.1.2 Sample preparation

The thermo-mechanical fatigue specimens consisted of a grid of four solder balls of approximate diameter 0.7 mm with 2.54 mm pitch as shown in Figure 3.3, chosen to represent a section of a ball grid array. Each sample consisted of two glass fibre reinforced polymer (FR-4) substrate plates diced to 5 mm × 5 mm with four circular pads etched onto each plate. The thickness of the FR-4 was 1.5 mm and the copper pads were of diameter 0.7 mm and thickness 35 µm, plated with 5 µm of tin. The solder was applied as a paste via a specially-designed stencil with four balls and the specimen formed by reflow soldering in a special jig.

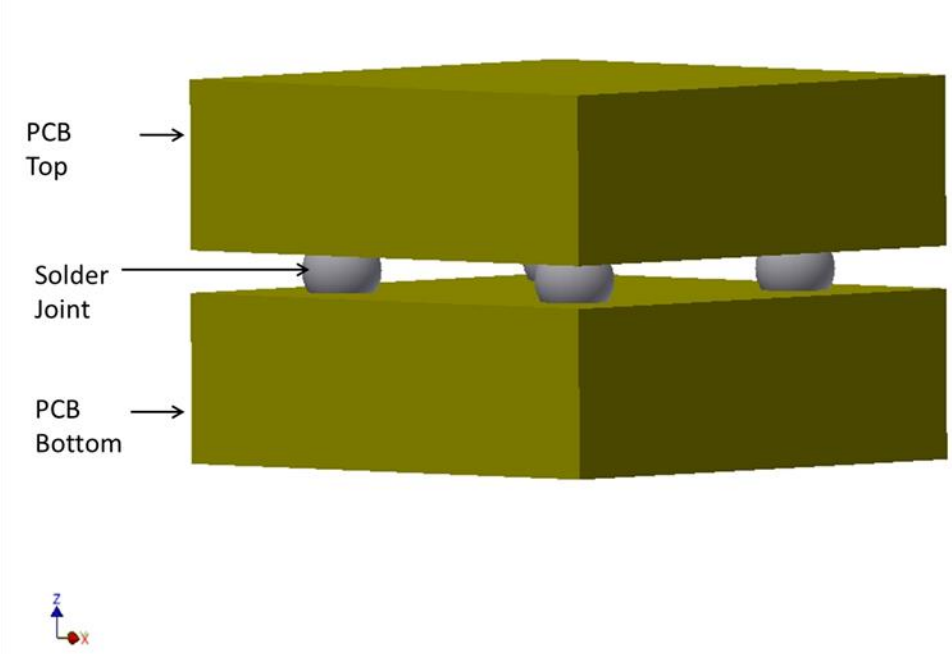

Figure 3.3: Schematic design of the solder joint specimen

The PCB was designed using PCB CAD software (Easy-PC by Number One Systems Ltd) and consisted of an array of elements based on a 5 mm × 5 mm grid with four circular pads of diameter 0.7 mm as shown in Figure 3.4. A copy of the design was then sent to a contractor (PCB-Pool) to manufacture the board, a sample of which is shown Figure 3.5. The board was later cut into square pieces as shown in Figure 3.6 using a dicing machine. The board is made from FR-4, an 8-ply glass-epoxy laminate of overall thickness 1.5 mm containing 40% glass fibres woven in a 0°/90° configuration [283].

A polished cross-section of the FR-4 material is shown in Figure 3.7, where it can be seen that the fibre bundles are roughly lenticular in cross-section and each fibre is of approximate diameter 7 μm.

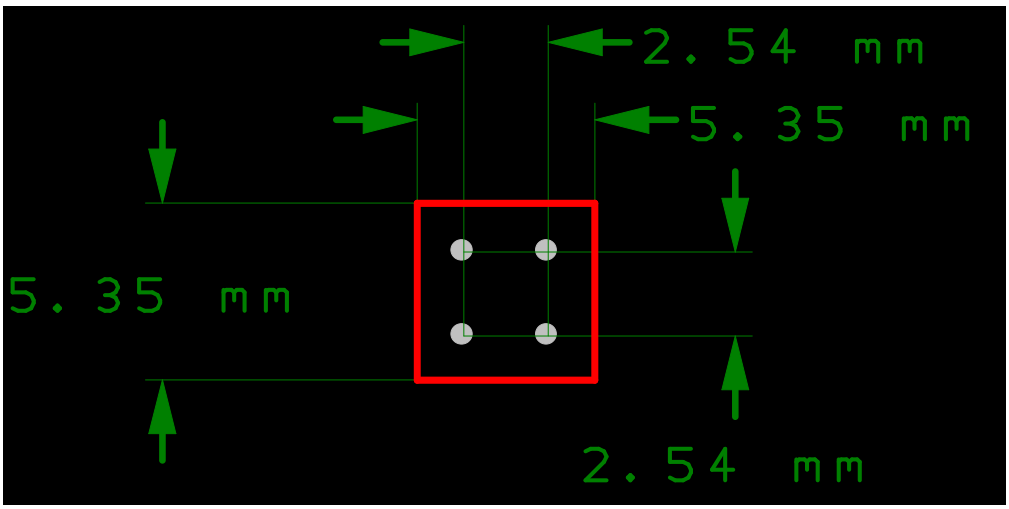

Figure 3.4: FR-4 substrate unit cell design

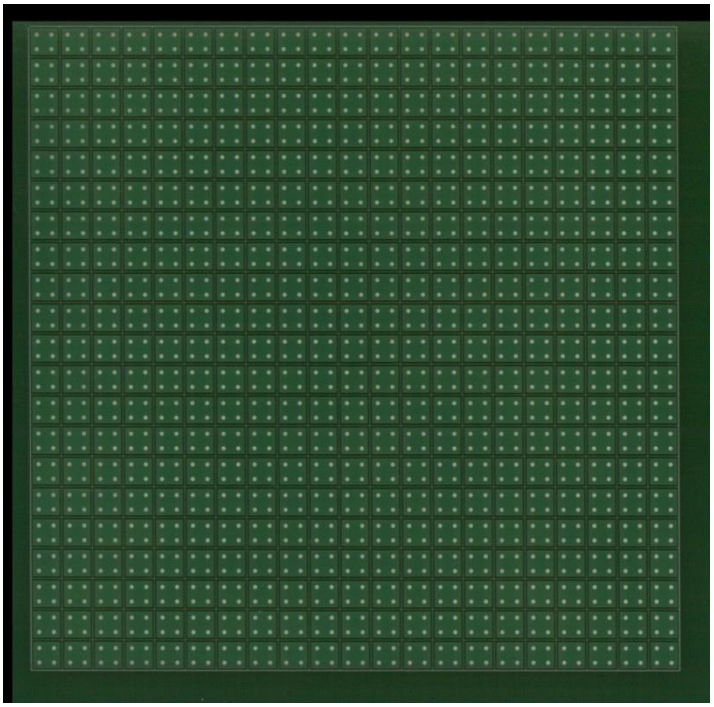

Figure 3.5: Manufactured FR-4 substrate board

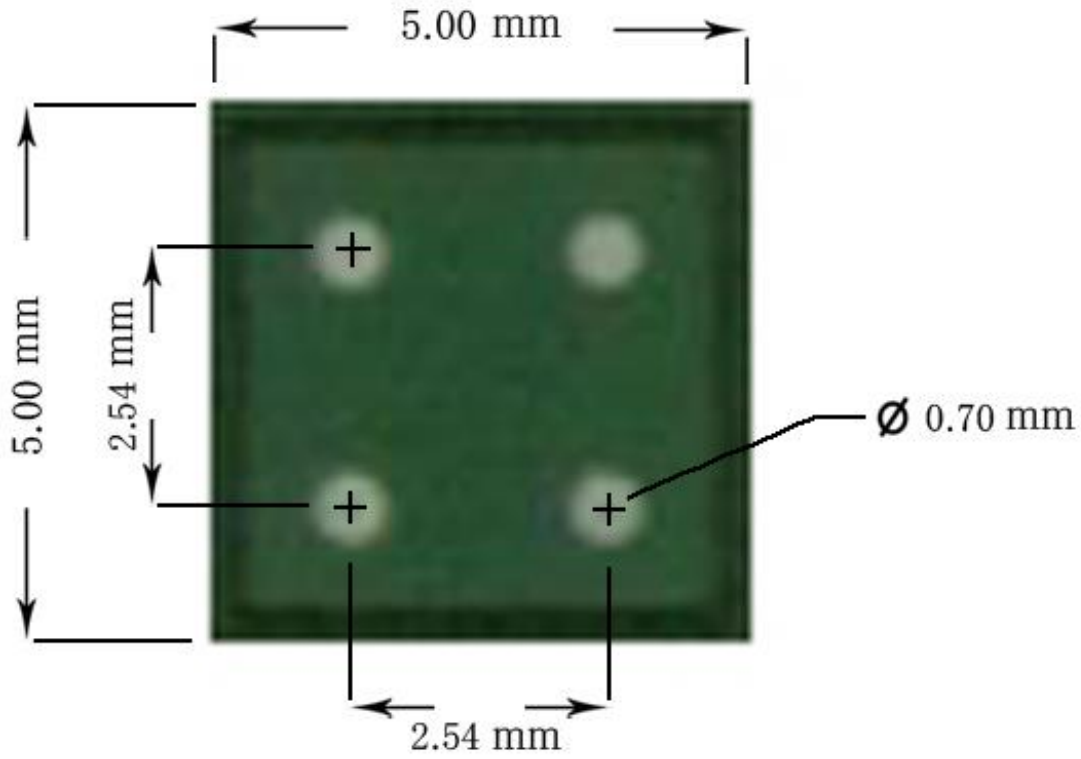

Figure 3.6: Typical FR-4 substrate after dicing

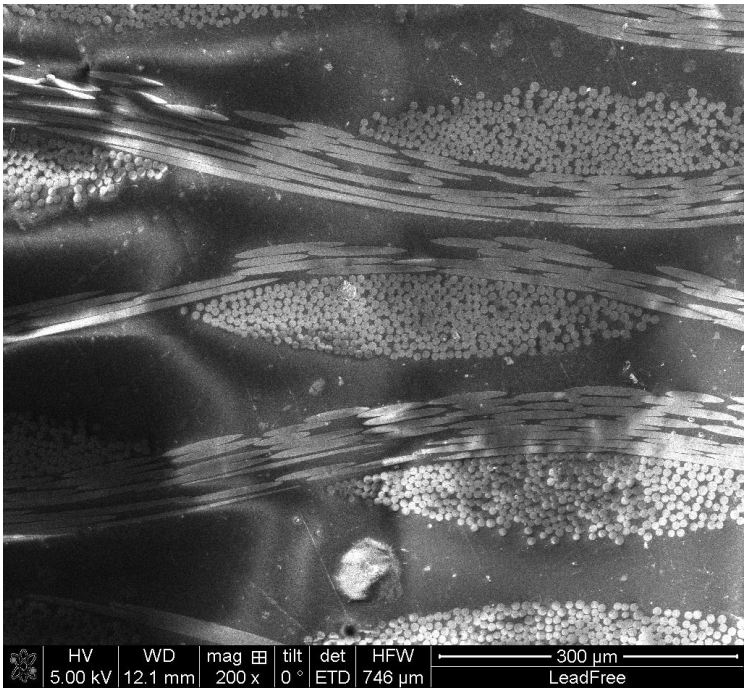

Figure 3.7: SEM image of cross section of FR-4 substrate

The values of the FR-4 orthotropic laminate elastic properties are listed in Table 3.5:

Table 3.5: Orthotropic FR-4 laminate properties [284]

E_x [MPa]	E_y [MPa]	E_z [MPa]	v_{yx}	v_{xz}	v_{yz}	G_{yx} [MPa]	G_{xz} [MPa]	G_{yz} [MPa]
12000	3000	12000	0.22	0.27	0.139	850	3100	850

The PCB was prebaked in an oven at 125°C for 24 hours before depositing the solder paste. This was to remove any moisture absorbed by the plastic PBGA body [285], which otherwise could evolve as vapour from the interface between the solder mask and package pad, blowing the solder away and causing an open circuit, with associated loss of bonding. A jig (stencil) was manufactured to apply the solder paste accurately to the PCB substrate and this is shown in Figure 3.8. A square cavity was machined part-way through a steel sheet to form a recess into which the substrate could be placed. Four holes were then drilled through the steel sheet at the bottom of the cavity to allow the solder paste to be inserted from the opposite side of the steel sheet. Before inserting the solder paste, the relative alignment of the holes with the copper pads on the PCB substrate was checked with an optical microscope. Once solder paste had been inserted into the holes it was pressed down against the copper with a specially-fabricated steel pin.

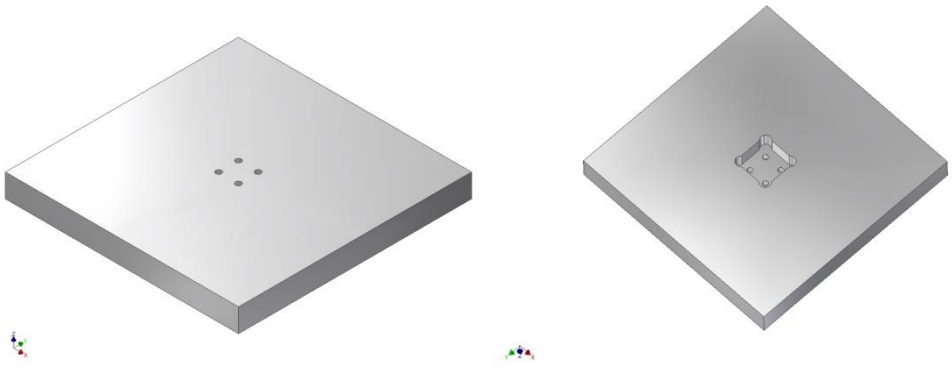

Figure 3.8: Solder paste alignment stencil: left, top view; right, bottom view

To avoid dispersing the solder paste, the pin was machined to a length which left an adequate amount of solder paste on the substrate as shown in Figure 3.9.

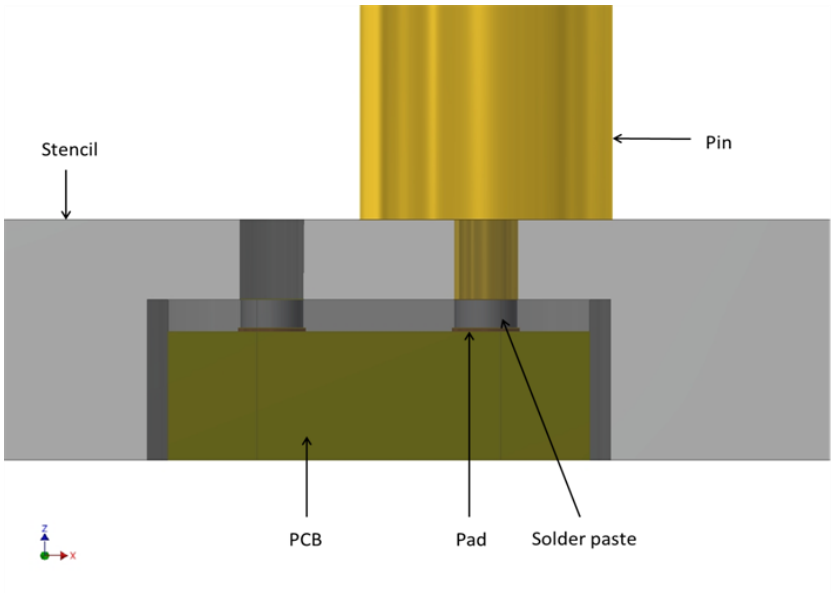

Figure 3.9: Stepped pin

The substrate was then removed from the jig leaving four pillars of solder paste applied to the copper surface, as shown in Figure 3.10. Both the jig and pin were cleaned with Multicor SC-01 flux prior to application of the solder.

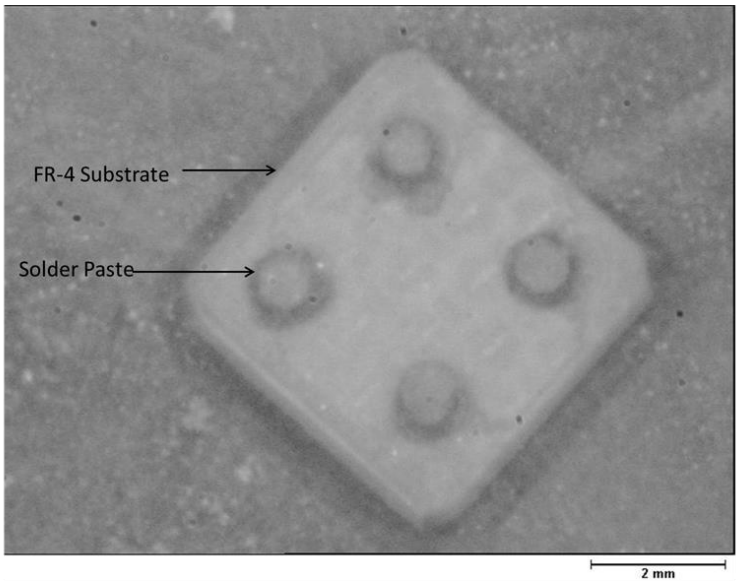

Figure 3.10: Substrate with solder paste applied

Another jig, shown in Figure 3.11 was manufactured to ensure correct relative alignment of the copper pads on both substrates. Spacers were used to achieve a uniform separation of 0.6 mm between the two substrates.

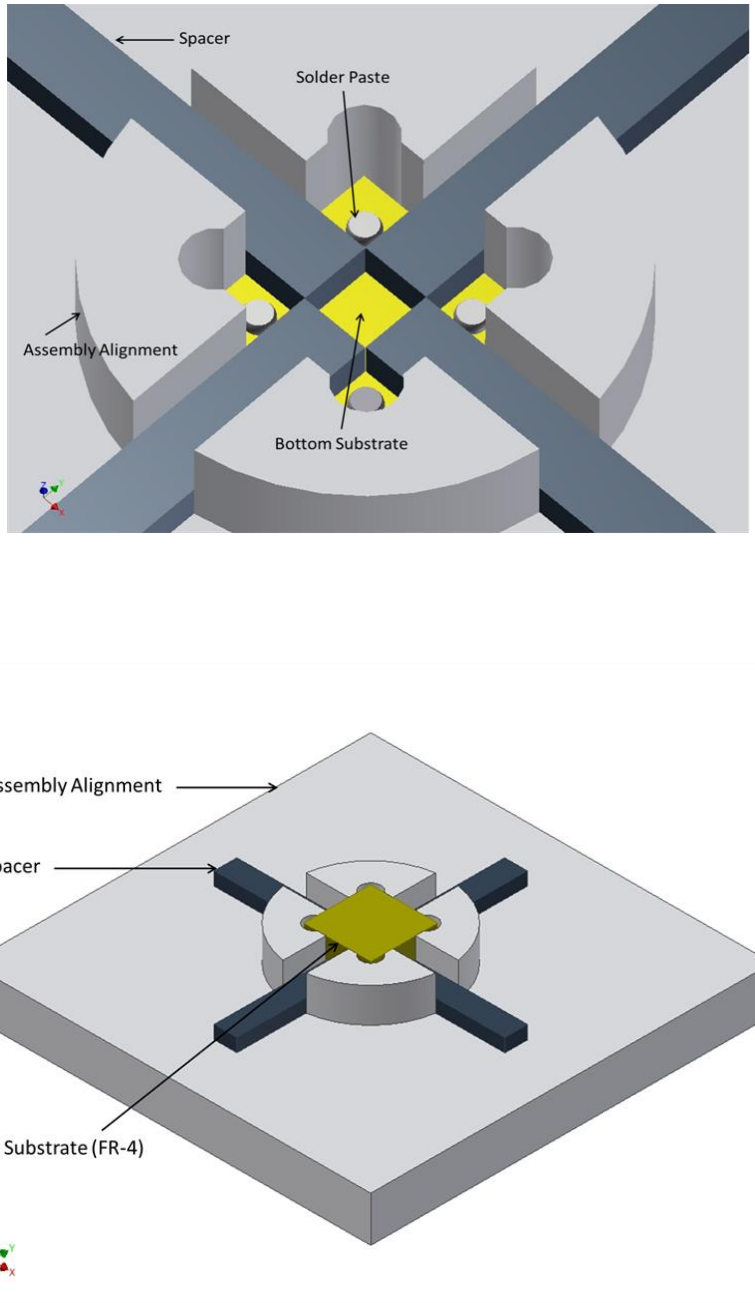

Figure 3.11: The entire sample-jig assembly with spacer: upper diagram shows bottom substrate view, lower diagram show top substrate view

The substrate with the solder paste pillars was placed together with another, identical bare substrate (i.e. with no solder paste) in the jig as shown in Figure 3.11, and the spacers slid into place. The entire assembly was then placed into a hot-air reflow oven

to melt the solder paste and join the substrates together. The assemblies were first preheated from room temperature to a soak temperature and held for 90 sec, as indicated in Table 3.6. The peak temperature was then raised to approximately 30-40°C above the melting point for 60 seconds. Following reflow, the specimen was pushed out of the jig by inserting a pin into a pre-drilled hole in the centre of the alignment jig. Figure 3.12 shows a typical assembly after reflow.

Table 3.6: Reflow profile parameters

Profile	Soak	Peak temperature [°C]	Time above liquidus [seconds]
Sn-37Pb	150-160°C (90 s)	220	60
Sn-3.8Ag-0.7Cu	150-160°C (90 s)	248	60

To isolate the behaviour of solder balls experimentally, a number of specimens were made replacing the diced FR-4 with copper. The calibration details are discussed in section *3.34*. Accordingly, copper plates were CNC - machined to the same dimensions as the FR-4 with projections of 0.7 mm diameter and 0.5 mm height to simulate the copper pads on the FR-4. To avoid flow of the solder over the entire copper surface, a PTFE mask was placed over the pads, as shown in Figure 3.13. Figure 3.14 shows a typical copper substrate sample after reflow.

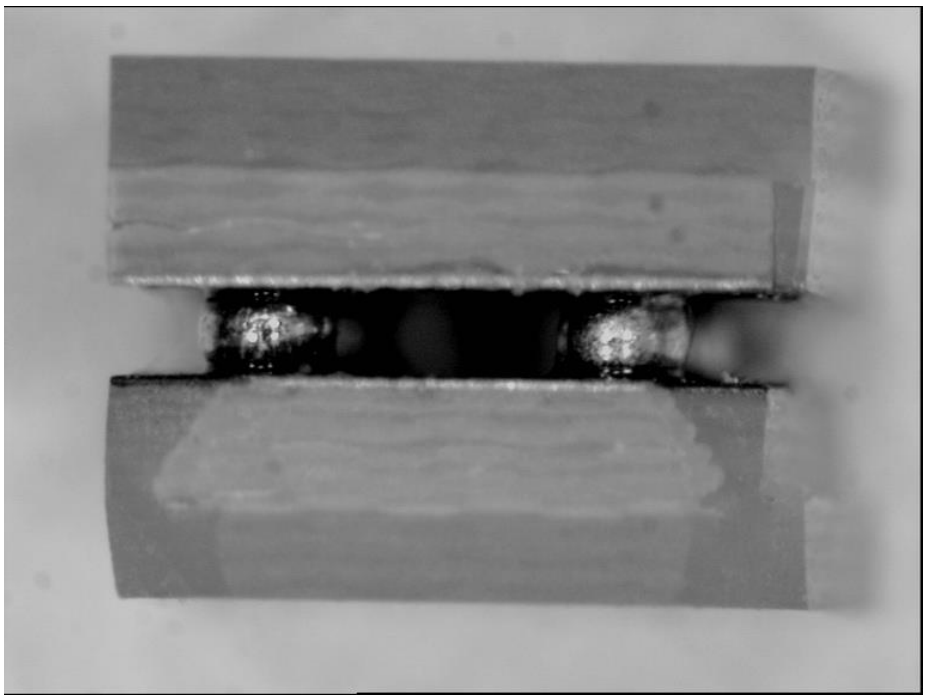

Figure 3.12: Typical 4-ball BGA test-piece

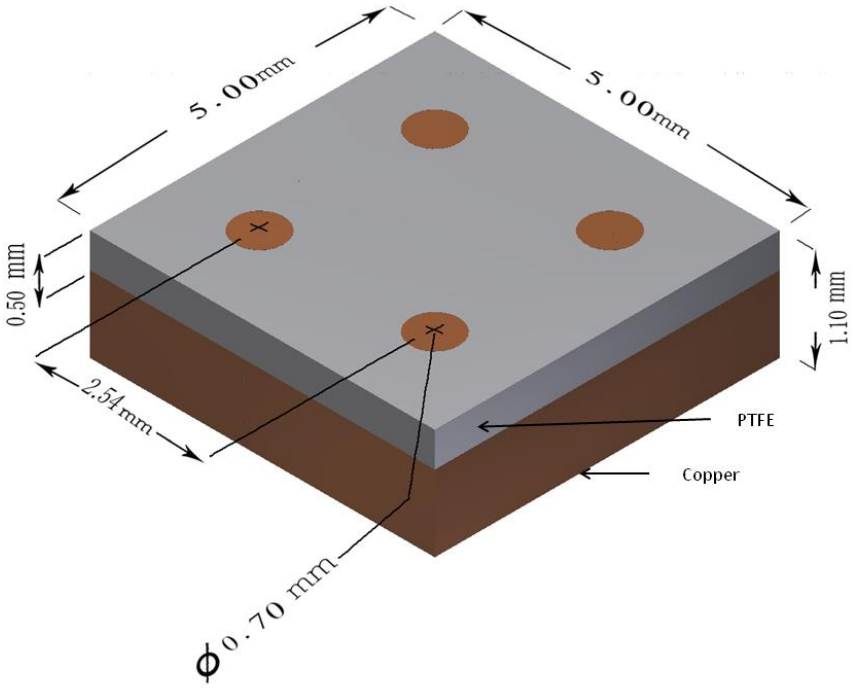

Figure 3.13: Copper substrate with PTFE mask, as machined

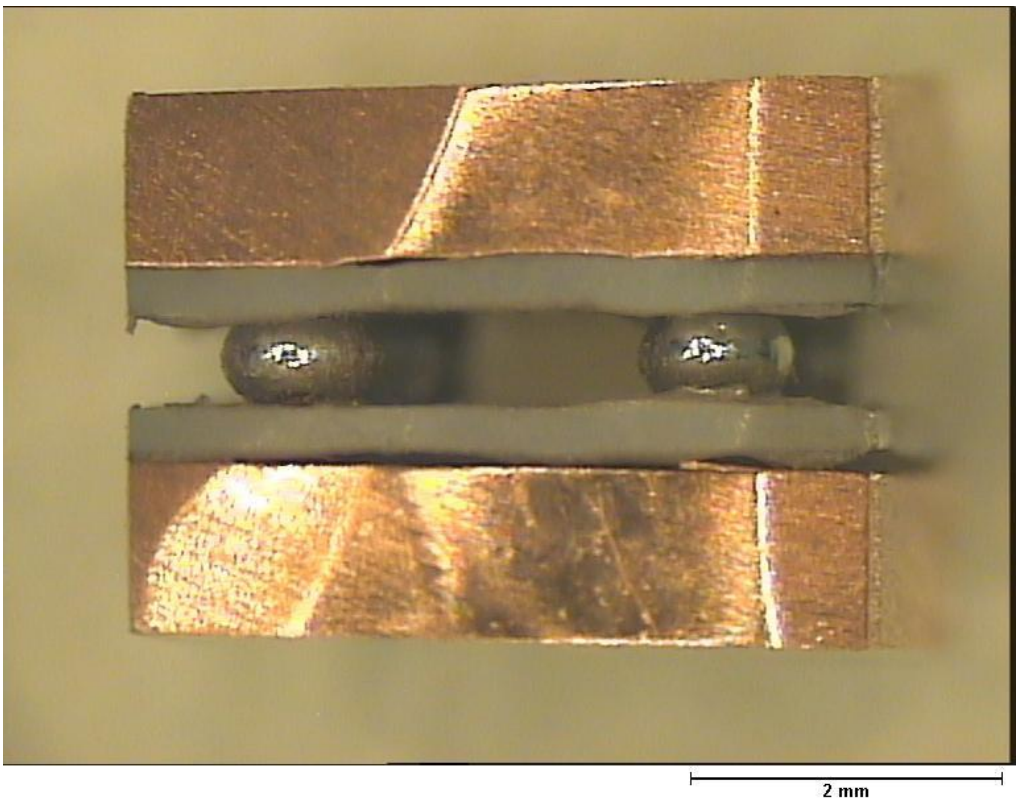

Figure 3.14: Typical 4 ball BGA test-piece with copper substrate

3.2 BGA test rig

The test rig was designed to load the BGA specimens in shear as this is the most common loading direction both in service and in other studies. The rig needed to be capable of applying loads up to 50 N and measuring shear displacements as low as 0.05 μm in both quasi-static and fatigue testing.

The test rig had three distinct elements, each of which required to be independently controllable and measurable, but each of which needed to be integrated with the others. The elements are:

- Temperature measurement and control
- Displacement (strain) measurement and control
- Force (stress) measurement and control

The test rig used to vary the three elements is shown schematically in Figure 3.15. The rig essentially consisted of an actuator to provide shear displacement, an LVDT to

measure the shear displacement and a load cell to measure the reaction force. It was decided at the outset that displacement would only be applied in a single direction as control would become rather difficult if two-way actuation were to be used, particularly in the presence of changing temperature. The shear force was applied through a metallic heat sink which had a square well machined into it, into which the sample fitted, held in place with a thin layer of adhesive of approximate thickness 0.15 mm. The sample was therefore loaded along the edge of the square piece of PCB, which in turn transferred the load to the solder bumps. The final micromechanical testing system as constructed is shown in Figure 3.16.

All components of the system were mounted on an aluminium frame onto the bottom of which was attached a linear slide. The substrate holder was fixed to the slide and a specimen could be placed onto the top of the bottom holder. A second, top substrate holder, a Peltier device, and the top heat sink could then be placed on top of the specimen. The stepper motor was mounted rigidly to the frame, and a compression spring was placed between a disc on the end of the stepper motor lead screw and the pin which bears against the top substrate holder. All interfaces between the slide and the top heat sink were coated in microelectronic heat sink compound to allow good conduction between the specimen heater and the sample.

The load cell was mounted between the top part of the linear slide and the frame, and a LVDT was mounted on the frame opposite the stepper motor with its tip touching the top substrate holder. A bubble level was used to ensure that the top and bottom of the sample were parallel by adjusting three rounded alignment screws, Figure 3.17.

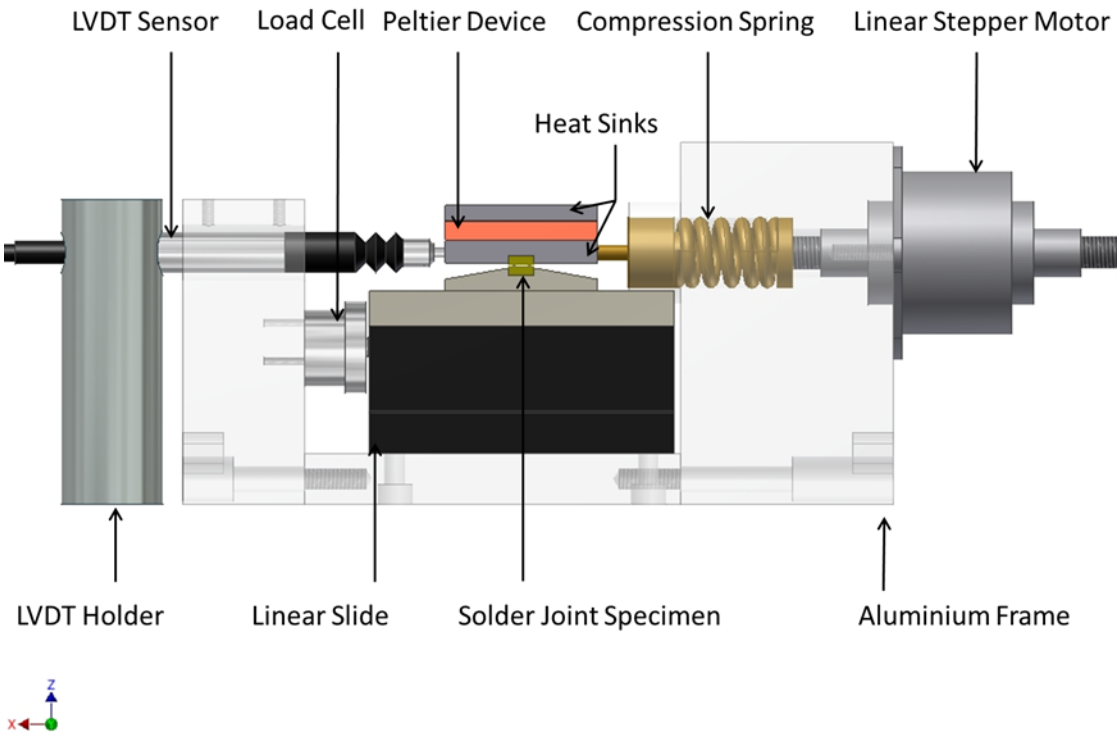

Figure 3.15: Diagrammatic illustration of overall experimental setup

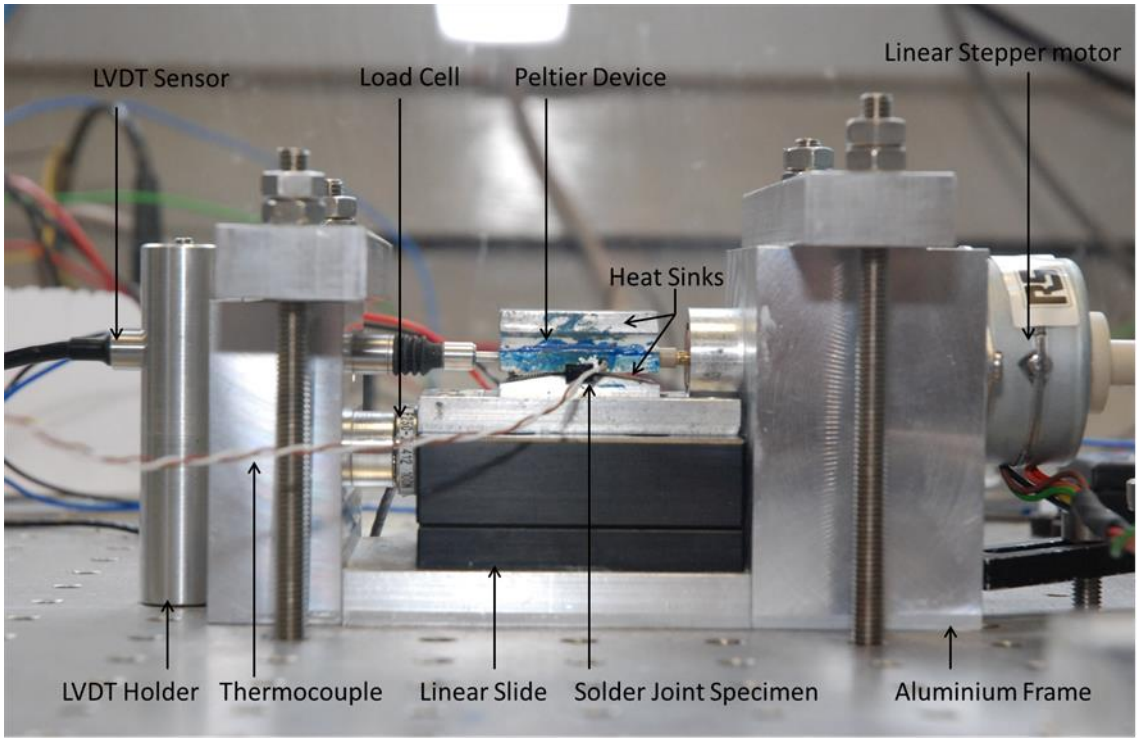

Figure 3.16: Photograph of the experimental setup

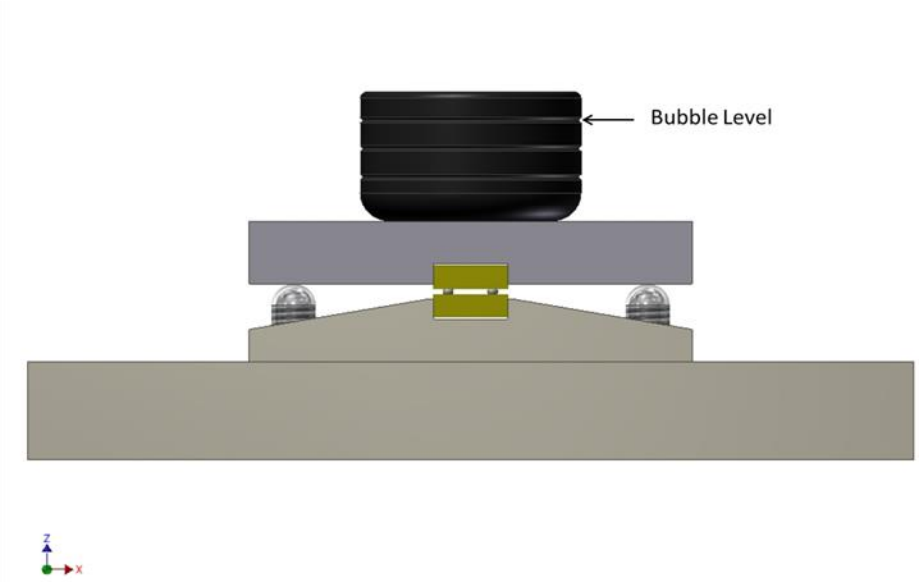

Figure 3.17: Sample assembly and alignment

3.2.1 Mechanical measurement and control

Mechanical testing of solder materials at a realistic scale involves measuring very small displacements at relatively high loads. Also, the inclusion of temperature cycling requires careful calibration to ensure that expansion and contraction of the rig do not interfere with the strain measurement. The sensors for this work (Load cell, LVDT, thermocouple) all proved to be linear within their working range and their respective calibrations are described below.

The load cell (Model F250 from Novatech) was based on resistance strain gauges with a 100N capacity in tension or compression and was used to measure the reaction force in the bottom substrate as the stepper motor pushes the top substrate. It was calibrated by loading and unloading a range of dead weights and the resulting curve is shown in Figure 3.18, each point being the average of ten measurements. The stiffness of the load cell is 6.2×10^{6} N/m. The load cell output was wired to a commercial strain gauge amplifier (Type-628, RDP Electronics) with switchable gain. Before calibration, the amplifier was zeroed.

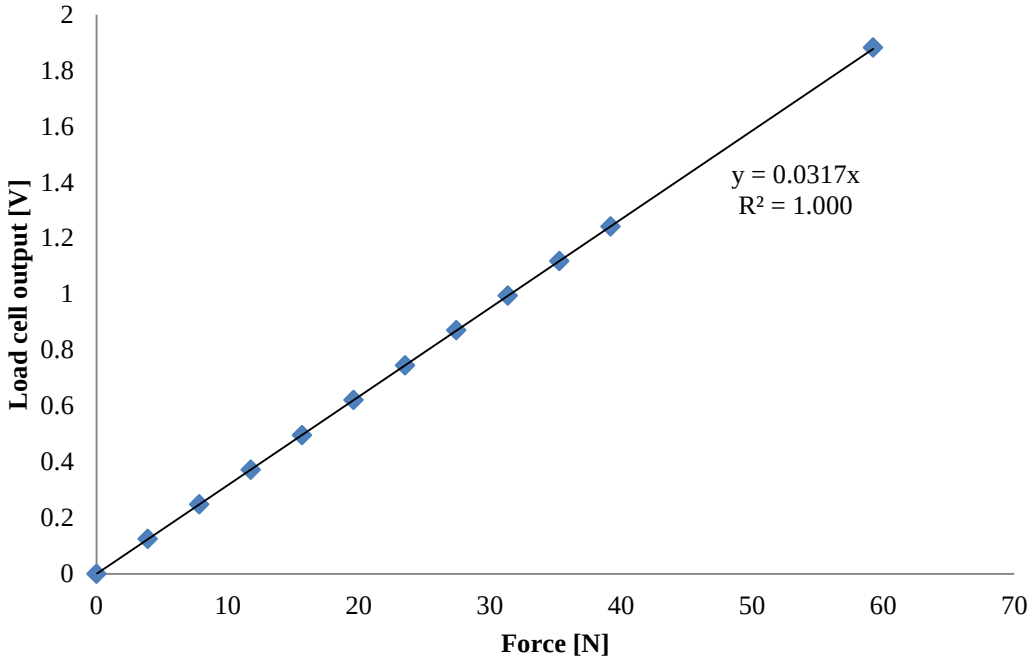

Figure 3.18: Calibration plot of load cell sensor

A highly sensitive, low range (-1000 μm to +1000 μm, linearity: 0.25% and uncertainty of calibration 0.05 μm) calibrated spring return displacement transducer LVDT (Model GT 1000-1.25, RDP Electronics) was used to measure the displacement of the top FR-4 substrate. Power was supplied to the LVDT from a ±15 V DC/500mA unit and a calibrated in line DC amplifier (Model: S7 AC, RDP Electronics, noise- voltage output 5mv peak to peak typical) was used to convert the transducer output to a voltage to be read through the DAQ. The LVDT was calibrated against a micrometer screw and the resulting curve is shown in Figure 3.19. Again each point is the average of ten measurements.

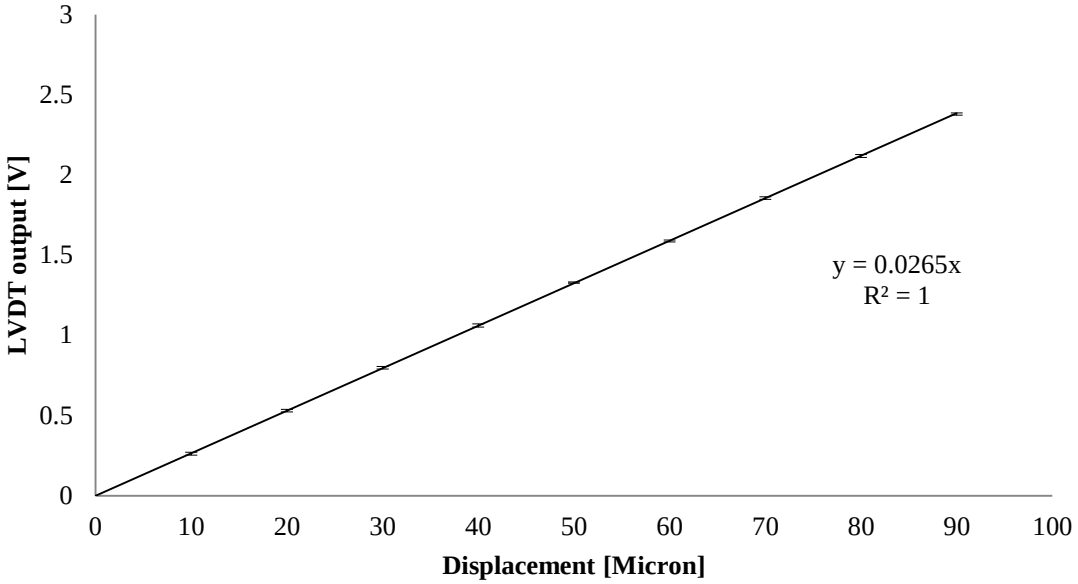

Figure 3.19: Calibration plot of LVDT sensor. The error bar at each calibration point is very small, due to high accuracy LVDT sensors

A unipolar, linear stepper motor (42DBL10 Series Mclennan) was used to achieve the precise displacement of the top substrate. A LabVIEW programme was devised to deliver the required stepper motor control signals *via* a control board. The stepper motor was capable of linear displacements in the forward or backward directions in steps of 12.7 μm, with a maximum deliverable force of 100 Newtons. The frequency of the direction pulse of the linear stepper motor was limited by the force, as shown in Figure 3.20. A compression spring was used to "soften" the system, allowing longer displacements for a given force to improve the resolution of the displacement control. Some preliminary tests with the mechanical system were carried out to measure the stiffness of the spring. The compression spring was placed between the stepper motor and the load cell, and the LVDT was used to measure the displacement of the output shaft, leading to the stiffness illustrated in Figure 3.21.

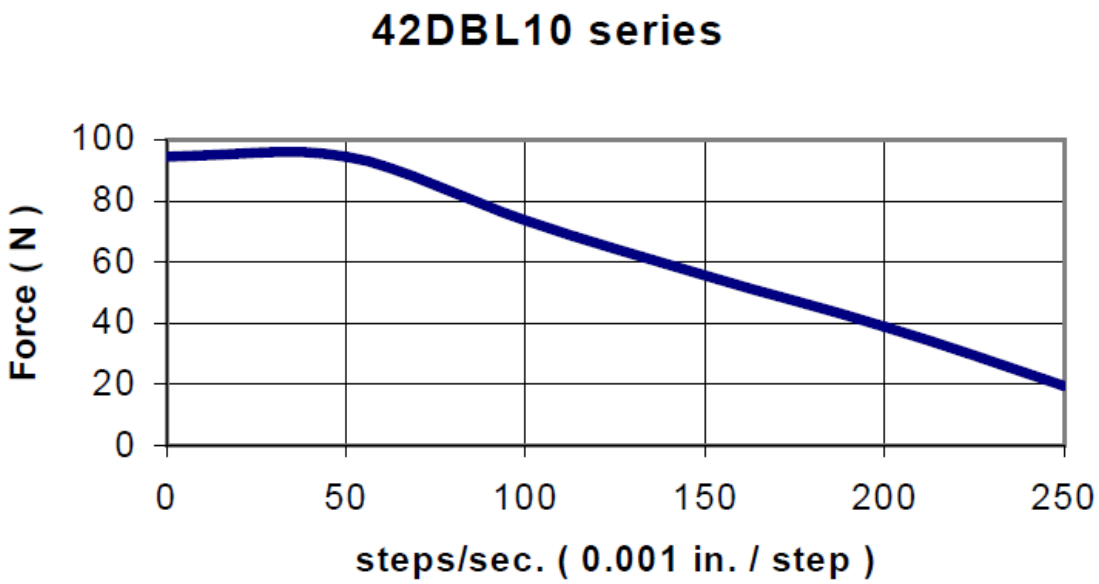

Figure 3.20: Frequency / load performance for linear stepper motor [286]

It was also necessary to ensure that the natural frequency of the loaded spring was not such as to interfere with load control. Using the stiffness, *k*, of 25.36 $^{kN}/_{m}$, the natural frequency can be estimated at a maximum loading of 50N as $\sqrt{\frac{k}{m}}$ = 22 sec^{-1}, which is well above the highest experimental oscillation frequency of 1.7 Hz.

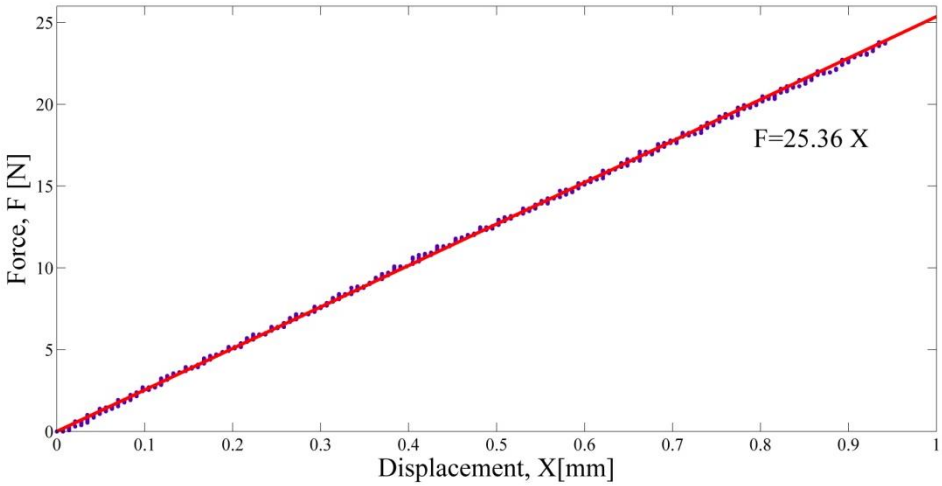

Figure 3.21: Load - displacement curve for sample spring

In order to measure the resultant friction force from the linear slide, another experimental setup were conducted, as shown in Figure 3.22. Another bi-directional load cell (Model DBBSMM-25Kg from Applied Measurements Limited) was mounted between the top part of the linear slide and the stepper motor. It was calibrated by

loading and unloading a range of weights and the resulting curve is shown in Figure 3.23.

The load cell output was wired to a commercial data track process instrument (Type Tracker 200 from applied measurements limited). The results show a linear relation between the two forces as shown Figure 3.24. The friction factor was found to be 1.113.

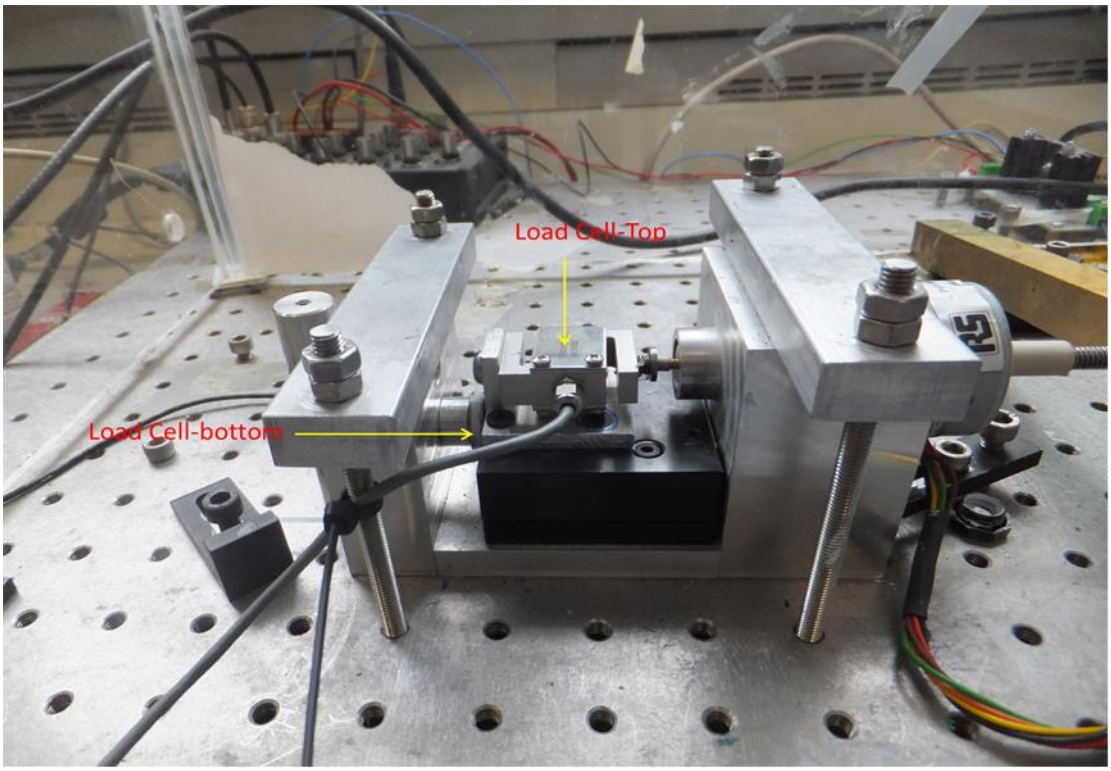

Figure 3.22: Photograph of the experimental setup to measure the friction force

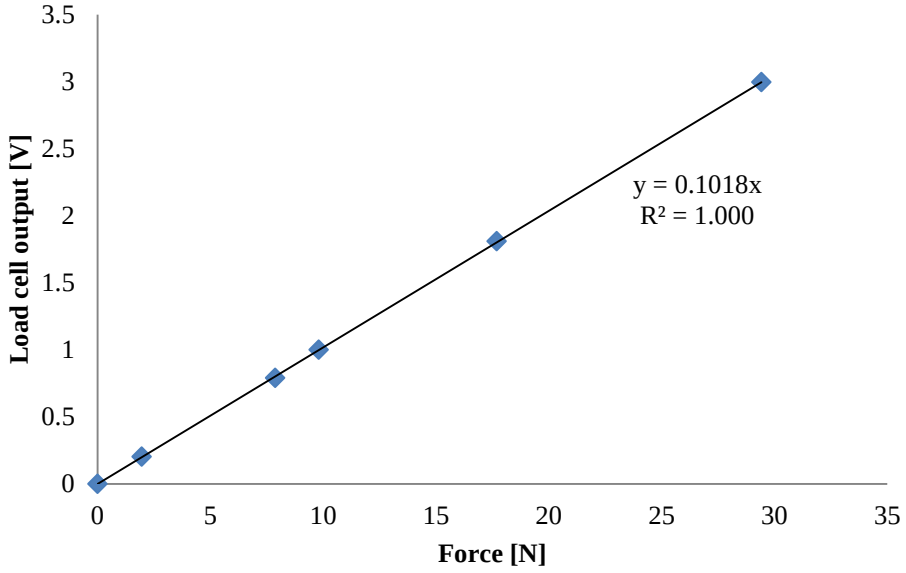

Figure 3.23: Calibration plot of load cell sensor

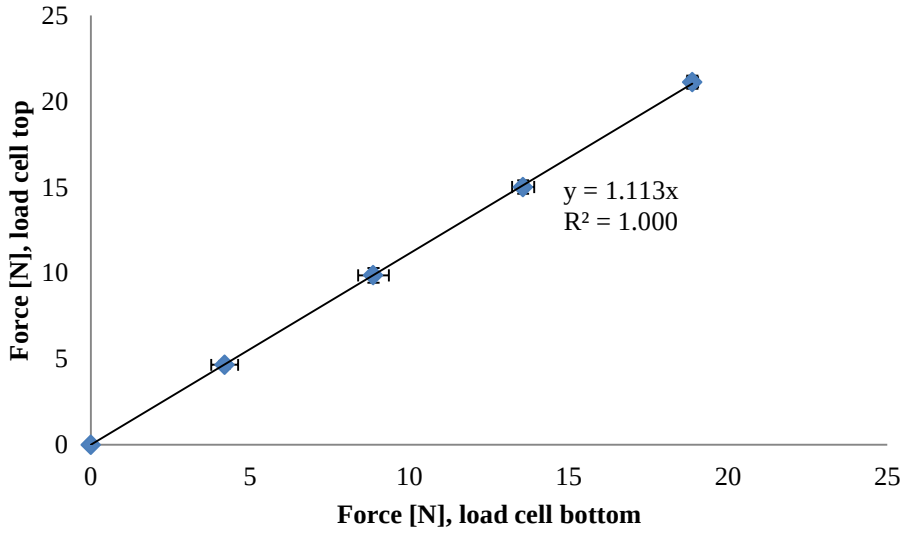

Figure 3.24: The relation between the load cell sensors

The data acquisition system was based on an in-house built desktop PC with a 12 bit, National Instruments (NI), PCI-6024 data acquisition interfacing card. This card is a multifunction analogue, digital and timing device without on-board switches or jumpers so that it can be configured and calibrated by software. Each channel can be programmed with a unique gain of 0.5, 1.0, and 10.0, and 100.0 to match the 12 bit analogue to digital converter (ADC) range and resolution. The data can be sampled from 20k samples/s up to 10M samples/s at each channel with a total on board memory of 32 MB. LabVIEW (Version 9) from National Instruments was used to develop a

programme to control and to obtain the maximum performance from the PCI-6024 card. This programme could be used to control sampling frequency, number of acquired data points per channel, number of records, input range, pre-trigger data, trigger channel and trigger level.

A simple rig was used to test the force controller and displacement controller, as shown in Figure 3.25. The main components were the stepper motor, displacement sensor, load cell, stepper motor driver box, power supply, data acquisition unit (DAQ) and desktop computer. The mechanical experimental methodology is based on pushing the top substrate using the stepper motor and measuring the shear force using the load cell which is fixed between the base plate and the top of the linear slide. A controlled sinusoidal input was applied to the linear stepper motor with either a fixed temperature or with sinusoidal temperature oscillation which may be at a different frequency and may or may not be in phase with the force oscillations. The force control loop was automated by means of a custom-designed programme (FCP, Force-control programme) which communicated to the sensors and linear stepper motor using the NI 6024E data acquisition board.

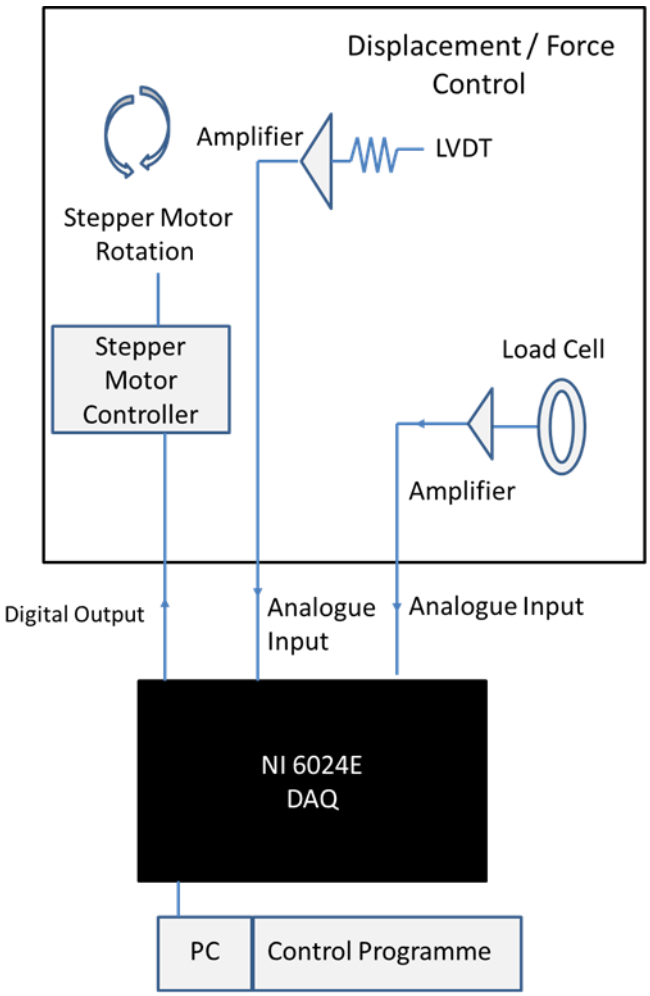

Figure 3.25: Block diagram illustrating the mechanical control

Figure 3.26 represents a summary of the functionality of the mechanical control programme. This force control programme (FCP) generates and acquires the necessary signals simultaneously in real time and was designed in LabVIEW (Version 9). Two main synchronized control signals are generated in the FCP and sent to the linear stepper motor; drive and direction. The main drive control parameters are frequency, duty cycle, idle state, and initial delay. Frequency is defined as the number of step rotation increments per second, duty cycle is the width of the pulse divided by the pulse period, idle state specifies the resting state of the output terminal and initial delay is the amount of time in seconds to wait before generating the first pulse. The other main synchronized control signal is the direction pulse which initiates either forward or backward stepper motor movement. The oscillation of the stepper motor was controlled by feedback from the load cell. The voltage from the load cell was connected to a reset dominant flip flop which meant that the Boolean control variable stayed true until the

sensor output reached the required (maximum) value after which it reset the Boolean control variable to false until the sensor output fell to the required (minimum) after which the next cycle started. The stepper motor therefore oscillated between the maximum and minimum force values.

A typical experiment would start with the stepper motor rotating in the positive direction. As it pushes the top substrate, force is measured by the load cell, which then returns a force signal back to the acquisition board. If the force is smaller than the maximum force then the stepper motor continues forward; if not, movement will be reversed. Once in reverse, forces larger than the minimum will continue reverse rotation of the stepper motor.

The acquired data from the FCP from an experiment was saved in .lvm file format, in which the force and displacement were recorded at 150 samples per second. The experiment was stopped by feedback from the LVDT when the sample is completely sheared.

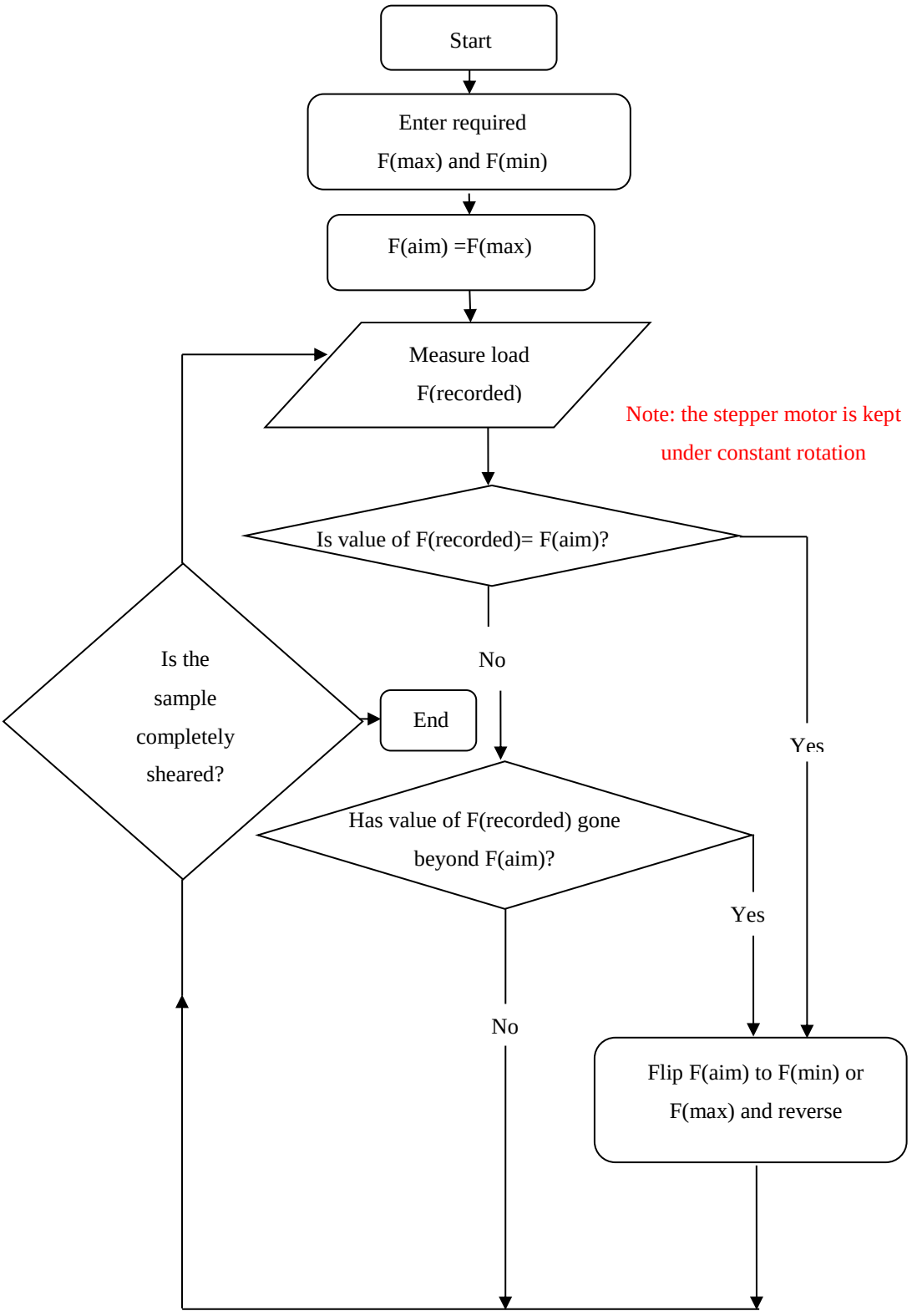

Figure 3.26: Summary of functionality of mechanical control programme

3.2.2 Temperature measurement and control

Much of the thermal cycling research performed on solder joints has used thermal chambers of the type used in electronics production. In the present study, there is a need for direct local control of the thermal and mechanical cycles and so a Peltier device sandwiched between two heat sinks, as shown in Figure 3.15, was used to control the specimen temperature. A simple arrangement was used to test the temperature control, the main components of which were the Peltier device, a power supply, a temperature controller based on an H-Bridge, a data acquisition unit (DAQ) and a desktop computer, as shown in Figure 3.27. The power supply was controlled by the H-Bridge to obtain a set value of the temperature of the thermocouple. A T-type thermocouple was used to measure the temperature between the two substrates. A data acquisition unit was used to capture data for temperature, and time.

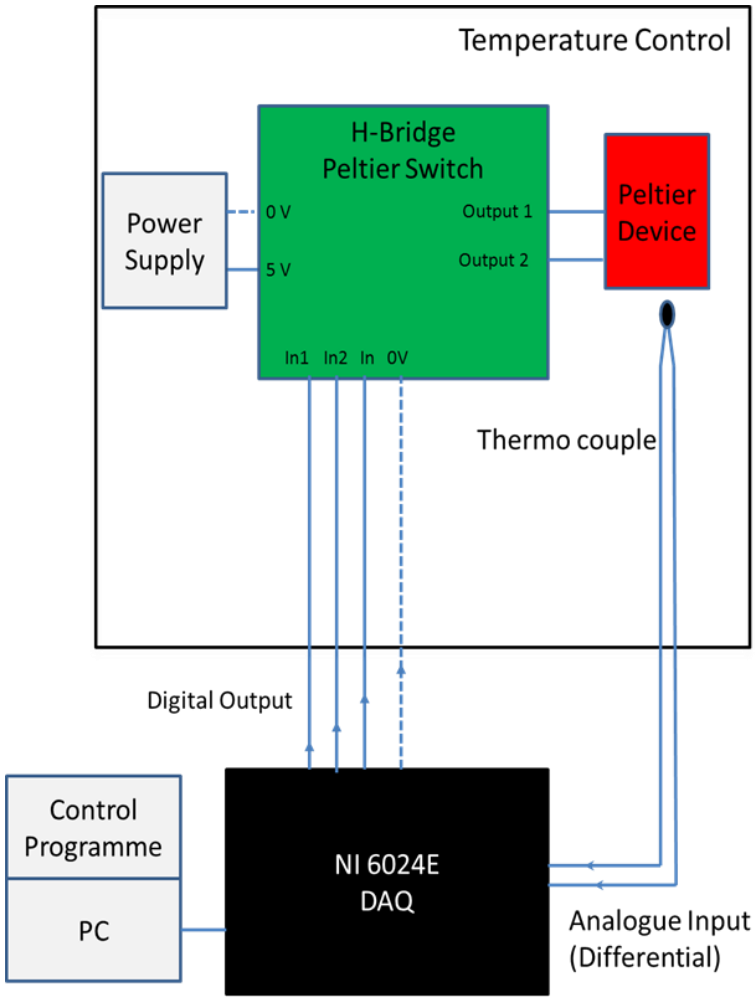

Figure 3.27: Block diagram illustrating the temperature control hardware

The Peltier device was mounted between two heat sinks each made from a block of aluminium alloy as seen in Figure 3.28. A thermally conducting adhesive (WLK 30) was used on each surface of the Peltier device to secure it and improve thermal transfer. The bottom heat sink had a well cut into it into which the sample was set, thermally conducting adhesive again being used to improve the thermal transfer from the aluminium block to the FR-4 substrate. The specimen temperature was measured using a T-type thermocouple placed between the two substrates near to the solder balls.

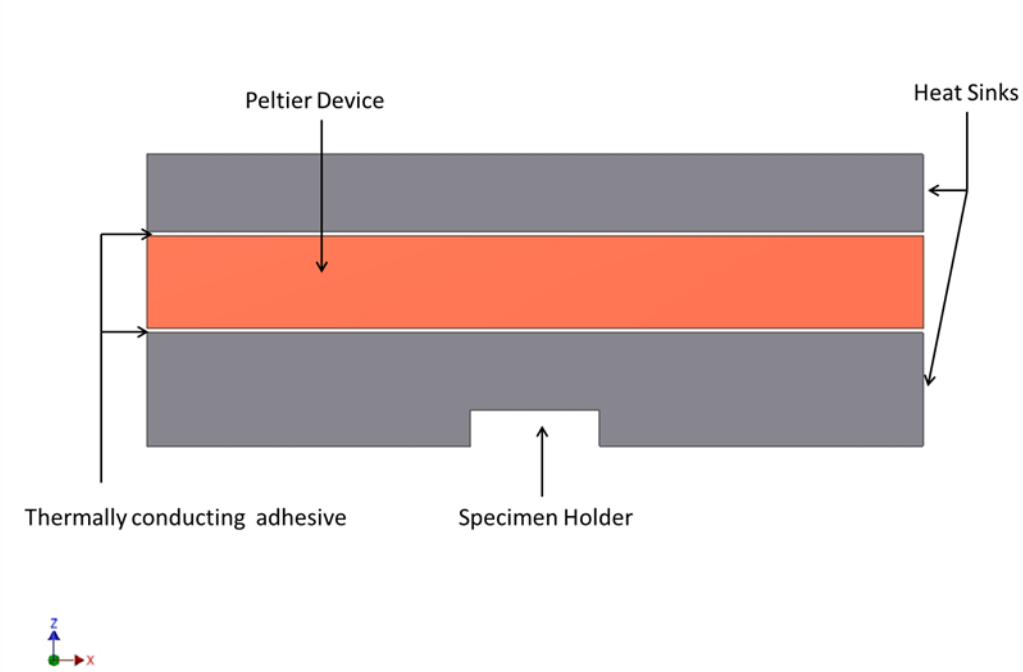

Figure 3.28: Peltier device with heat sinks

The Peltier device was used to generate heat by applying a voltage across it. The device is shown in Figure 3.29 and its specifications are given in Table 3.7.

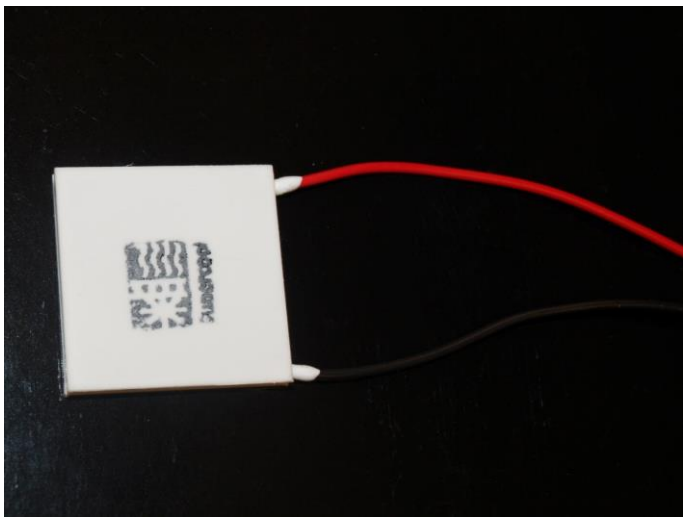

Figure 3.29: Peltier device (37.9 W and 3.9 A) used for heating specimen substrate

Table 3.7: Parameters of Peltier device

Parameter	Value
Dimensions ($L \times W \times H$), mm	30 × 30 × 3.6
Maximum Power, W	37.9
Maximum current, A	3.9
Maximum Voltage, V	15.7
Maximum temperature, ^{o}C	150
Maximum temperature difference, ΔT_{max}, C^{o}	74

For sizing purposes, the heater can be modelled as a simple slab heat exchanger. In order to be able to raise the temperature of the substrate, the heater has to be able to supply more heat than is lost from the surface, and this can be estimated roughly from the forced convection of the surface of the heat sink.

$$Q^{0} = (T_s - T_a) h\, A \qquad (3.9)$$

where

A = is the total surface area of the heat sink.

T_s = is the maximum temperature of interest.

T_a = is the ambient temperature.

h = is the heat transfer coefficient, $[\frac{\mathrm{W}}{\mathrm{m^2K}}]$.

Using a heat transfer coefficient of for a gas-solid interface (2-25 $\frac{\mathrm{W}}{\mathrm{m^2K}}$ [287]) thus gave an estimated heat flux of about 0.1 W for the maximum temperature of the fatigue test (80C°).

Now that the heat flux is known, the temperature gradient across the heat sink can be calculated using a simple conduction calculation, assuming steady-state:

$$Q^0 = -kA\frac{dT}{dx} = kA\frac{T_s - T_h}{h} \tag{3.10}$$

where *k* is the thermal conductivity of the aluminium alloy, *h* is its thickness and *A* is its surface area. For the heat flux calculated above, the temperature gradient across the heat sink was estimated to be 1.25C°, which is negligible for design purposes.

The transient (important in assessing the rate at which the temperature increases) can be assessed roughly using the semi- infinite solid solution for conduction in a slab with constant surface flux [288]:

$$T - T_a = 2\frac{Q^0}{A}\frac{\sqrt{\alpha t}}{K}\mathrm{erfc}\frac{X}{2\sqrt{\alpha t}} \tag{3.11}$$

This shows that the characteristic thermal diffusion distance is approximately $2\sqrt{\alpha t}$ where

erfc = is error function complement

α= is thermal diffusivity

Setting the diffusion distance to the thickness of the FR-4, t_f allows a rough estimate of the time over which significant temperature change might be achieved:

$$t_f = 2\sqrt{\alpha t} \tag{3.12}$$

$$t = \frac{t_f^2}{2\alpha} \tag{3.13}$$

Taking a literature value for α [289] gives $t = 1.5$ sec when the t_f =1.5 mm, which is acceptable for a practical implementation.

Temperature control was achieved using a custom designed temperature control programme (TCP) which used the thermocouple output signal to control the Peltier element *via* the NI-6024E data acquisition board. The control programme generated and acquired the necessary signals simultaneously in real time and was designed in LabVIEW (Version 9).

Three main synchronized digital control signals were generated in the TCP and sent to the H-bridge; **In**, **In1** and **In2**. To operate the Peltier device, **In** should be high (5V), **In1** should be high (5V) and **In2** low (-5V), which sets the device as a heater. If the values of **In1** and **In2** are flipped, the device is set as a cooler.

The thermocouple was located close to the solder balls (between the two FR-4 substrates) to measure instantaneous temperature. This measured temperature is then compared to the set point (desired temperature). The result of this comparison is then sent to a software routine controlling the Peltier device accordingly to the desired effect: heating, and off. Switching was achieved using a Pulse Width Modulation (PWM) circuit and typically the Peltier saw its applied voltage switch between +5 Volts (heating) and 0 Volts (off). The thermal management circuitry was interfaced to the control PC *via* a Data acquisition card using digital inputs and outputs (here a NI 6024E DAQ was used).

The thermal cycling control loop was automated by means of a custom designed thermal cycling-control programme (TCCP). This software generates and acquires the necessary signals in real time and was written in LabVIEW v.9. Switching from cooling to heating was achieved using an H-bridge circuit and typically the Peltier saw its applied voltage switch between +5 Volts (heating) and -5 Volts (cooling). Typically this programme would perform in an analogous way to a, RS flip-flop circuit: when one set extreme is reached, the Peltier element polarity invers to then reach the opposite set extreme, effectively cycling the solder ball temperature between a maximum and

minimum of the set temperature range. Figure 3.30 represents a summary of the functionality of the thermal cycling control programme.

Figure 3.31 (top) shows a typical result of this at a controlled temperature of 35°C, Figure 3.31 (middle) at a controlled temperature of 75°C, and Figure 3.31 (bottom) shows a typical result of temperature cycling between 35°C and 75°C.

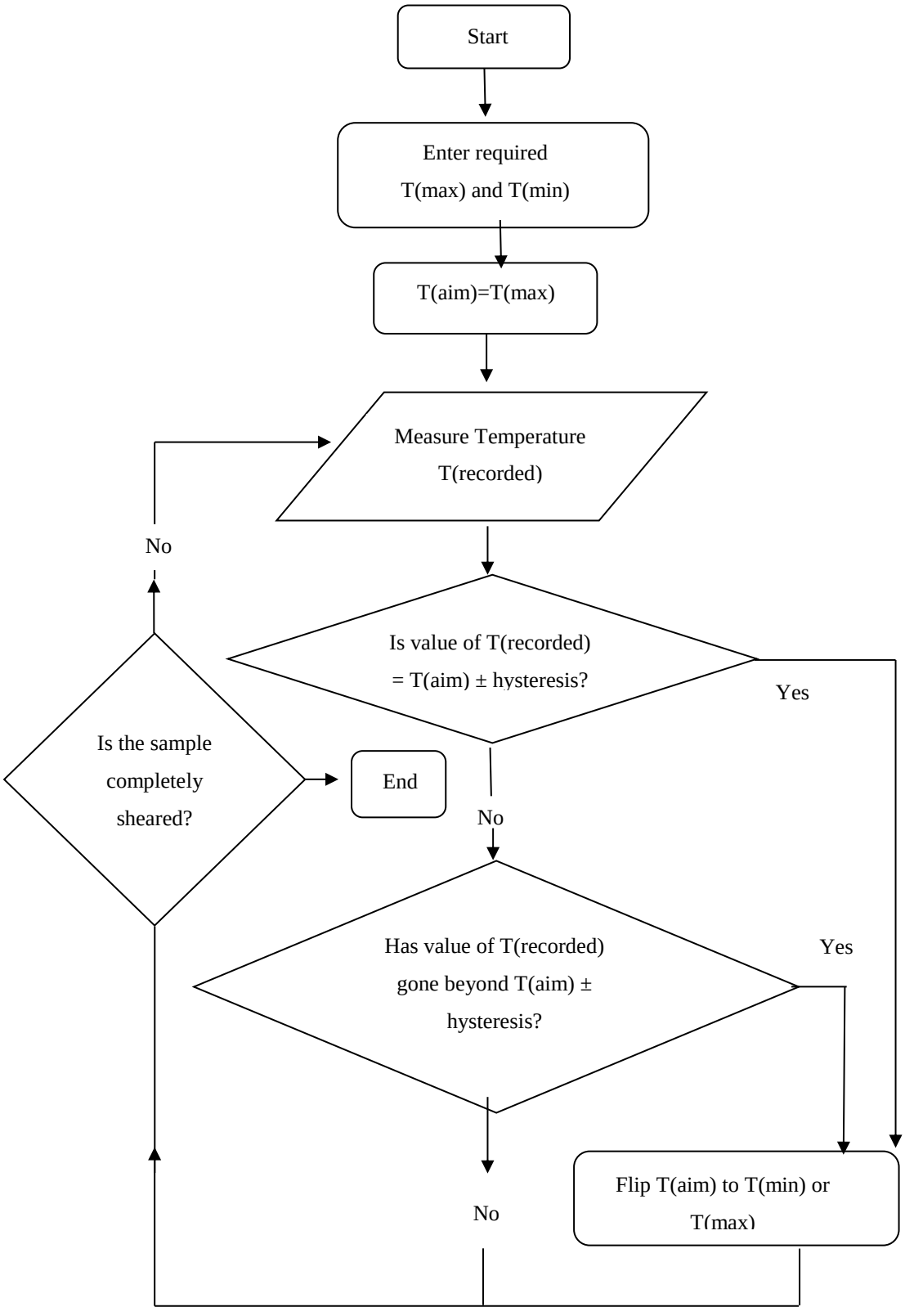

Figure 3.30: Summary of functionality temperature of control programme

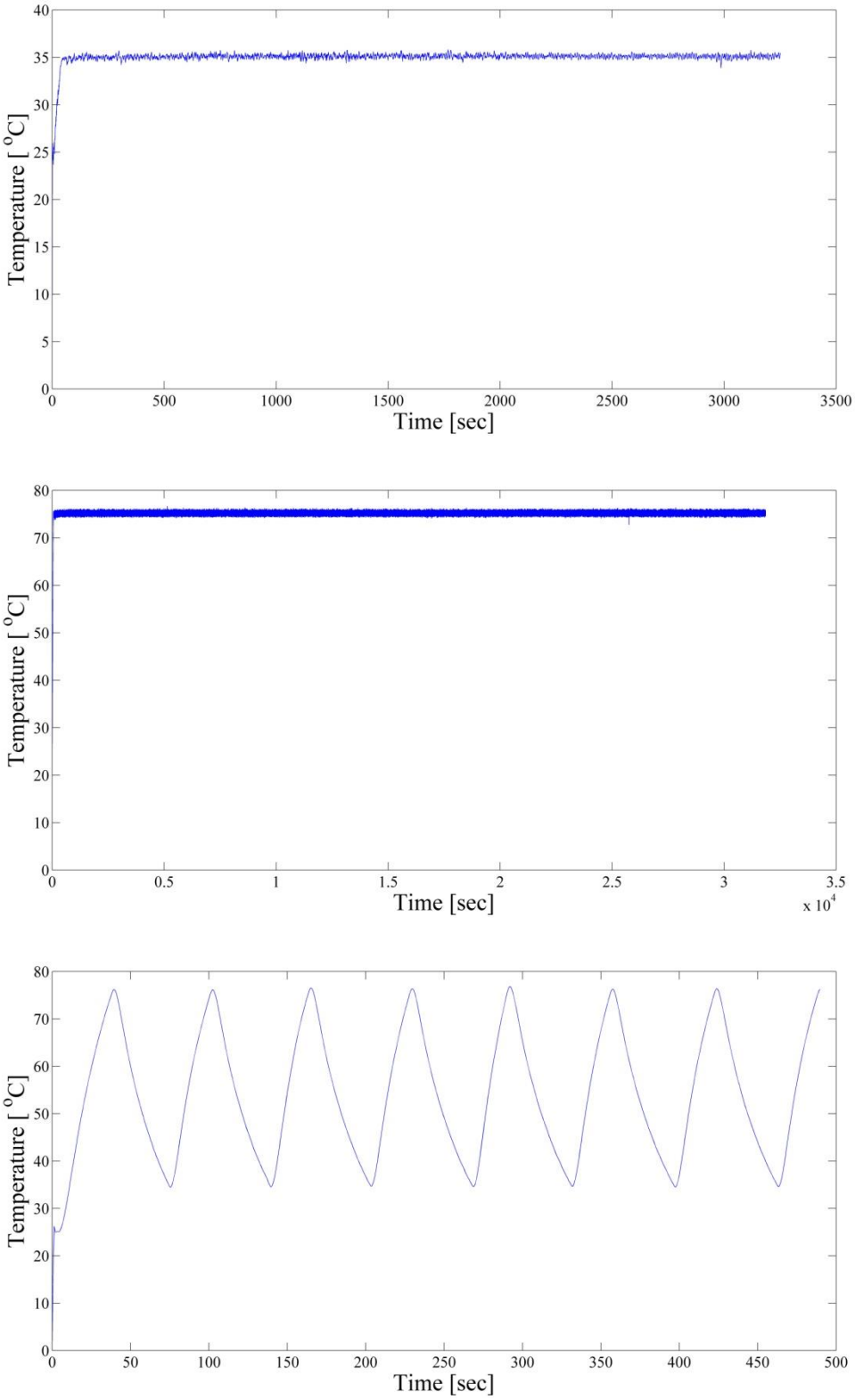

Figure 3.31: Typical experimental results from controlled temperature experiments

3.2.3 Experimental measurement and control system

The mechanical tests were conducted in closed loop force control using the linear stepper motor actuator. Testing was conducted in shear mode where the shear displacement was increased with the load cell measuring the reaction force used for control of the actuator. The data acquisition interfacing card was used to collect the data as well as providing the feedback control signal to the linear stepper motor actuator. The setup was capable of conducting tests at elevated temperature using the Peltier device. The thermocouple placed between the two substrates was used for providing closed loop feedback for control of the Peltier device for isothermal and thermal cycling tests.

Thus, the experimental work requires the measurement and control of force, displacement, and temperature in real time, which was achieved by combining the two foregoing control systems through the NI 6024 data acquisition interfacing card. Figure 3.32 illustrates the overall layout of the system.

The three primary experimental variables (force, displacement and temperature) were sampled simultaneously and conditioned, using a self-designed programme, at a rate of 150 Hz, while converting the respective voltage outputs to Newtons for force, microns for displacement and °C for temperature. To investigate the mechanical behaviour of the solder joints, both monotonic and dynamic loadings were used, in both of which cases the force, displacement, and temperature were measured in real time. The signal processing was done using a Matlab routine.

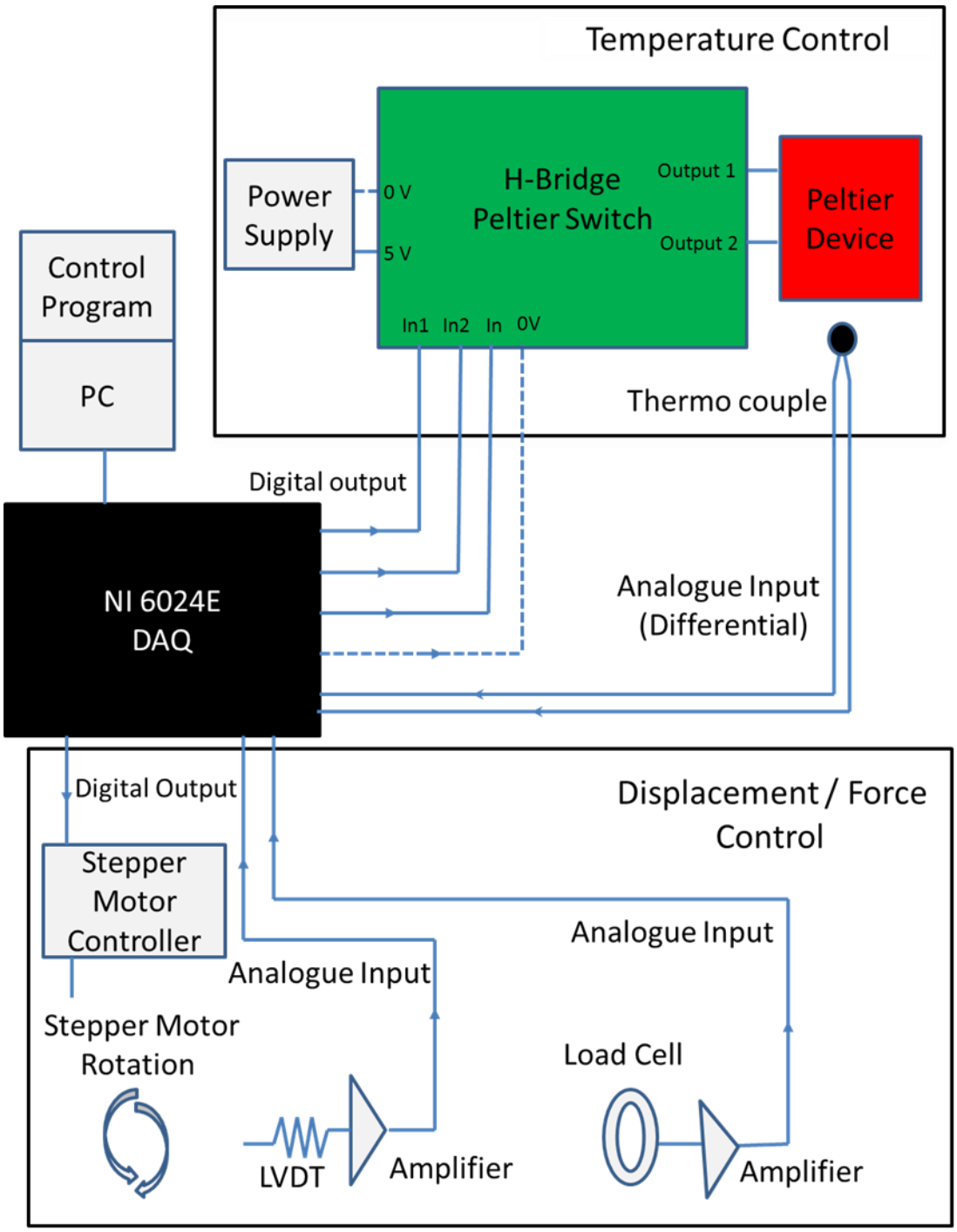

Figure 3.32: Block diagram illustrating combined mechanical and temperature control

3.2.4 Performance of control system

To characterise the response of the equipment, it was run in four configurations (load control at room temperature, 35^{o}C, 75^{o}C and temperature cycling. For each test the spectrum of the signal obtained from the output of the load cell was computed using Fourier transform for a sufficient of cycles until failure and the maximum and minimum forces of each cycle were also calculated.

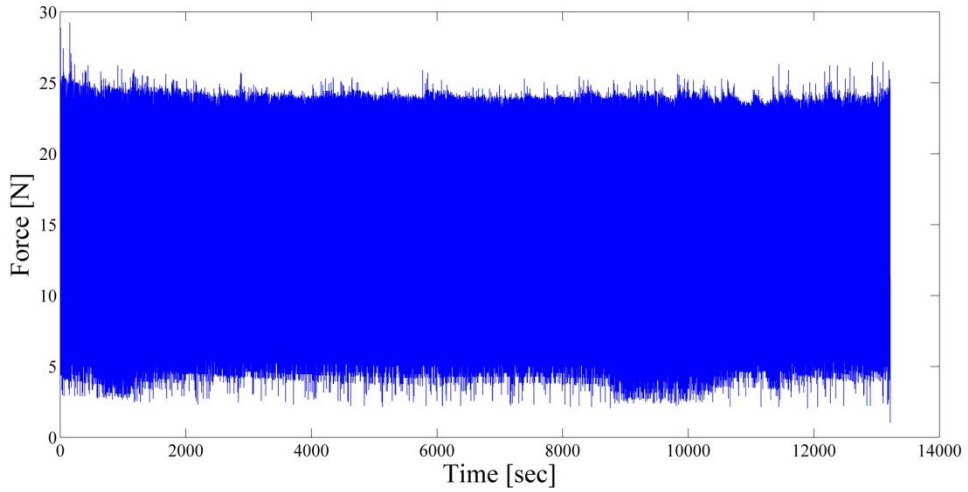

Figure 3.33: Raw force data under isothermal fatigue load control at room temperature

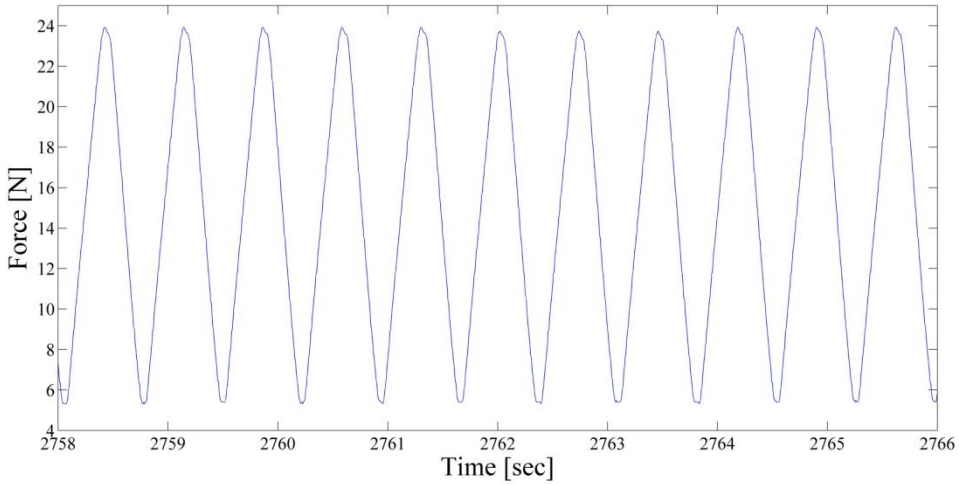

Figure 3.34: Magnified raw force data under isothermal fatigue load control at room temperature

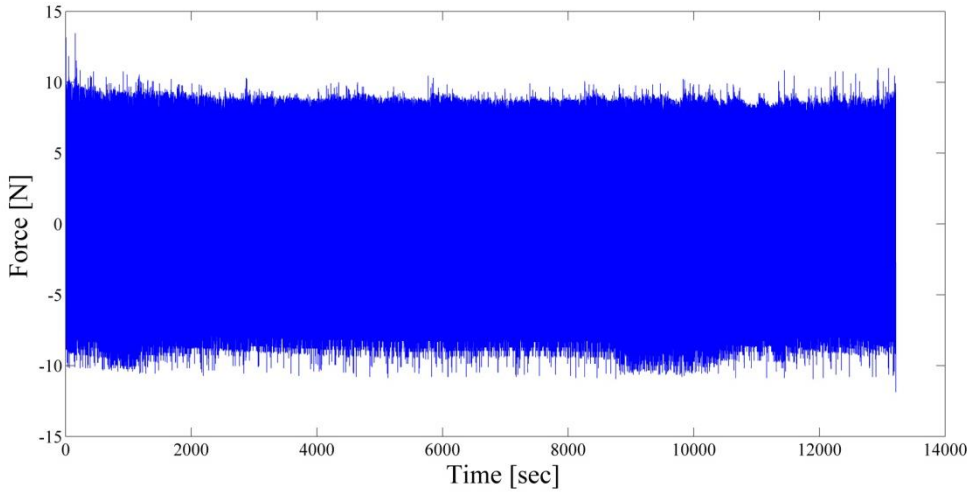

Figure 3.35: Normalised force data under isothermal fatigue load control at room temperature

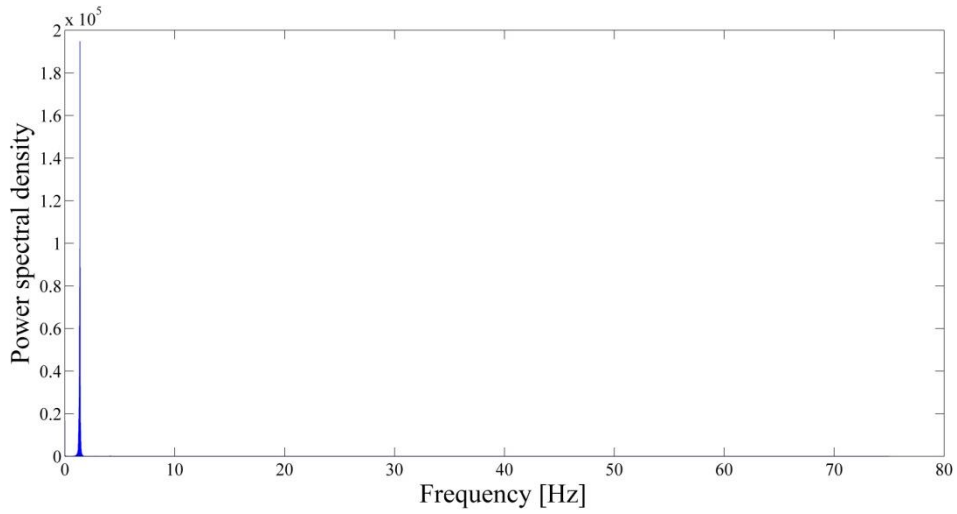

Figure 3.36: The magnitude of the power spectral density against frequency at room temperature

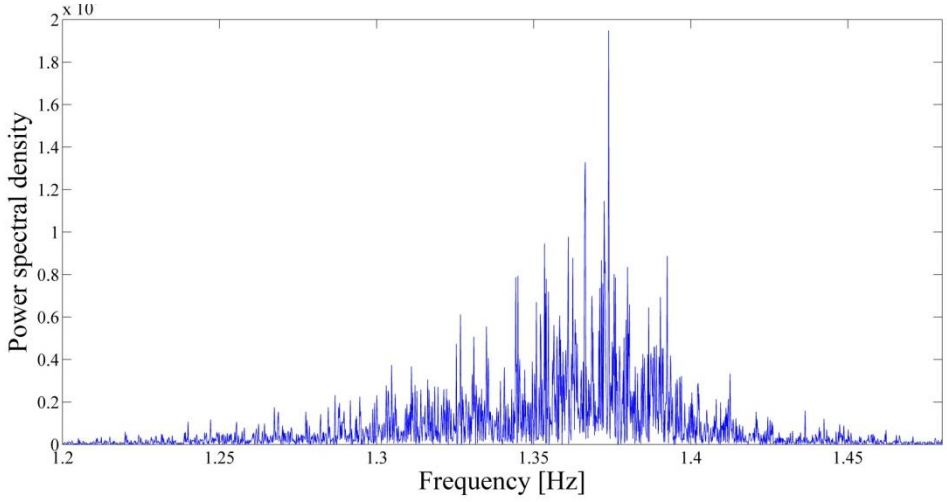

Figure 3.37: Magnified magnitude of the power spectral density against frequency at room temperature

The mean frequency was calculated using the Fourier transform and was found to be 1.36 Hz when was expected to be 1.5 Hz.

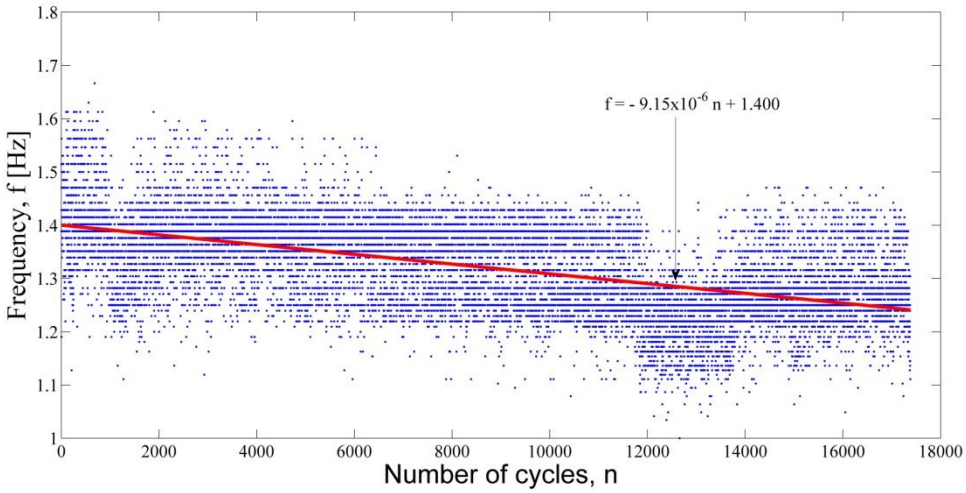

Figure 3.38: Frequency versus number of cycles at room temperature

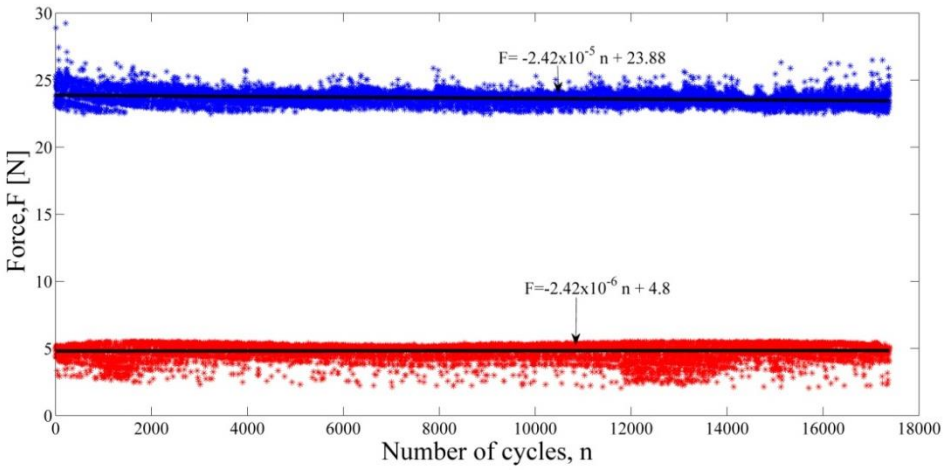

Figure 3.39: Maximum and minimum force versus number of cycle at room temperature

In order to understand how the dynamic behaviour of the system changed with the time, the frequency, maximum and minimum forces of each cycle were calculated and plotted against cycles number, and these are shown in Figures 3.38 and 3.39. As can be seen, the frequency falls off slowly, but significantly with number of cycles whereas the maximum and minimum forces show barely significant change.

Table 3.8 summarises the response of the equipment in the designed system under four loading configurations.

Table 3.8: Summary of the response of the equipment

Loading condition	Maximum force change percentage	Minimum force change percentage	Measured mean frequency Fourier transform [Hz]	Expected frequency [Hz]	Frequency change percentage
Room temperature	-1.7	+0.87	1.3597	1.45	-10
35°C	+0.48	+4	1.3311	1.4	-2.7
75°C	-1.8	-6	1.5656	1.72	-5.4
Thermal cycling	+0.5	-4.4	1.0808	1.1	-8.7

By comparing the mechanical dynamic behaviour of the system under different loading conditions, it becomes apparent that only the frequency changes in a consistent way reducing with number of cycles to failure by a small amount. This frequency a decrease is thought to be due to an increase in the number of steps (the top substrate is moving due to the applied shear force) required to achieve the desired force.

3.3 Sample characterisation

Before and after mechanical testing, it was important to characterise the samples as closely as possible. This involved a range of procedures to characterise the solders, including microscopic examination to establish the phase structure, heat treatment to simulate the effect of prolonged exposure on microstructure during the thermo-mechanical experiments and micro-hardness testing to establish local mechanical properties. Also, the behaviour of the test specimen assembly needed to be characterised to isolate as far as possible deformations of other components than the solder in the load path. The procedures are described the following subsections.

3.3.1 Metallography

Both leaded and lead-free solder alloys are very soft with low recrystallisation temperatures and so need to be carefully prepared for metallographic examination. Samples were placed edge-on into moulds and immersed in a special room temperature curing epoxy (Epoxicure resin). Once the resin had hardened, the sample face was

rough-ground back until the polishing plane was close to a diameter of two solder balls. Thereafter grinding and polishing were performed on a universal polishing machine. Specimens were wet ground using 240, 600, 800, 1000, 1200, and 4000 grit silicon carbide papers in sequence with water as the lubricant with about 5 minutes per step. The specimens and the paper were cleaned between each grinding step to remove loose particles of abrasive and specimens were manipulated carefully to minimise probability that abrasive particles could become embedded in the solder. Specimens were polished using a similar grinding technique, again serially using 9 μm, 1 μm and 0.5 μm diamond paste on a canvas cloth. Next, 0.5 μm alumina suspension was used to remove any scratch marks, followed by a final finish using colloidal silica polish on a microcloth. Samples were examined under an optical microscope between polishing steps and stages were repeated if necessary.

The lead-free solder specimens were etched in a dilute solution of 2% concentrated hydrochloric acid (HCl), 6% concentrated HNO_3 and 92% H_2O for about 3 seconds.

For optical microscope and scanning electron microscope (SEM) metallography, samples had to be only lightly etched and had to be examined when fresh. The leaded solder samples had sufficient contrast in the as-polished state and were therefore not etched.

3.3.2 Hardness measurement

Two samples of each of the leaded and lead-free solder specimens prepared as above were examined with a micro hardness testing machine (Model: MVK-H1) using a Vickers indenter with a 10 g load. In order to correlate with the metallographic examination, hardness scans were made along the lateral and longitudinal axes of each ball examined, giving total of approximately 28 points on each ball.

3.3.3 Heat treatment

Three samples of each of the leaded and lead-free solder specimens were subjected to a 10-hour exposure at 80ºC, which corresponded to the maximum temperature for the longest fatigue test, hence representing the largest change in microstructural coarsening. After heat-treatment, these samples were subjected to the same metallographic and hardness characterisation as the unexposed samples.

3.3.4 Sample mechanical characterisation

In order to carry out realistic thermal and mechanical fatigue tests, it is necessary to apply the loads to the FR-4 substrate, and the most convenient displacement measurement is done at the loading points. Since the solder balls are not the only material in the load path, it was necessary to characterise the samples carefully so that the shear deformation of the solder could later be recovered from the displacement measurements. Figure 3.40 (top) shows the main components in the load path, the FR-4 (which is in compression and shear), the solder balls and the copper solder pads (which are in shear) and the adhesive holding the sample in the sample holder (which is in compression and shear). To characterise the relative effects of these components, a series of dummy specimens were tested, one set in which the FR-4 was replaced by copper (Figure 3.40 middle), and one in which everything except the adhesive was replaced by copper (Figure 3.40 bottom).

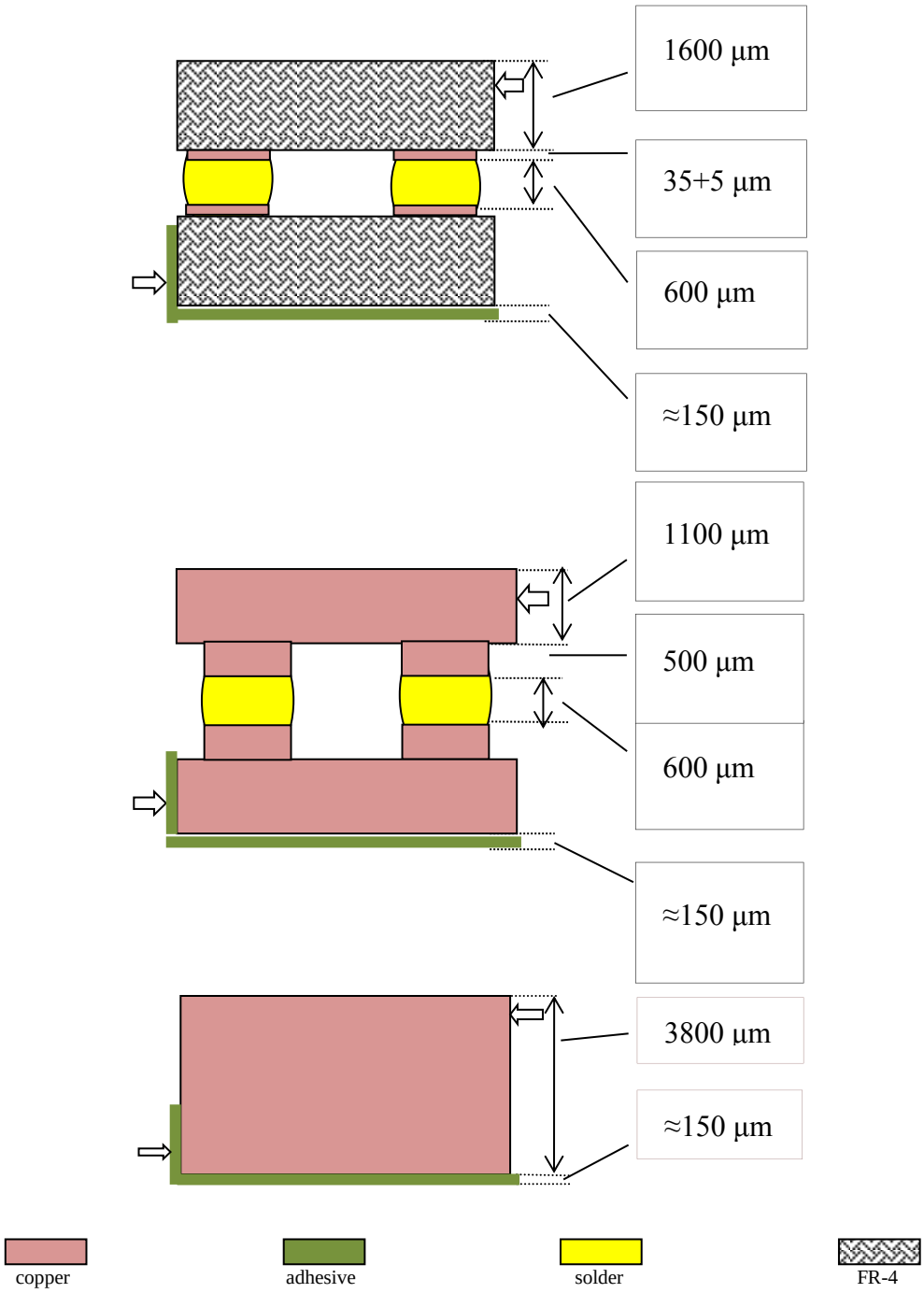

Figure 3.40: Materials and load paths for specimen mechanical characterisation

For each configuration, monotonic and cyclic force control tests were performed at room temperature and at 75°C. The results of the copper block - adhesive assembly are shown in Figure 3.41. Each test being repeated for a total of 10 times with the test sample being rebonded each time. As can be seen, the specimens show a distinct, but reproducible, bilinear behaviour with a knee at around 12 N and also significant

hysteresis on unloading, which is again reproducible. Since the stress in the copper at 12 N is only about 0.5 MPa, corresponding to a lateral shear displacement of about 0.04 μm, it can be concluded the measured displacement is almost entirely due to the tension, compression and shear of the adhesive layer. The curves shown in Figure 3.41 can therefore be taken as the grip stiffness and subtracted from all measured curves to give specimen stiffness.

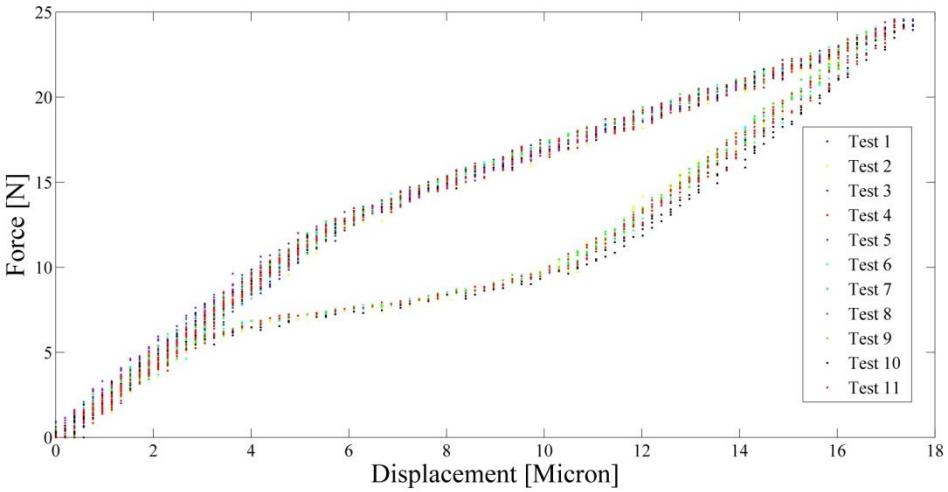

Figure 3.41: Force versus displacement for copper- adhesive assembly (grip stiffness) at room temperature

The load-displacement curves for the copper substrate and FR-4 substrate solder joints at room temperature are shown alongside the grip stiffness in Figure 3.42. Each test was repeated for five different FR-4-solder assemblies and three different copper-solder assemblies. As can be seen, there is a significant increase in compliance when the copper block is replaced by four composite copper-solder-copper columns, and a further increase in compliance when the copper columns are replaced by a compliant anchor (the FR-4).

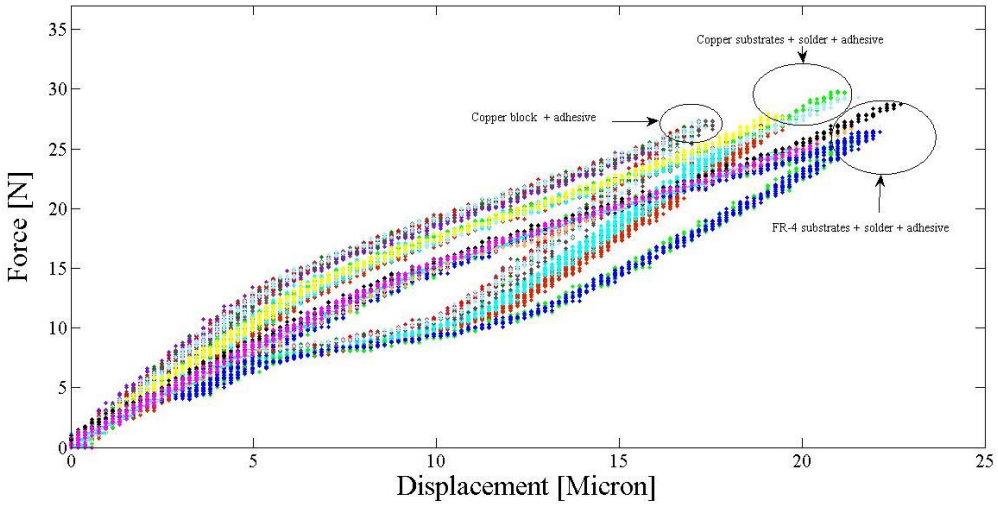

Figure 3.42: Force versus displacement for all configurations at room temperature

In order to better understand the behaviour of the test rig, a series of FEA calculations were carried out on the copper block and adhesive assembly with varying thickness of adhesive and elastic moduli. The load path through the whole assembly was simulated as shown in Figure 3.43 for the copper block dummy specimen. The FEA model of the assembly without the specimen is represented in Figure 3.44, showing the application of loads and constraints.

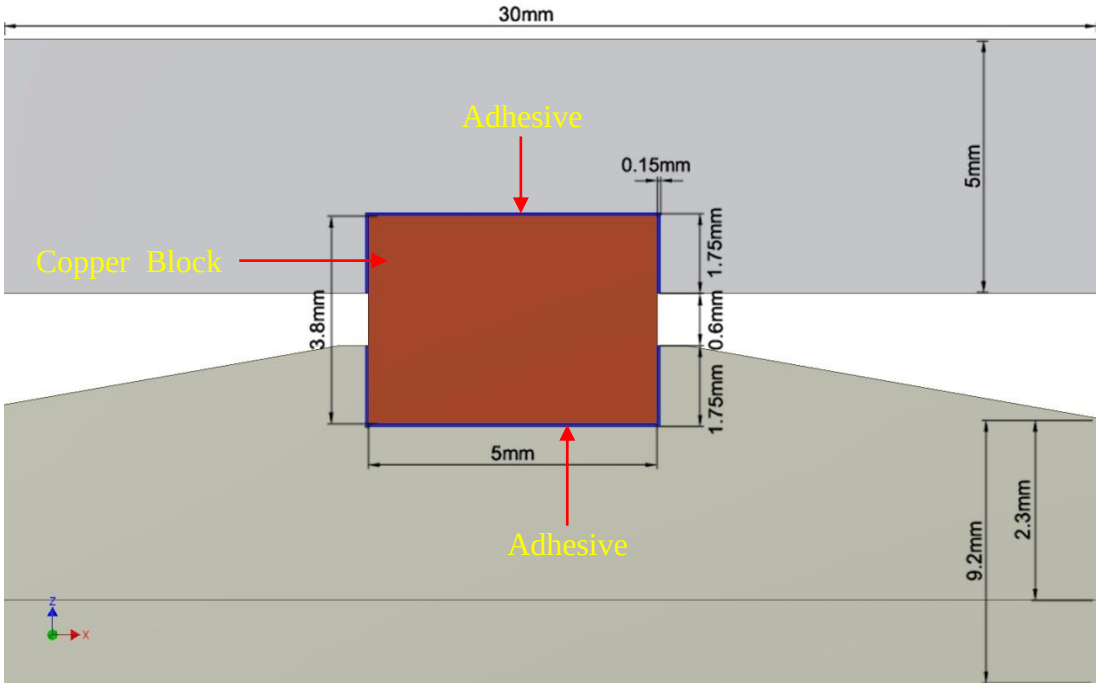

Figure 3.43: Load path for grip stiffness assessment using FEA

The following loads and boundary conditions were applied on the FEA model to replicate the test set-up;

- On the top aluminium holder a monotonically increasing load was applied over a circular contact surface with diameter equal to the shaft of the stepper motor (4.15 mm).
- On the bottom holder a constraint was applied which restricted its motion in all directions.

Unfortunately, the elastic modulus and Poisson's ratio of the thermally conductive adhesive WLK was not given in the data sheet and there is a wide range of published values of mechanical properties of epoxy adhesives. The value used initially can be found in Table 3.9.

Table 3.9: Material properties used in FEM model

Materials		Elastic modulus [GPa]	Poisson's ratio	Reference
Aluminum	at room temperature	69	0.33	[290]
	at 93°C	66	0.33	[291]
Copper	at room temperature	110	0.34	[290]
	at 93°C	92	0.34	[291]
Adhesive	at room temperature	1	0.3	[292]
	at 100°C	0.1	0.3	[292]

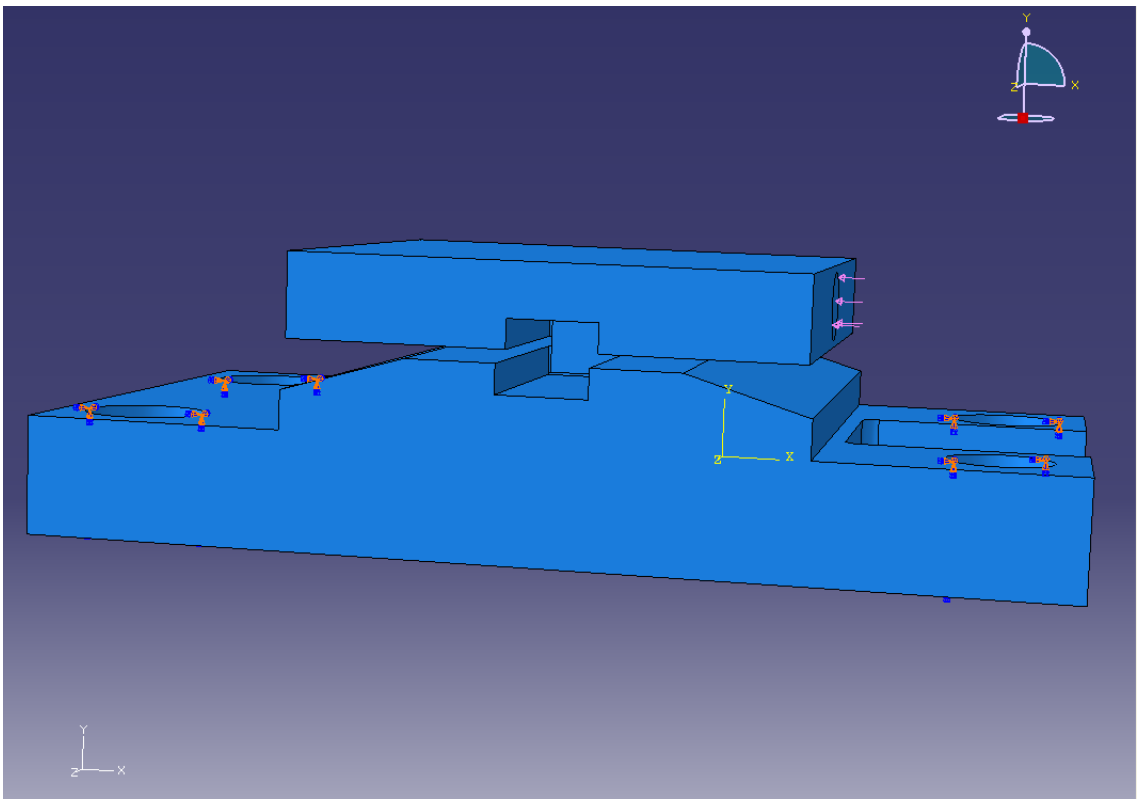

Figure 3.44: FEA Model for grip assembly without specimen

The calculated FEA displacement field at a load of 20 N for the holder assembly with the copper block specimen in place is shown Figure 3.45. A detailed view of the adhesive layers is shown in Figure 3.46 and it is evident from the FEA that, as expected, the distortion is concentrated in the adhesive and that this leads to a rotation of the top fixture relative to the bottom with corresponding tension, compression and shear in the adhesive.

Figure 3.47 shows the calculated stiffness for the simulation, along with ones where the adhesive thickness and adhesive modulus are varied a factor of 4.

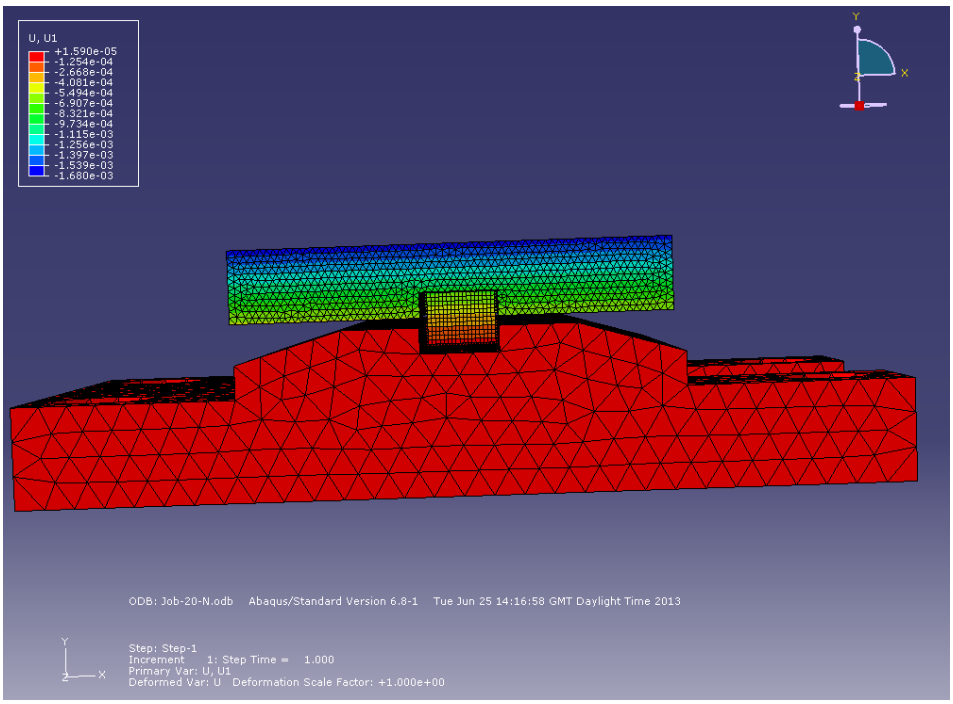

Figure 3.45: Displacement of assembly with copper block under 20 N shear force

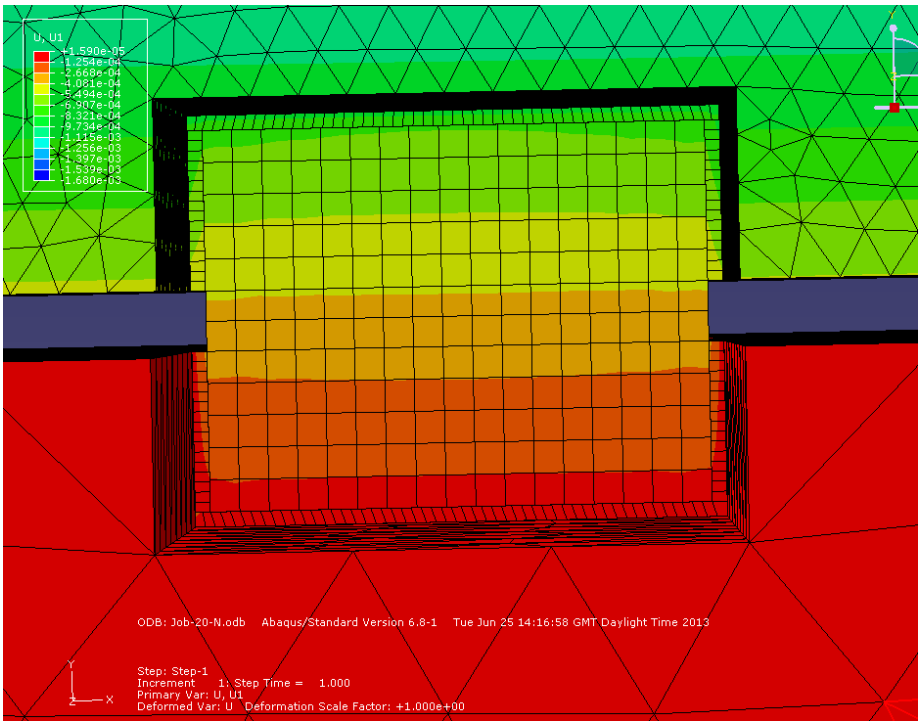

Figure 3.46: Detailed view of the adhesive layer for simulation show in Figure 3.45

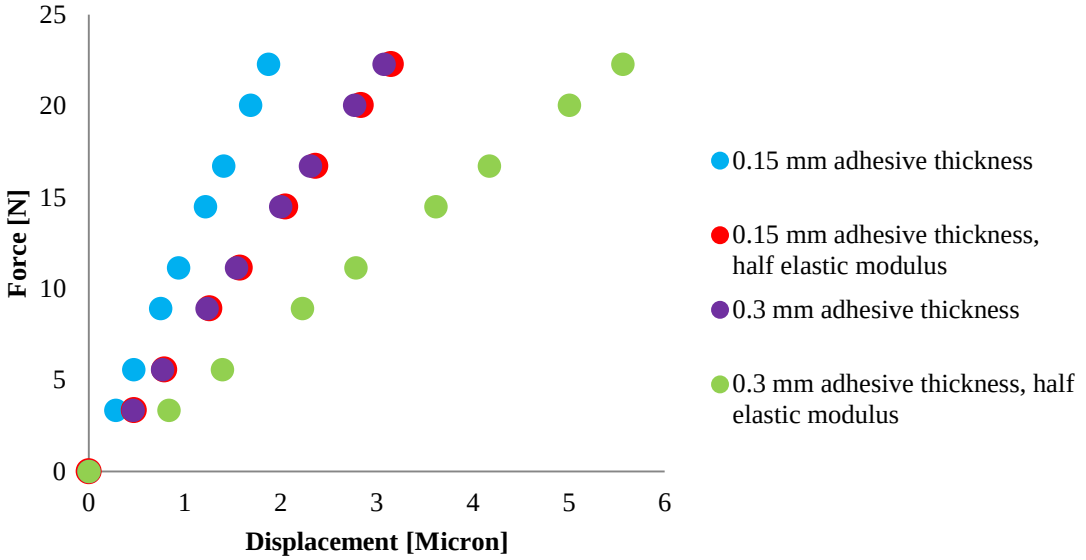

Figure 3.47: Simulated load-displacement curve for specimen assembly with copper block

The load cell manufacturer's data sheet gives a compliance of 6.2 N/μm and this can be added to the grip compliance as shown in Figure 3.48.

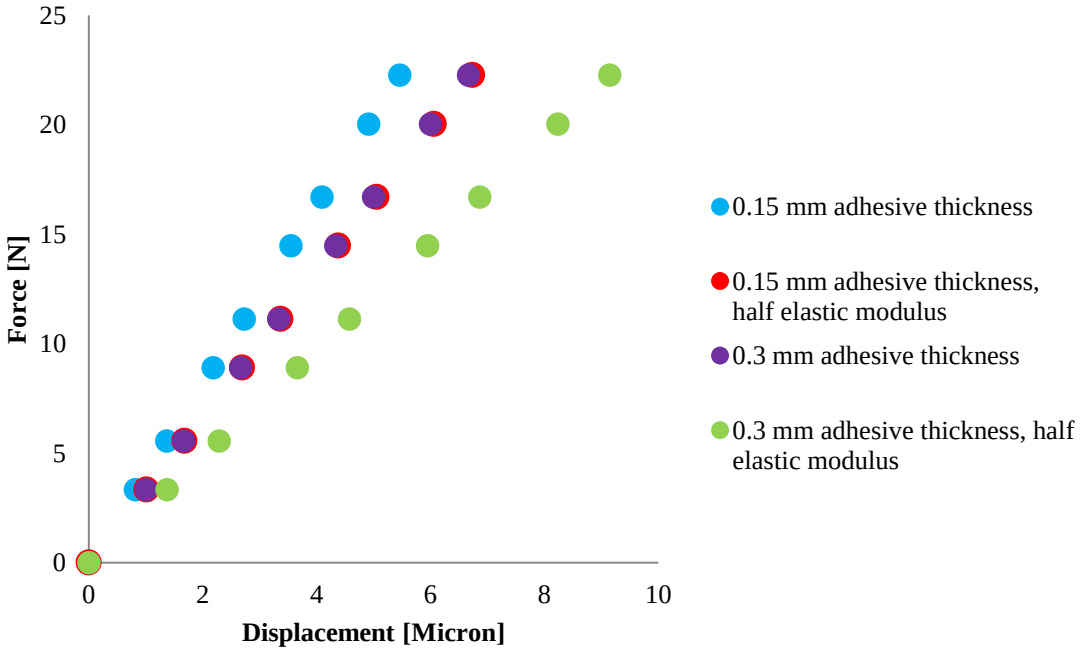

Figure 3.48: Simulated load-displacement curve for specimen assembly with copper block including load cell compliance at room temperature

Finally, Figure 3.49 shows a comparison between the FEA results and an average of the 10 experimental results for the copper block/adhesive specimen assembly.

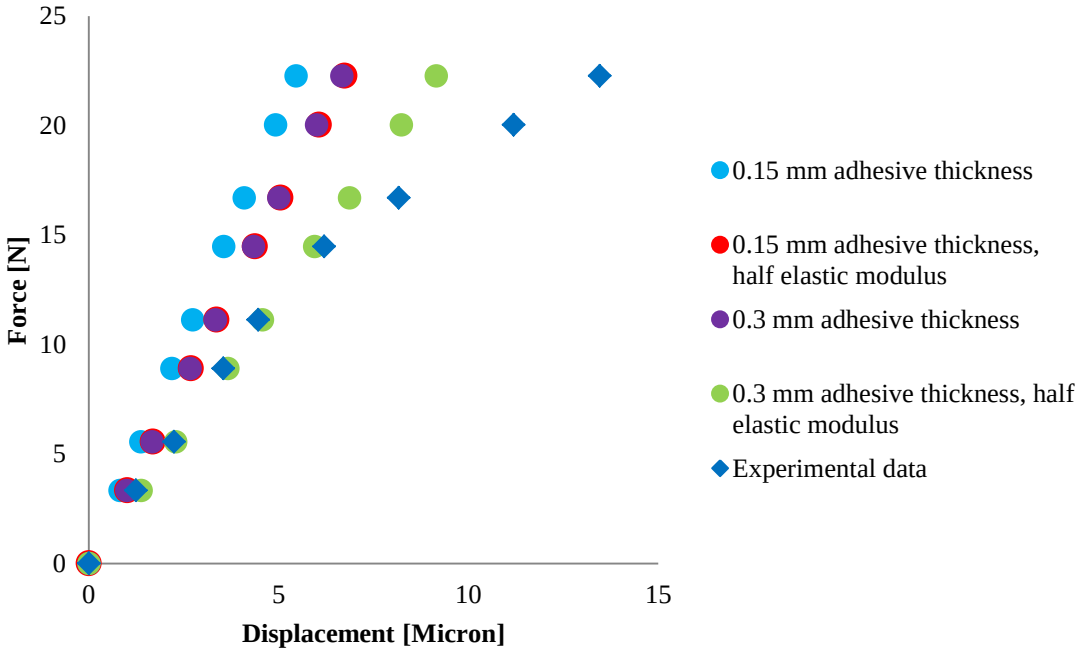

Figure 3.49: Comparison of FEA and measurement of fixture stiffness at room temperature (including load cell compliance)

This behaviour is in accord with Jousset *et al* [293] who found the adhesives to behave differently during experiments than from experimental by FEA. In order to identify the parameters of the material model, Jousset *et al* minimised the following least-squares function:

$$f(displacement) = \sum_{n=1}^{n} \left((measured\ displ\ ) - (FEM\ estimated\ displ) \right)^2 \quad (3.14)$$

Using genetic and gradient methods. Convergence was achieved after 25 iterations of varying the parameters used in the FE model.

Since it is not a primary aim of current work to model the adhesive, the experimental grip compliance was simply subtracted from the data.

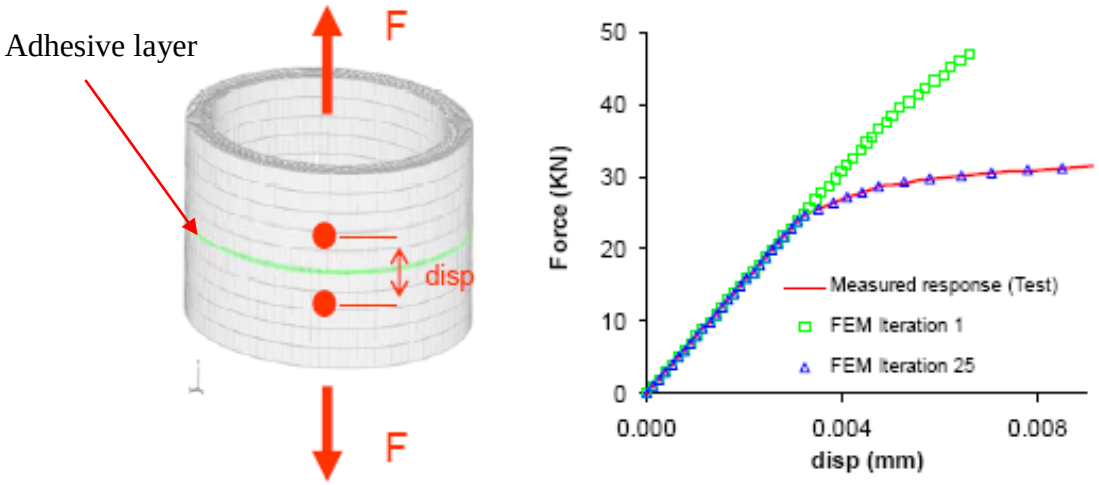

Figure 3.50: Experimental setup and results of convergent simulated and experimental load displacement tests, involving an adhesive joint [293]

Figure 3.51 shows the mean displacement of the copper substrate solder joint (copper substrates assembly) after removal of the mean measured grip compliance. The error bars were produced by subtracting the minimum measured value of the copper block displacement at a given load from the maximum of the solder joint displacement and *vice versa*, thus taking into account both the grip effect and its potential error.

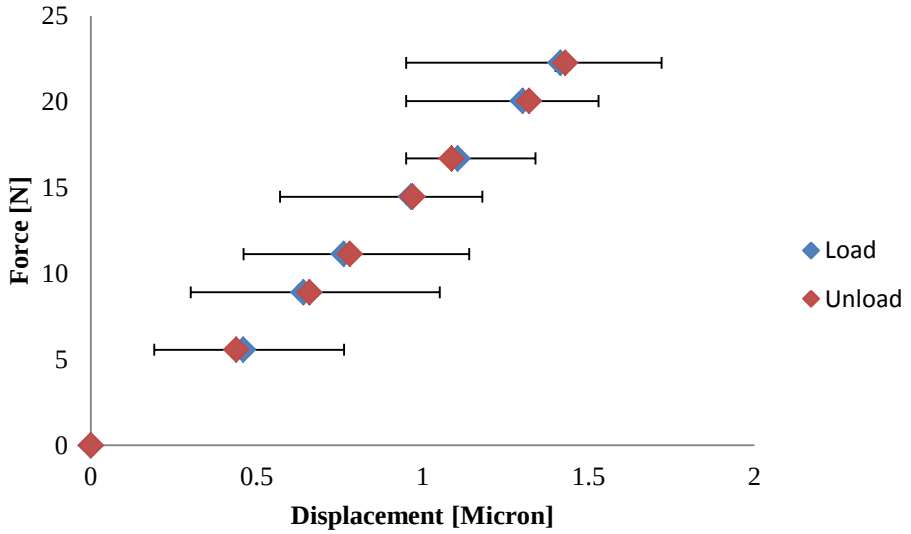

Figure 3.51: Displacement of lead-free solder joint after removing other contributions at room temperature

Figure 3.52 shows the results of the displacement of the solder joint plus FR-4 substrate assembly after grip compliance correction. Again, the error bars were calculated by subtracting the minimum value of the grip from the maximum of the solder joint and *vice-versa*.

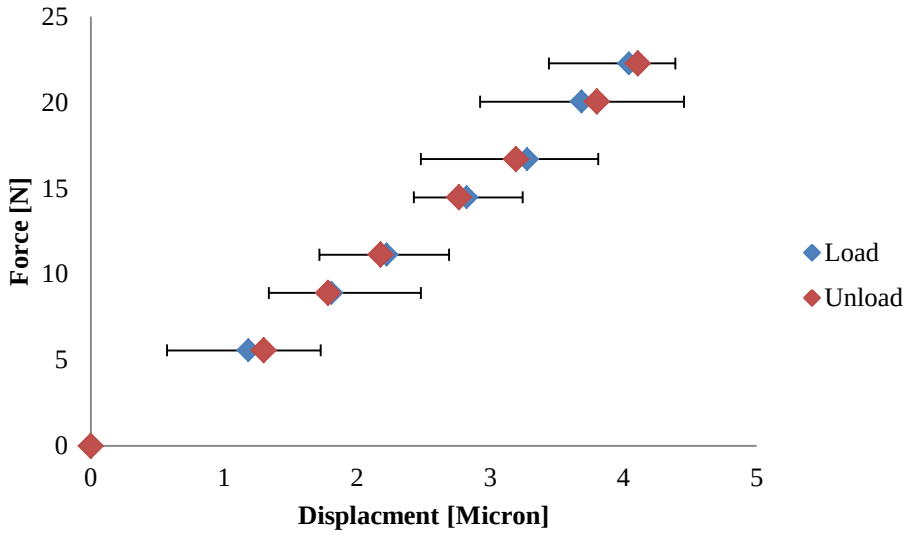

Figure 3.52: Displacement of lead-free solder joint plus FR-4 substrates after removing other contributions at room temperature

Figure 3.53 shows a comparison between the force/displacement behaviour of the lead-free solder joints wheras there is a substantial effect on complaince, neither exhibits a particularly large hysterisis up to 22.5 N load with and without a FR-4 substrate during the loading and unloading.

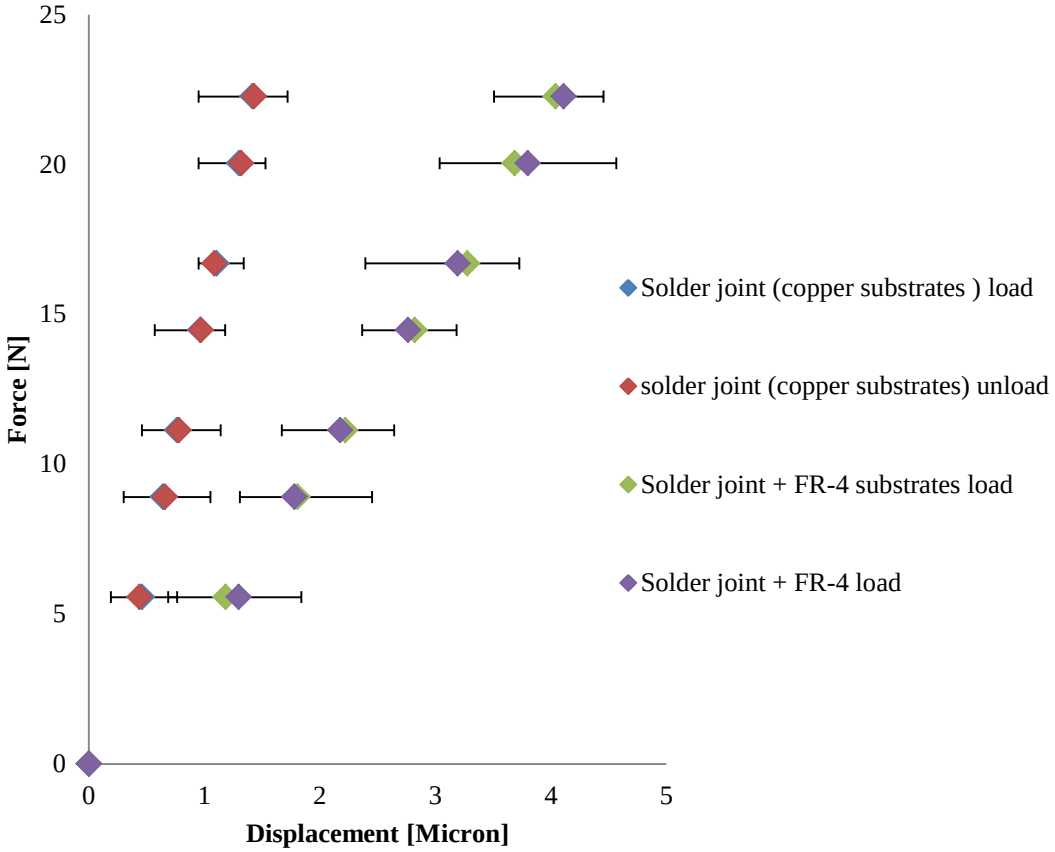

Figure 3.53: Comparison between the force/displacement behaviour of the lead - free solder joint and the lead - free solder joint plus FR-4 substrates at room temperature

The experimental results of the copper block-adhesive assembly at 75°C are shown in Figure 3.54. Each test was repeated for a total of 5 times with the test sample being rebonded each time. Again, the adhesive stiffness was simulated in FEA, this time using an estimated modulus using the values in Table 3.9. Figure 3.55 compares simulated stiffness with measured stiffness, again varying the modulus and thickness of the adhesive. Comparing this with Figure 3.49 shows that the stiffness assumption is closest to the experiment, as opposed to the least stiff assumption at room temperature.

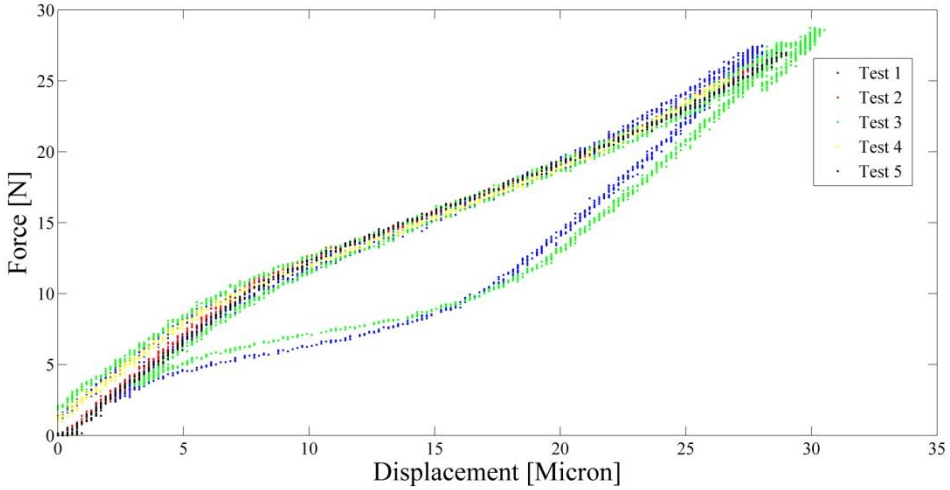

Figure 3.54: Force versus displacement for copper sample at elevated temperature 75°C

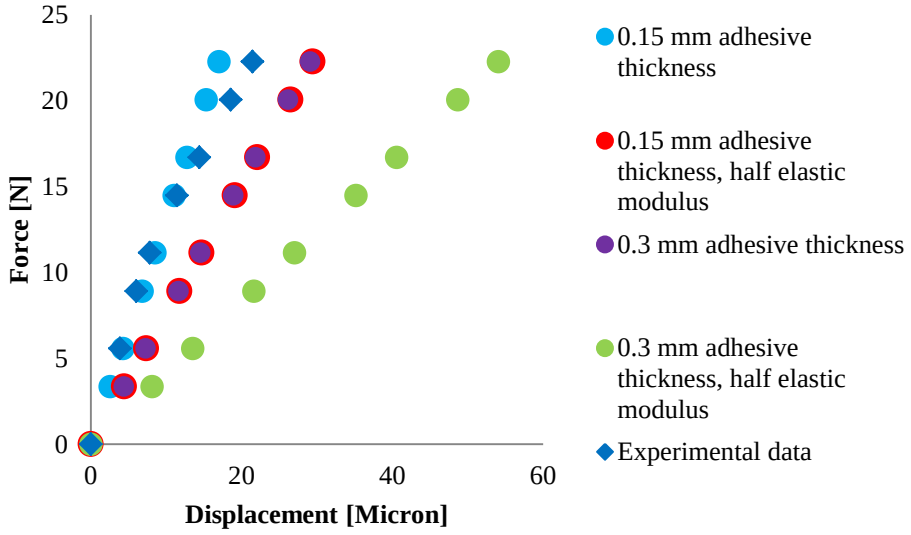

Figure 3.55: Comparison of FEA and measurement of fixture stiffness at elevated temperature 75°C (including load cell compliance)

Figure 3.56 shows the raw results for the monotonic tests were conducted on lead-free solder joint alloys with and without FR-4 substrates and copper substrates at 75°C. Figure 3.57 shows a comparison between the corrected force/displacement behaviour of the lead-free solder joint with and without a FR-4 substrate during loading and unloading at 75°C.

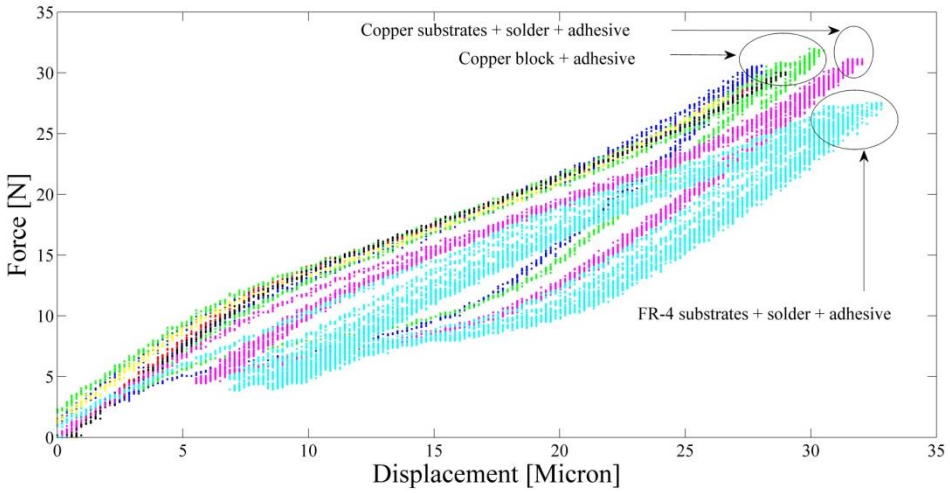

Figure 3.56: Force versus displacement not calibrated at elevated temperature 75°C

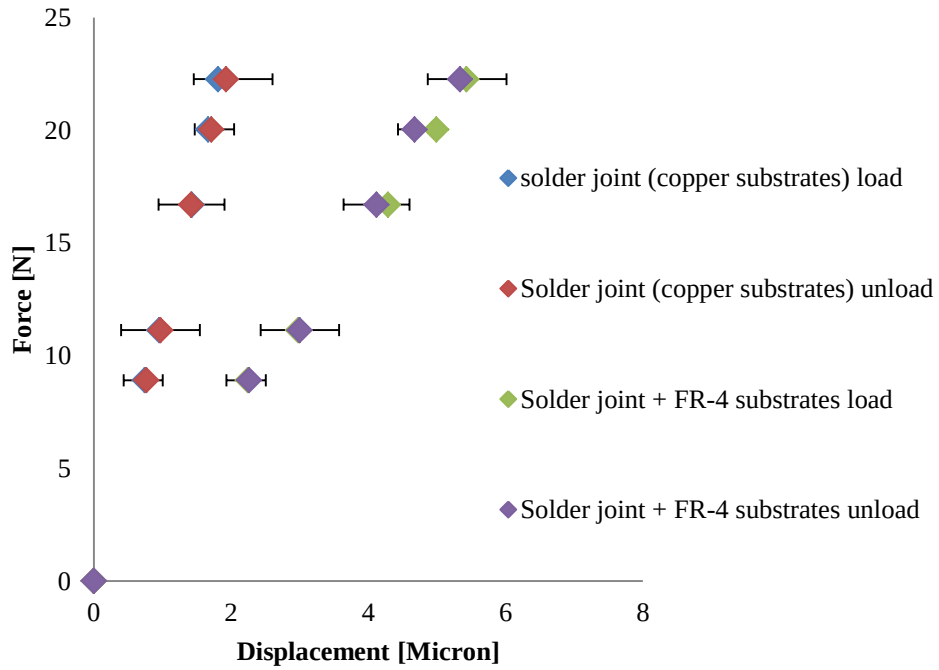

Figure 3.57: Comparison between the force/displacement behaviour of the lead- free solder joint with and without a FR-4 substrate at 75°C

Finally Figure 3.58 shows a comparison between the corrected force/displacement behaviour of the lead-free solder joints at room temperature and at 75°C. Adhesive tests using leaded solder were only carried out at room temperature with a FR-4 substrate and the corrected values for these are also shown in Figure 3.58, with the raw data being seen in Figure 3.59.

Overall, it is clear that between the substrates and the solder have a measurable effect on load-displacement behaviour.

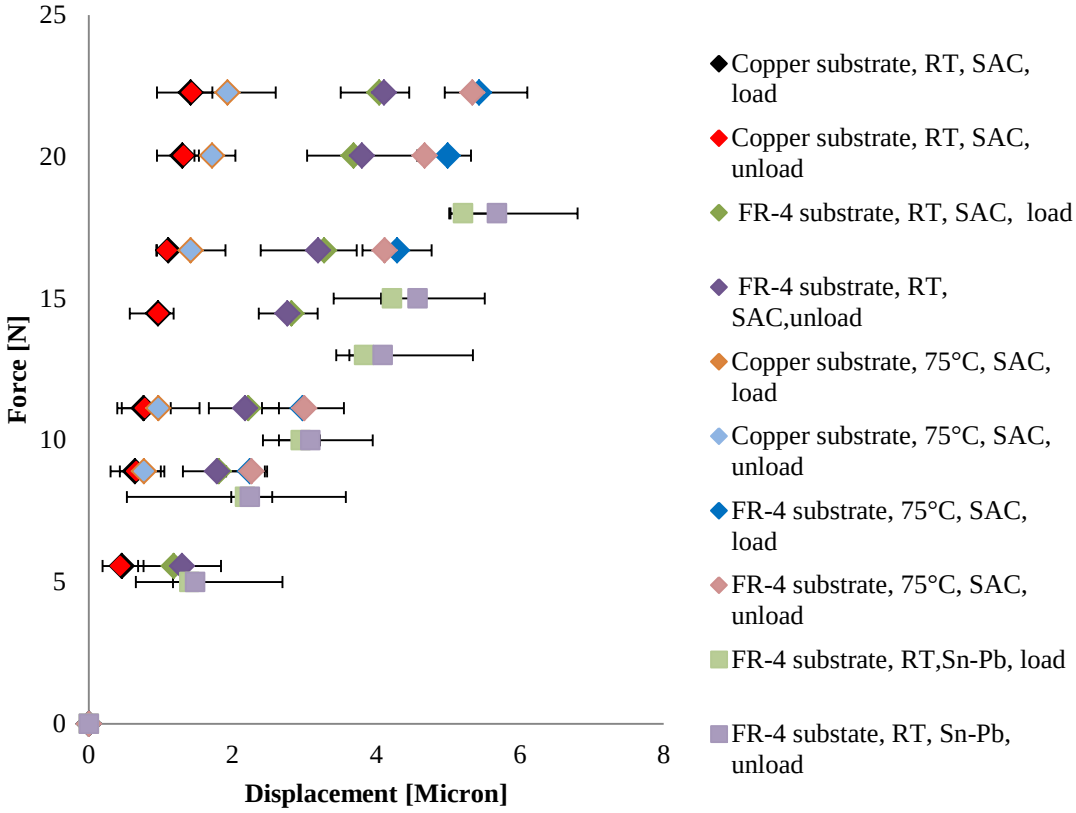

Figure 3.58: Comparison between the corrected force/displacement behaviour of leaded and lead -free solder joints at room temperature and elevated temperature 75°C

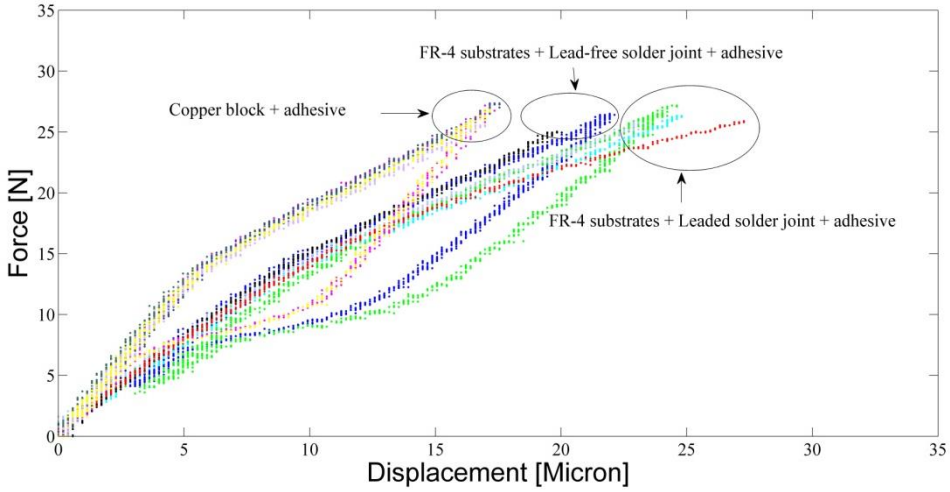

Figure 3.59: Force versus displacement not calibrated at room temperature

In order to test the system thermal stability, a test was conducted with a lead-free solder specimen held at a constant temperature 75°C for 10 hours without applying any

external force. The resulting force-time and displacement-time plots are shown in Figure 3.60 and Figure 3.61 and it is clear that these variations are insignificant in the force and displacement measured in the tests.

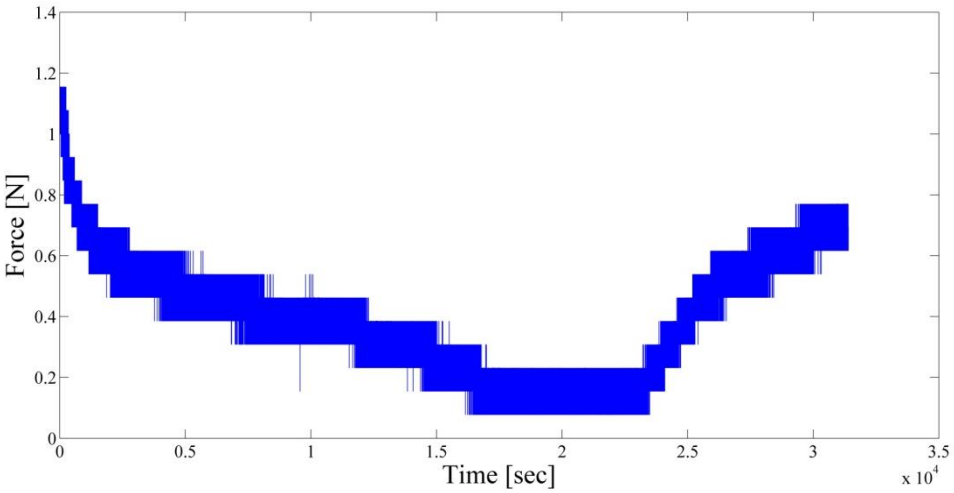

Figure 3.60: Force versus time in thermal stability test

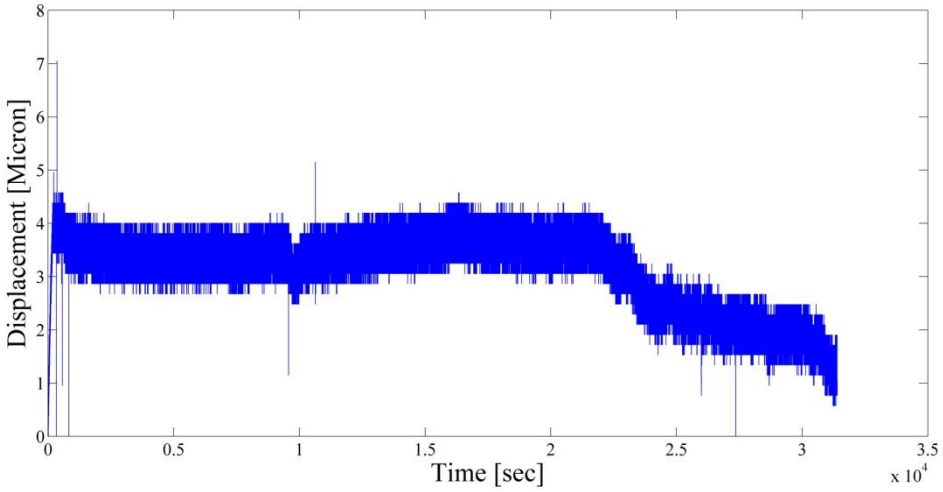

Figure 3.61: Displacement versus time in thermal stability test

3.4 Experimental procedure

The experiments were chosen in order to understand the degradation mechanisms due to combined mechanical and thermal cycling in ball grid array solder joints.

To this end, the thermal cycles were decoupled from the mechanical ones, since thermal fatigue is simply due to a mismatch strain and, if desired thermal cycles mast be carried out at the same frequency at in-phase with the mechanical cycles.

In order to be as realistic as possible, the samples were prepared in the same way as commercial (practical) BGA, but with a small number of elements to maximise the sensitivity to the solder itself. Similarly, care was taken over calibration so that the actual shear strain in the solder could be measured.

The test conditions were chosen to complement published values but with enough overlap that results should be checked for consistency with the literature. Similarly, care was taken to characterise the microstructures of the solders so that these could be compound with literature and with the joint durability.

The tests were arranged in three groups;

- Isothermal (relatively high cycle) fatigue tests, carried out at a room temperature, 35°C and 75°C.
- High cycle fatigue tests, in which the temperature was cycled between 35°C and 75°C, but at a different frequency to the mechanical cycles.
- Low cycle fatigue tests, in which the mechanical and thermal cycles were at the same frequency, the cycles being either in-phase or out-of-phase.

Tables 3.10 to 3.12 summarise the systematic tests. All tests were carried out on both leaded and lead-free solder specimens.

Table 3.10: Summary of isothermal (HCF) tests. Each test was carried out at room temperature, at 35°C and at 75°C

Shear stress range [MPa]	Stress ratio	Frequency [Hz]
10.4	1.9/12.3	1.8
11.6	2.1/13.7	1.5
12.6	2.3/14.9	1.3
14.2	2.4/16.6	1

Table 3.11: Summary of variable temperature (HCF) tests. The all test temperature was cycled between 35°C and 75°C

Shear stress range [MPa]	Stress ratio	Frequency [Hz]
10.4	1.9/12.3	1.8
11.6	2.1/13.7	1.5
12.6	2.3/14.9	1.3
14.2	2.4/16.6	1

Table 3.12: Summary of variable temperature (LCF) tests. The all tests temperature was cycled at the same frequency as the stress both in-phase and out-of-phase with it

Shear stress range [MPa]	Stress ratio	Frequency [Hz]
14.8	2.7/17.5	0.011
15.6	2.9/18.5	0.011
16.5	3.2/19.7	0.011

Chapter 4: Results of Mechanical Tests

This chapter covers the results of the systematic mechanical tests carried out on BGA samples of leaded (Sn-37Pb) and lead-free (Sn-3.8Ag-0.7Cu) solders. The chapter starts with a brief review of how fatigue and thermal fatigue data are normally handled. This is followed by sections on the detailed results on fatigue life, cyclic deformation and creep behaviour. In each section, isothermal high cycle fatigue tests, the variable temperature high cycle fatigue tests and the low cycle fatigue tests (as summarised in Tables 3.10 to 3.12) are dealt with in turn. The quantification of the microstructures is dealt with in the next chapter.

4.1 Fatigue data analysis

In applications where a structure may be subject to both thermal and mechanical cycles, such as solder joints, it is often useful to separate thermal and mechanical components of applied stress, according to whether the cyclic stress arises due to differential thermal effects, mechanical effects, or both. Three types of thermal-mechanical cycling can be identified; in-phase (IP), out-of-phase (OoP) or neither (nIP), shown schematically alongside conventional isothermal fatigue in Figure 4.1. In the first two cases, the frequency of the thermal and mechanical cycles must be the same. Out-of-phase cycling tends to occur when there is a significant time lag between the change in temperature and the development of the thermal stress, which only happens in systems with rapidly varying temperature and/or high thermal inertia, which is unlikely in solder joints. However, it is quite possible for part of the fatigue loading in a solder joint to be associated with direct mechanical loading of a different frequency to the thermal cycles, in which case there will be no relationship between the phases of the thermal and mechanical cycles (nIP).

Thermo-mechanical fatigue experiments can also be classified according to the type of control exerted:

(1) Strain (or displacement) controlled, where the amplitude of load may change during the experiment as the compliance changes.

(2) Stress (or load) controlled, where the amplitude of load is held constant during the experiment. Load controlled fatigue tests are typically performed at constant stress ratio (R) defined as:

$$R = \frac{\sigma_{min}}{\sigma_{max}} = \frac{\tau_{min}}{\tau_{max}} \quad (4.1)$$

Generally speaking, strain control is more appropriate where there is significant plasticity (low cycle fatigue), but is very difficult to achieve. Load control is generally easier to manage, but comparing, or interpreting the results can be more difficult.

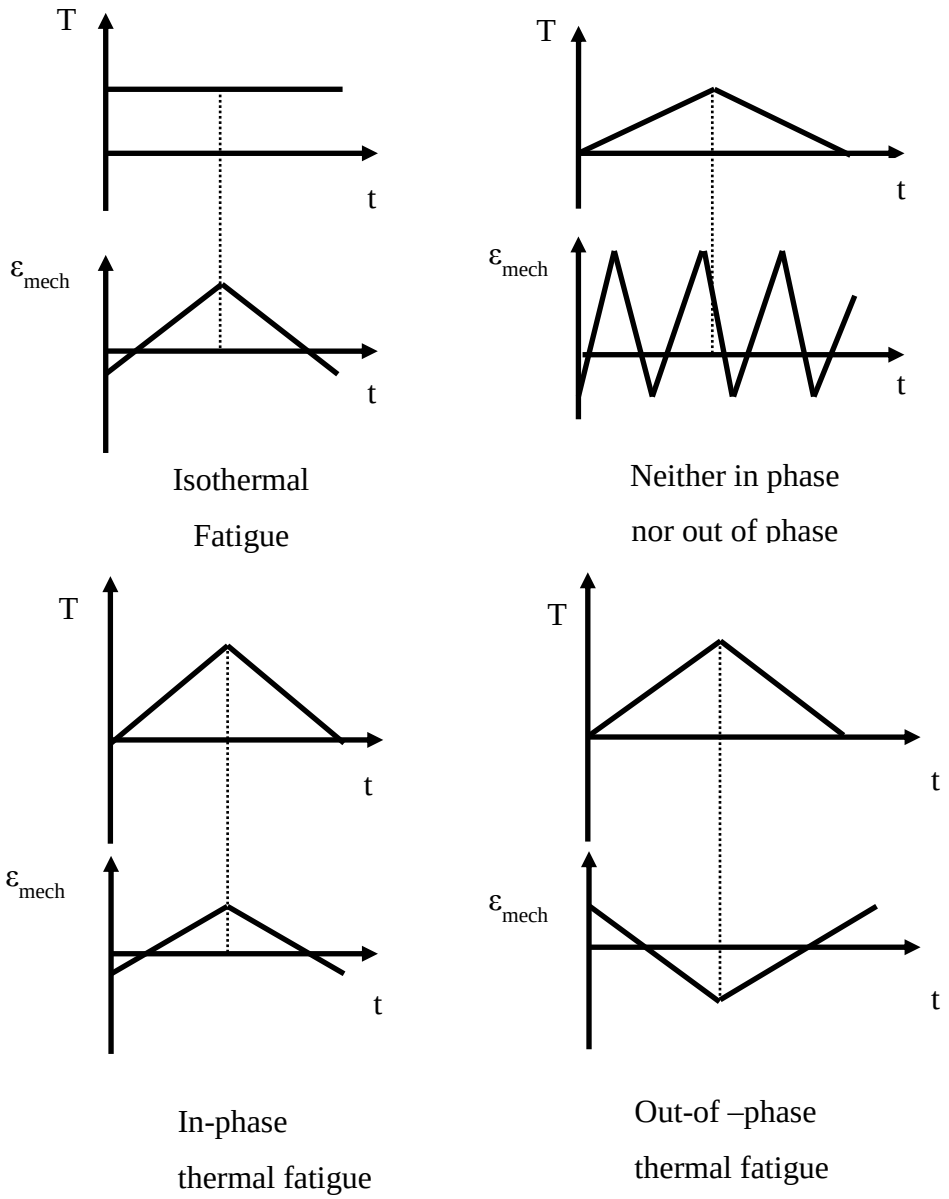

Figure 4.1: Special cases of phase in thermo-mechanical fatigue experiments

A simplified representation of the progression from localised deformation to fatigue damage is shown in Figure 4.2. Broadly speaking, cyclic deformation first gives rise to

localised plasticity at any stress raiser on the material surface (more rarely in the bulk). These localised processes may give rise to macroscopic cyclic hardening or cyclic softening depending on the alloy microstructure, the temperature and the load regime. At some stage, the localised deformation will give rise to enough stress intensity that it can be regarded as a crack, which will then propagate macroscopically in a plane at right angles to the maximum principal stress, accelerating as it progresses across the section, although the localised deformation at the crack tip remains in shear at an angle of around 45° to the maximum principal stress.

In practice, this progression from localised plastic deformation to plastic crack extension means that, irrespective of the type of control used, each cycle is mechanically distinct and a more complete picture can be obtained using the stress-strain hysteresis loop, which depends on the control mode and also whether the material exhibits cyclic hardening or cyclic softening (Figure 4.3); indeed, some materials can switch between cyclic hardening and softening during a fatigue test.

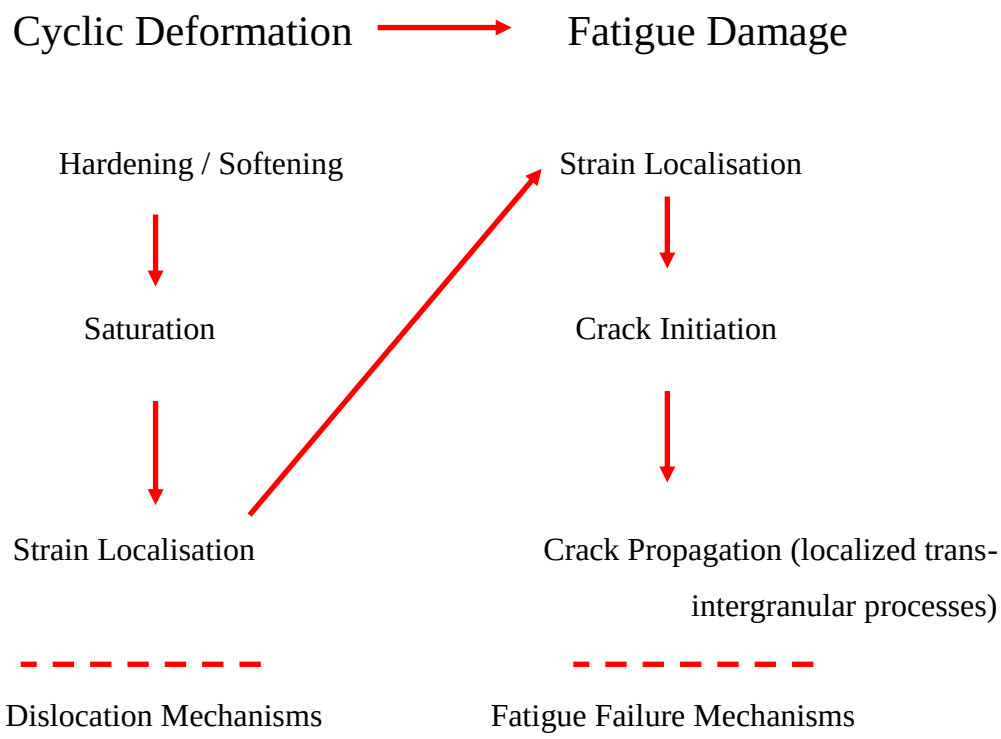

Figure 4.2: The sequence of processes during fatigue of metallic materials [294]

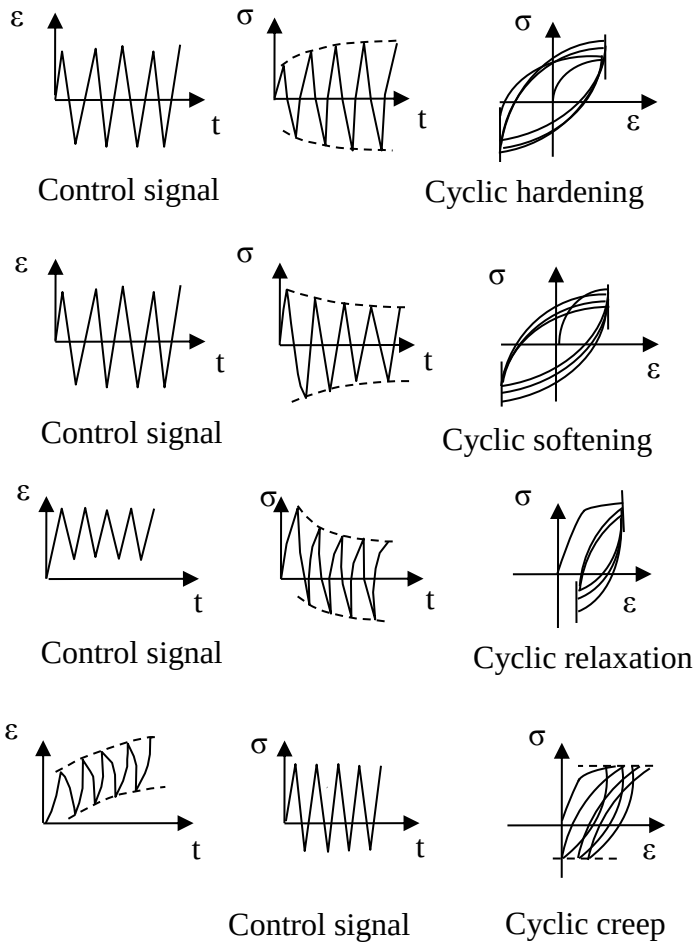

Figure 4.3: A schematic representation of transient cyclic deformation processes [295]

Four distinct fatigue design approaches can be identified, each of which has a methodology and one or more means of testing in order to determine the fatigue properties of interest, Table 4.1. The stress-life and strain-life methods do not separate any of the physical phenomena within the material and are simply based on the number of cycles of given amplitude to failure. Solders under thermal cycling loads in which the solder experiences both elastic and inelastic deformation (including both time independent plastic deformation and time-dependent creep deformation) normally display shorter lives (low cycle fatigue) and the strain-life approach is more commonly used. On the other hand, the fracture mechanics approach requires the pre-supposition of an initial crack size and therefore only describes the crack propagation stage. The strain energy approach considers both the stress and the strain and is potentially able to describe both high cycle and low cycle fatigue. As has been seen in Chapter 3,

measuring the actual strain in the solder in BGA presents significant challenges, not always addressed by those reporting fatigue properties, so stress-life, strain-life and strain energy results will all be extracted here.

Table 4.1: General fatigue design philosophy [296]

Design philosophy	Design methodology	Principal testing data description
Safe-life, infinite -life	Stress-life	$(\tau - N)$
Safe-life, finite-life	Strain-life	$(\gamma - N)$
Damage tolerant	Fracture mechanics	$\left({}^{da}/_{dN} - \Delta K\right)$
Safe-life	Stress/strain energy based	$(\tau, \gamma - N)$

4.2 Fatigue life of leaded (Sn-37Pb) and lead-free (Sn-3.8Ag-0.7Cu) solder joints

This section presents stress-life results, which are based on the number of the cycles to failure obtained under load control, with four different stress amplitudes for each of the three loading conditions; isothermal, nIP stress and temperature cycling, and IP/OoP stress and temperature cycling. In each case, the nominal shear stress range was calculated by dividing the force by the total nominal cross-sectional area of the solder balls and standard S-N curves are plotted of stress range against the logarithm of the number of cycles to failure. Tests were terminated at 10^5 cycles if the assembly had not failed and were classed as run-outs.

4.2.1 Isothermal high cycle fatigue tests

Figures 4.4 to 4.6 show the fatigue lives of the leaded and lead-free solder assemblies at room temperature, 35°C and 75°C, respectively. As can be seen, all the curves show the broadly expected shape of decreasing life with increasing stress range. Also, the lead-free alloy assemblies exhibit a consistently longer fatigue life than those made with leaded solder and this difference increases as the temperature increases. Finally, the difference between leaded and lead-free assembly performance tends to decrease as the stress range increases, except at the highest temperature where it remains about the same over the range studied.

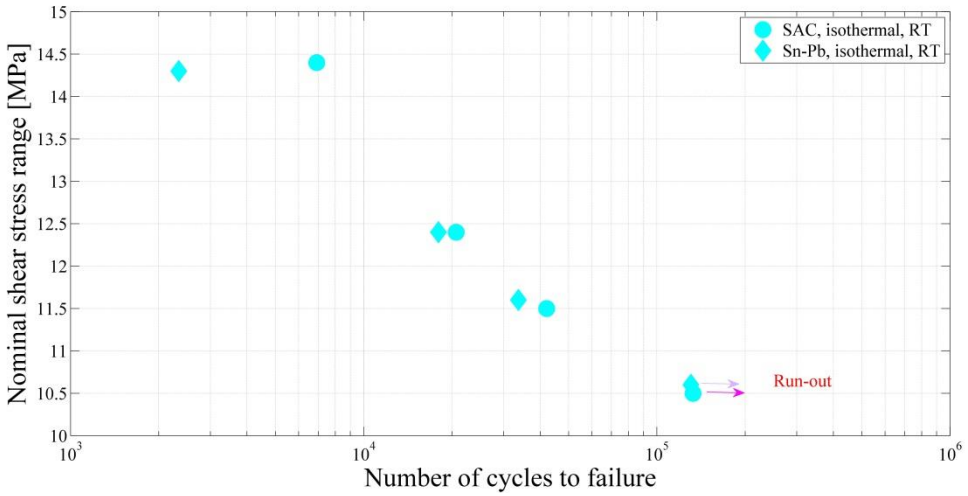

Figure 4.4: Stress amplitude vs. number of cycles to failure for leaded and lead-free solder joints under isothermal mechanical fatigue loading test at room temperature

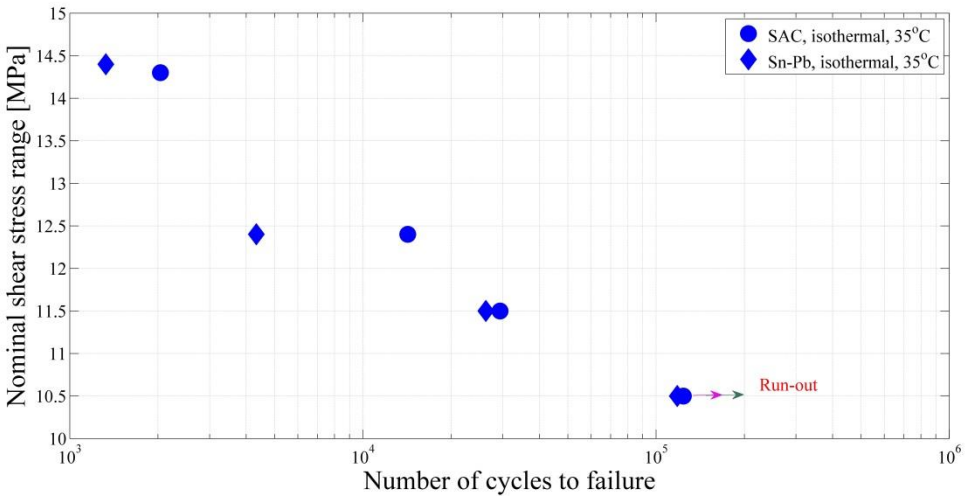

Figure 4.5: Stress amplitude vs. number of cycles to failure for leaded and lead-free solder joints under isothermal mechanical fatigue test at 35°C

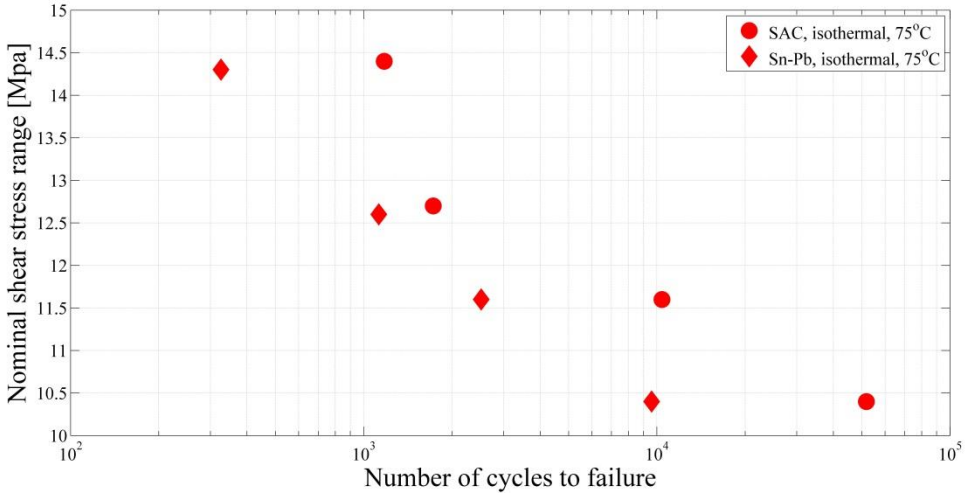

Figure 4.6: Stress amplitude vs. number of cycles to failure for leaded and lead-free solder joints under isothermal mechanical fatigue loading at 75°C

Figures 4.7 and 4.8 summarise the lifetime behaviour of leaded and lead-free solder alloys at the three different temperatures, Figure 4.8 plotted on log-log axes with the best fit lines for:

$$\log S = \log S_1 + m\log N \qquad (4.2)$$

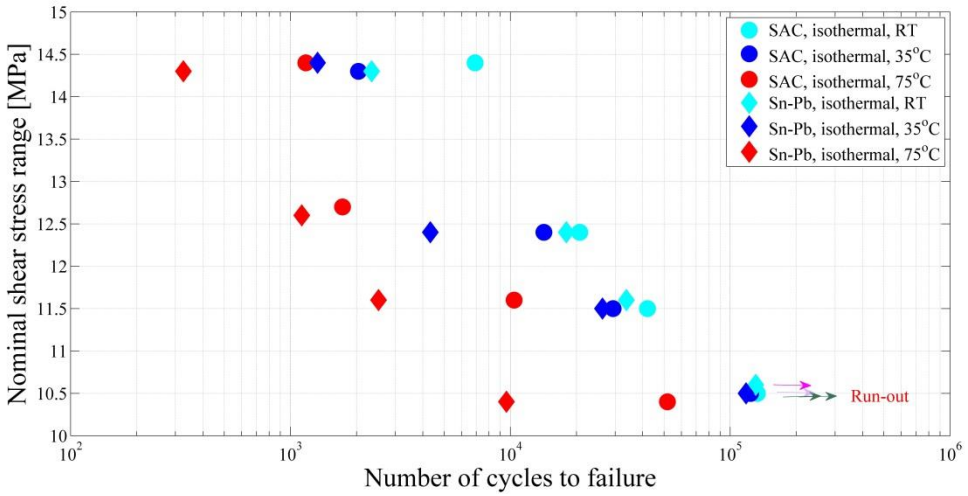

Figure 4.7: Comparison stress-life behaviour for leaded and lead-free solder joints under isothermal mechanical fatigue loading at room temperature, 35°C, and 75°C

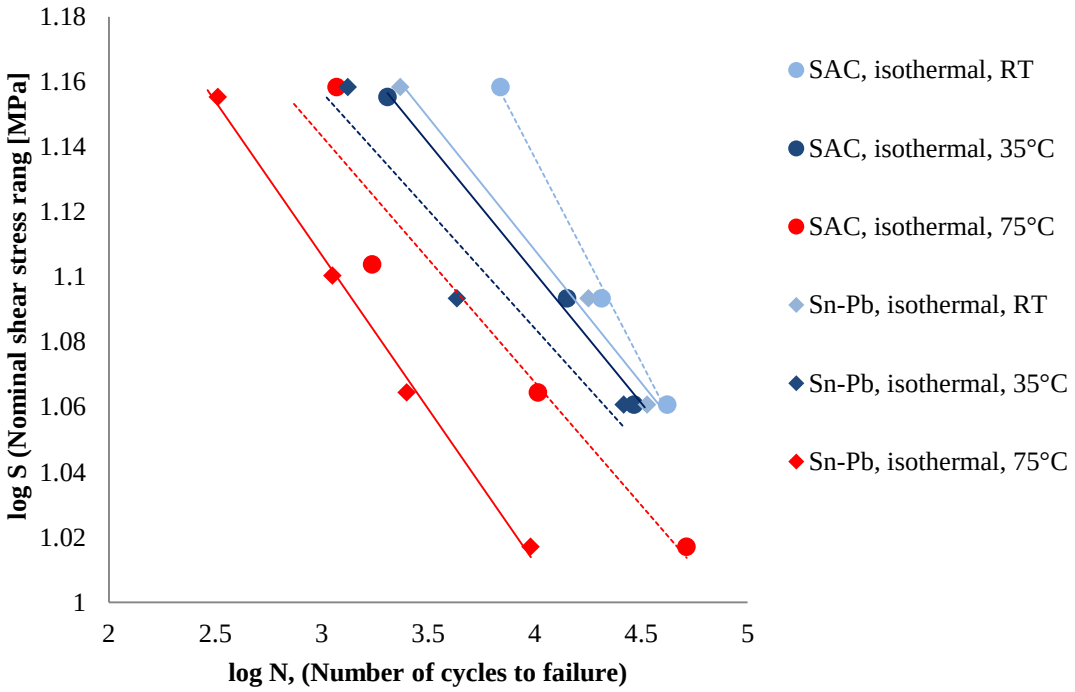

Figure 4.8: Comparison stress-life behaviour for leaded and lead-free solder joints under isothermal mechanical fatigue loading at room temperature, 35°C, and 75°C (including fit lines)

4.2.2 Variable temperature (35 to 75°C) high cycle fatigue (HCF) with temperature and stress not cycled at the same frequency (nIP)

These tests were included to assess if there was an inherent effect of temperature cycling over and above that which is associated with thermal strain, so a reduced set of stress-life tests were repeated at the same frequency, but with a superimposed low frequency temperature cycling between 35°C and 75°C. Since the thermal and mechanical cycles are neither in-phase nor out-of-phase, if there were no additional effect, the samples might be expected to behave as isothermal tests with a mean temperature of 55°C.

Figures 4.9 and 4.10 summarise the lifetime behaviour under nIP temperature cycling and, comparing Figure 4.10 with Figure 4.8 shows the temperature cycling curves to lie roughly mid-way between the 35°C and 75°C isothermal curves.

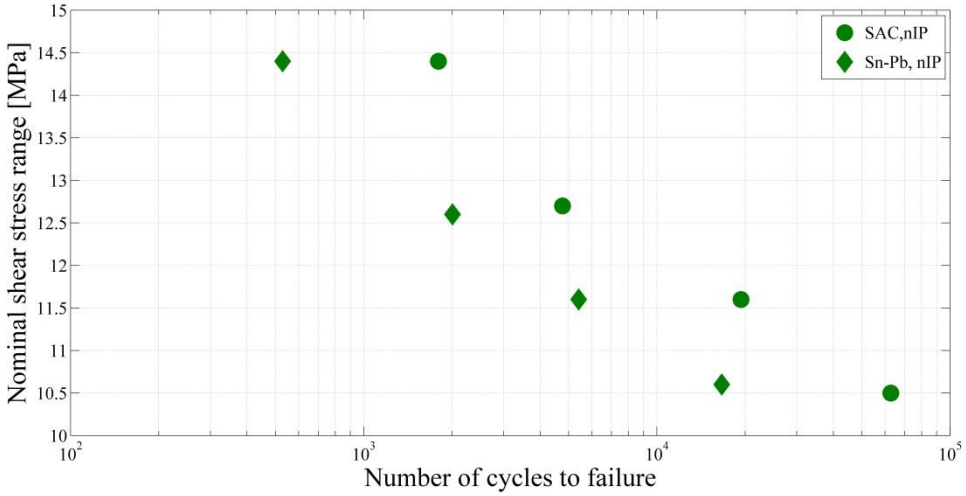

Figure 4.9: Stress amplitude vs. number of cycles to failure for leaded and lead-free solder joints under nIP thermo-mechanical fatigue testing

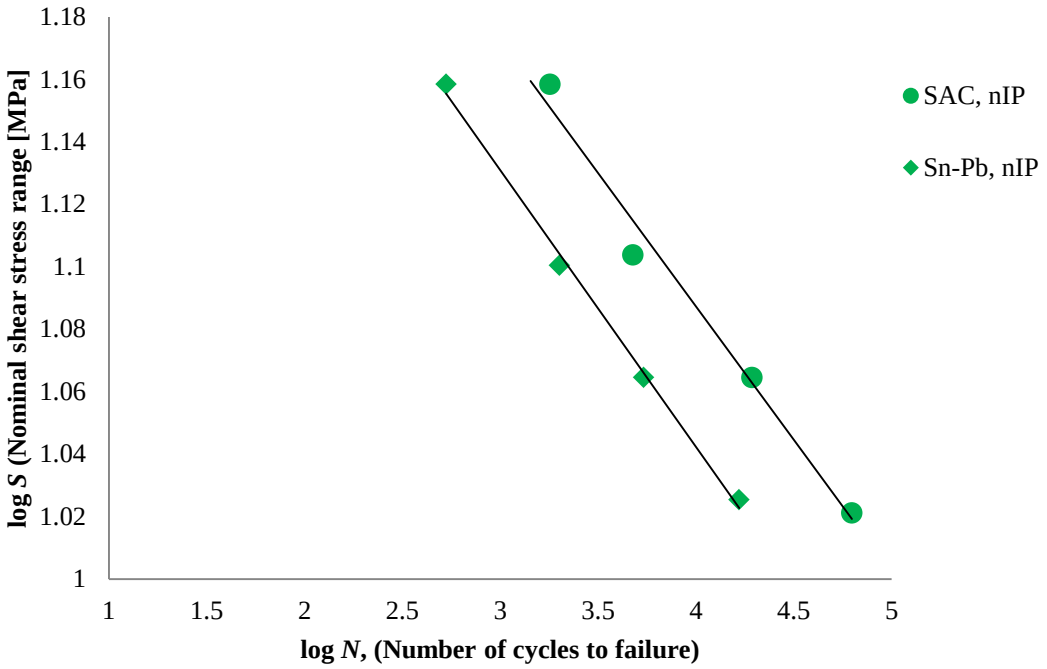

Figure 4.10: Stress amplitude vs. number of cycles to failure for leaded and lead-free solder joints under nIP thermo-mechanical fatigue testing (including fit lines)

4.2.3 Variable temperature (30 to 80°C) low cycle fatigue (LCF) with temperature and stress cycled at the same frequency

Figures 4.11 and 4.12 show mechanical stress range *vs*. number of cycles to failure for leaded and lead-free solder joints under IP and OoP loading, respectively.

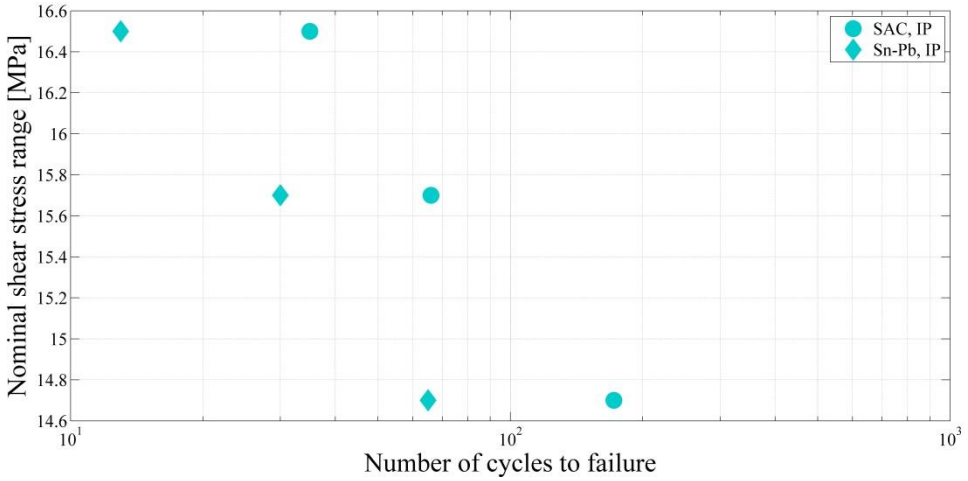

Figure 4.11: Stress amplitude vs. number of cycles to failure for leaded and lead-free solder joints under IP thermo-mechanical fatigue test

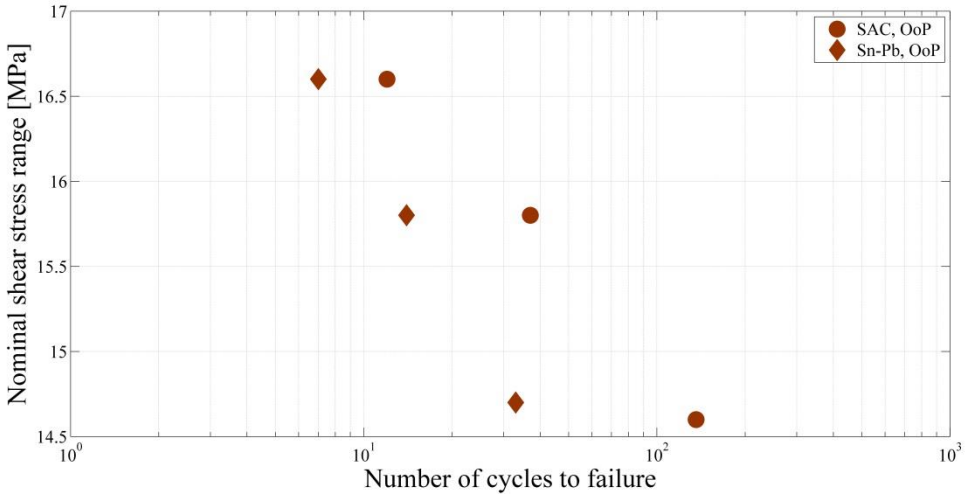

Figure 4.12: Stress amplitude vs. number of cycles to failure for leaded and lead-free solder joints under out phase (OoP) thermo-mechanical fatigue test

Figures 4.13 and 4.14 summarise compare the lifetime behaviour of leaded and lead-free solder alloys under (IP) and (OoP) loading. Besides the already-made observation that the lead-free alloy fatigue life is better, it is clear that OoP loading results in shorter fatigue life than does IP loading. The effect is most pronounced in the lead-free solder at high stress range, and least pronounced also for the lead-free solder at high stress range. The effect is more-or-less constant for the leaded solder at all stress ranges studied.

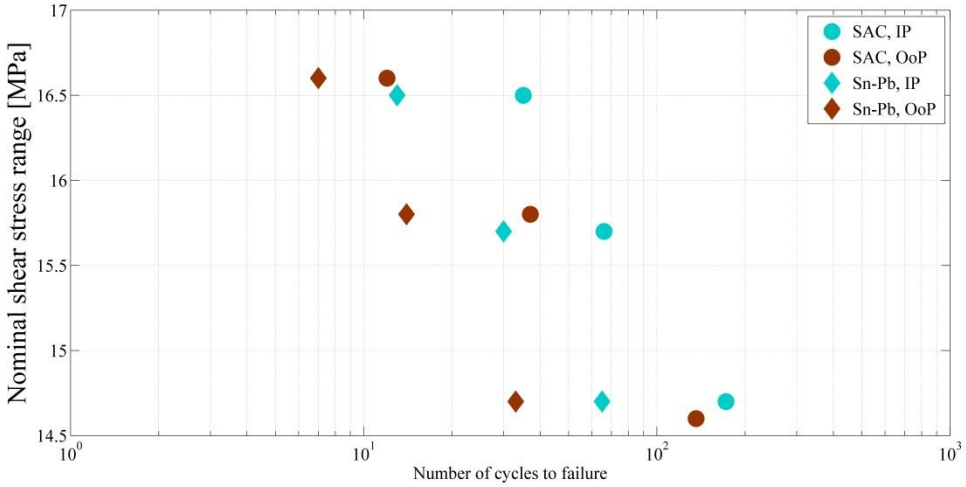

Figure 4.13: Comparison stress amplitude vs. number of cycles to failure for leaded and lead-free solder joints under IP and OoP thermo-mechanical fatigue testing

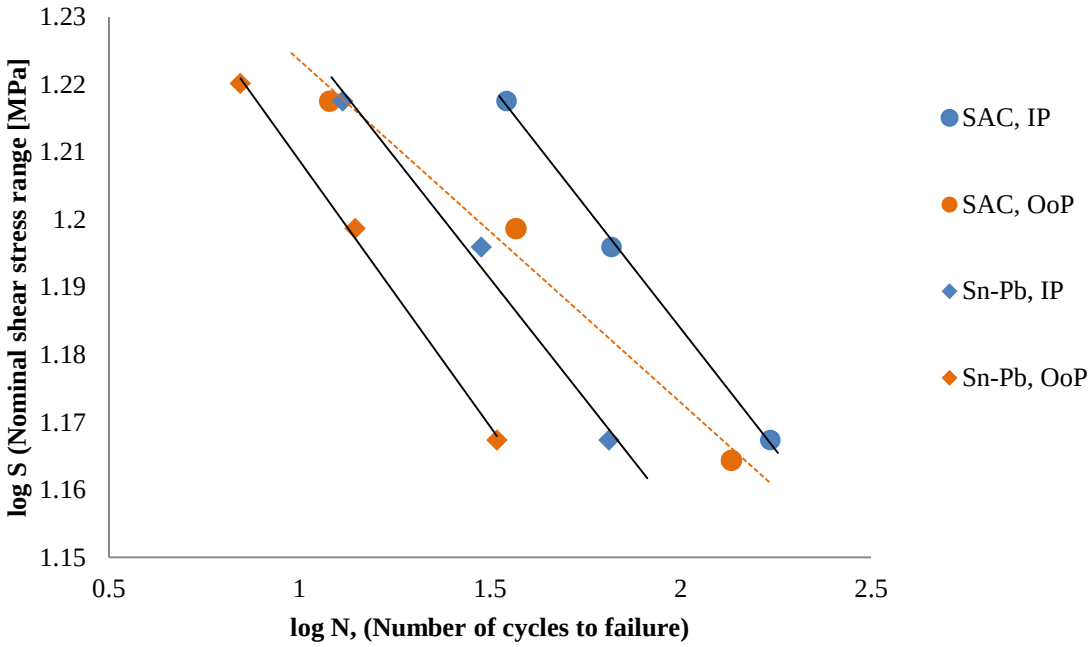

Figure 4.14: Comparison stress amplitude vs. number of cycles to failure for leaded and lead-free solder joints under IP and OoP loading (including fit lines)

4.2.4 Summary of fatigue life results

Figure 4.15 collect all of the stress-lie data and presents these for the two alloys. The relevant best fit relationships using Equation 4.2 are collected in Table 4.2. Perhaps the most striking additional observation in the collected data is the abrupt discontinuity in behaviour between the low-cycle and high-cycle stress-life relationships, over and

above the effect of mean or maximum temperature. This aspect is discussed in more detail in the next chapter in the light of the work of other investigators and also the stress-strain behaviour in the tests described in the following sections of this chapter.

The other additional observation that can be made is that the behaviour of the lead-free alloy is more scattered than the leaded alloy, an effect that is attenuated somewhat in the R^2 values in Table 4.2 because it is a log-log relationship. It seems likely that this scatter, associated with relative inhomogeneity of the lead-free microstructure as shown in the next chapter.

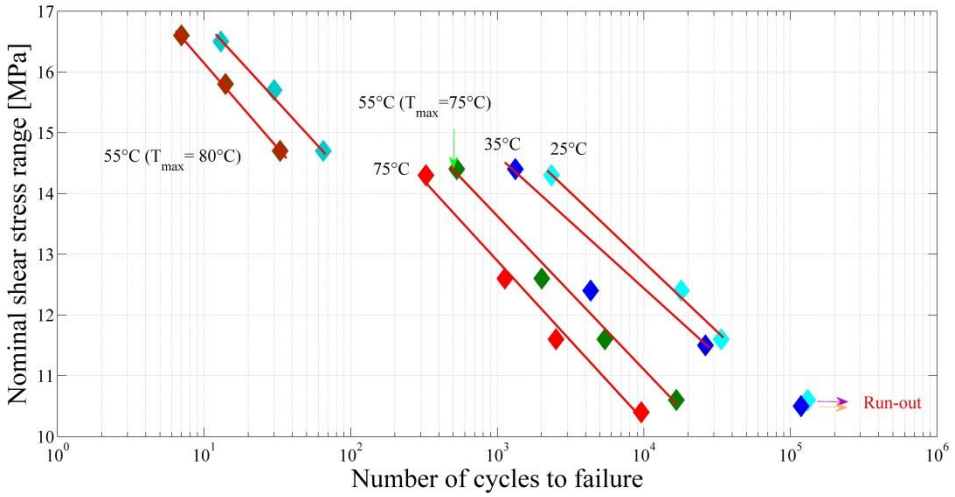

(a) Sn-Pb data

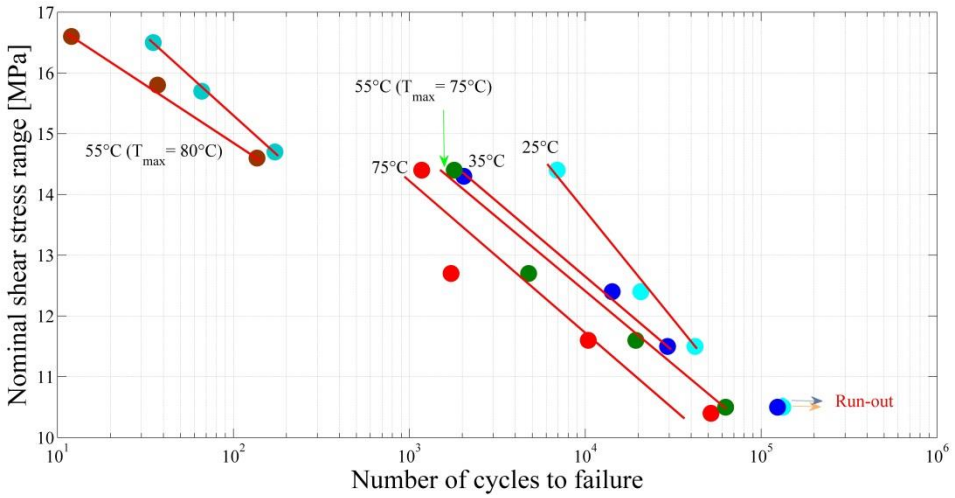

(b) SAC data

Figure 4.15: Comparison stress amplitude vs. number of cycles to failure for leaded and lead-free solder joints under isothermal mechanical and thermo-mechanical fatigue tests

Table 4.2: Constants obtained from the best fit lines of log-log stress range versus number of cycles to failure

Test conditions	m	log S_1	S_1	R^2
		Sn-3.8Ag-0.7Cu		
RT	-0.1256	1.6391	43.561	0.9957
35°C	-0.08	1.4212	26.375	0.9934
75°C	-0.0756	1.3702	23.453	0.9168
nIP	-0.0853	1.4286	26.828	0.9821
IP	-0.0722	1.3284	21.301	0.9987
OoP	-0.0507	1.2742	18.801	0.9845
		Sn-37Pb		
RT	-0.0815	1.4344	26.730	0.9887
35°C	-0.0726	1.3747	23.697	0.9082
75°C	-0.0945	1.3902	24.558	0.9962
nIP	-0.0886	1.3969	24.940	0.9967
IP	-0.0716	1.2987	19.892	0.9894
OoP	-0.0786	1.2873	19.377	0.9978

4.3 Cyclic deformation behaviour of solder joints (softening and hardening)

Figure 4.16 shows the displacement curve for an isothermal fatigue load control test. As can be seen, the mean value of the displacement increases and the displacement range decreases over the 1.7×10^4 cycles up to failure of the specimen. Both of these effects are a consequence of the load control and also of the fact that the shear force is not reversed so that any recovery relies on the elastic component of the deformation. Whereas this type of loading is not necessarily representative of real joints, nor are the results easily compared with other workers using displacement control, the results do provide additional insight into short- and long-term temporal response of the alloys.

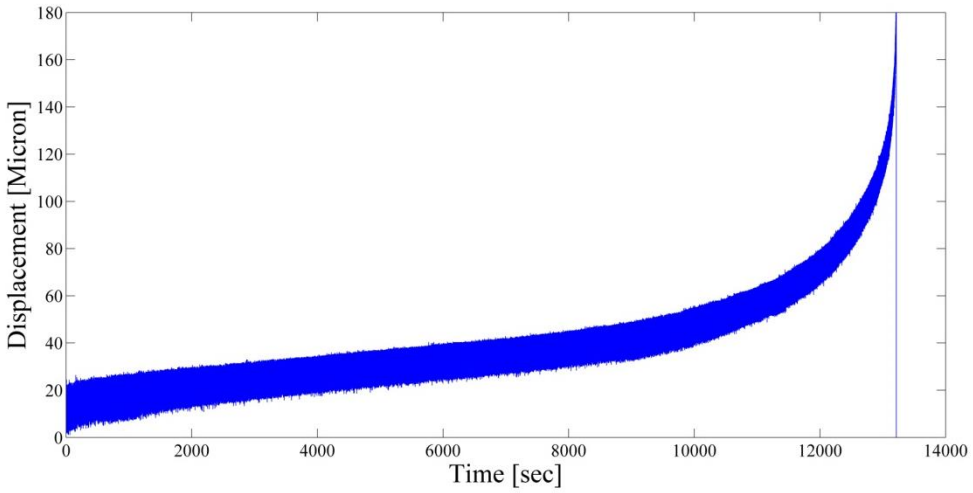

Figure 4.16: Displacement curve for Sn-Pb alloy under isothermal load control at room temperature at stress range of 12.6 MPa

In order to effect the analysis, the mean trend of the displacement-time graph was obtained by taking one cycle moving average and the mean value subtracted from every data point in the series effectively isolating the periodic part of the displacement behaviour with a mean of zero, as showing in Figure 4.17. This section is concerned with analysing this cyclic behaviour, whereas the long-term mean trend curves will be analysed in the next section.

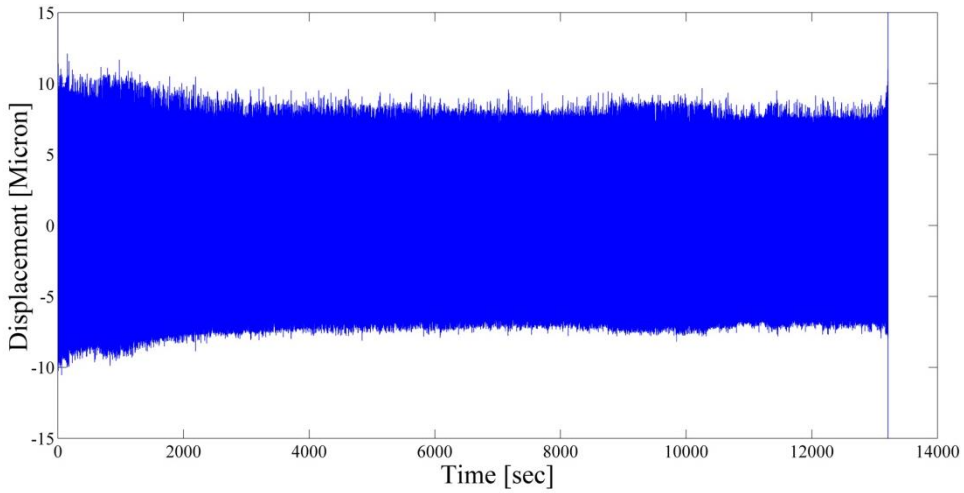

Figure 4.17: Periodic part of displacement curve for Sn-Pb alloy under isothermal load control at room temperature at stress range of 12.6 MPa

Maximum and minimum displacements were determined for each cycle as shown in Figure 4.18 and then the values for every 35 cycles were averaged as shown in Figure 4.19, the last 25 being discarded. Similarly, the displacement range was calculated for

every cycle by subtracting the maximum displacement from the minimum displacement as shown in Figure 4.20 and gain the average of each 35 cycles was calculated, Figure 4.21. The averaged curves of the type shown in Figures 4.19 and 4.21 are discussed in the following sections.

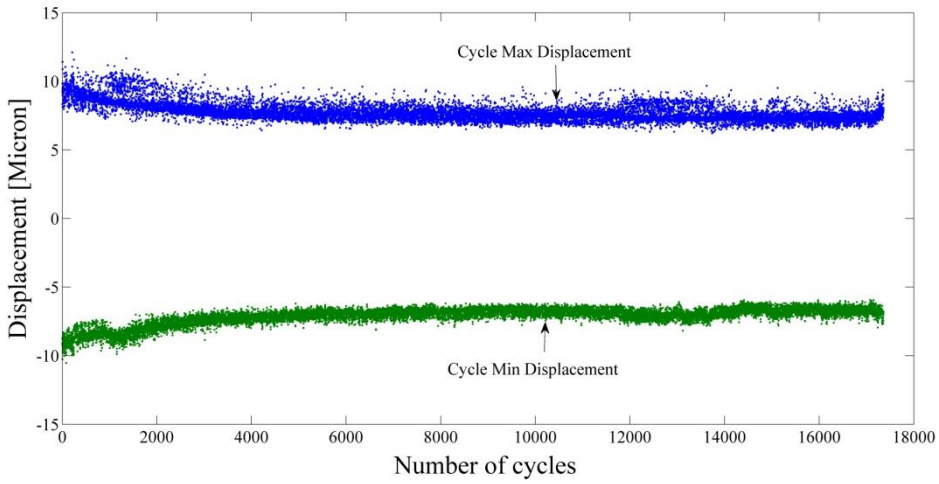

Figure 4.18: Maximum and minimum displacement curve for Sn-Pb alloy under isothermal load control at room temperature at stress range of 12.6 MPa

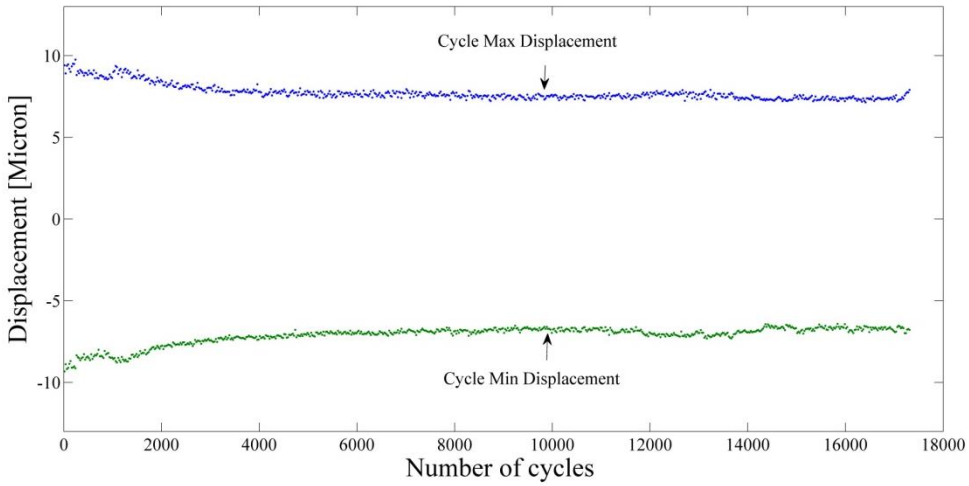

Figure 4.19: Averaged maximum and minimum displacement curve for Sn-Pb alloy under isothermal load control at room temperature at stress range of 12.6 MPa

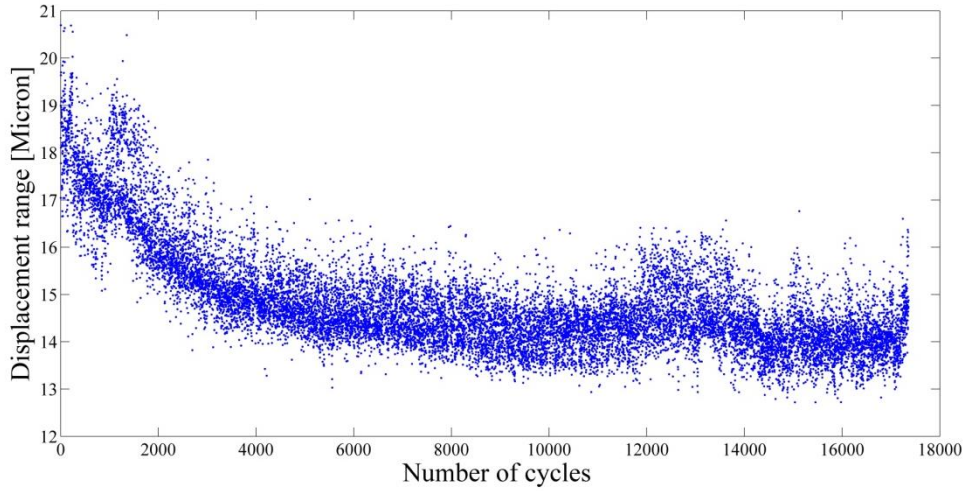

Figure 4.20: Displacement range curve for Sn-Pb alloy under isothermal load control at room temperature at stress range of 12.6 MPa

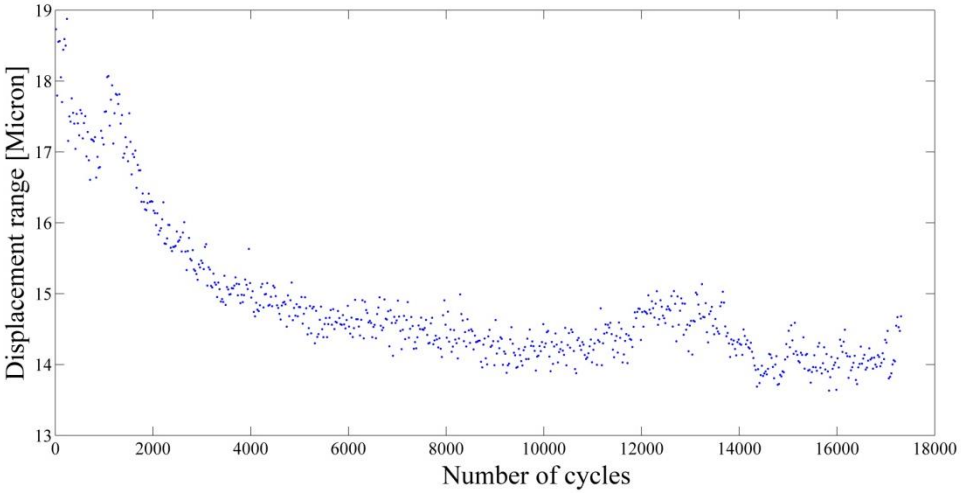

Figure 4.21: Averaged displacement range curve for Sn-Pb alloy under isothermal load control at room temperature at stress range of 12.6 MPa

4.3.1 Cyclic deformation of leaded (Sn-37Pb) solder

Figures 4.22 to 4.25 show the evolutions of maximum and minimum displacement and displacement range for the room temperature isothermal tests on Pb-Sn. Two graphs are shown for each evolution in order to see more clearly and comparatively the initial stages. As can be seen, the 11.6 MPa test exhibits substantial initial cyclic hardening, followed by a longer period of cyclic softening. Above this stress, there is still initial cyclic hardening, but the specimens fail before any softening occurs. For the lowest stress range, the displacement range remains substantially constant throughout the life.

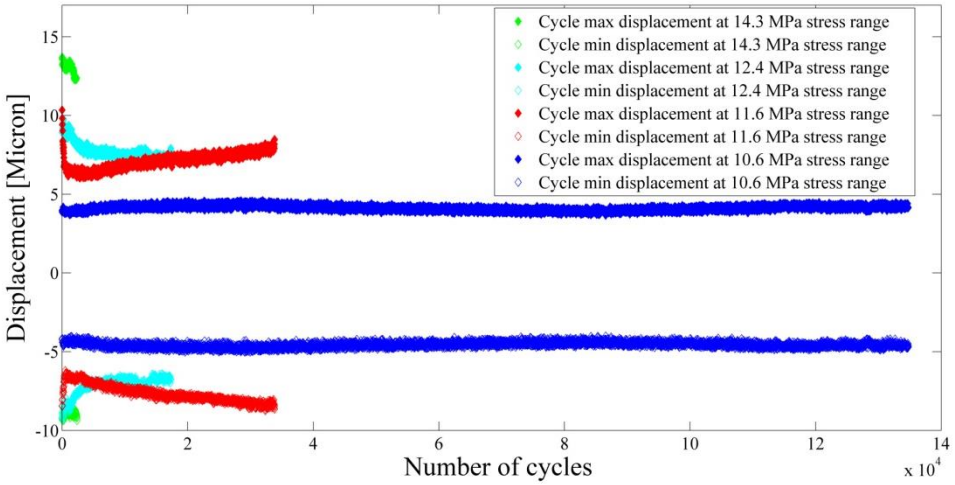

Figure 4.22: Maximum and minimum displacement evolution under load controlled isothermal fatigue of leaded (Sn-37Pb) solder at room temperature

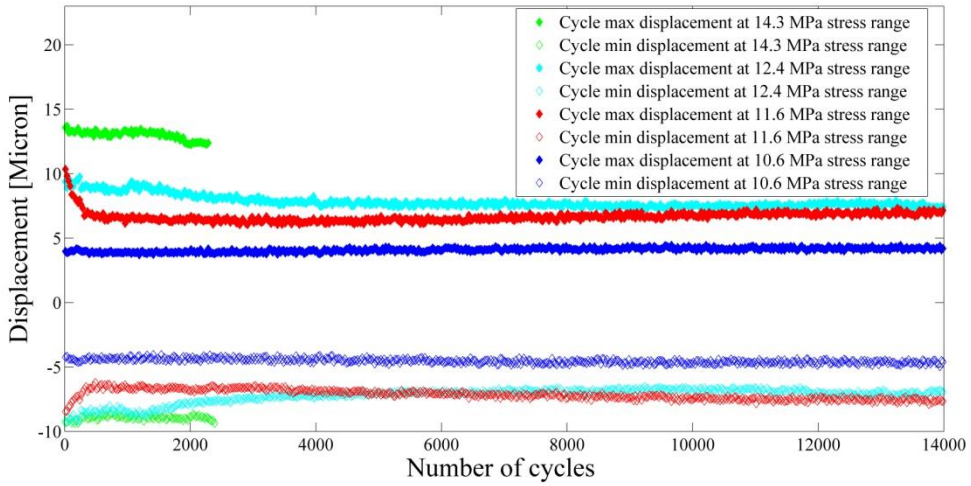

Figure 4.23: Maximum and minimum displacement evolution under load controlled isothermal fatigue of leaded (Sn-37Pb) solder at room temperature (detail)

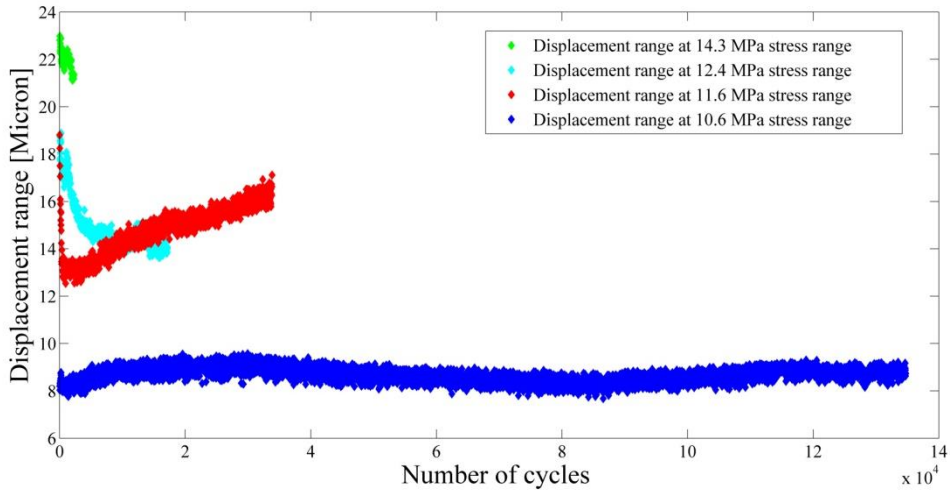

Figure 4.24: Displacement range evolution under load controlled isothermal fatigue of leaded (Sn-37Pb) solder at room temperature

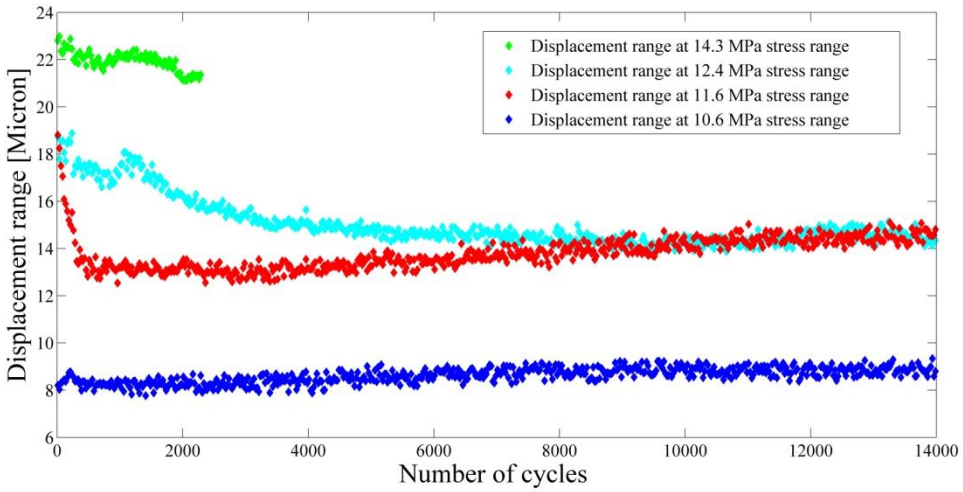

Figure 4.25: Displacement range evolution under load controlled isothermal fatigue of leaded (Sn-37Pb) solder at room temperature (detail)

Figures 4.26 to 4.31 show the corresponding evolutions of displacement range for the elevated temperature isothermal tests on Pb-Sn, including the nIP tests which have an effective average temperature of 55°C. In all cases the initial period of cyclic hardening is replaced by cyclic softening and in some cases there is an upturn in cyclic softening towards the end of life. Besides reducing life, it appears that increasing temperature reduces the cycling rate.

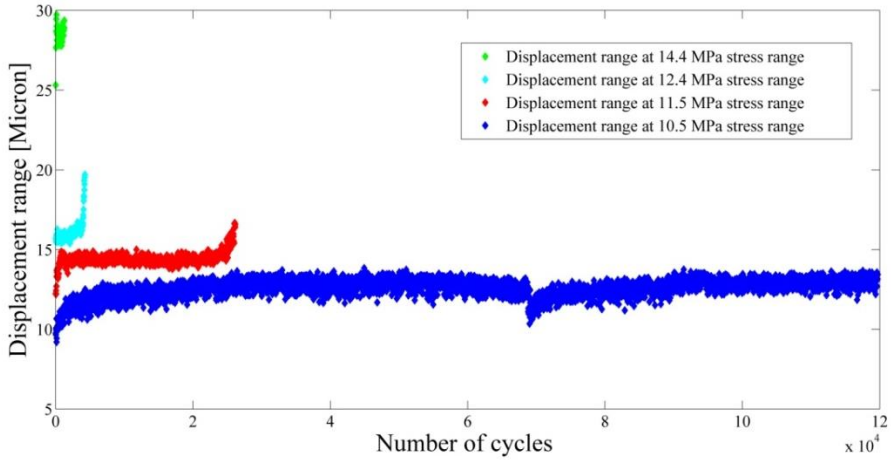

Figure 4.26: Displacement range evolution under load controlled isothermal fatigue of leaded (Sn-37Pb) solder at 35°C

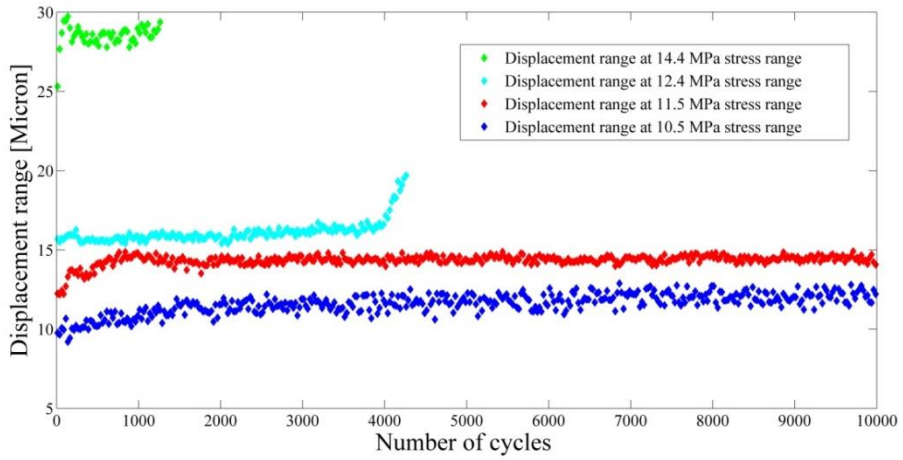

Figure 4.27: Displacement range Displacement range evolution under load controlled isothermal fatigue of leaded (Sn-37Pb) solder at 35°C (detail)

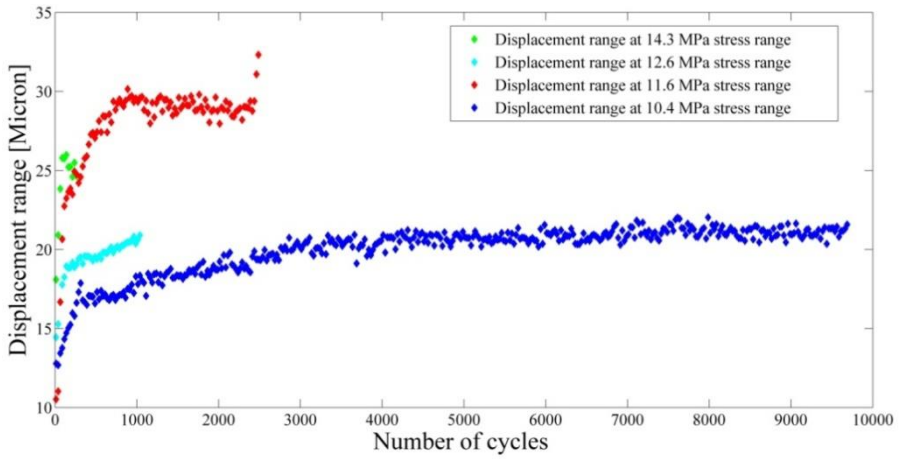

Figure 4.28: Displacement range evolution under load controlled isothermal fatigue of leaded (Sn-37Pb) solder at 75°C

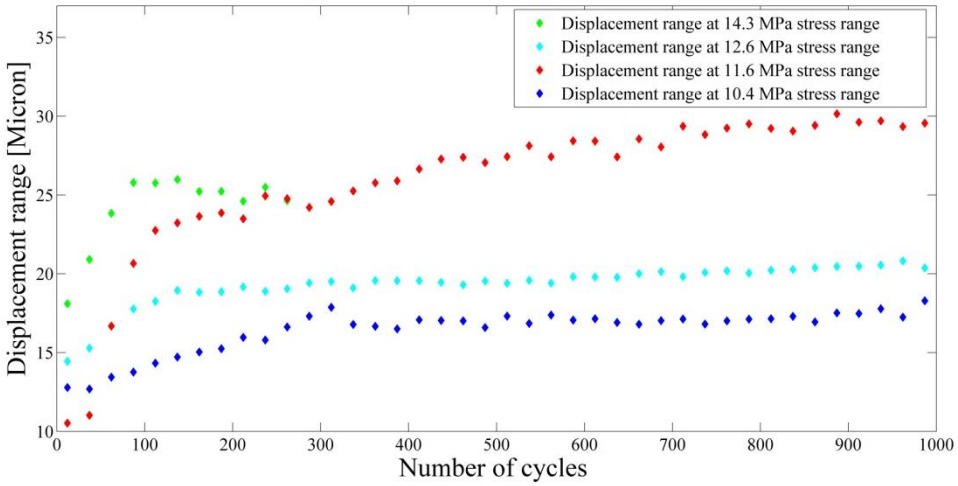

Figure 4.29: Displacement range Displacement range evolution under load controlled isothermal fatigue of leaded (Sn-37Pb) solder at 75°C (detail)

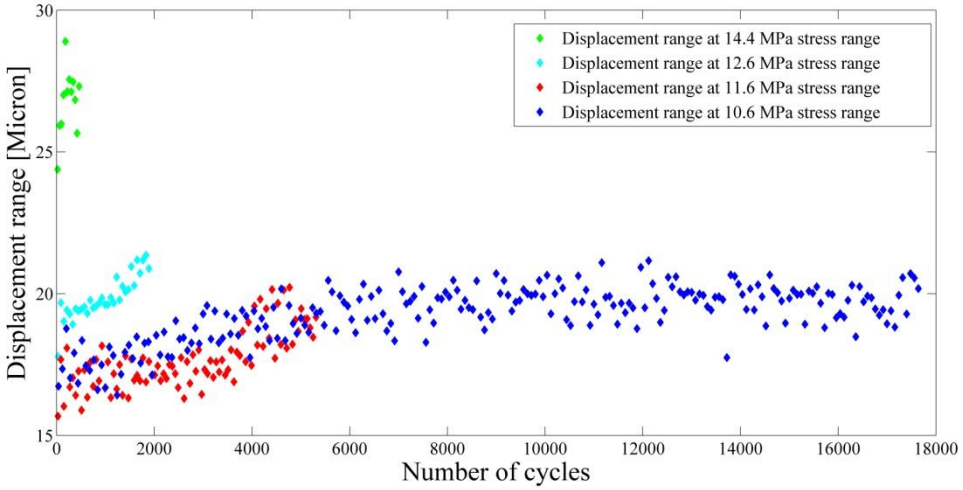

Figure 4.30: Displacement range evolution under load controlled nIP fatigue of leaded (Sn-37Pb) solder (effective temperature 55°C)

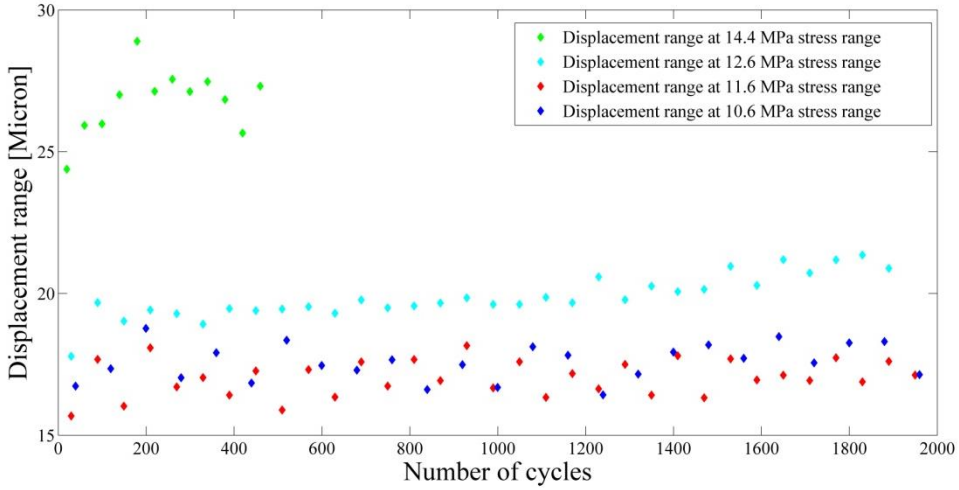

Figure 4.31: Displacement range evolution under load controlled nIP fatigue of leaded (Sn-37Pb) solder (effective temperature 55°C) (detail)

The low-cycle fatigue tests for Pb-Sn similarly show cyclic softening throughout their fatigue life, although at lower loads there is a slight tendency towards a gentle “bathtub” shape.

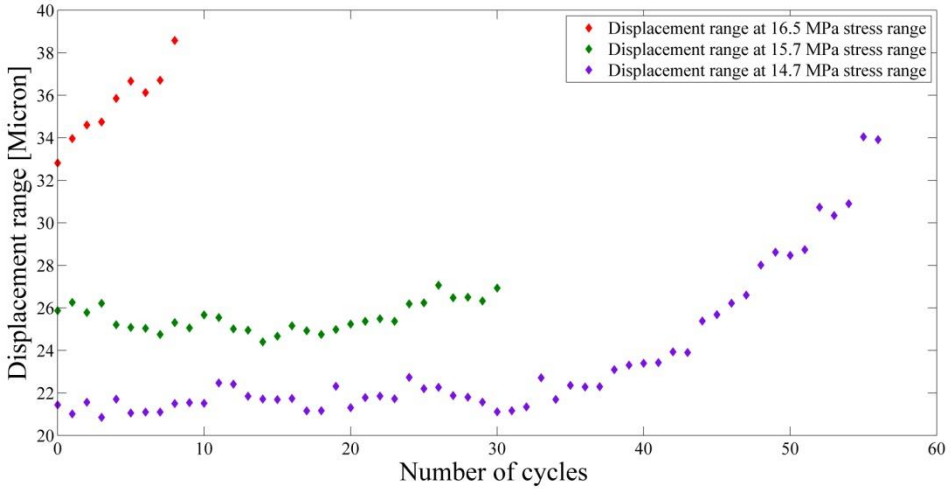

Figure 4.32: Displacement range evolution under load controlled IP fatigue of leaded (Sn-37Pb) solder

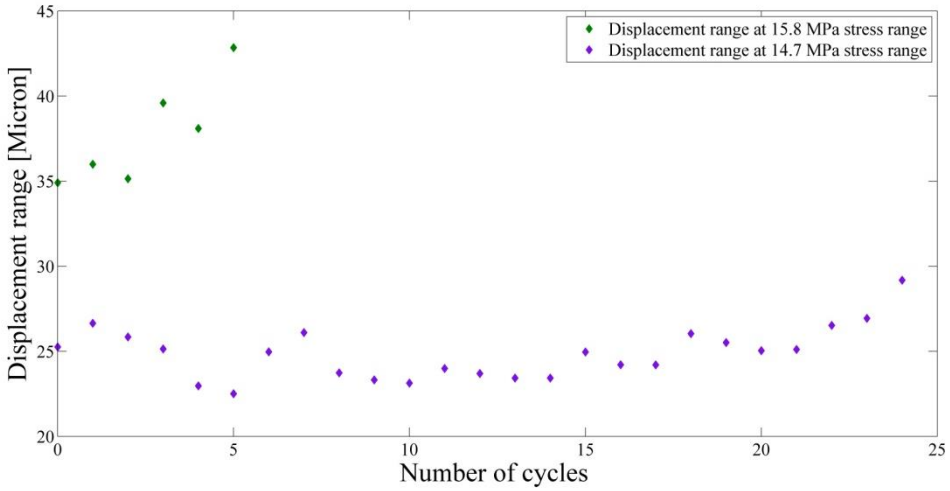

Figure 4.33: Displacement range evolution under load controlled OoP fatigue of leaded (Sn-37Pb) solder

4.3.2 Cyclic deformation of lead-free (Sn-3.8Ag-0.7Cu) solder

The cyclic behaviour of the lead-free alloy is shown in Figures 4.34 to 4.43 in the same format as for the leaded alloy. The behaviour is broadly similar, although the regimes of hardening and softening are somewhat more erratic, consistent with the scatter in stress-life observed in the previous section.

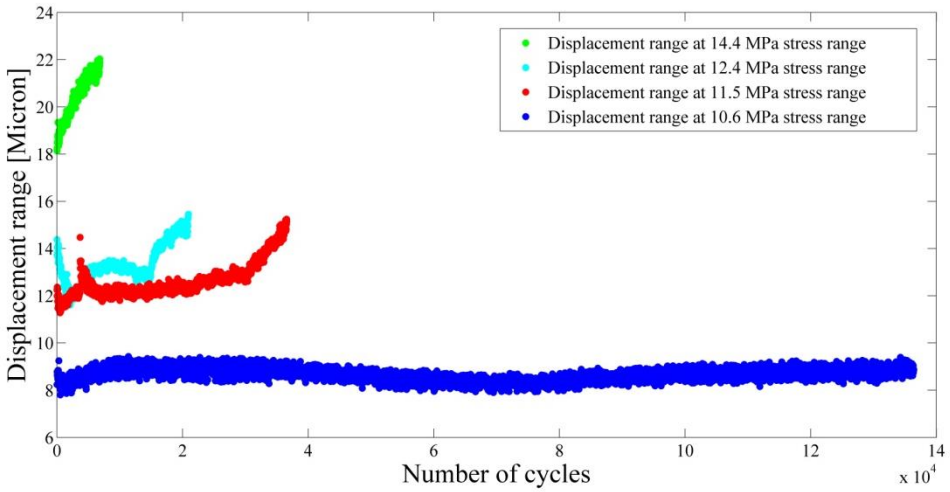

Figure 4.34: Displacement range evolution under load-controlled isothermal fatigue of lead-free (Sn-3.8Ag-0.7Cu) solder at room temperature

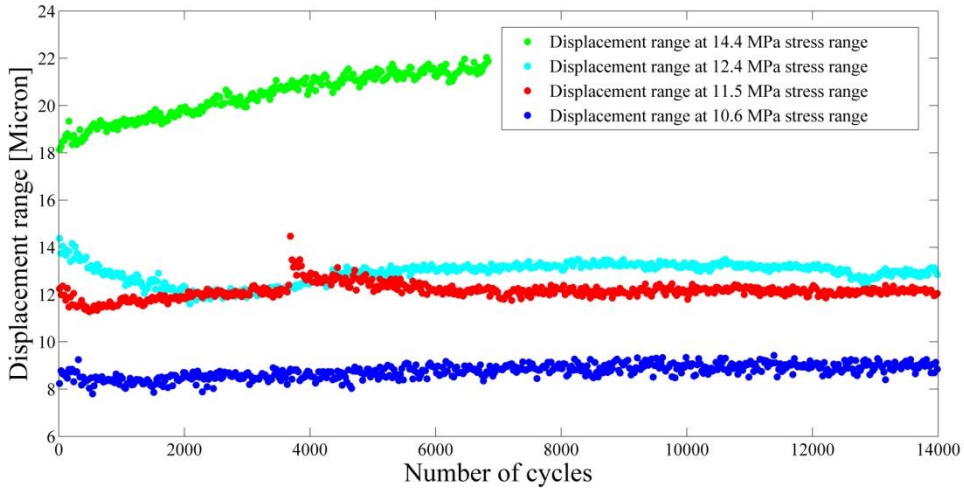

Figure 4.35: Displacement range evolution under load-controlled isothermal fatigue of lead-free (Sn-3.8Ag-0.7Cu) solder at room temperature (detail)

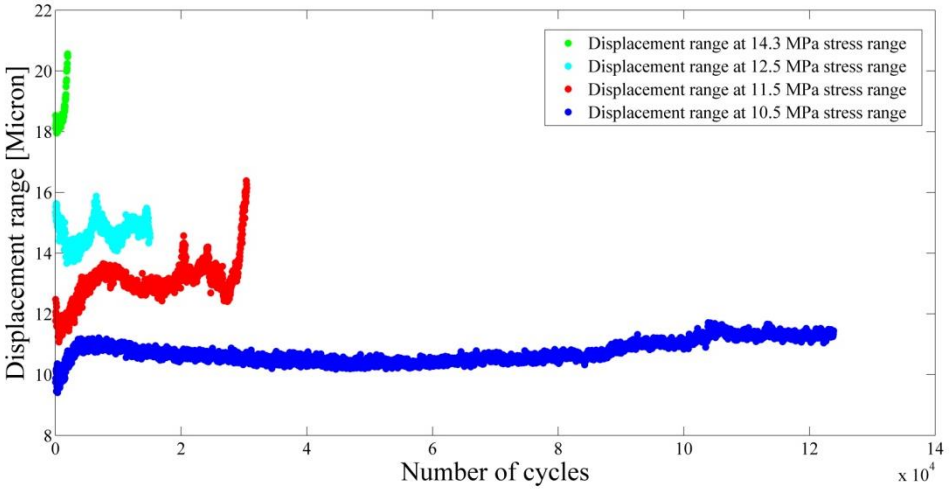

Figure 4.36: Displacement range evolution under load-controlled isothermal fatigue of lead-free (Sn-3.8Ag-0.7Cu) solder at 35°C

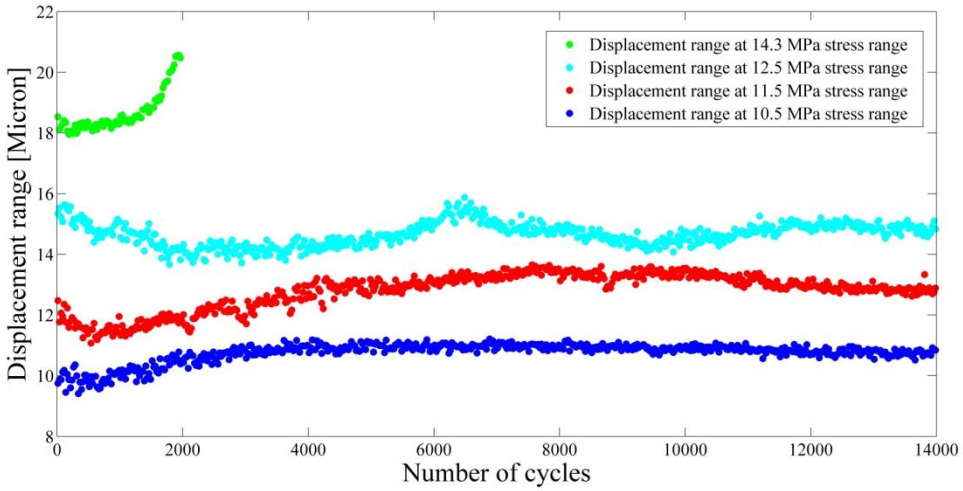

Figure 4.37: Displacement range evolution under load-controlled isothermal fatigue of lead-free (Sn-3.8Ag-0.7Cu) solder at 35°C (detail)

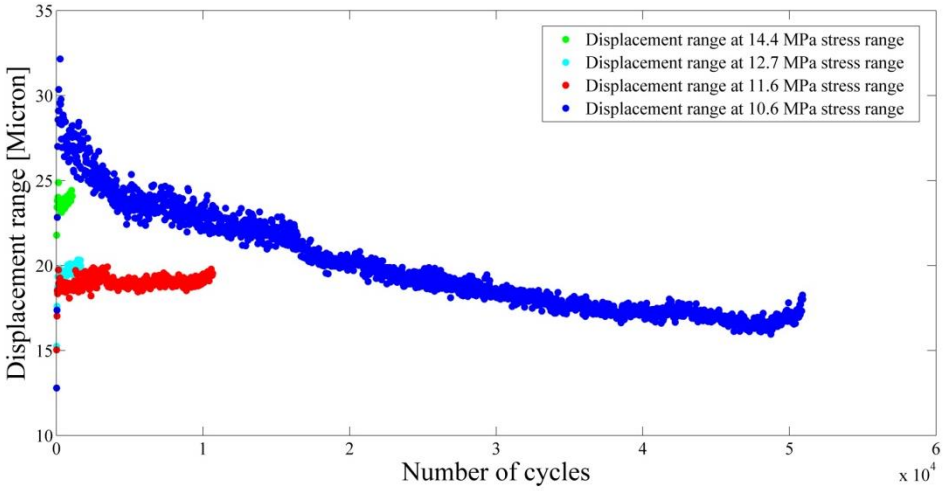

Figure 4.38: Displacement range evolution under load-controlled isothermal fatigue of lead-free (Sn-3.8Ag-0.7Cu) solder at 75°C

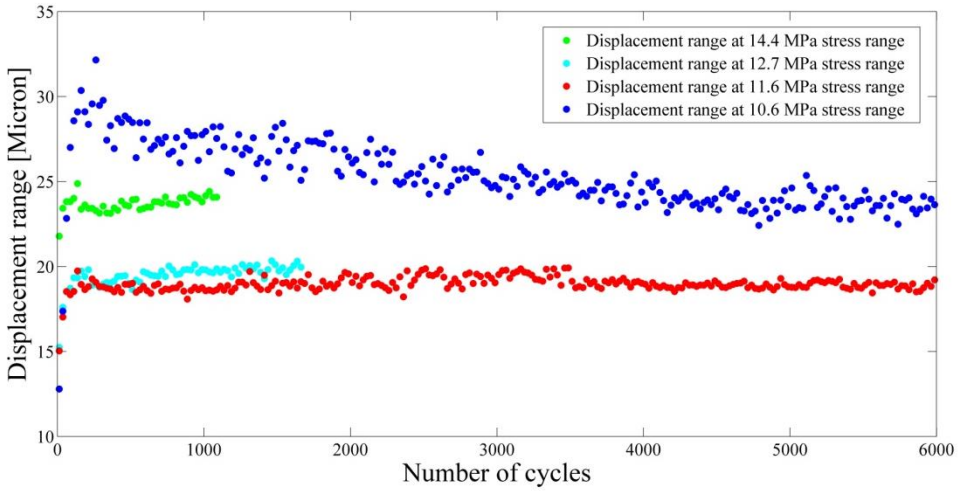

Figure 4.39: Displacement range evolution under load-controlled isothermal fatigue of lead-free (Sn-3.8Ag-0.7Cu) solder at 75°C (detail)

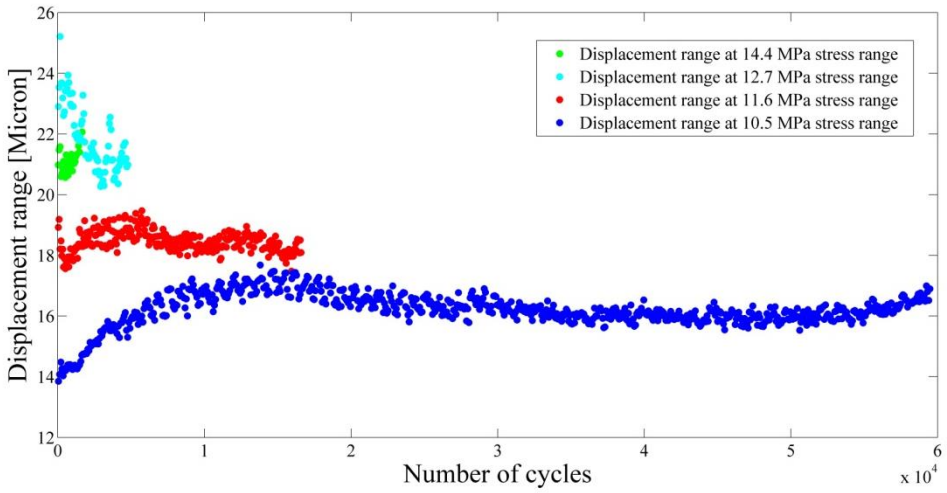

Figure 4.40: Displacement range evolution under load-controlled nIP fatigue of lead-free (Sn-3.8Ag-0.7Cu) solder

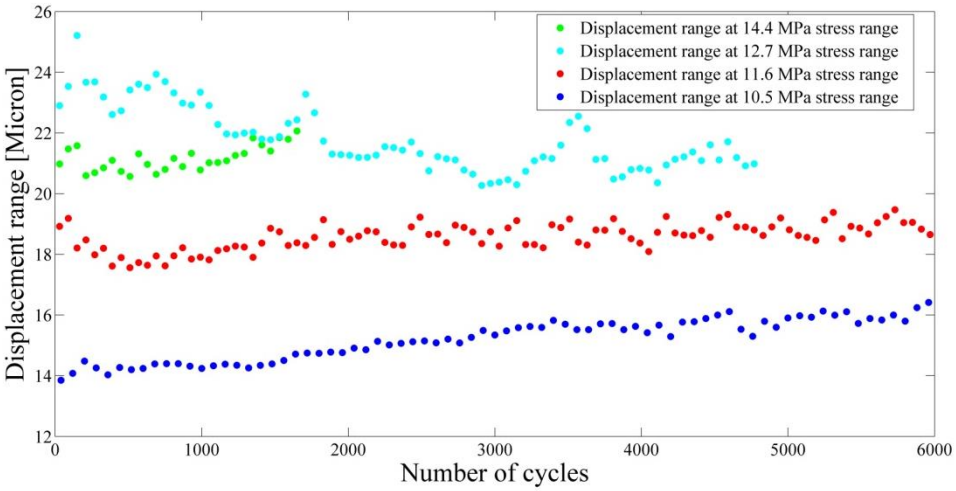

Figure 4.41: Displacement range evolution under load-controlled nIP fatigue of lead-free (Sn-3.8Ag-0.7Cu) solder (detail)

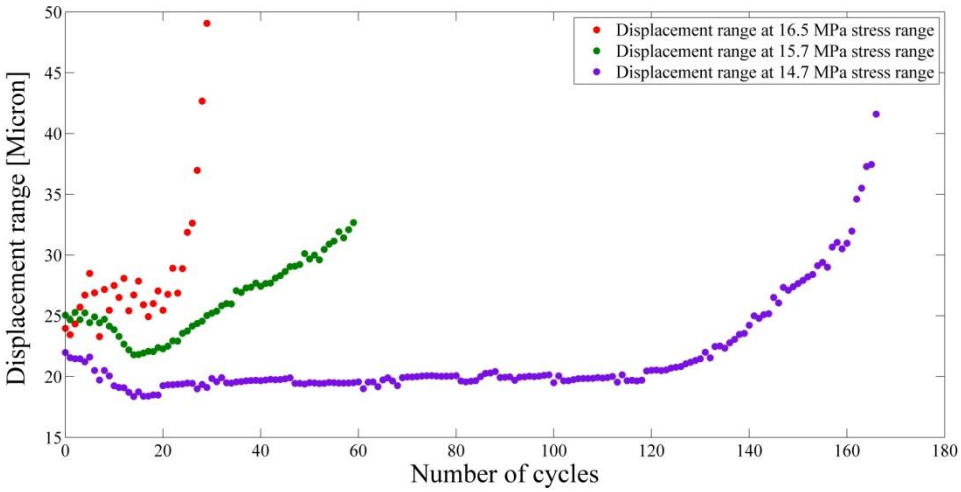

Figure 4.42: Displacement range evolution under load-controlled IP fatigue of lead-free (Sn-3.8Ag-0.7Cu) solder

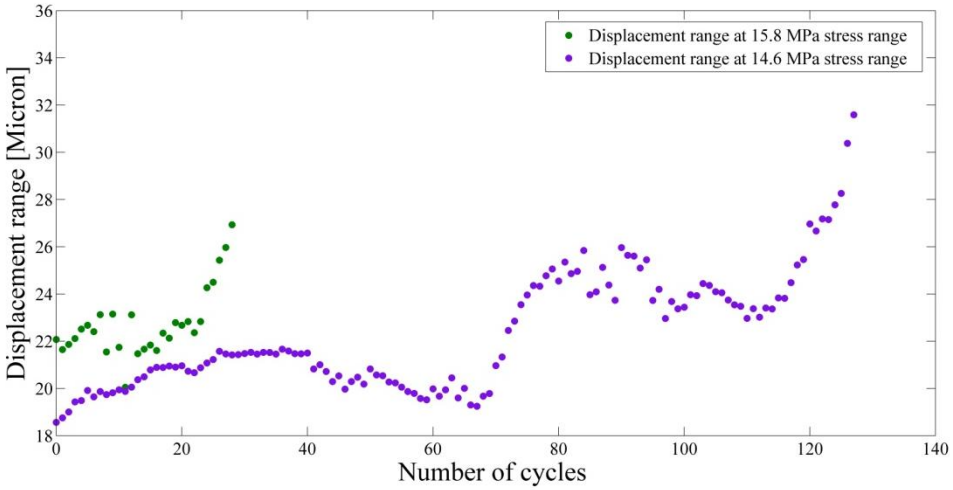

Figure 4.43: Displacement range evolution under load-controlled OoP fatigue of lead-free (Sn-3.8Ag-0.7Cu) solder

4.3.3 Summary of cyclic deformation behaviour

Table 4.3 summarises the cyclic deformation behaviour in all of the tests. As can be seen cyclic hardening is the exception, most tests resulting in continuous cyclic softening.

From the table given below, it has been concluded that by increasing the temperature for both alloys the average rate of hardening or softening per cycle will decrease. Also when stress range is increased the average rate per cycle will also increase. At the same level of stress the different alloys have different average rate per cycle. In most of the

cases at the same temperature and for same level of stress the Sn-Pb has higher average rate per cycle than SAC.

Table 4.3: Summary of cyclic deformation behaviour

Test / alloy	***S* [MPa]**	**Life [Cycle]**	**Pattern**	**Displacement range [μm]**			**Rate of hardening / softening [μm. cycle^{-1}]**
				Initial	***Mid-life***	***Final***	
Iso RT / SnPb	14.3	2300	H	23	22	21	-8.7×10^{-4}
	12.4	17970	H	18.5	15	14	-2.5×10^{-4}
	11.6	33860	H-S	18.5	15.8	17	-4.4×10^{-5}
	10.6	130600	N	8	8	8	0
Iso RT / SAC	14.3	6915	S	18.3	21	22	5.3×10^{-4}
	12.4	20680	H-S	14.4	13.4	15.5	5.3×10^{-5}
	11.6	42050	S	12.3	12.5	15.2	6.9×10^{-5}
	10.6	132800	N	9	9	9	0
Iso 35°C / SnPb	14.3	1328	S	25.3	28.6	29.3	3×10^{-3}
	12.4	4328	S	15.5	16.3	19.53	9.2×10^{-4}
	11.6	26240	S	12.2	14.7	16.6	1.6×10^{-4}
	10.6	118000	S	9.6	13	13.4	3.2×10^{-5}
Iso 35°C / SAC	14.3	2038	S	18	18.4	20.5	1.2×10^{-3}
	12.4	14210	H-S	15.3	14.8	15.4	7×10^{-6}
	11.6	29340	S	12.4	13.1	16.3	1.3×10^{-4}
	10.6	123800	S	9.7	10.5	11.4	1.3×10^{-5}
Iso 75°C / SnPb	14.3	326	S	18.1	25.2	25.5	2.2×10^{-2}
	12.4	1125	S	14.4	19.8	20.8	5.6×10^{-3}
	11.6	2414	S	10.5	29.5	32	8.9×10^{-3}
	10.6	9594	S	12.7	20.6	21.5	9.1×10^{-4}

Continued

Table 4.3: Summary of cyclic deformation behaviour

Iso 75°C / SAC	14.3	1175	S	21.7	23.4	24	1.9×10^{-3}
	12.4	1725	S	12.3	19.6	20.3	4.6×10^{-3}
	11.6	1040	S	15	18.7	19.5	4.3×10^{-3}
	10.6	51830	S-H	12.7	19.1	18	1.0×10^{-4}
nIP / SnPb	14.3	529	S	24.3	27	27.3	5.6×10^{-3}
	12.4	2008	S	17.7	19.6	20.9	1.5×10^{-3}
	11.6	5408	S	15.6	17.4	19.2	6.6×10^{-4}
	10.6	16640	S	16.7	20.1	20.2	2.0×10^{-4}
nIP / SAC	14.3	1798	S	20.9	21.1	22	6.1×10^{-4}
	12.4	4762	H	22.9	21.3	20.9	-4.1×10^{-4}
	11.6	19360	H	18.9	18.4	18	-4.6×10^{-5}
	10.6	62770	S	13.8	16.8	16.9	4.9×10^{-5}
IP / SnPb	16.5	13	S	32	35.8	38.5	5.0×10^{-1}
	15.7	30	H-S	25.8	24.9	26.9	3.0×10^{-2}
	14.7	65	S	21.4	22.3	33.9	1.9×10^{-1}
IP / SAC	16.5	35	S	23.9	26.7	49	7.0×10^{-1}
	15.7	66	S	25	25.4	32.6	1.2×10^{-1}
	14.7	172	H-S	21.9	20.2	41.6	1.1×10^{-1}
OoP/ SnPb	15.7	14	S	34	39	42	5.7×10^{-1}
	14.7	33	N-S	25	25	29.1	1.2×10^{-1}
OoP / SAC	15.7	37	H-S	22	21	26.9	1.3×10^{-1}
	14.7	136	S	18	19.6	31.5	9.9×10^{-2}

4.4 Long-term displacement behaviour (creep)

Solder joints experience interaction of fatigue and creep, during cyclic loading in service conditions. So the author decided to determine the values of creep activation energy from displacement drift under cyclic loading using experimental data at four test temperatures.

This section presents the results of the long-term trend mean displacement (described at the beginning of section 4.3) for leaded (Sn-37Pb) and lead-free (Sn-3.8Ag-0.7Cu) solder joints at room temperature, 35°C, 75°C, and 55°C.

4.4.1 Creep of leaded (Sn-37Pb) solder under shear loading

Figure 4.44 shows the 60-cycle mean displacement trend over the fatigue life of the three non-run-out isothermal room-temperature tests for the Sn-Pb alloy. The lowest stress range shows classical primary, secondary and tertiary creep stages, whereas, at higher stress ranges, the primary creep is shortened. The steady-state creep rate $\dot{\gamma}$ was obtained by numerically differentiating the curves and assessing the steady-state rate from the 7 points averaged slope by putting the best fit line through the visibly horizontal portion as shown in Figure 4.45.

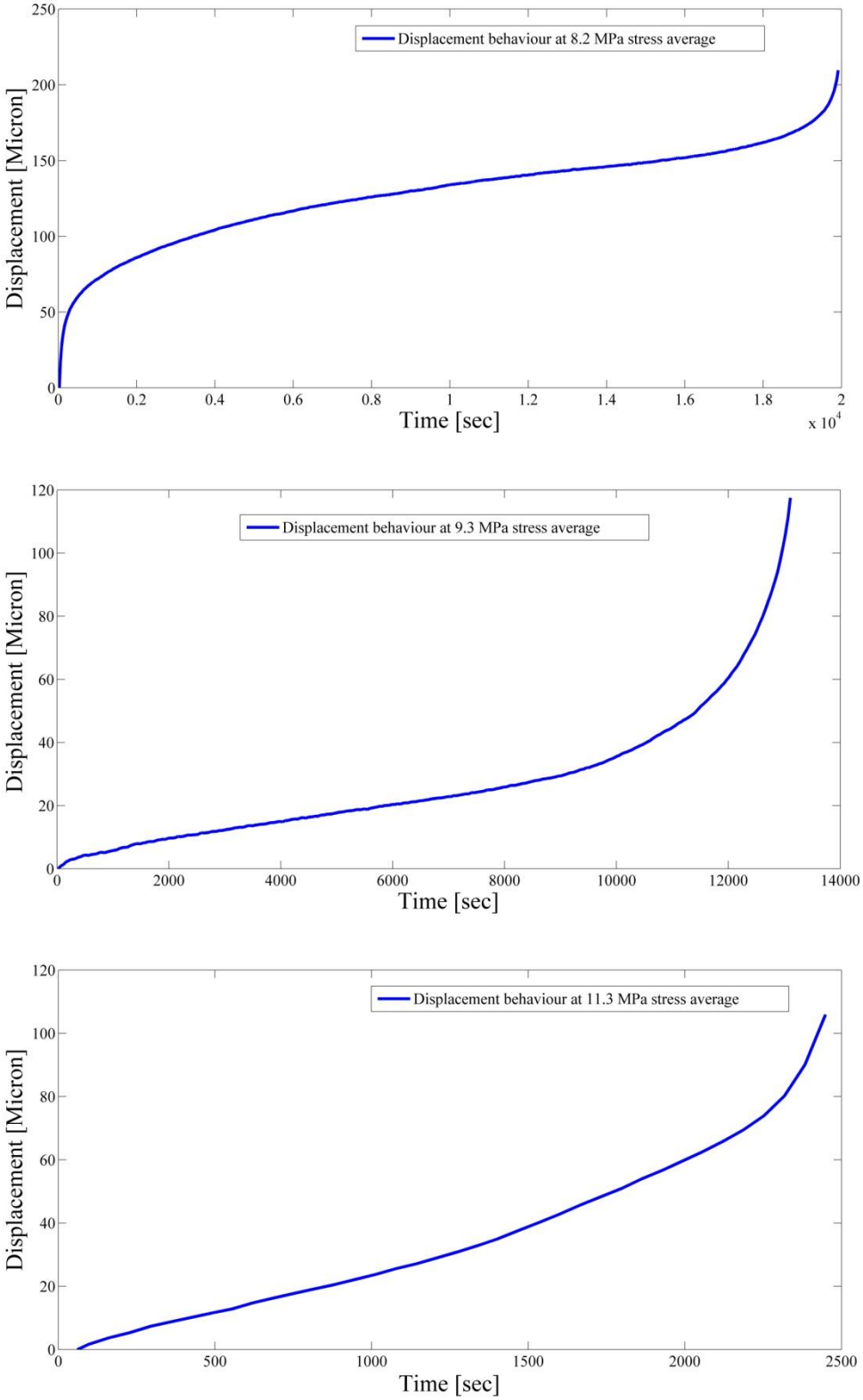

Figure 4.44: Trend in mean displacement of leaded (Sn-37Pb) solder specimens under isothermal fatigue loading at room temperature

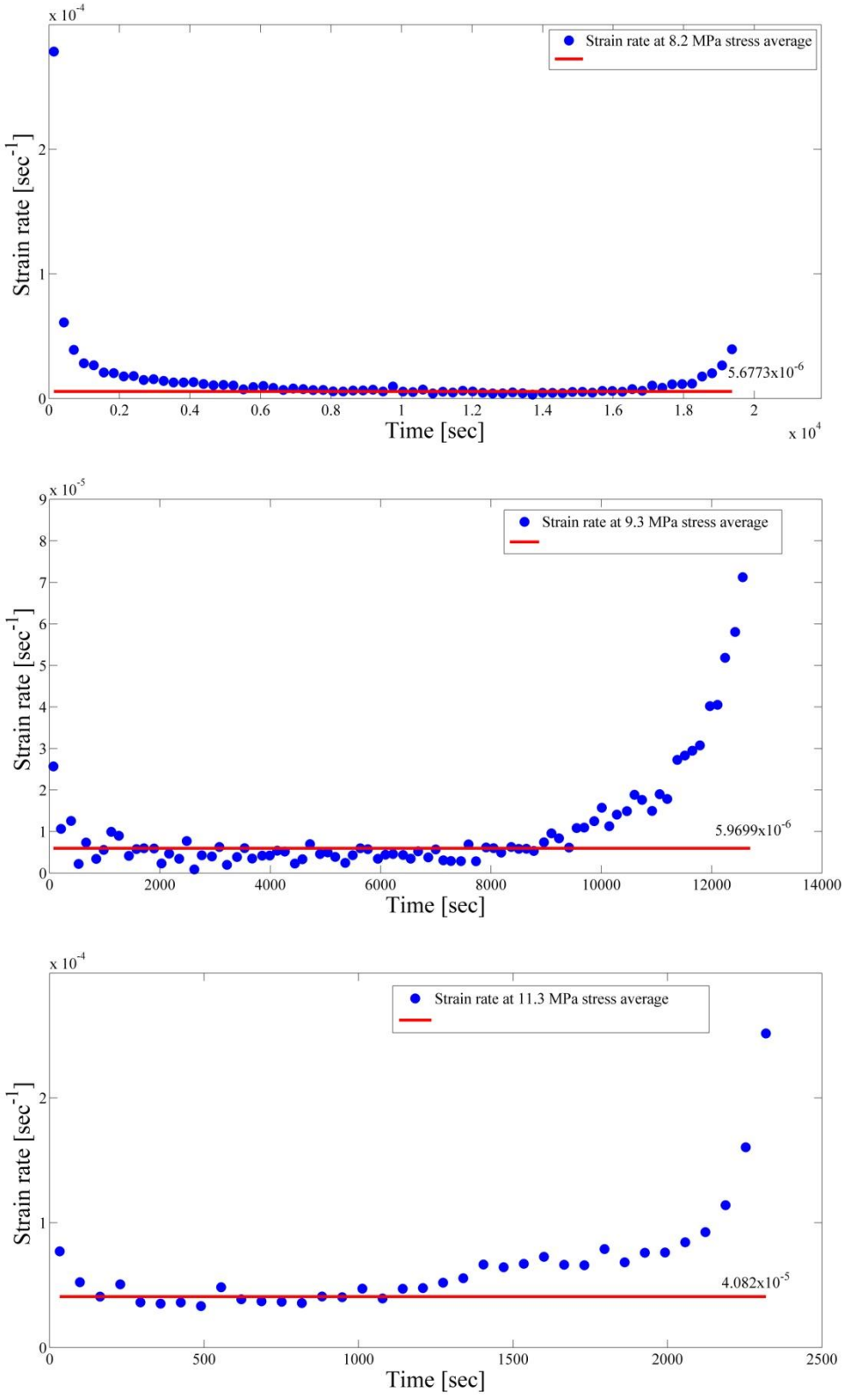

Figure 4.45: Trend in mean displacement rate of leaded (Sn-37Pb) solder specimens under isothermal fatigue loading at room temperature

The relationship between steady state creep rate and stress is often described by Norton's Law:

$$\dot{\gamma} = A\tau^n \qquad (4.3)$$

where:

A= constant, dependent upon temperature, given by

$A = A_0 e^{\frac{-Q}{RT}}$

n = creep/stress exponent

so that *A* and *n* can be determined by plotting $\log(\dot{\gamma})$ against $\log(\tau)$.

$$\log\dot{\gamma} = n\log\tau + \log A \qquad (4.4)$$

The best- fit lines yielding values of *n* (slope) and log*A* (intercept), as shown in Figure 4.46. At constant temperature, a value of creep or stress '*n*' exponent can determined, from the gradient of the line produced.

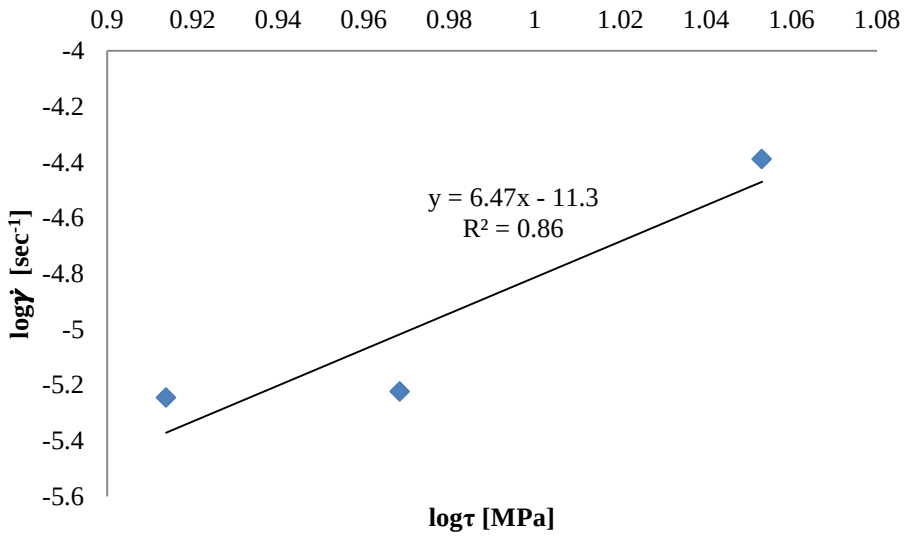

Figure 4.46: Determination of creep parameters A and n for leaded (Sn-37Pb) solder at room temperature

Not all of the creep curves were quite as conventional as the one shown above. For example, the mean displacement evolutions for isothermal testing of Sn-Pb at 35°C are shown in Figure 4.47 with the anomalous decreasing initial mean displacement at 8.2 MPa stress range being shown with a red question mark. This anomaly is tracked through the remaining analysis (Figures 4.47, 4.48 and 4.50), and does not appear to affect the bigger picture of determining the creep parameters.

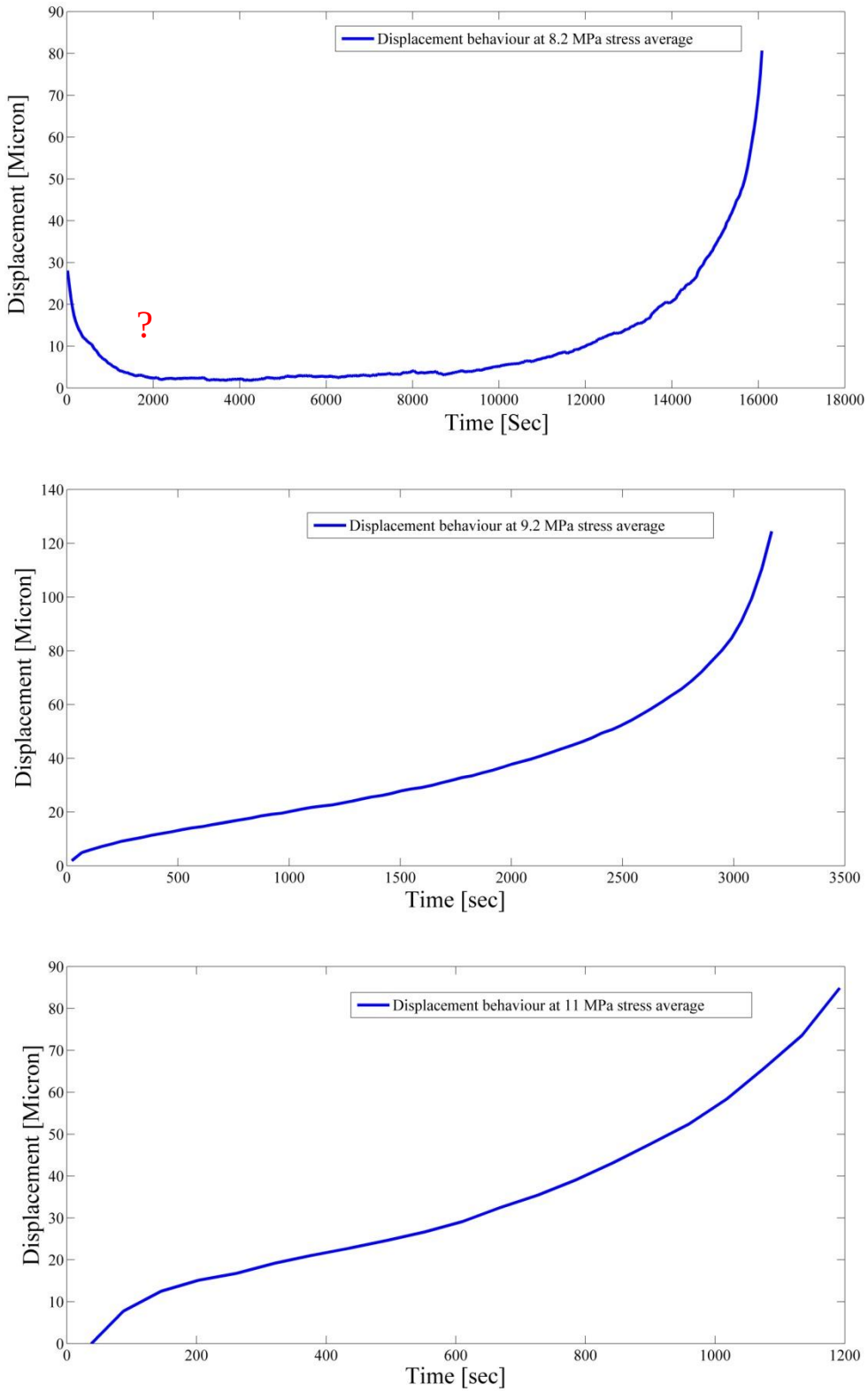

Figure 4.47: Trend in mean displacement of leaded (Sn-37Pb) solder specimens under isothermal fatigue loading at 35°C

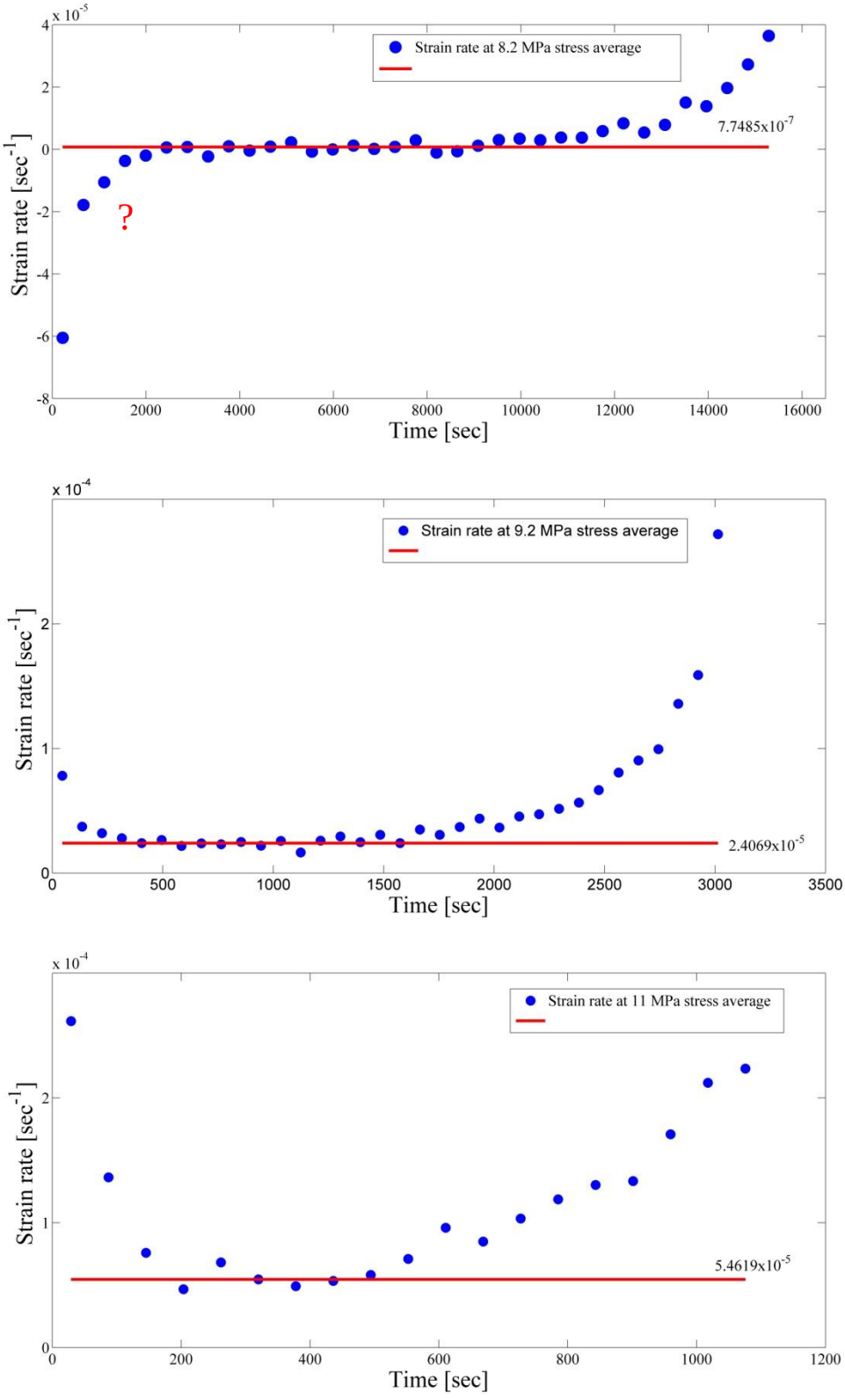

Figure 4.48: Trend in mean displacement rate of leaded (Sn-37Pb) solder specimens under isothermal fatigue loading at 35°C

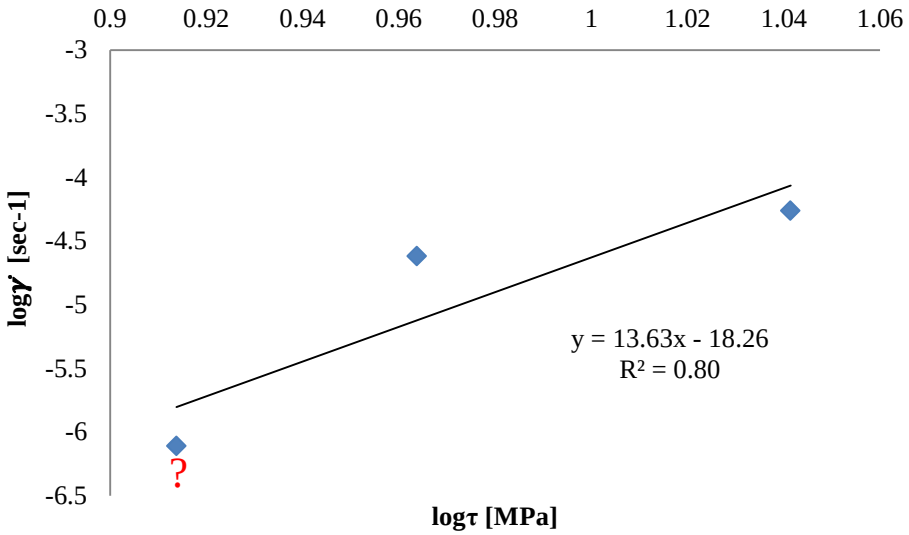

Figure 4.49: Determination of creep parameters A and n for leaded (Sn-37Pb) solder at 35°C

The remaining creep parameter estimations for Sn-Pb are shown in Figures 4.50 and 4.51 again with the points associated with any anomalous curves being highlighted with red question marks.

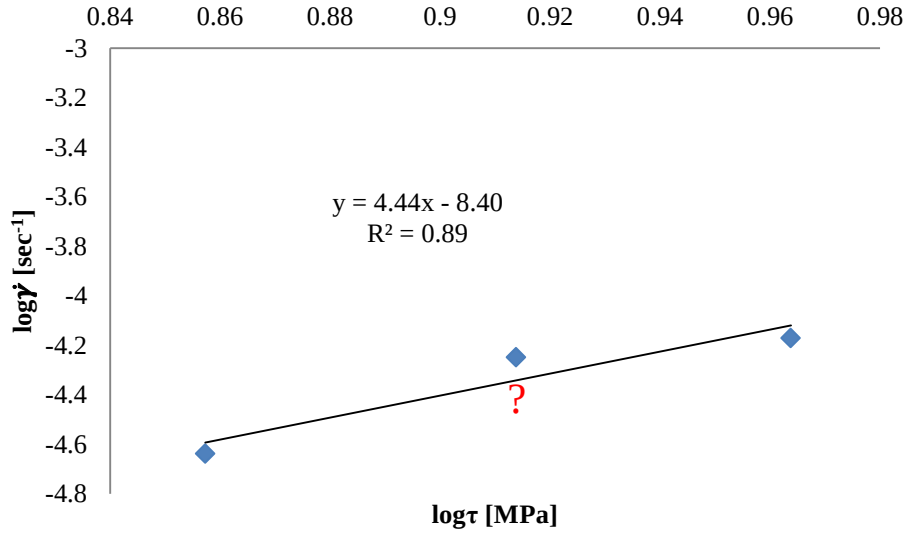

Figure 4.50: Determination of creep parameters A and n for leaded (Sn-37Pb) solder at 75°C

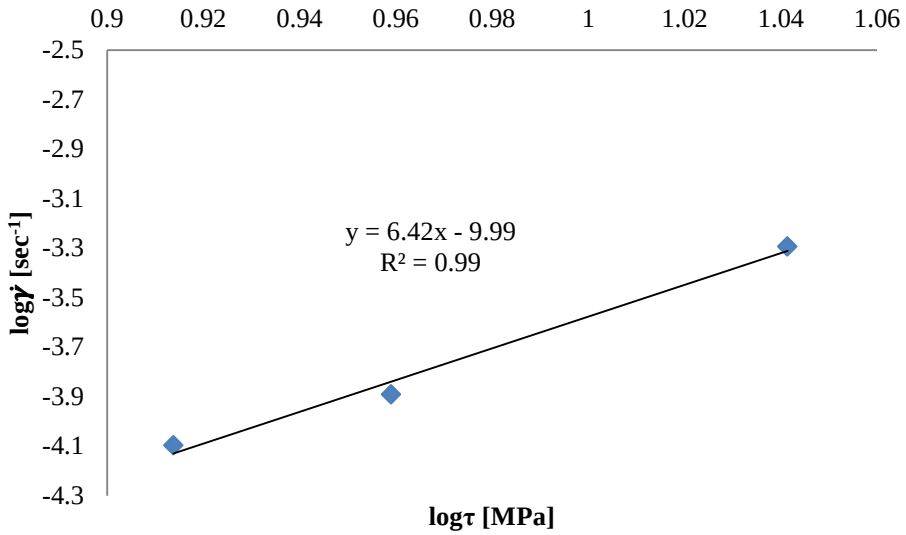

Figure 4.51: Determination of creep parameters A and n for leaded (Sn-37Pb) solder in nIP tests (i.e. at 55°C)

Table 4.4 summarises the values of *A* and *n* determined in the foregoing. As can be seen the values of *n* is not constant for all of the tests (as required from Norton's Law), the values at 35°C being particularly large, which can be traced to the anomalous point in Figure 4.52. The large value of *n* has a consequent effect on *A*, which is the result of a long extrapolation to the extent that the value of *A* at 35°C is well outside the expected sequence of increasing *A* with temperature. A similar, although less obvious, opposite effect might have occurred at 75°C. In order to avoid such error propagation in the determination of the activation energy for creep, *Q*, the values of *A* in Table 4.4 were not used to determine *Q*.

Table 4.4: Norton's Law parameters for leaded (Sn-37Pb) solder as determined from Equation 4.4

Temperature conditions	***n***	**log *A***	***A***
Room temperature	6.4704	-11.284	5.199×10^{-12}
35°C	13.63	-18.259	5.508×10^{-19}
55°C	6.416	-9.9928	1.0167×10^{-10}
75°C	4.4448	-8.4045	3.940×10^{-9}

As mentioned above, the creep rate increases exponentially with temperature according to the Arrhenius equation so the full relationship between steady state creep rate, stress and temperature is

$$\dot{\gamma} = A_0 \tau^n \exp\left(-Q/_{RT}\right) \tag{4.5}$$

Q = activation energy

n = stress exponent

A_0= constant

R= Universal Gas Constant, 8.314 J/mole.K

T = absolute temperature, (K)

This equation can be rearranged into the form:

$$log\dot{\gamma} = logA + nlog\tau - \left(Q/_{RT}\right) \tag{4.6}$$

The relevant Arrhenius plots are shown in Figure 4.52 and, clearly, there is some variation in the (supposedly constant) value of Q, although this is less severe than for n. Given this latter point, the weighted mean value of Q was calculated using the R^2 values:

$$\frac{Q}{R} = \frac{3731.8 \times 0.9378 + 2273.2 \times 0.6968 + 3298.5 \times 0.5616}{0.9378 + 0.6968 + 0.5616} = 3158.221$$

giving a final value of Q = 26.25 kJ/mol.

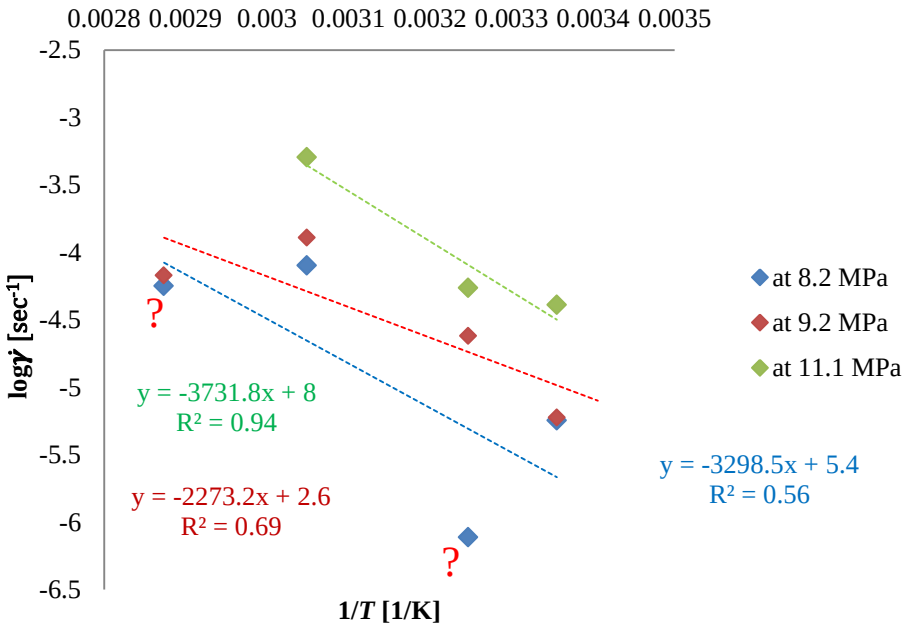

Figure 4.52: Determination of activation energy for leaded (Sn-37Pb) solder under shear loading

4.4.2 Creep of lead-free (Sn-3.8Ag-0.7Cu) solder under shear loading

Figures 4.53, 4.54, 4.55 and 4.56 show the determination of the Norton parameters for the lead-free solder at RT, 35°C, 75°C and 55°C, respectively. As can be seen, there are relatively few anomalous points, and the fit is rather better than for the leaded solder.

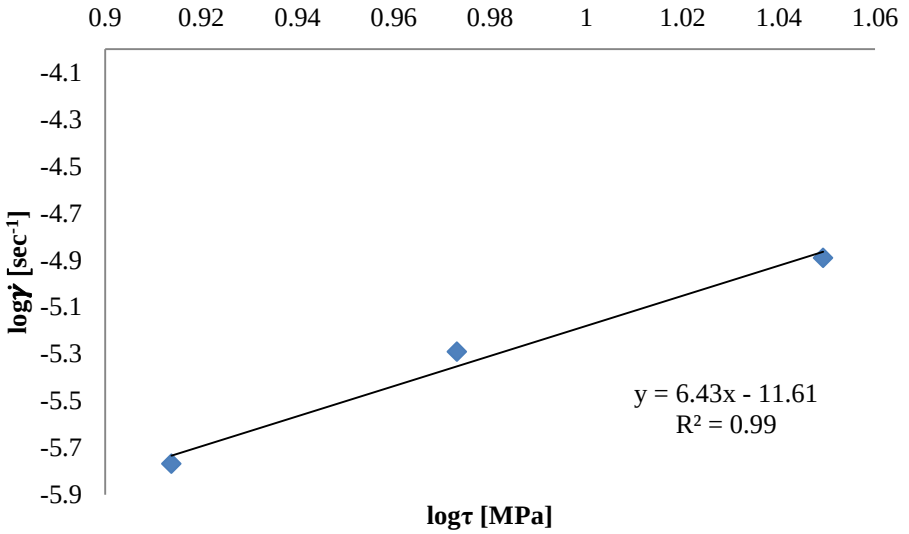

Figure 4.53: Determination of creep parameters A and n for lead-free (Sn-3.8Ag-0.7Cu) solder at room temperature

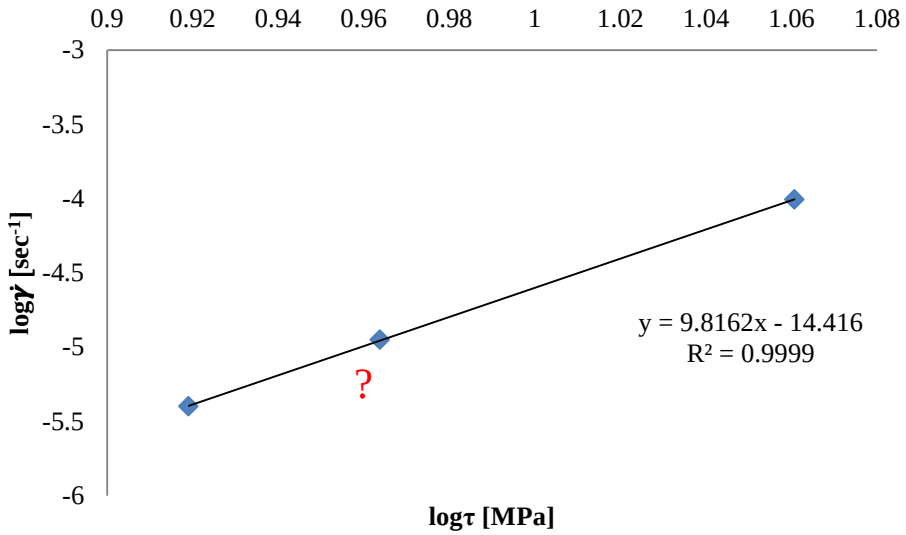

Figure 4.54: Determination of creep parameters A and n for lead-free (Sn-3.8Ag-0.7Cu) solder at room temperature at 35°C

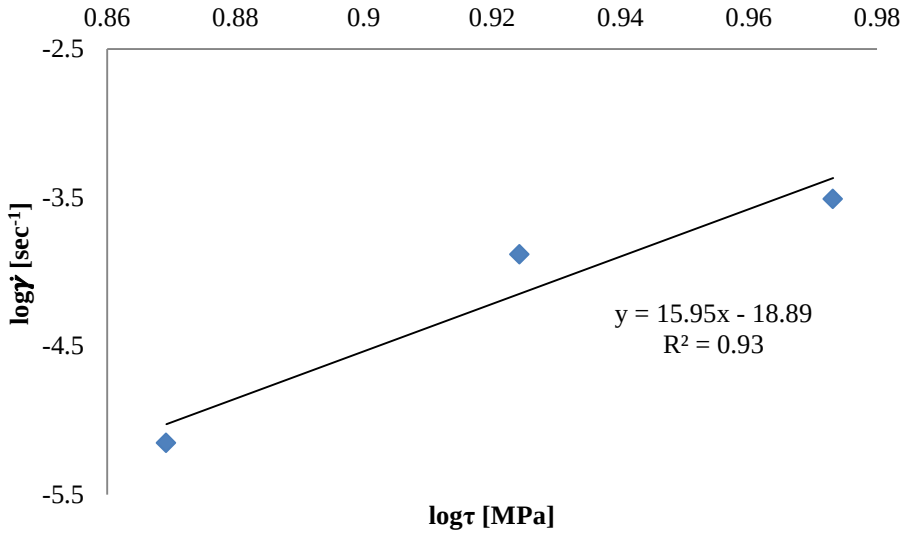

Figure 4.55: Determination of creep parameters A and n for lead-free (Sn-3.8Ag-0.7Cu) solder at room temperature at 75°C

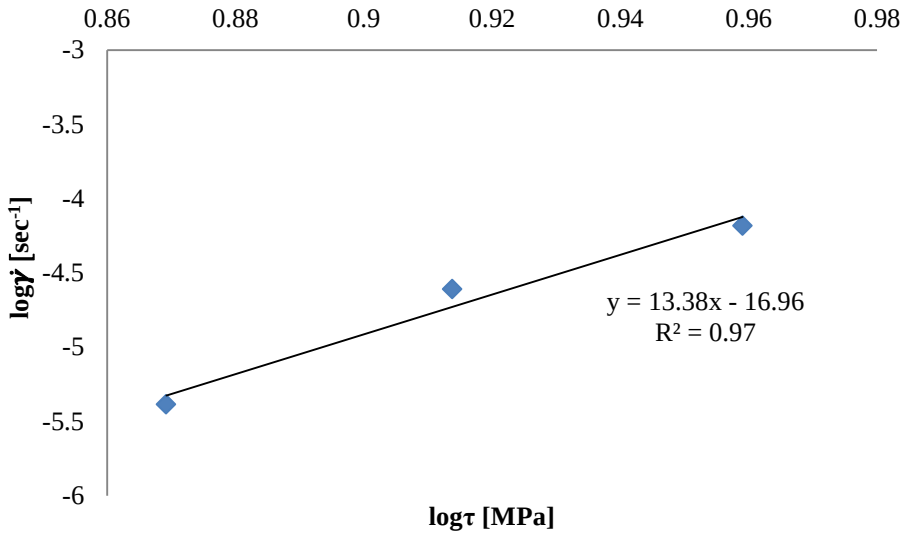

Figure 4.56: Determination of creep parameters A and n for lead-free (Sn-3.8Ag-0.7Cu) solder at room temperature at 55°C

The parameters are summarised in Table 4.5 and, as can be seen, the values of *n* increase with temperature and the effect of this is that the extrapolated value of *A* decrease with increasing temperature, contrary to what is expected.

Table 4.5: Norton's Law parameters for lead-free (Sn-3.8Ag-0.7Cu) solder as determined using Equation 4.4

Temperature condition	***n***	**log *A***	***A***
Room temperature	6.4294	-11.61	2.454×10^{-12}
35°C	9.8162	-14.416	3.837×10^{-15}
55°C	13.381	-16.956	1.106×10^{-17}
75°C	15.951	-18.892	1.282×10^{-19}

Again, the value of *Q* was obtained using an Arrhenius plot for each of the temperatures (Figure 4.57) and the weighted mean average (using the R^2 values) was found to be Q = 28.08 kJ/mol.

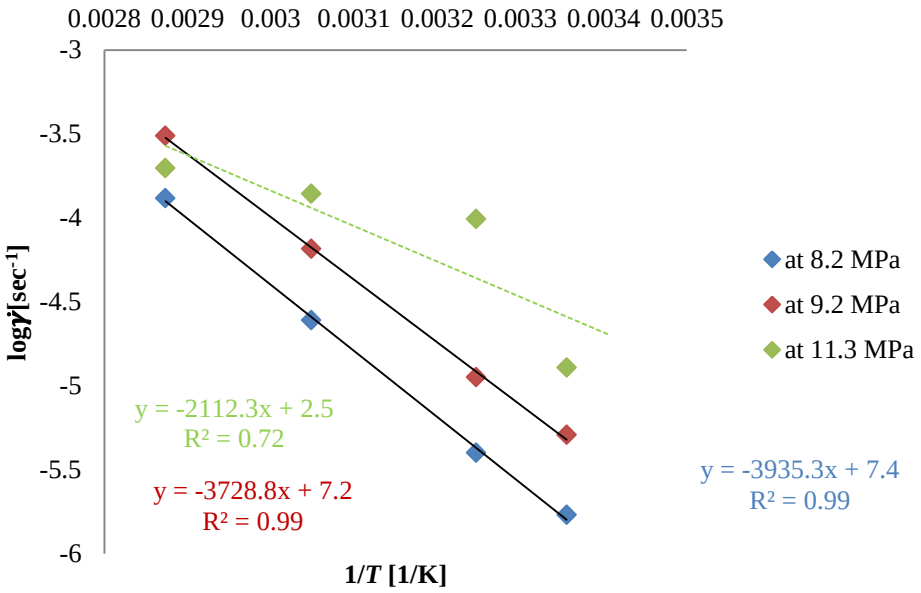

Figure 4.57: Diagram showing the determination of activation energy for lead-free (Sn-3.8Ag-0.7Cu) solder joint under shear loading (measured from derivation of the strain versus times curves)

4.4.3 Summary of creep measurements

The following main observations can be made:

- For lead-free solder joints, the creep exponent *n* (using Norton's law) increased monotonically with increasing temperature, whereas its behaviour was somewhat erratic for the leaded solder, with one clearly anomalous value. In both alloys, the extrapolated values of *A* were unreliable for determining the activation energy.
- Values of the creep activation energy for lead-free solder joints are greater than for leaded, meaning that they are more resistant to thermal softening.
- Neither set of steady-state data were fully accounted for by Norton's Law, which may be partly due to individual anomalous samples, or it may simply be (as is likely for the lead-free solder) that a different creep law is required to explain the behaviour. Certainly, in many cases, the steady state component was a relatively small proportion of the overall creep.

Chapter 5: Macrostructure and Microstructure Characterisation

This chapter is concerned with the results of the microscopic and mechanical characterisation of the solder joints, including the ageing tests. It is divided into sections on; macrostructure characterisation (including the solder ball shape and radius of curvature), fracture surface characterisation, micro hardness testing and microstructure characterisation of both leaded and lead-free solder balls before and after ageing.

5.1 Macrostructure characterisation

A number of tests were done to provide a semi-quantitative assessment of the detailed shape and consistency of the solder balls. The results of these are described below in terms of what they indicate about the likely variation in shear stress from the nominal value of force divided by the maximum spherical cross-sectional area.

5.1.1 Ball shape

It was possible to assess the ball size and shape roughly by examining the gap between substrate plates, Figure 5.1. As can be seen, the solder ball diameter was reasonably consistent in the as-reflowed initial condition.

It was also possible to examine a limited number of ball cross-sections under the SEM and these are shown in Figure 5.2. These sections were used to assess the radius of curvature at the contact between solder and substrate as well as the width of the ball at the contact plane as well as the height. Figures 5.3 to 5.6 show the measurements indicated in Figure 5.2 in histogram form. Although there are no published data for stress concentration factors for shear, a combination of values for bending and torsion [297], would indicate that local stress could be around twice the nominal stress at the substrate plane. Also, the nominal stress at the substrate plane can be expected to be somewhat larger than the indicative value based on 700 μm diameter pads. The variation from the expected height of 600 μm affects the conversion of displacement to strain and, also, a non-uniform height can introduce additional bending moments at the solder balls.

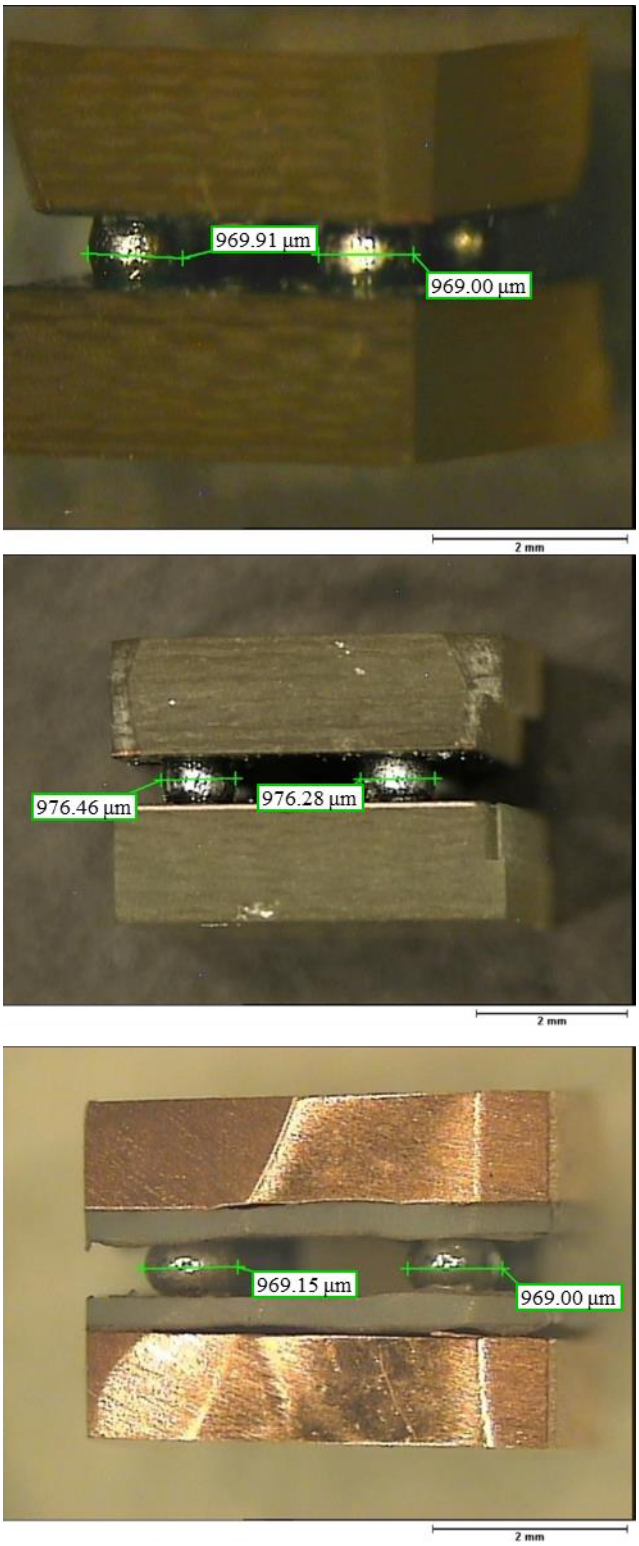

Figure 5.1: Typical 4 ball BGA test - pieces in as- reflowed condition showing diameter assessment (scale bars 2mm)

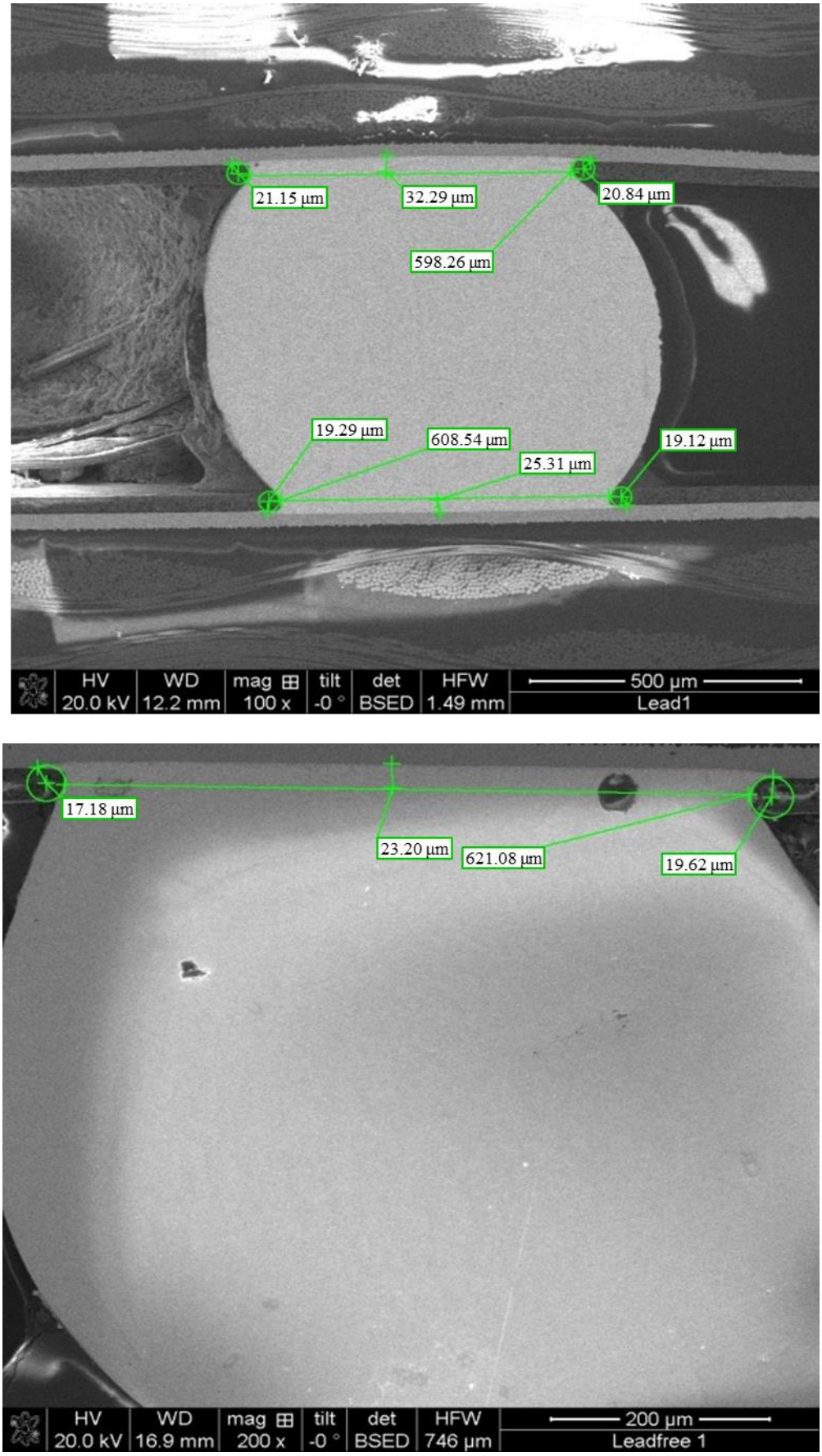

Figure 5.2: Measurements of the radius of curvature, height and width of solder balls

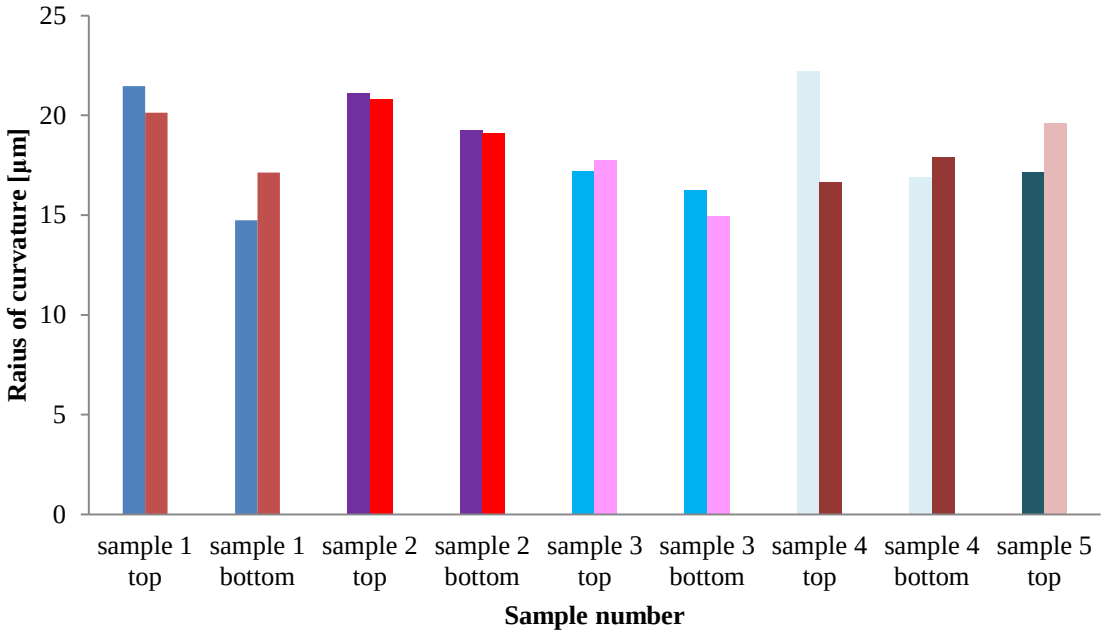

Figure 5.3: Summary of the radius of curvature measurement obtained using different samples

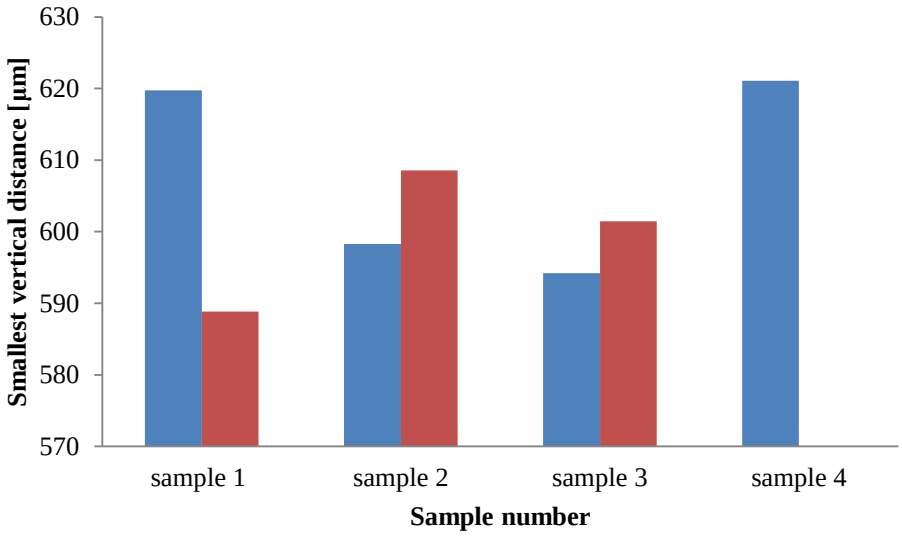

Figure 5.4: Summary of the smallest horizontal measurement obtained using different samples

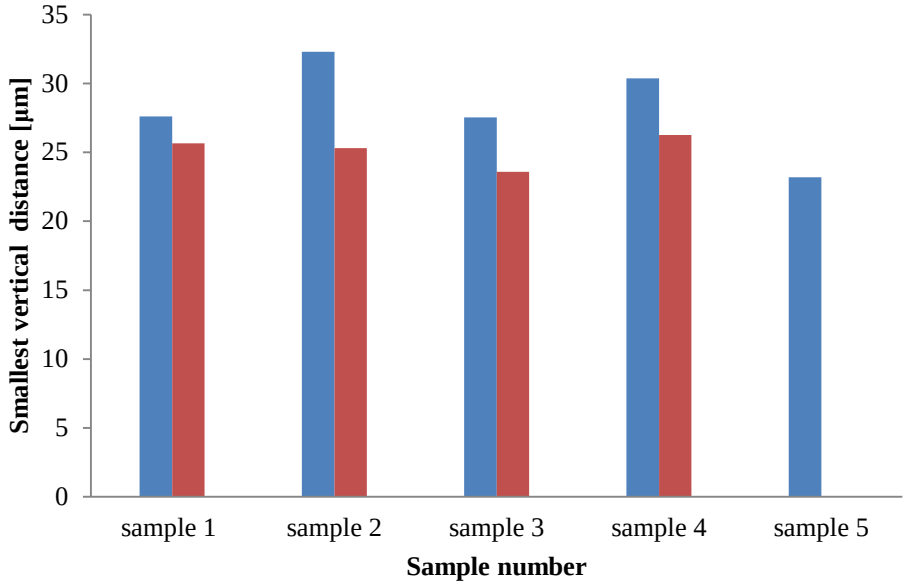

Figure 5.5: Summary of the smallest vertical distance between substrate and the smallest width of solder balls measurement obtained using different samples

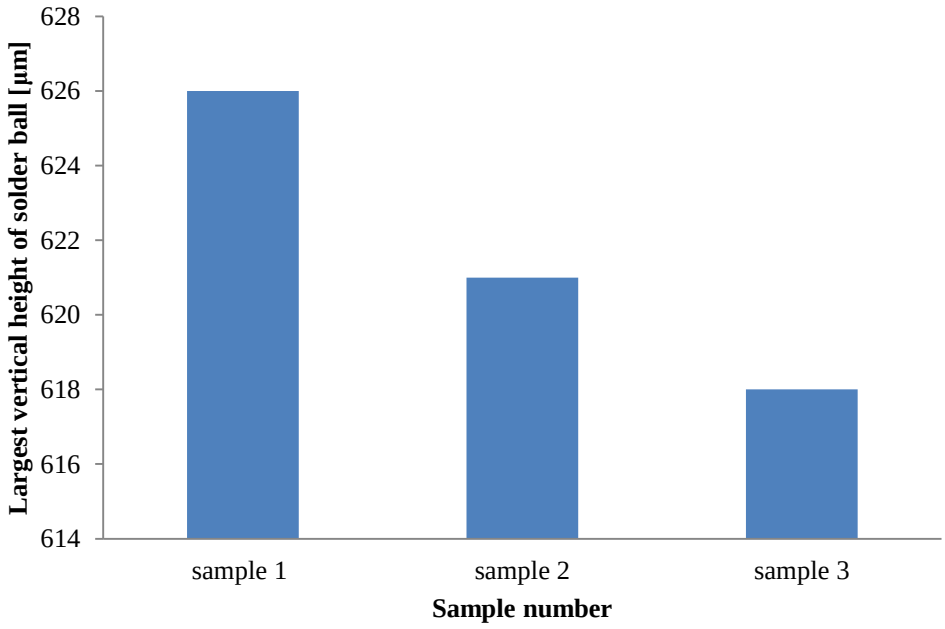

Figure 5.6: Summary of the largest vertical height of solder ball measurement obtained using different samples

5.1.2 Voids

Voids are generally thought of as an assembly defect which may actually benefit solder joints by slowing the crack progression by blunting and keeping the path in the ductile solder rather than allowing the faster growth at the IMC / solder interface. The blunting effect of voids gives initiated cracks a place to terminate and allows dislocations generated in the interconnect neck a free surface at which to annihilate [298].

As is shown in Figure 5.7 the number of voids in the sectioned samples was quite limited. Figure 5.8 shows examples of voids found on the fracture surface after testing. The effect of voids on the stress can be calculated using the normalized void area:

$$\frac{\sum A_v}{A} \qquad (5.1)$$

where:

A_v = void area [μm^2]

A= contact surface [μm^2]

and, overall, the normalized void area at the fracture surface on the samples viewed was about 1%. 40% of fatigued samples were examined.

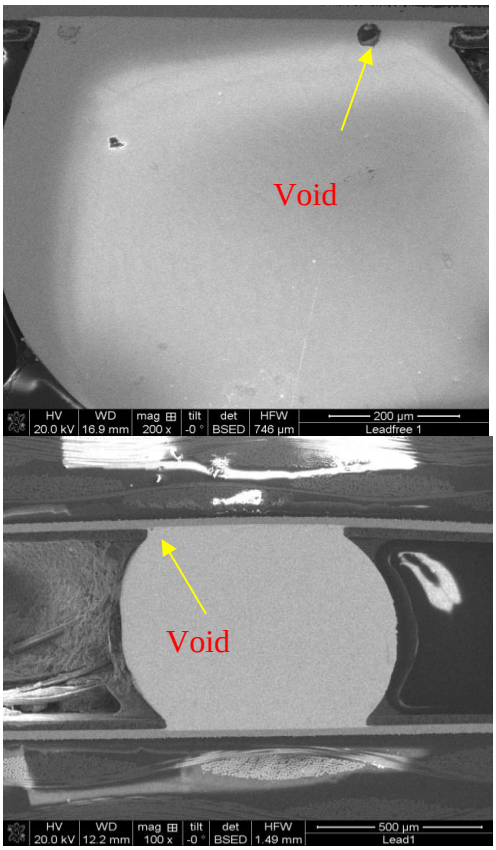

Figure 5.7: Voids observed in sections of as- reflowed assemblies which had not been loaded

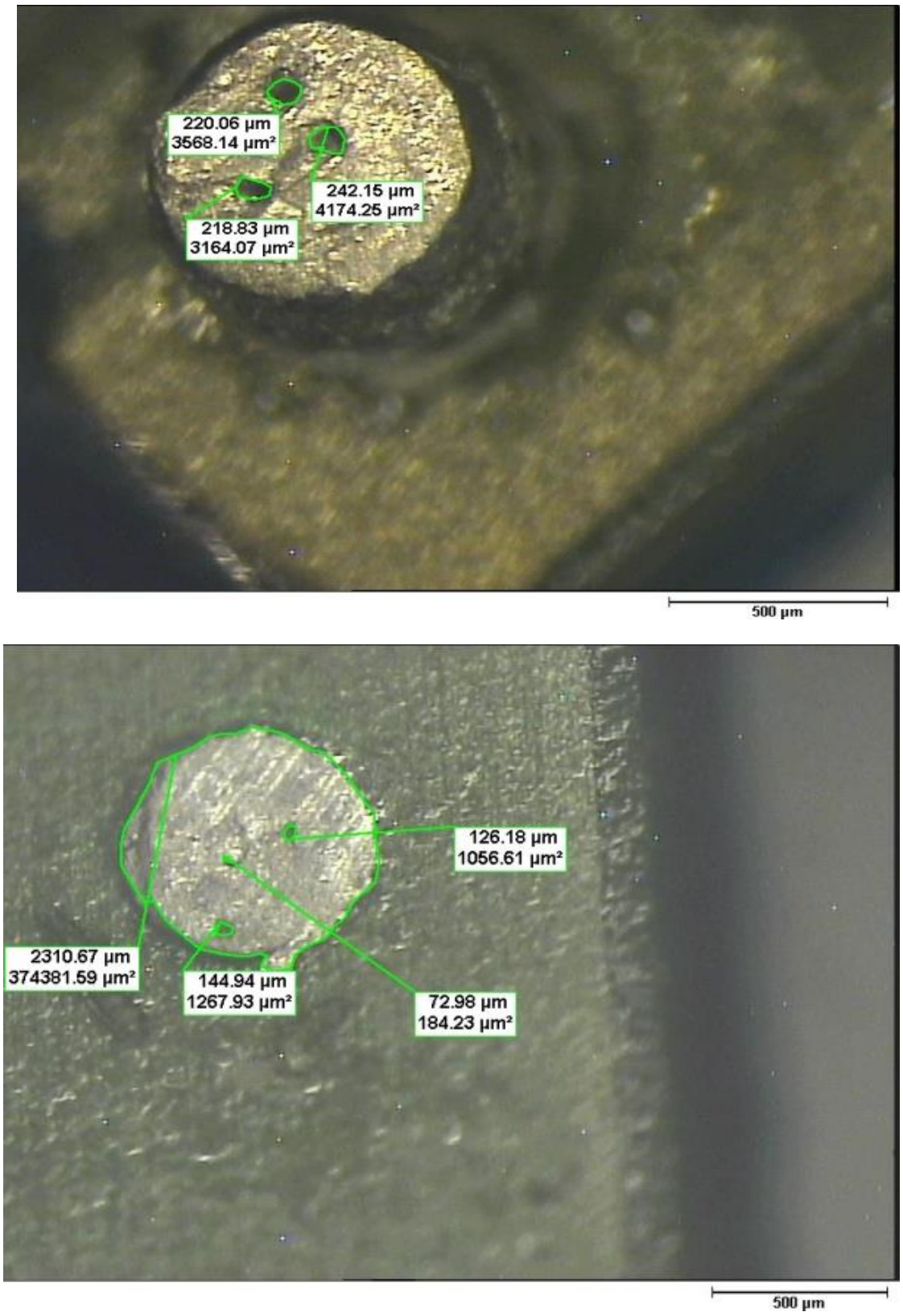

Figure 5.8: Voids observed on fracture surfaces after fatigue testing

5.2 Fractographic observations

A representative fracture surface of a fatigued solder ball is shown in Figure 5.9. Most specimens showed a smeared fracture surface due to failure by shearing through the solder matrix, which can be noted from the spherical dimples present in the solder. In general, the joints failed at the point of highest stress, which as might be expected, is the plane of smallest diameter, influenced by the stress concentration at the fillet and the behaviour of the rest of the balls in the assembly.

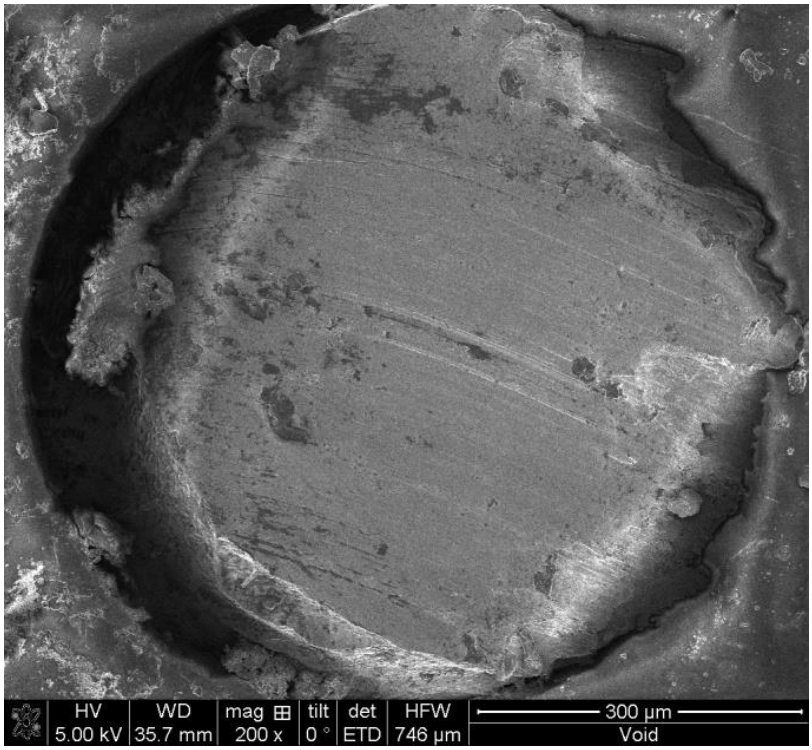

Figure 5.9: Fracture surface of a fatigued solder ball

To determine the location at which the shearing crack occurred, the height of solder left on the substrate was measured as shown in Figure 5.10. The measured height of solder projecting above the substrate ranged from about 15 to 68 µm the relevant location being represented in Figure 5.11.

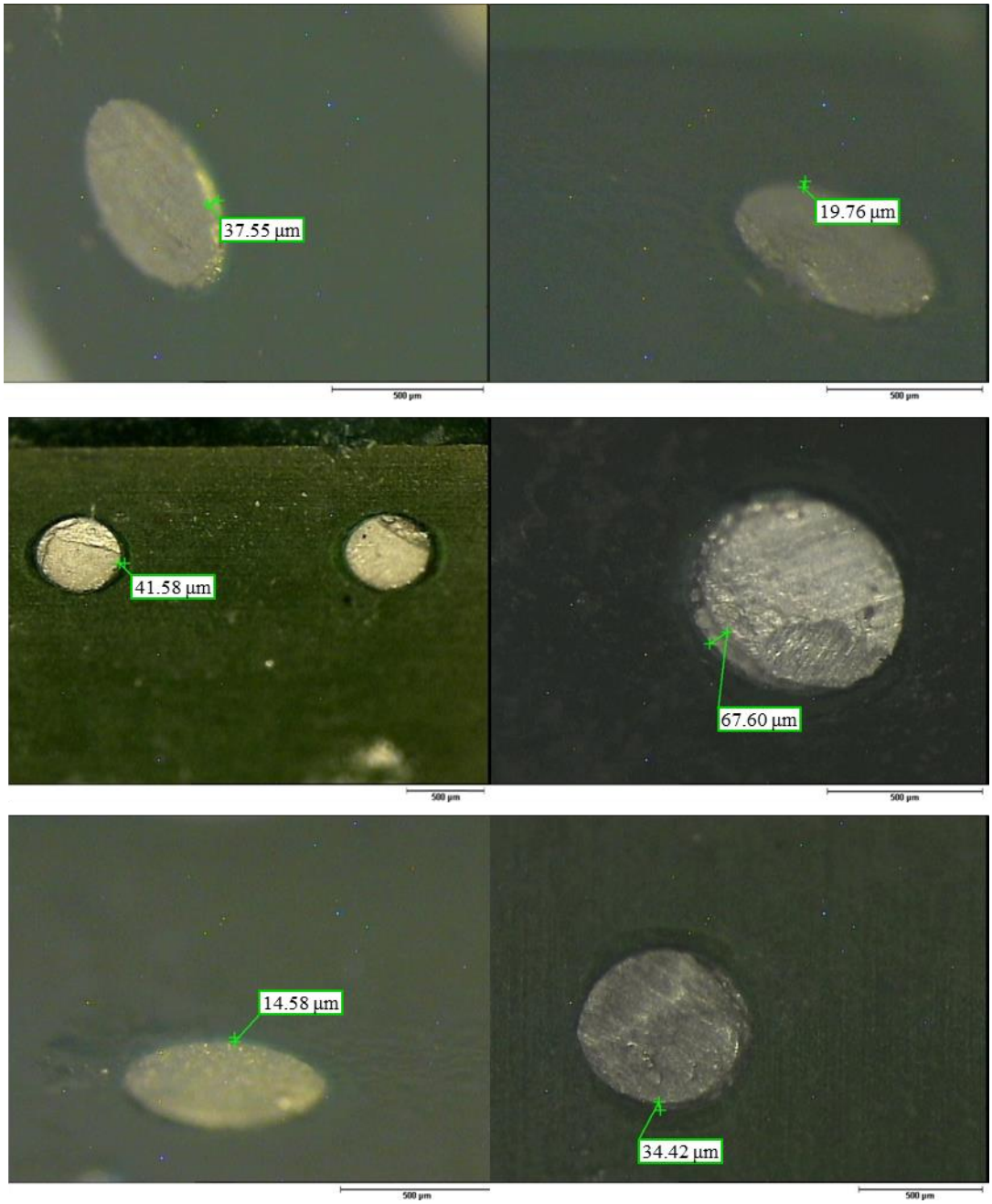

Figure 5.10 Heights of solder projecting above substrate after fatigue failure (scale bars 500 µm)

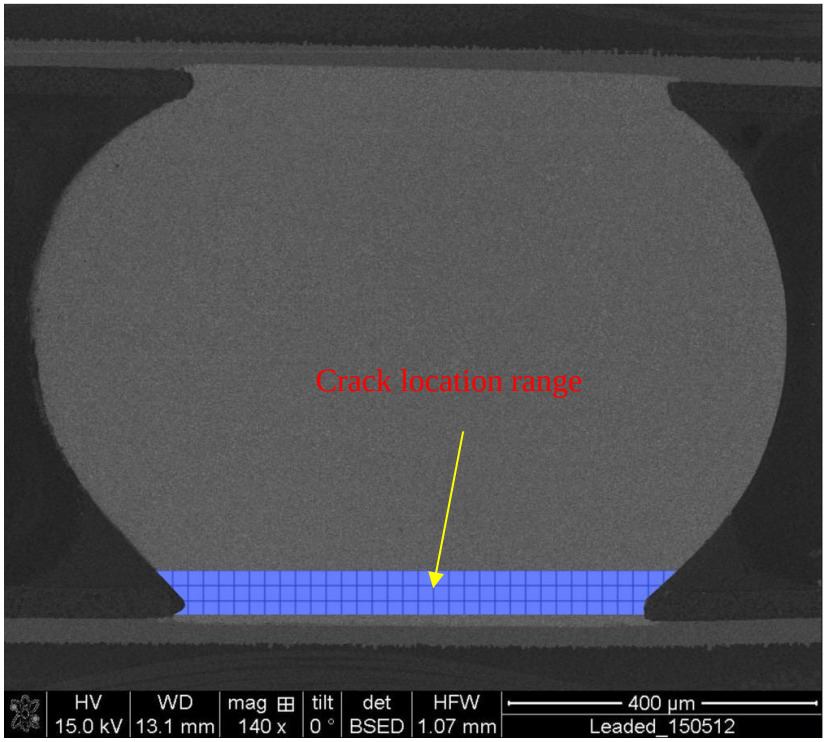

Figure 5.11: Cross-sectional image of specimen in as- reflowed condition showing the range of locations in which cracks were observed in fatigued specimens

5.3 Micro hardness measurements

Table 5.1 summarises the 60 or so micro hardness measurements take on each alloy in each conditions and shows the overall change in hardness resulting from the 10 hours ageing exposure at 80°C. Both alloys show a decrease in hardness after ageing, with the hardness of the leaded alloy decreasing by about 6% and that of the lead-free alloy by about 12%.

Table 5.1: Hardness values before and after ageing

Alloy	**Hardness [HV]**	
	Before ageing	**After ageing**
Sn-37Pb	12.6±0.4	11.9±0.5
Sn-3.8Ag-0.7Cu	17.0±0.5	14.9±0.9

Because the variation in measured hardness was a significant proportion of the change on ageing, it was important to assess the hardness distribution across the ball cross

section. Figure 5.12 shows sample indentations for each condition and shows that the variation in hardness has no particular pattern across a given solder ball.

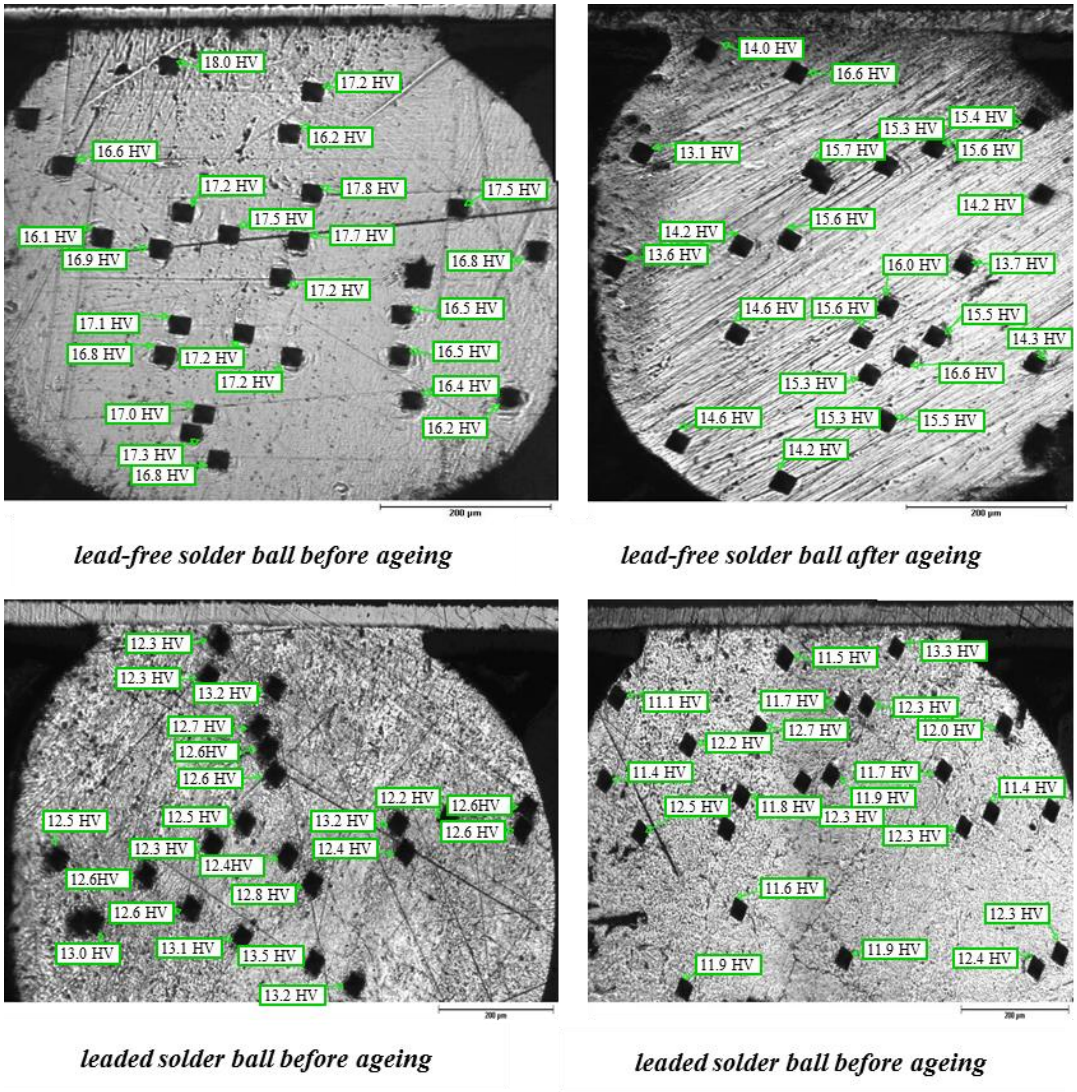

Figure 5.12: Optical micrographs showing the indentation maps in solder balls (scale bars 200 µm)

Figures 5.13 and 5.14 show histograms of the hardness before and after ageing for the lead-free solder and the leaded solder, respectively. It is clear that the hardness of both solders decreases after the ageing.

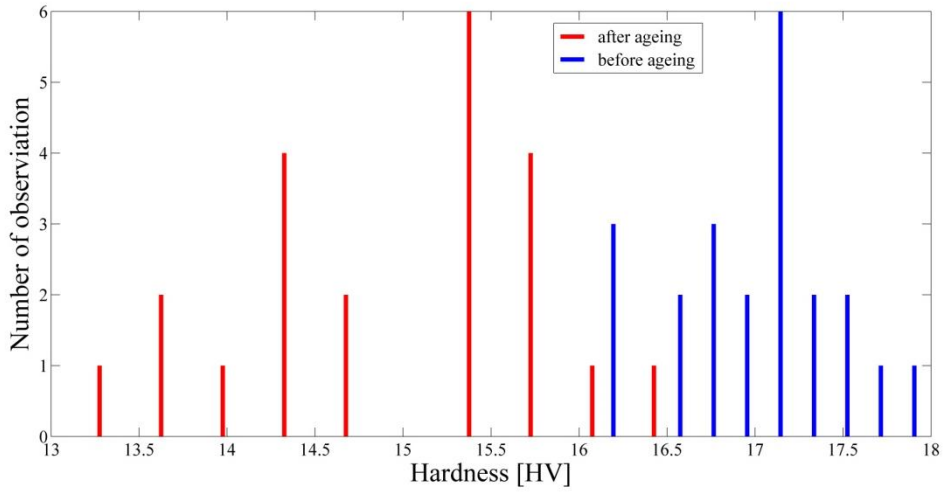

Figure 5.13: Histogram of lead -free solder hardness before and after ageing

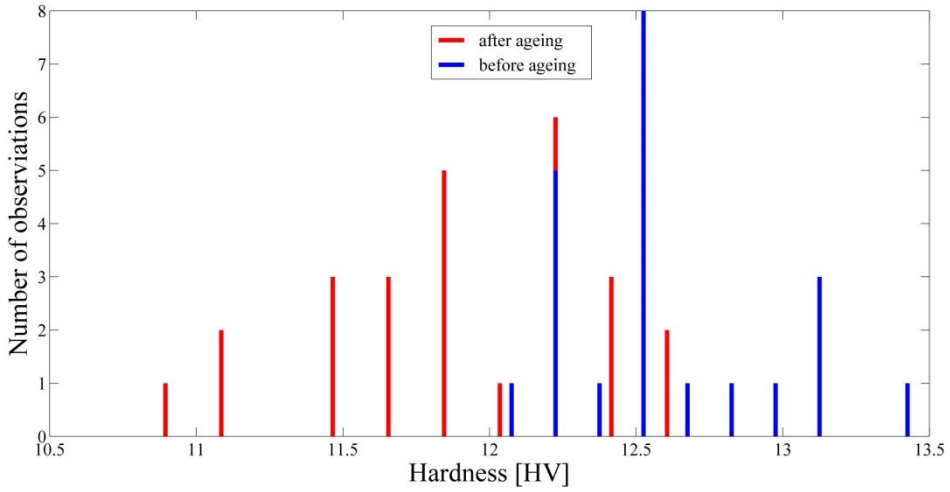

Figure 5.14: Histogram of leaded solder hardness before and after ageing.

5.4 Microstructure characterisation

Having established that there is a change in hardness of both alloys on ageing, it might be expected that this would be reflected in changes in microstructure, specifically, the morphology, size, and distribution of the constituent phases in a metallic system. This section aims to quantify these changes on the basis of quantitative examination of representative micrographs of both alloys.

5.4.1 Microstructural characterisation of leaded solder

Figures 5.15 and 5.16 show representative back-scattered scanning electron micrographs of the un-etched leaded solder before and after ageing. The structure consists of a relatively homogeneous distribution of the lead-rich phase (light areas) in a darker matrix of the tin-rich phase. It is evident that there is significant coarsening of the lead-phase grains, although it is difficult to assess whether or not the volume fraction has changed.

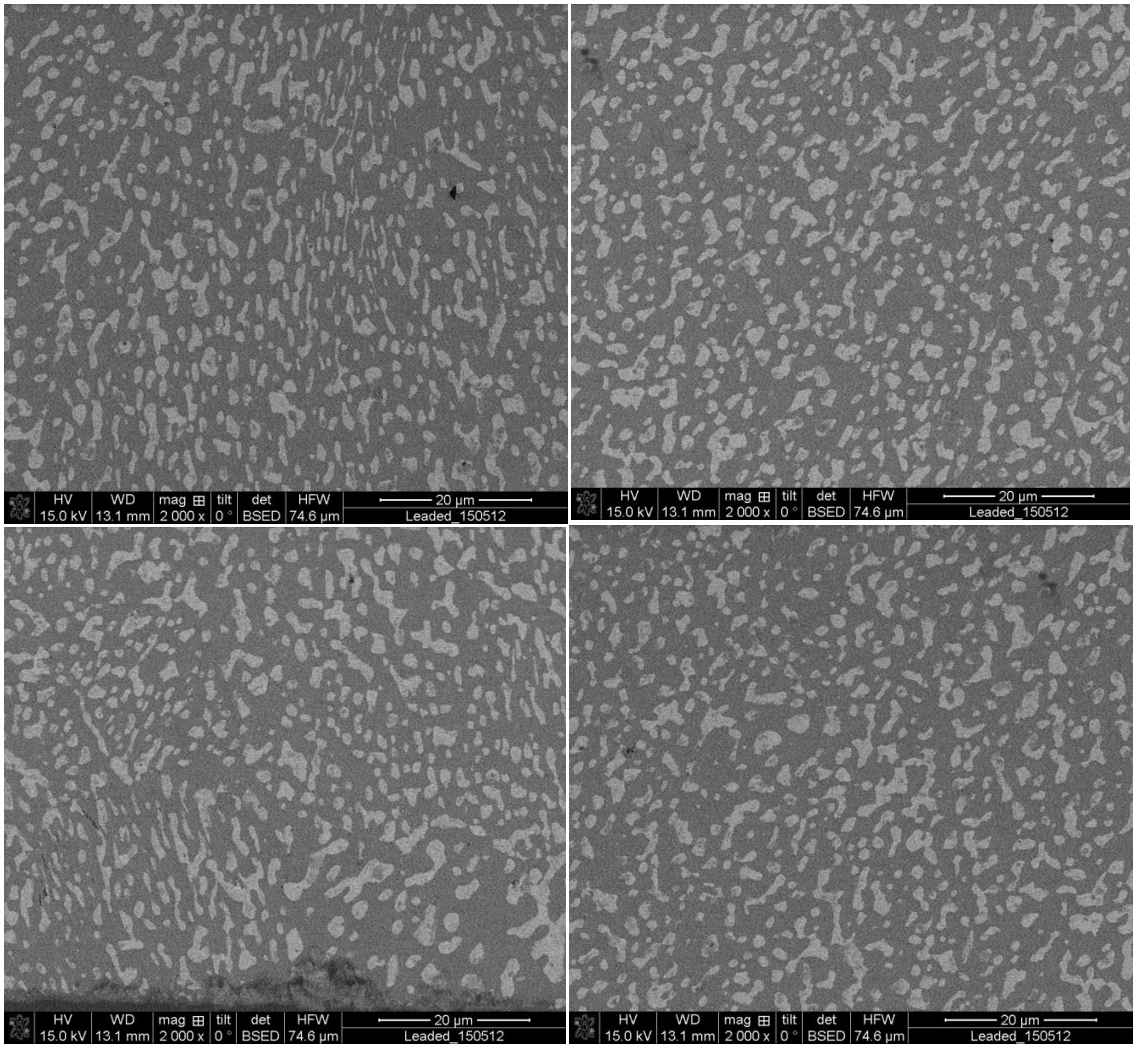

Figure 5.15: Back-scatter SEM images of eutectic (Sn-37Pb) solder before ageing

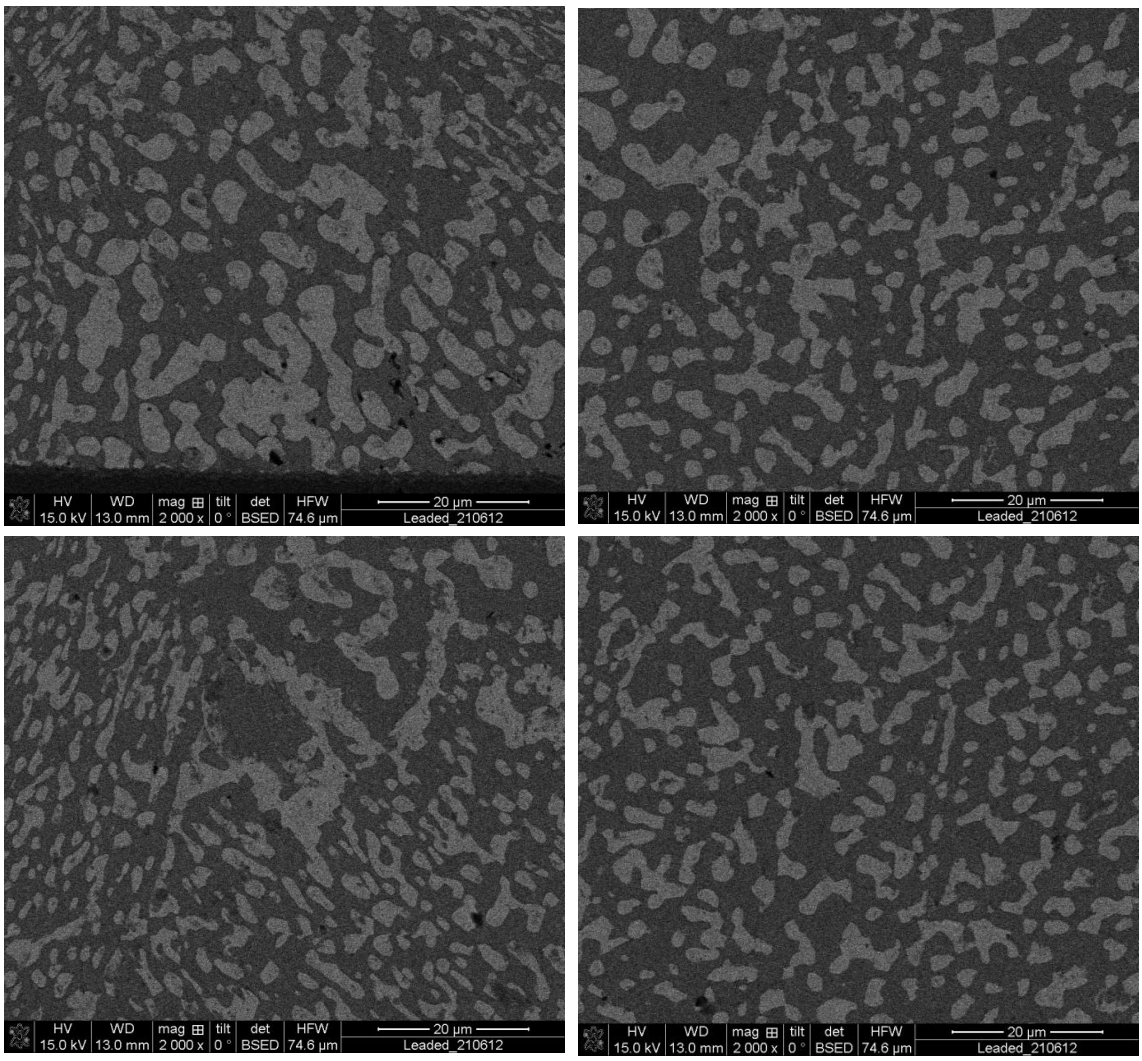

Figure 5.16: Back-scatter SEM images of eutectic (Sn-37Pb) solder after ageing at 80°C for 10 hours

National Instruments' "NI Vision Assistant" software was used to analyse the images to obtain the particle area for the entire image, then the volume fraction lead phase and the areas of the individual lead-phase islets. A script was designed to analyse the images as shown in Figure 5.17 and the final output was a measure of volume fraction and islet size for the lead-rich phase.

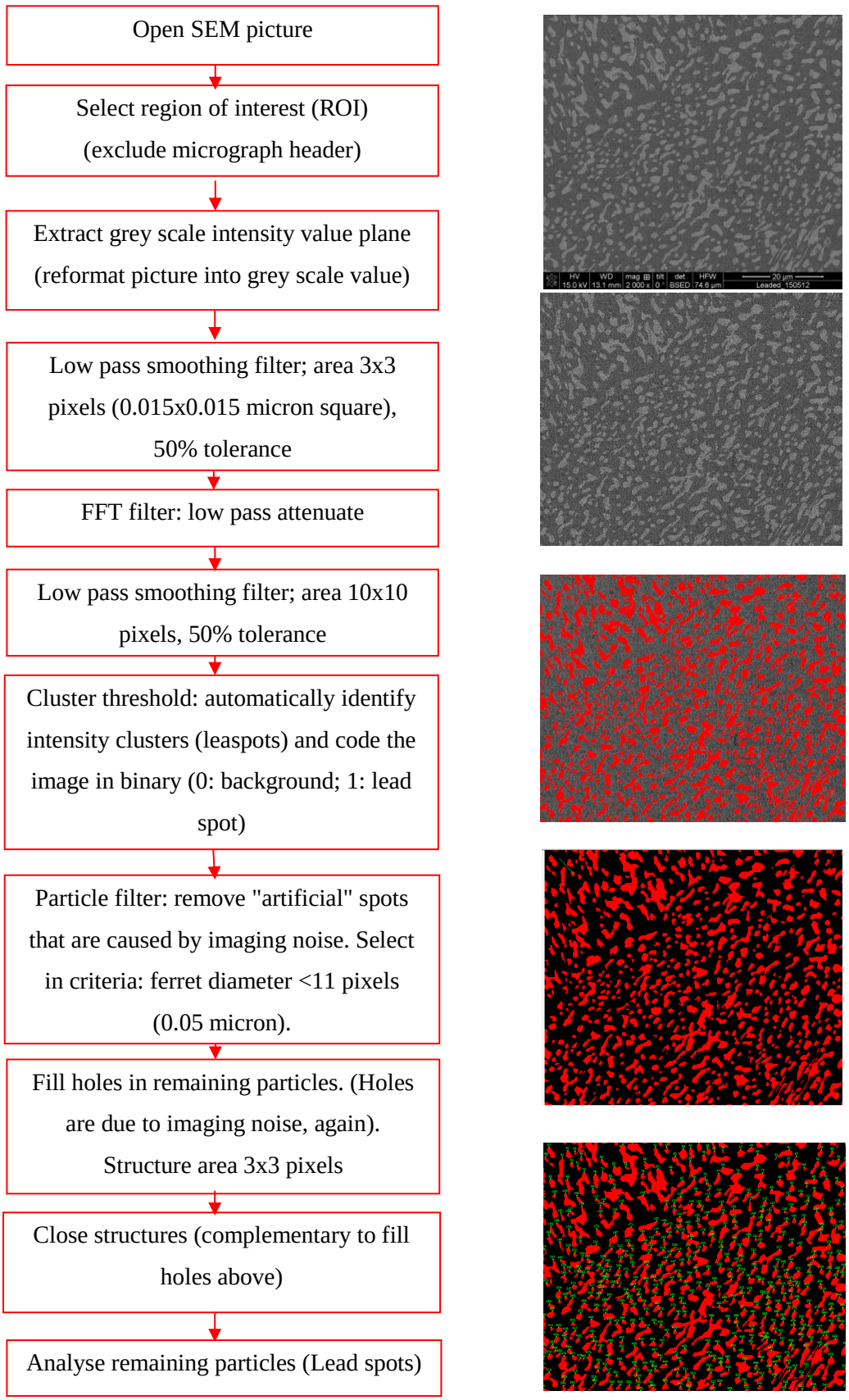

Figure 5.17: Logic diagram of the NI script for analysis of leaded solder images

Table 5.2 summarises the results of the metallographic analysis in terms of the means and standard deviations of the lead islet size (area) and the lead-rich phase volume fraction.

Table 5.2: Mean area and volume fraction, for the lead phase before and after ageing

Sn-37Pb	Mean area [μm^2]	Standard deviation	Volume fraction	Standard deviation
Before ageing	2.67	4.13	0.262	0.022
After ageing	5.03	8.09	0.323	0.025

Figure 5.18 shows the data on volume fraction as a histogram and, comparing this with Figure 5.14, shows that, at least, some of the reduction in hardness on ageing is associated with a larger amount of the softer, lead-rich phase.

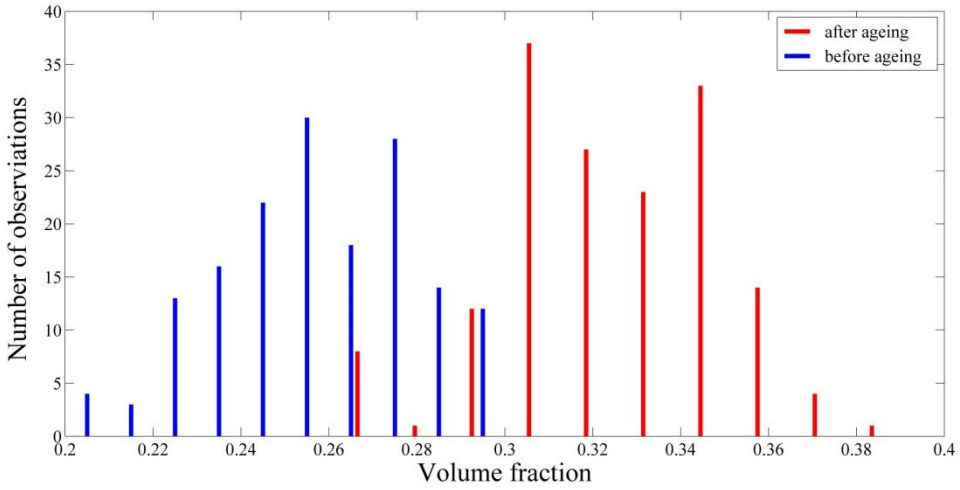

Figure 5.18: Histogram of lead phase particles volume fraction distributions before ageing

The (assumed normally distributed) standard deviation for particle size shown in Table 5.2 was rather large compared with the mean, so a more representative distribution function was sought to fit the data. Figure 5.19 shows the before-ageing size distribution fitted to a two- parameter lognormal probability density function (PDF):

$$(x|\mu,\sigma) = \frac{1}{x\sigma(2\pi)^{0.5}}\exp\left[-\frac{1}{2}\left(\frac{lnx-\mu}{\sigma}\right)^2\right] \qquad (5.2)$$

where σ and μ are the fitting parameters.

The mean and Standard deviation (SD) of the Log-normal distribution are given by

$$Mean = \exp\left(\mu + \frac{\sigma^2}{2}\right) \quad (5.3)$$

$$SD = [\exp(2\mu + 2\sigma^2) - \exp(2\mu + \sigma^2)]^{0.5} \quad (5.4)$$

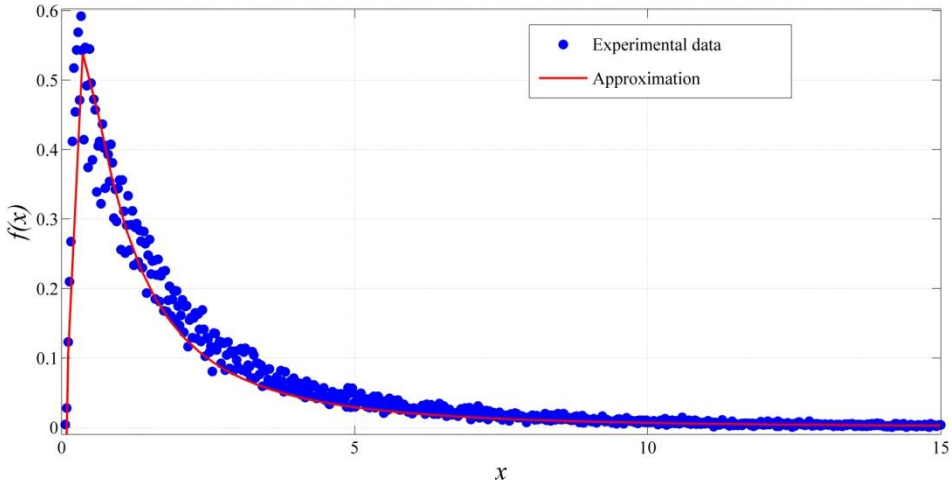

Figure 5.19: Probability density function (PDF) and Lognormal parameters for the lead phase area before ageing with x-axis truncated at 15

The lognormal parameters for lead islet size are listed in Table 5.3 and, as can be seen, they do not alter the general observation that the mean islet size has changed considerably on ageing. Despite this being a larger change, it is not thought that this is the primary cause of the softening because the islets are not conventional hard, second phase particles in the sense that the intermetallics in the lead-free solder are.

Table 5.3: Lognormal parameters for the lead phase size before and after ageing

Sn-37Pb	**Lognormal fitting parameters**			
	***σ* [μm^2]**	***μ* [μm^2]**	**Mean area [μm^2]**	***SD***
Before	0.07361	1.273	2.42	2.92
After	0.08836	1.402	4.87	7.25

As well as the changes on ageing, it was of interest to know if the microstructure showed any significant changes across the solder ball. Figures 5.20 and 5.21 show maps of the volume fraction of lead-rich phase before and after ageing and Figures 5.22 and

5.23 show the same data plotted with axial and radial position. Figures 5.24 to 5.25 show the corresponding data for lead-islet size. These distributions do not show any particular pattern of microstructure which would suggest that one part or another of the solder ball is more susceptible to failure.

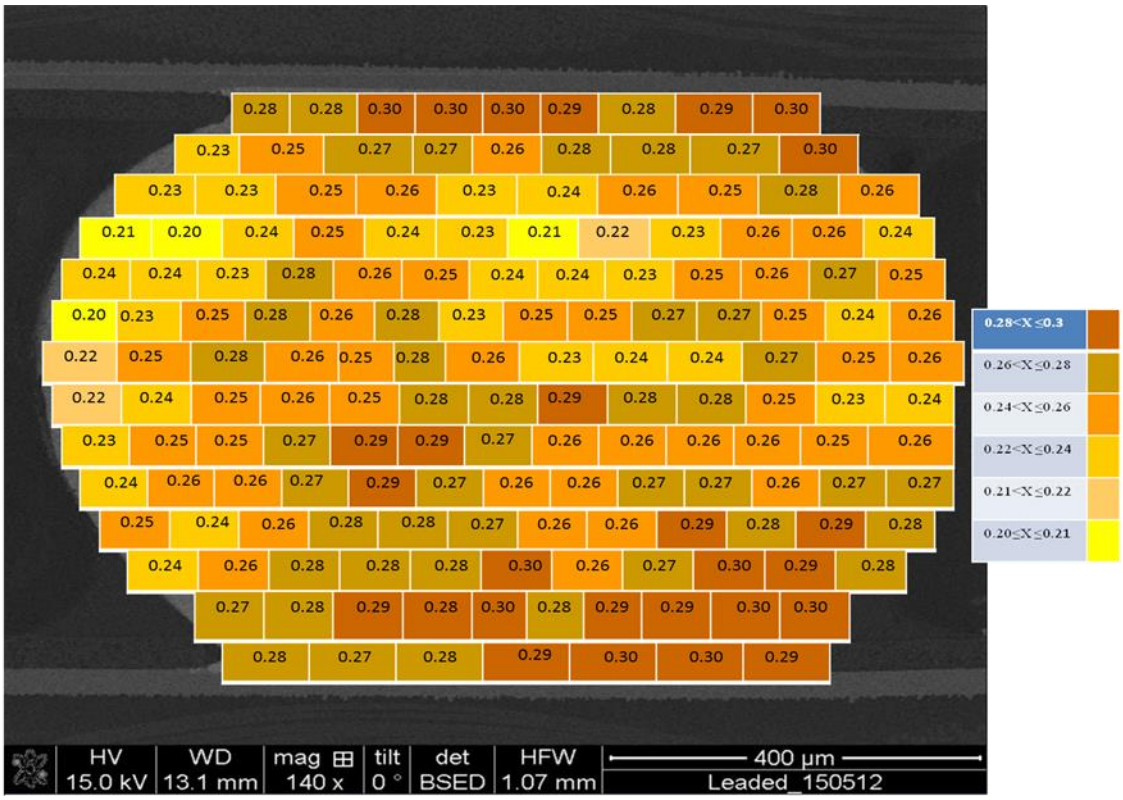

Figure 5.20: Map of volume fraction of lead phase before ageing

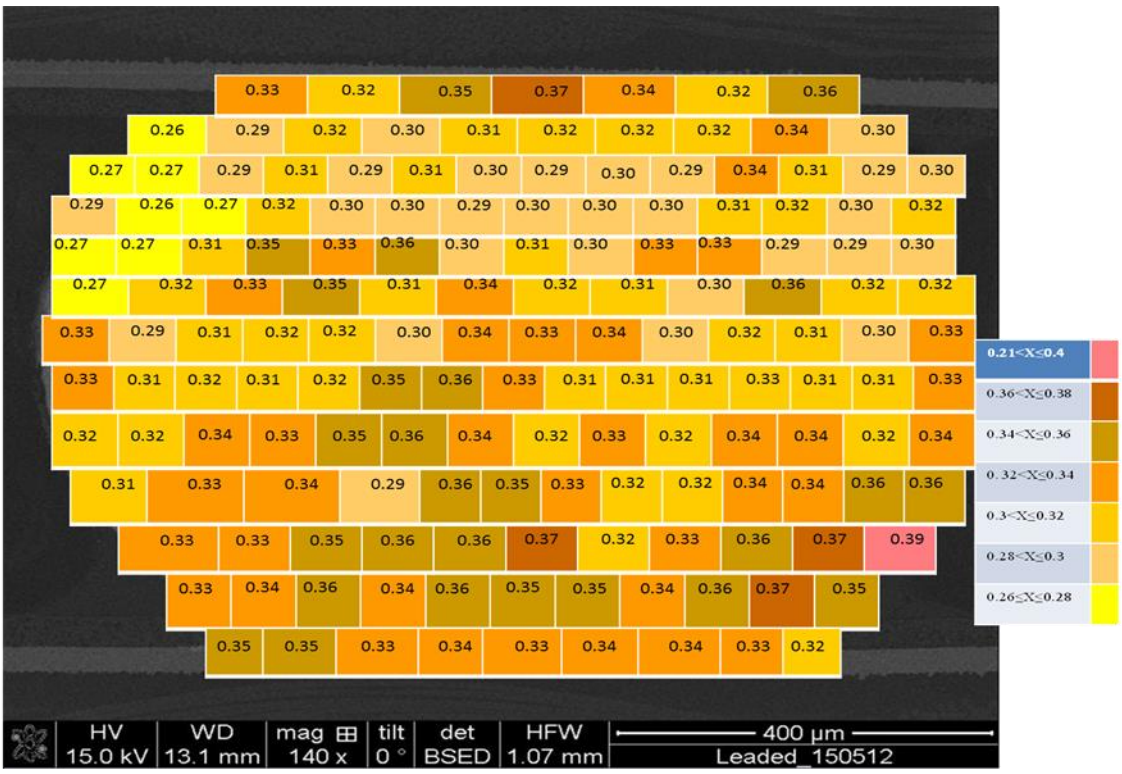

Figure 5.21: Map of volume fraction of lead phase after ageing

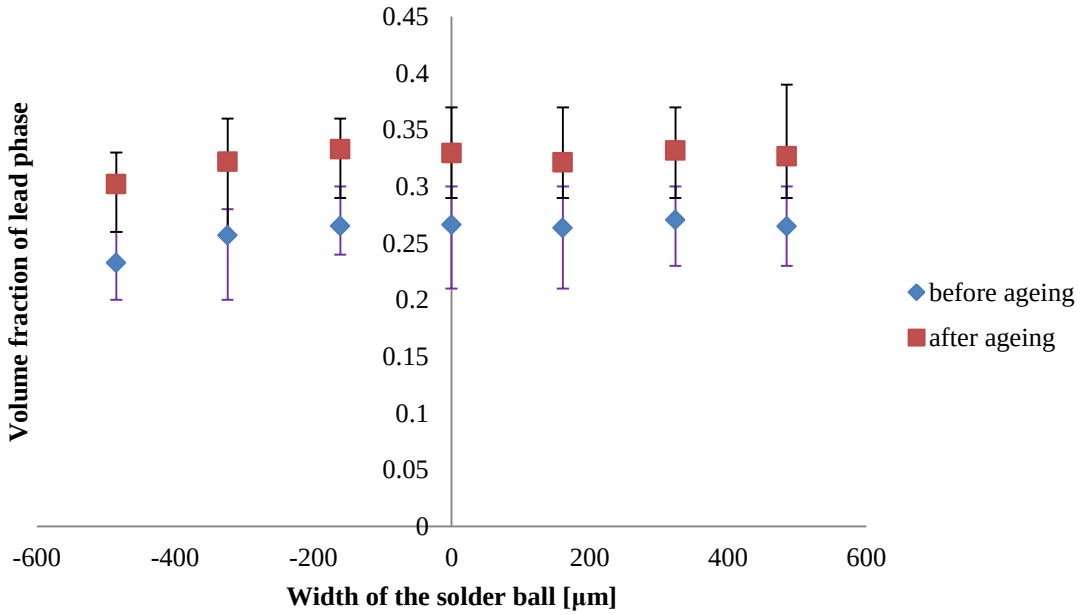

Figure 5.22: Variation of volume fraction of lead phase particles across the width of solder ball before and after ageing

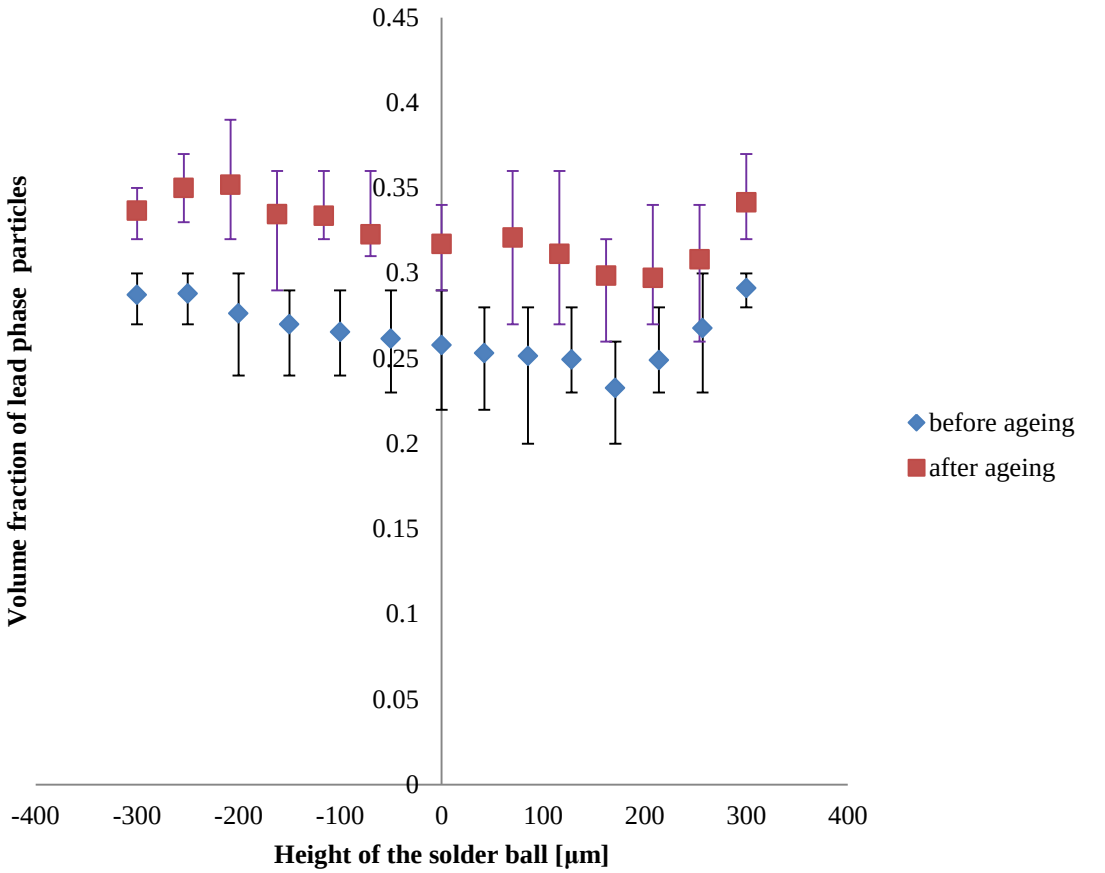

Figure 5.23: Variation of volume fraction of lead phase particles along the height of solder ball before and after ageing

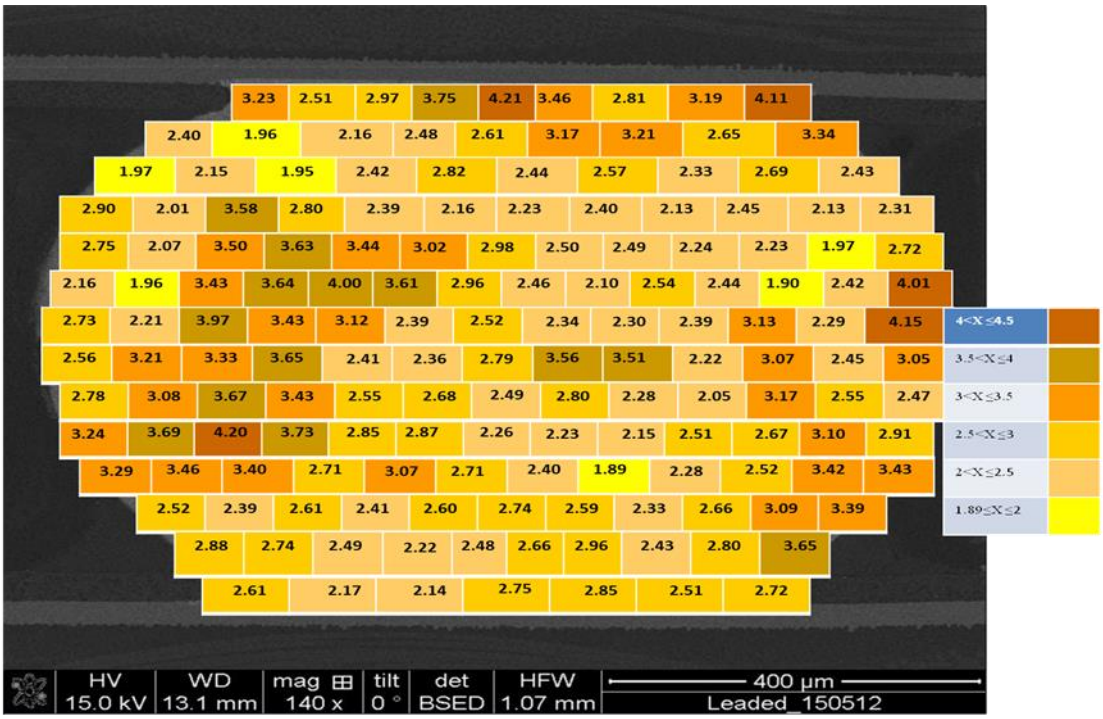

Figure 5.24: Map of mean size of lead phase particles before ageing

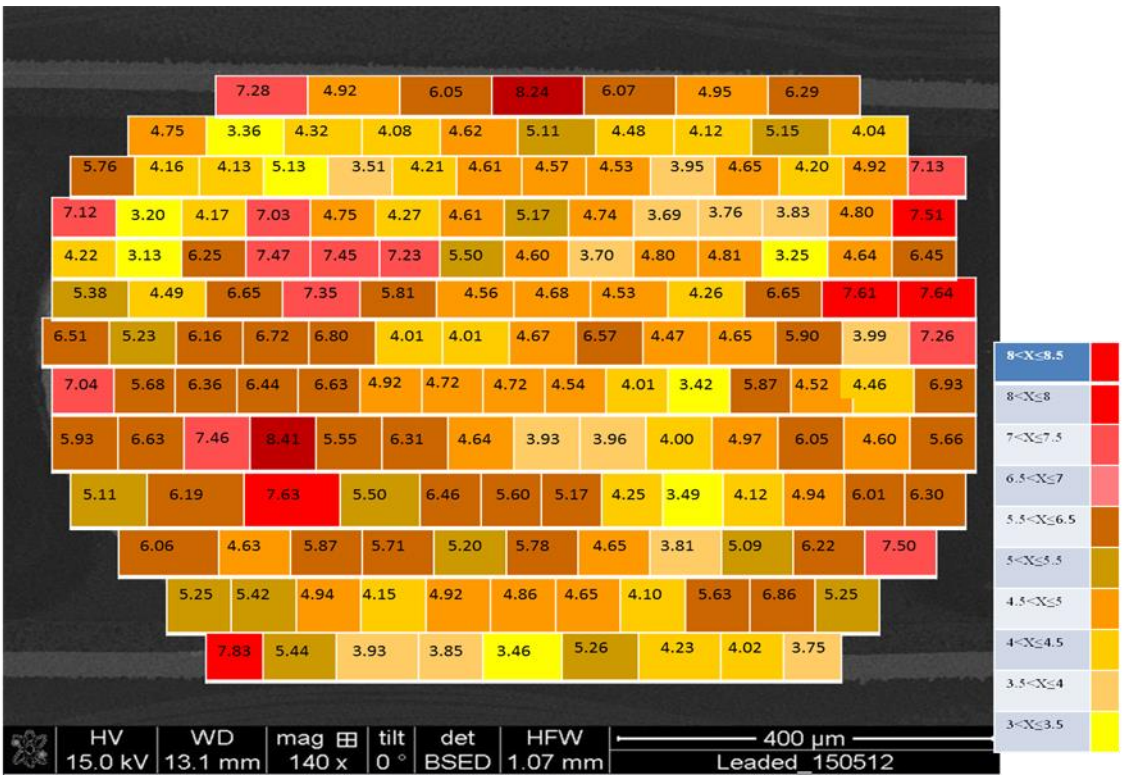

Figure 5.25: Map of mean size of lead phase particles after ageing

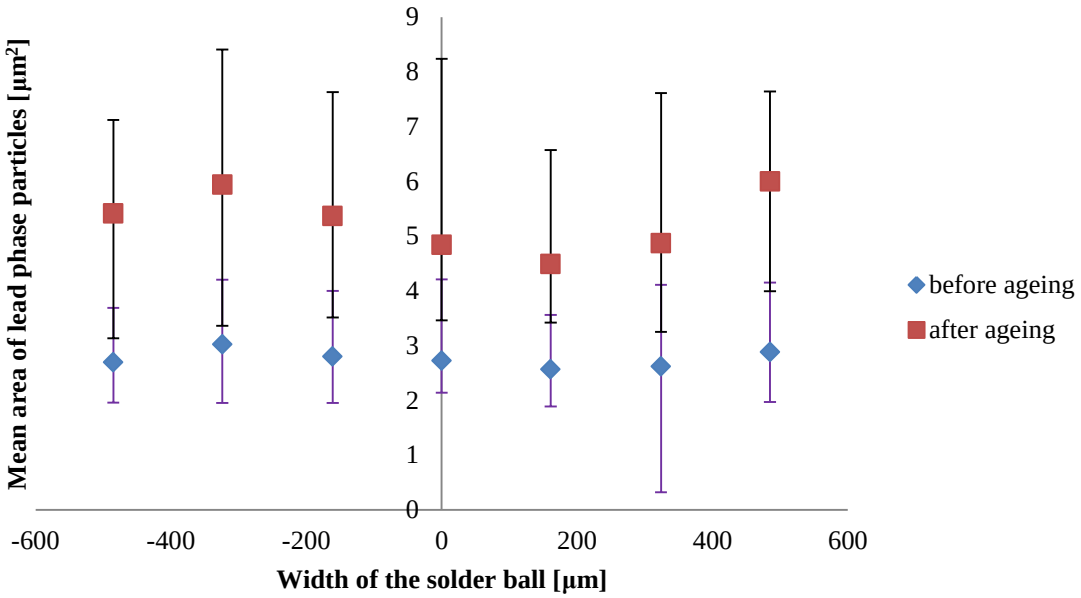

Figure 5.26: Variation of mean size of lead phase particles across the width of solder ball before and after ageing

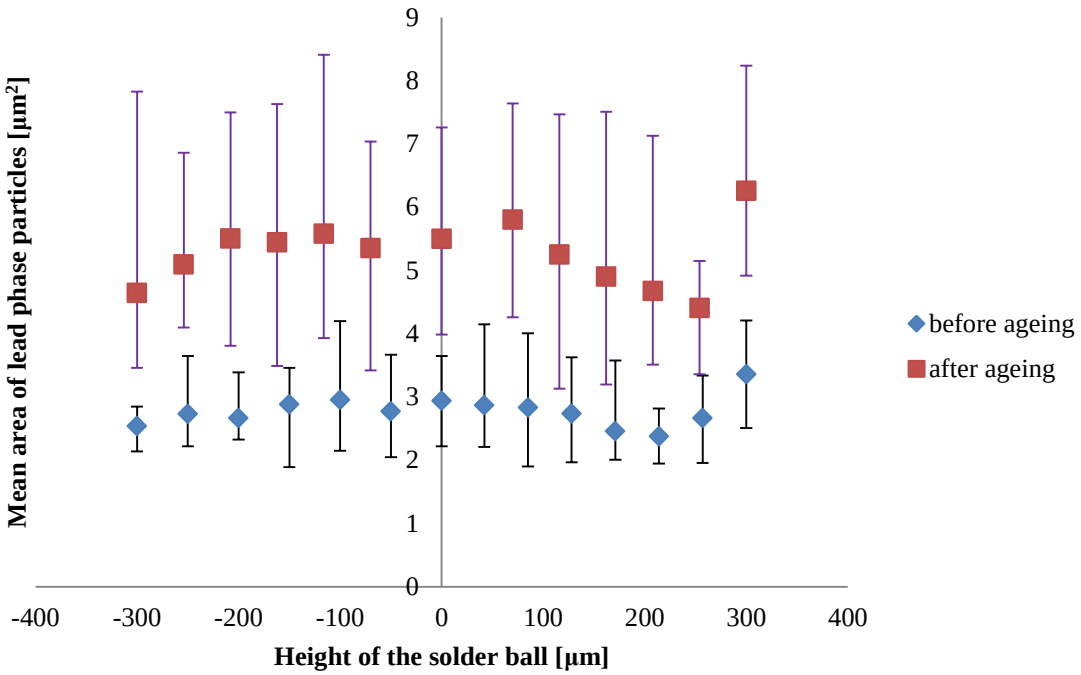

Figure 5.27: Variation of mean size of lead phase particles along the height of solder ball before and after ageing

Figure 5.28 shows a selection of SEM micrographs of the reaction layer formed at the interface between the leaded solder and the FR-4 copper substrates before and after ageing. It is clear from this figure there are no defect in the reaction area.

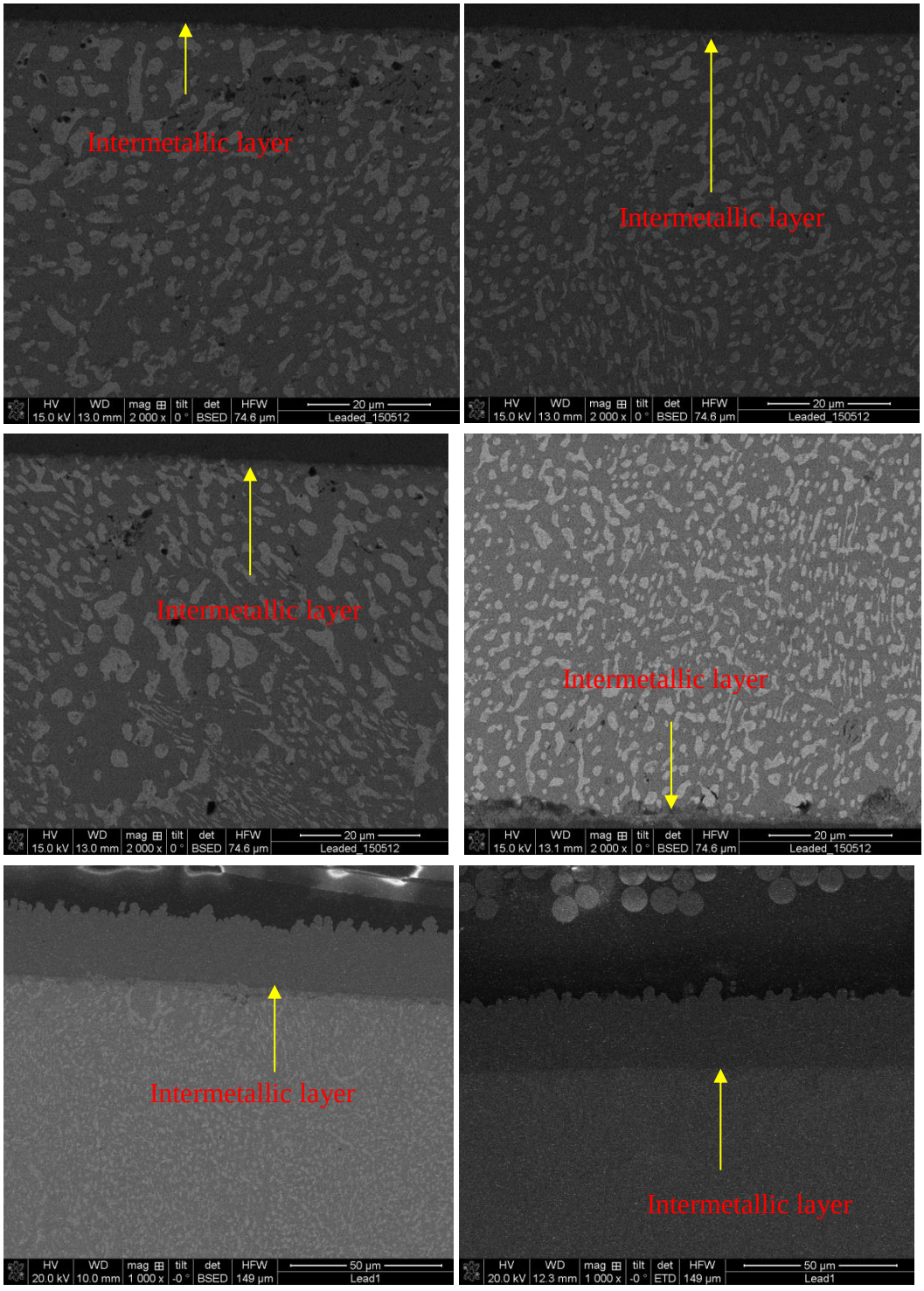

Figure 5.28: SEM micrographs using backscattered electronic imaging, showing intermetallic Cu substrate/leaded solder interface

5.4.2 Microstructure characterisation of lead-free solder joint

Figures 5.29 and 5.32 show a selection of optical and SEM micrographs in the unetched and etched condition to give an overview of the microstructure of the lead-free solder before ageing. Figures 5.33 and 5.34 show a selection of optical and SEM micrographs in the etched condition after ageing. As expected from the phase diagram (see Chapter 3) the microstructure consists mainly of a mixture of precipitate-free β-Sn dendrites, between whose arms is a very fine interdendritic eutectic (mixture of Sn, Ag_3Sn and Cu_6Sn_5). Another feature of the microstructure is the presence of relatively large, isolated primary Ag_3Sn, Cu_6Sn_5 particles, the Ag_3Sn assuming an acicular (needle) shape and the Cu_6Sn_5 taking a more disc-like morphology with distinctive hexagonal boundaries.

These micrographs together illustrate the fundamentally different nature of the microstructure of the lead-free alloy compared with the leaded solder. Although both are fundamentally eutectics with a β-Sn dendritic matrix, the primary dendrites are much more pronounced in the lead-free alloy. Also, although the intermetallic compounds (IMCs) constitute only a small fraction of the final microstructure, they have a much greater effect on the mechanical strength [299]. However, this also means that the strength will be critically dependent on the amount, size and distribution of the IMCs, not least because very large particles will introduce brittle paths into the solder and increased chance of local or global brittle fractures.

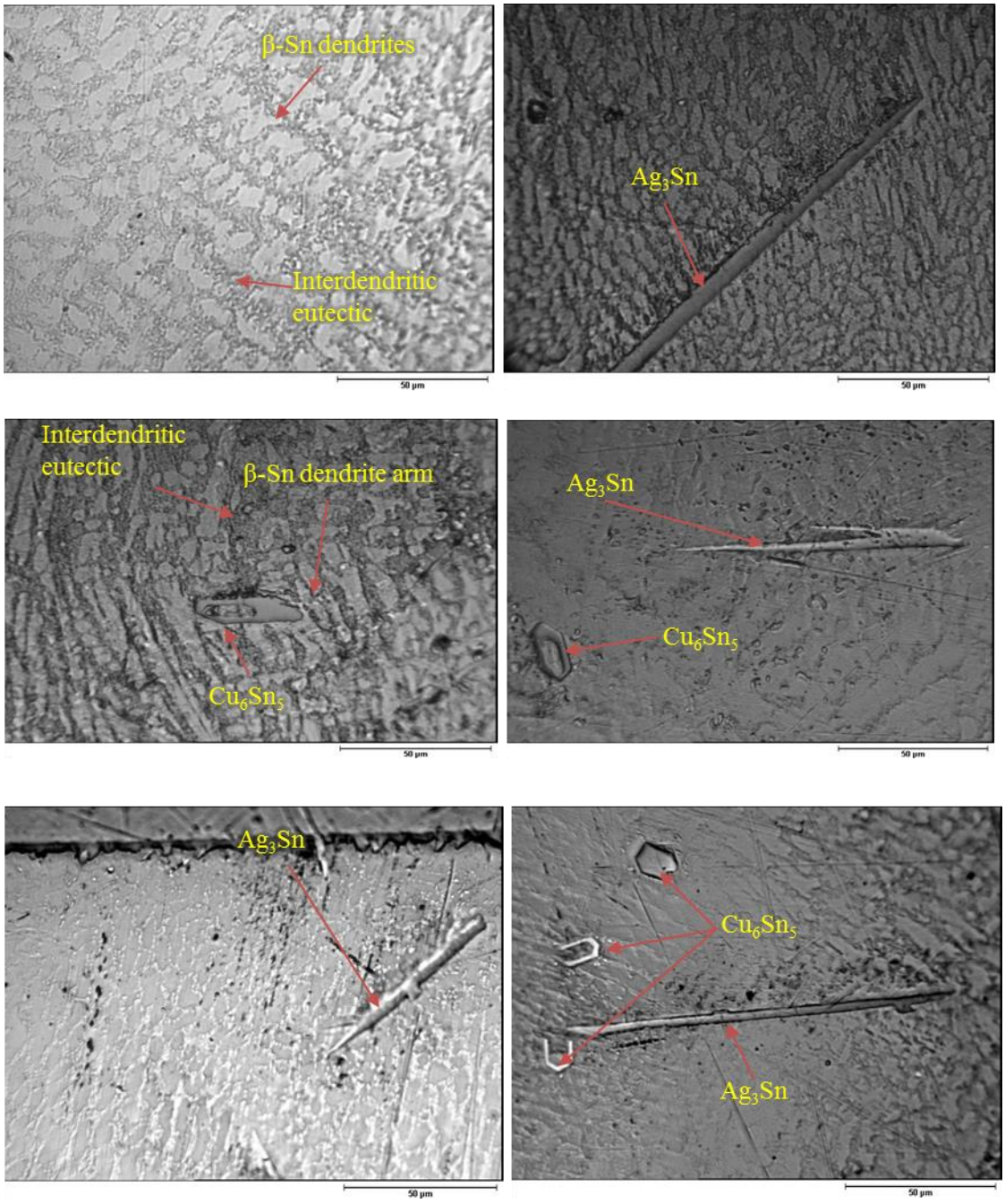

Figure 5.29: Optical microstructure of un-etched lead-free solder before ageing (scale bars 50 μm)

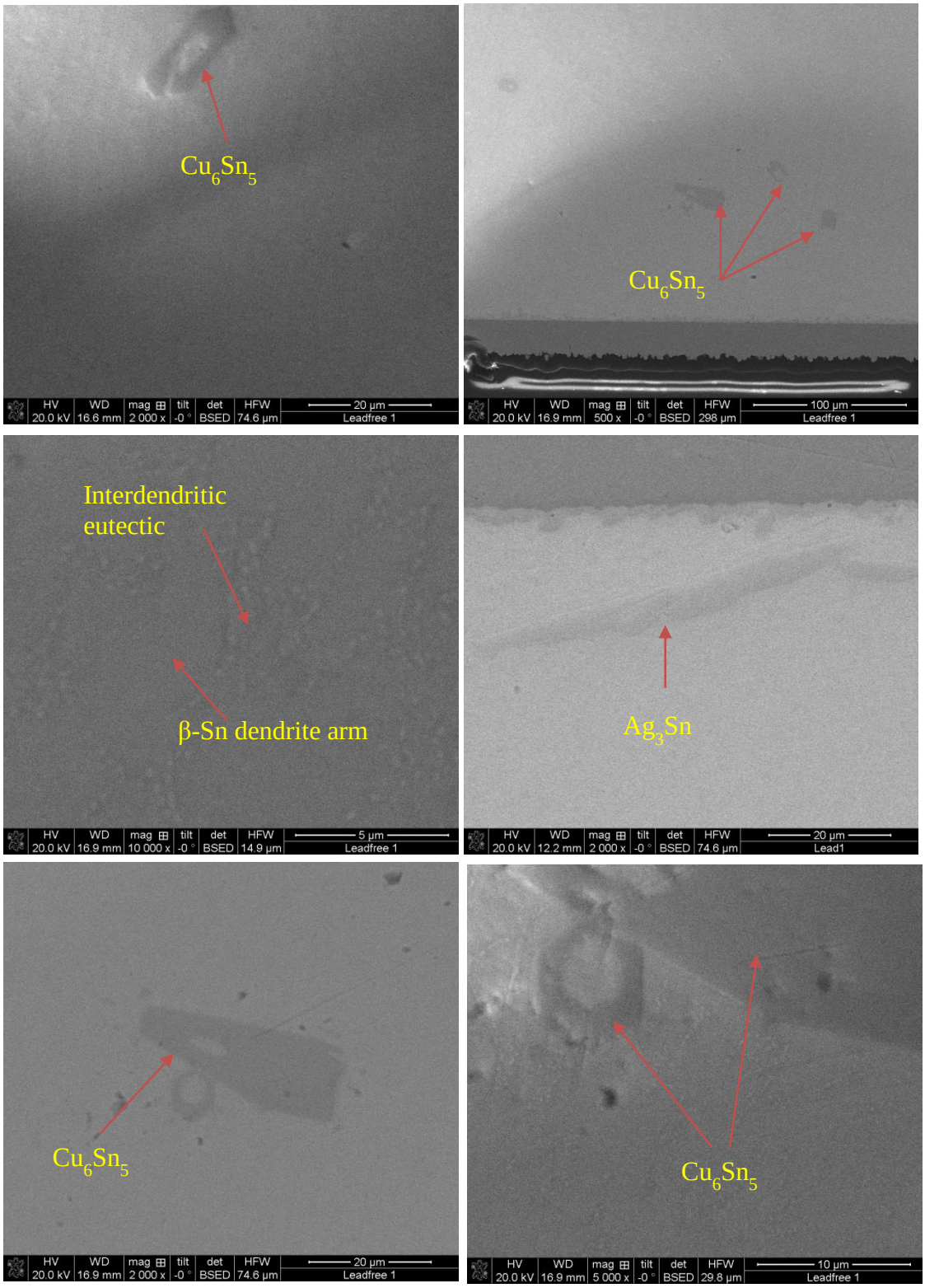

Figure 5.30: SEM microstructure of un-etched lead-free solder before ageing

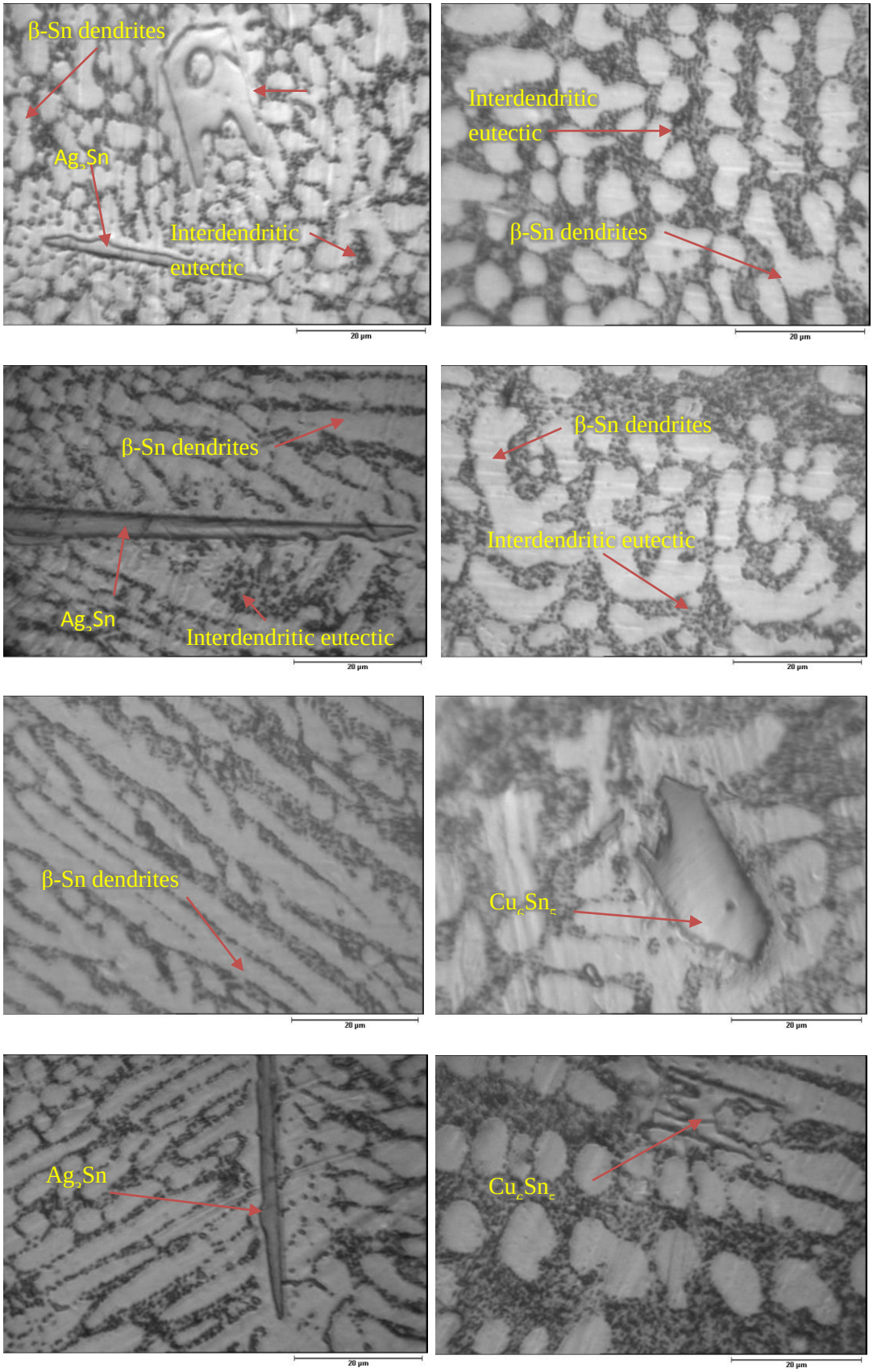

Figure 5.31: Optical microstructure of etched lead-free solder before ageing (scale bars 20 μm)

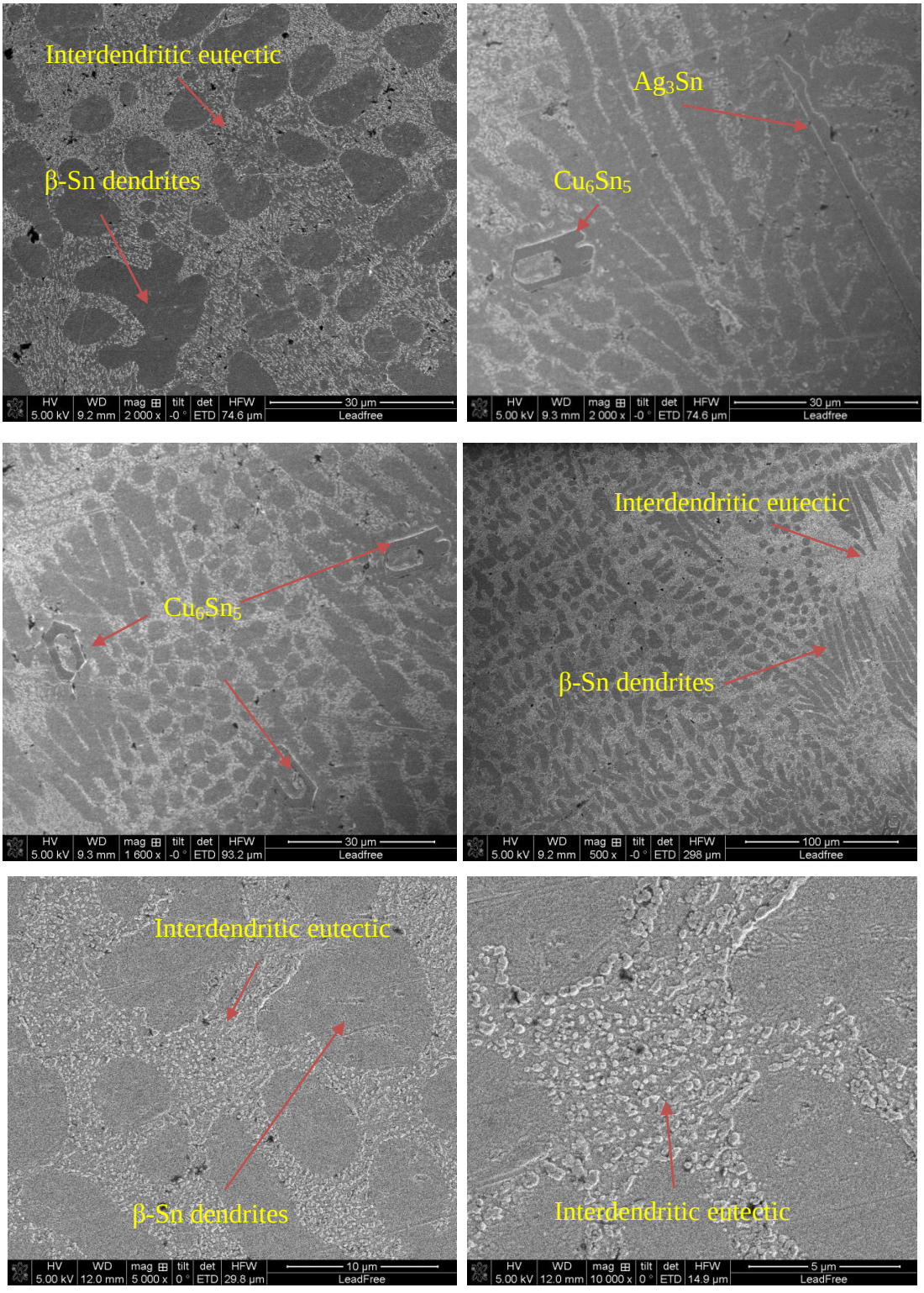

Figure 5.32: SEM microstructure of etched lead-free solder before ageing

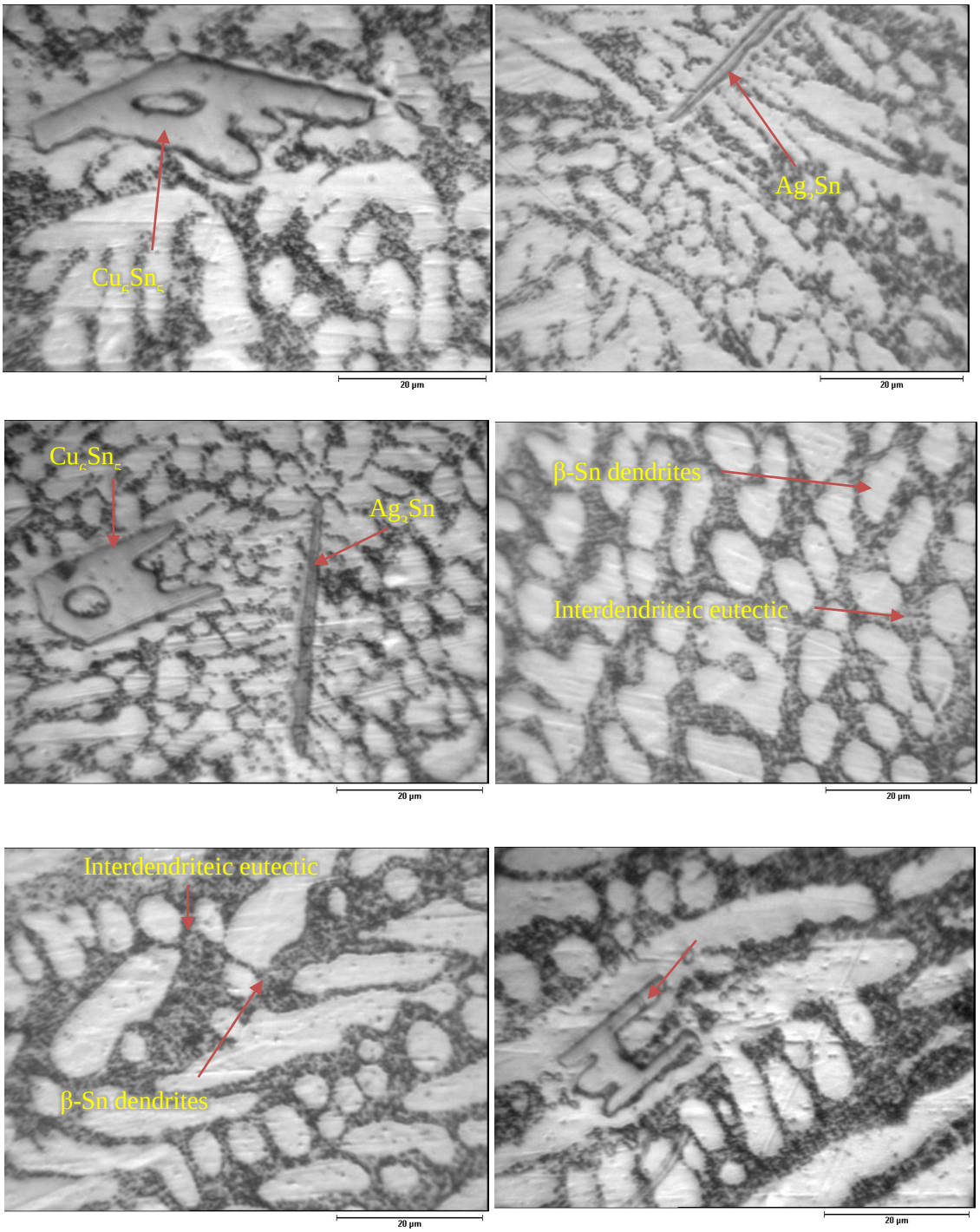

Figure 5.33: Optical microstructure of etched lead-free solder after ageing (scale bars 20 µm)

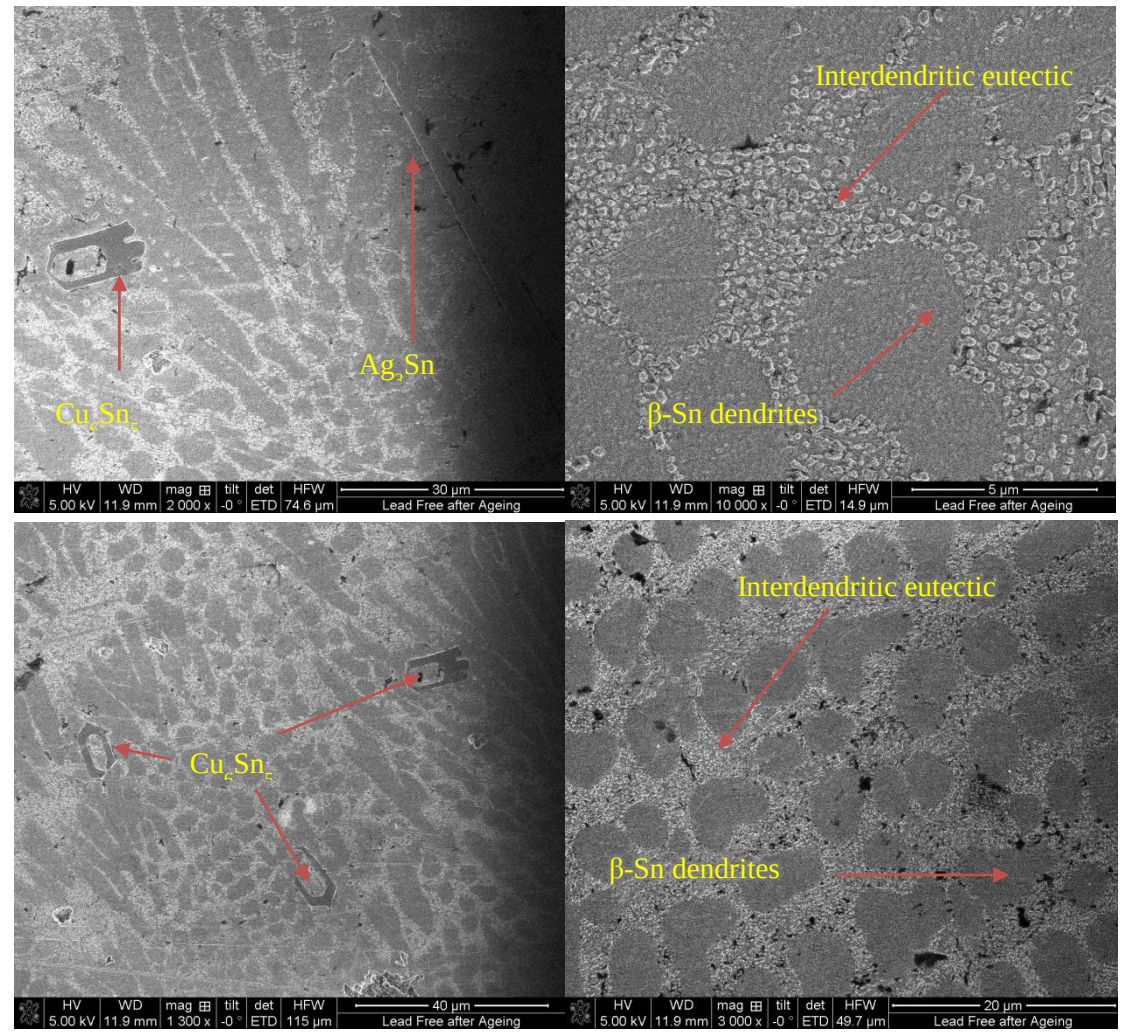

Figure 5.34: SEM microstructure of etched lead-free solder after ageing

There are a number of ways in which the microstructure of Sn-based lead-free solder alloys could be characterised in a generic way for monitoring microstructural evolution or for assessing new alloys. The following are possible parameters that could be used based on the above observations:

- Overall morphology (fine or coarse) of the solder
- Size, shape (e.g. globular, acicular or plate-like) and distribution of the IMCs.
- Arm length of β-Sn dendrites.
- β-Sn dendrite arm spacing.
- Volume fractions of each phase and primary Sn eutectic volume ratio
- Intermetallic growth at the solder joint and copper pad interface.

Because of the heterogeneity and the rather large size of some of the particles, it was decided to assess the microstructural; changes on ageing by locating the same features before and after ageing in the SEM and comparing dimensions. The measurements taken were; dendrite arm gap (essentially the thickness of the interdendritic eutectic), β-Sn dendrite arm length and dendrite globule area, and key dimensions of primary Ag_3Sn and Cu_6Sn_5 particles. The raw manual measurements are shown in Figures 5.35 and 5.36 for the pre-aged condition, and Figures 5.37 and 5.38 for the post-aged condition.

Figures 5.39 to 5.43 show the changes (per observation) for each of the five microstructural features mentioned above in chart form. As can be seen, the large primary IMC particle sizes increase by around 10%, although this probably does not have a pronounced effect on hardness. The tin globule linear dimensions increase by a little more (around 15%), but, when this is expressed as an area (a measure of the volume fraction), the increase is more in the region of 20%. Taken with the reduction in interdendritic eutectic thickness (again of around 20%), this suggests that the eutectic particles are coarsening considerably. Unfortunately, it was not possible to measure the size of the eutectic particles directly as these were beyond the resolution of the etched structure and the SEM gave insufficient contrast to resolve them in the unetched condition. However, there is sufficient evidence to attribute the reduction in hardness from ageing to the coarsening of particles in the ternary eutectic.

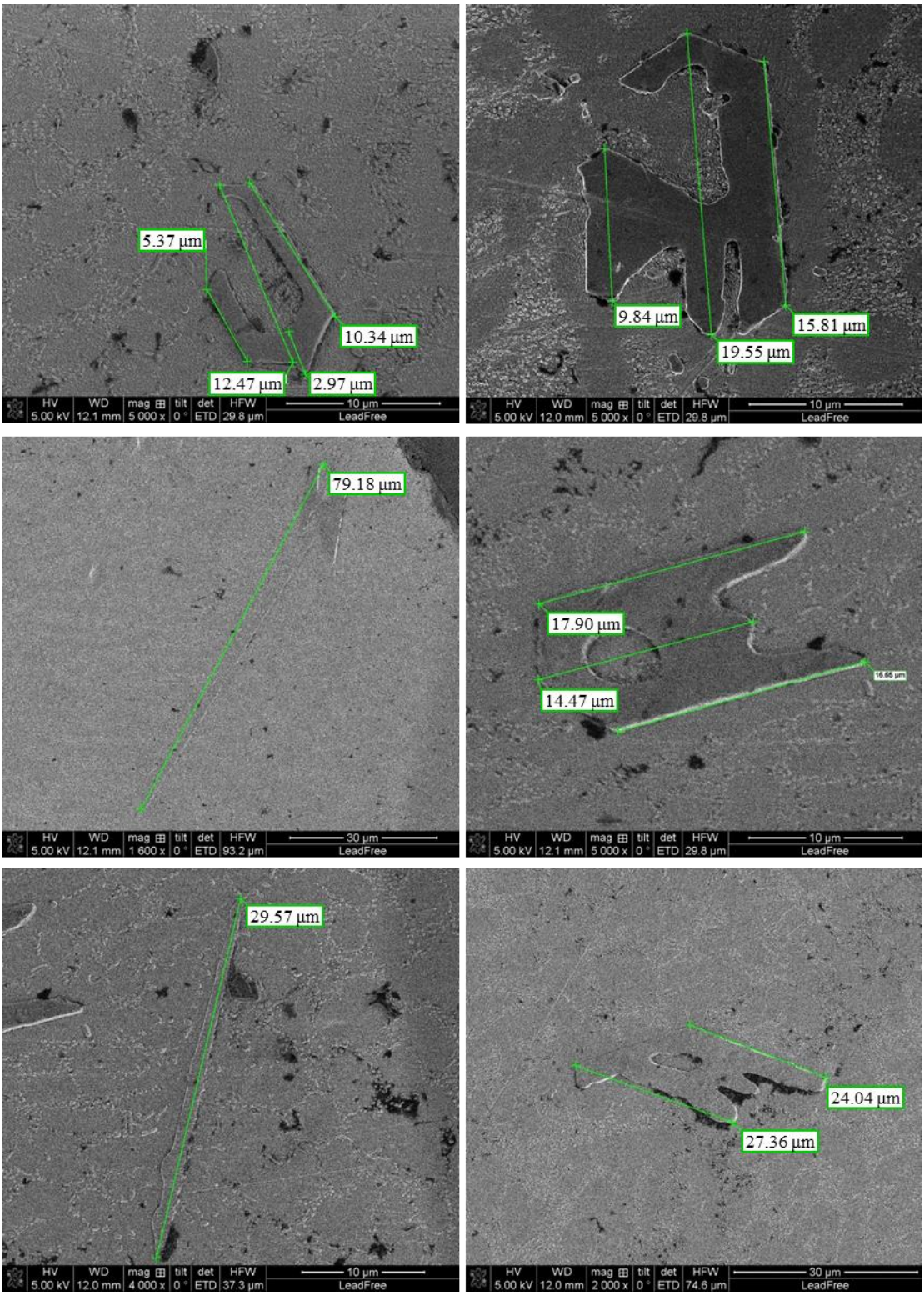

Figure 5.35: SEM measurements of microstructure of primary Ag_3Sn and Cu_6Sn_5 particles lead-free solder before ageing - I

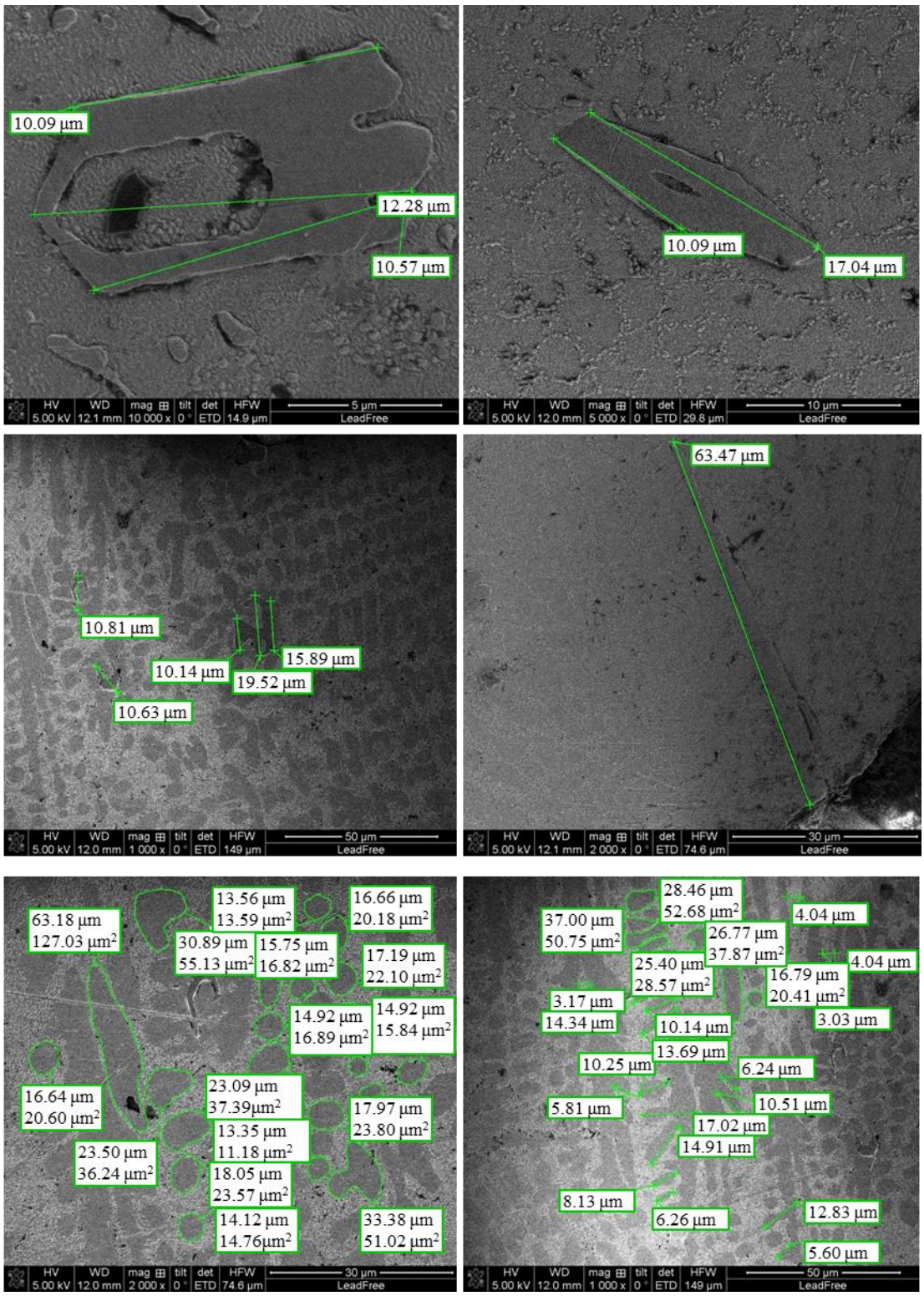

Figure 5.36: SEM measurements of microstructure of primary Ag_3Sn and Cu_6Sn_5 particles as well as β-Sn dendrite arm length and dendrite globule area, lead- free solder before ageing- II

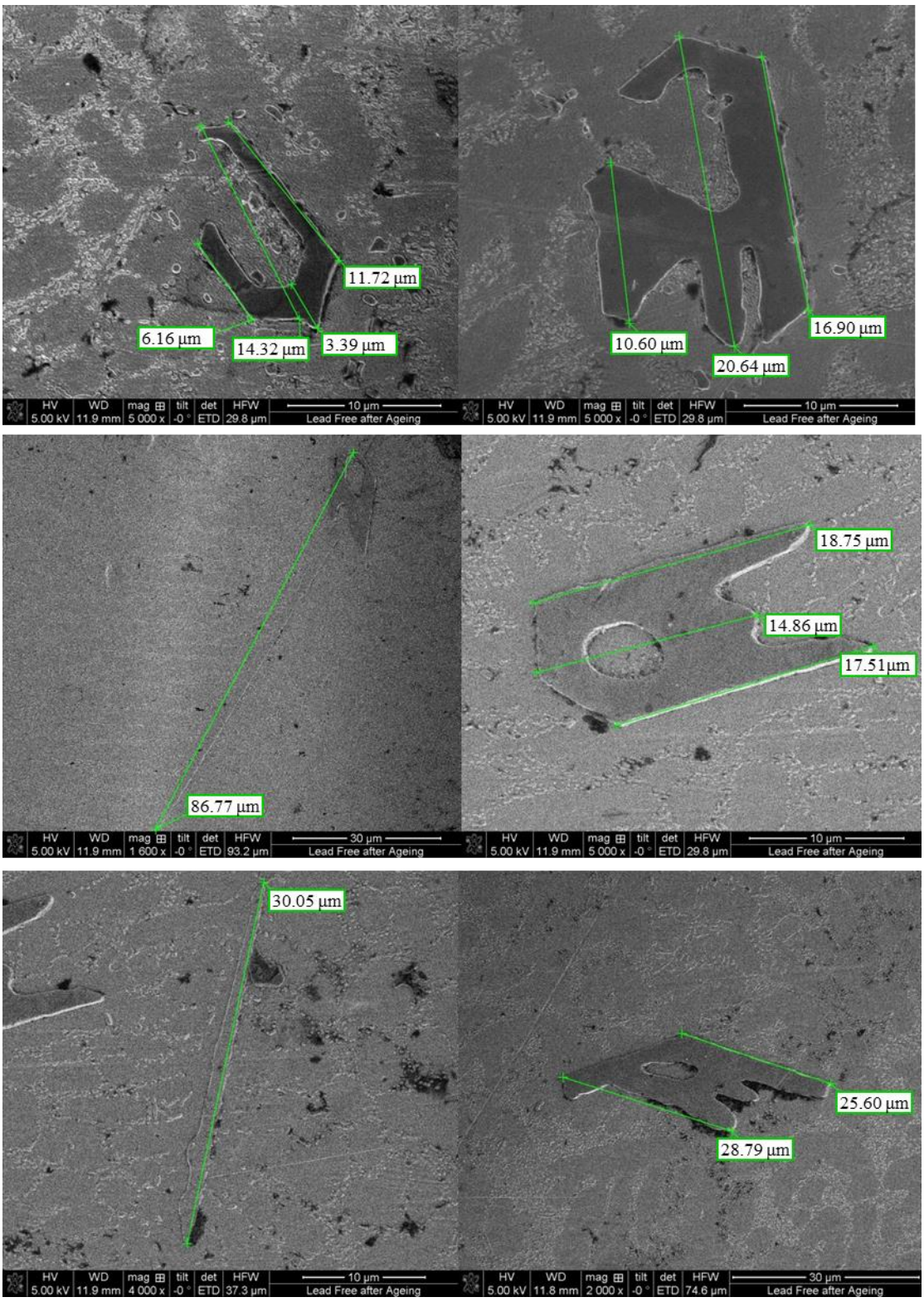

Figure 5.37: SEM measurements of microstructure of lead- free solder after ageing which show an increase in length when compared to before as shown by the measurements- I

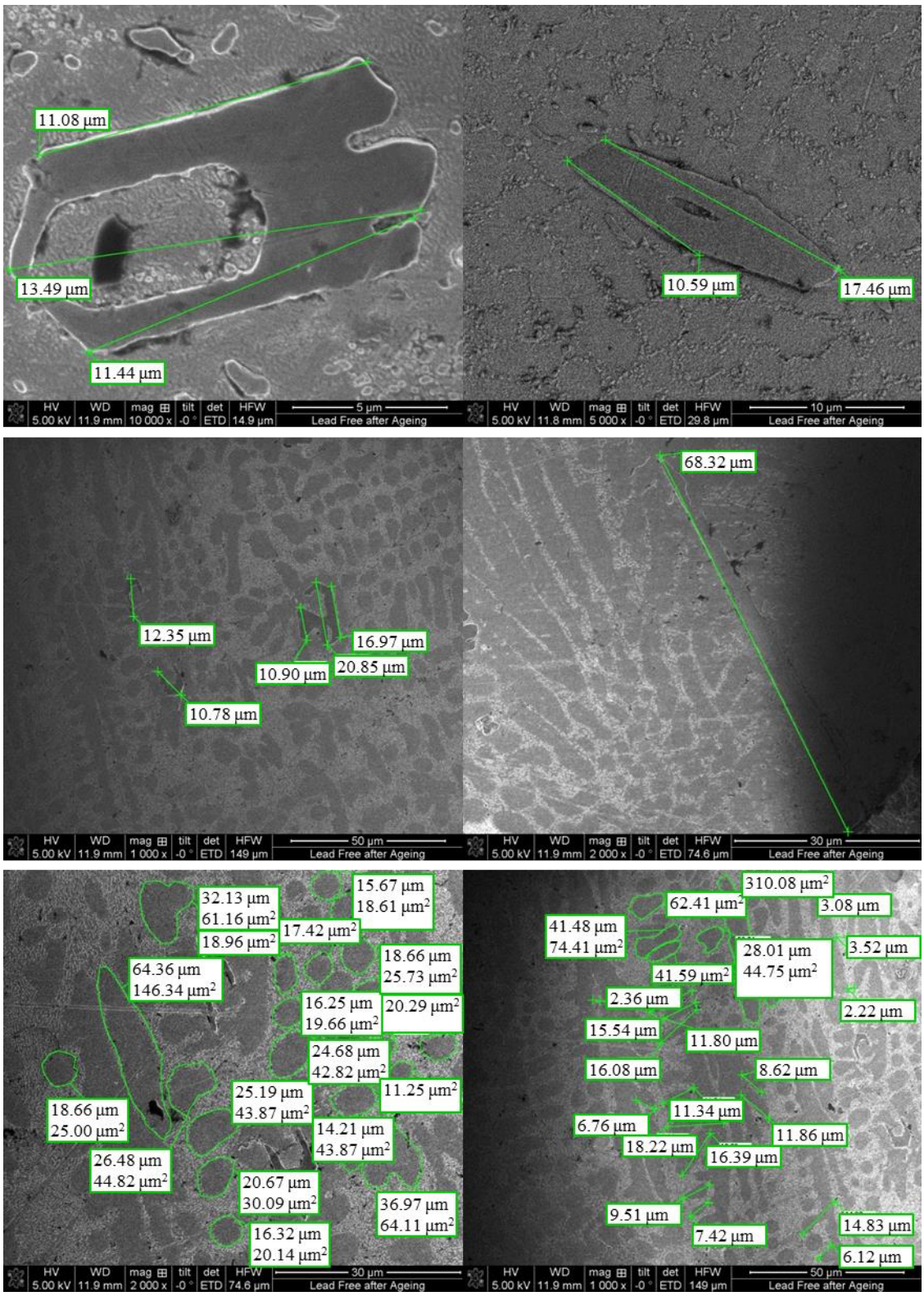

Figure 5.38: SEM measurements of microstructure of lead- free solder after ageing which shows that the primary Ag_3Sn and Cu_6Sn_5 particles as well as dendrite globule area and β-Sn dendrite arm length have increased - II

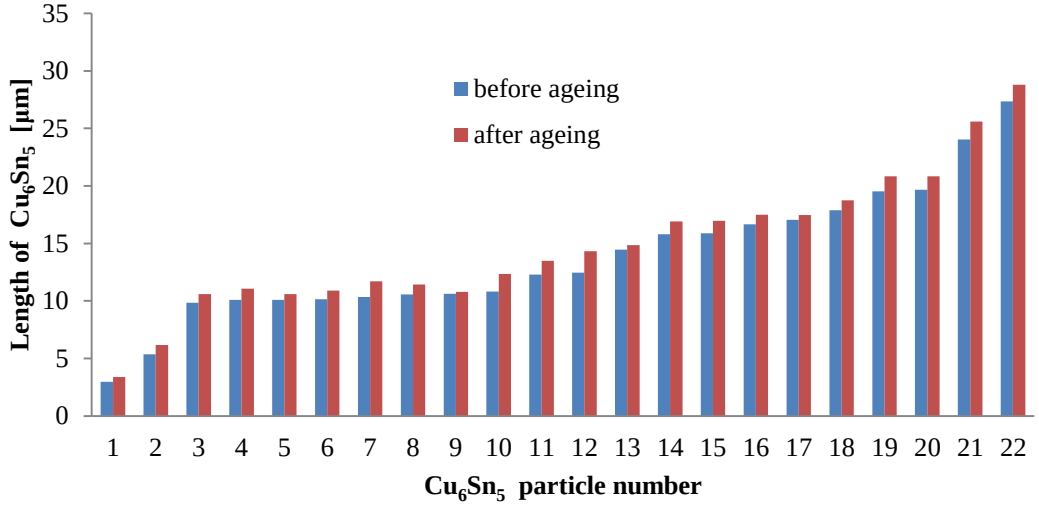

Figure 5.39: Comparison between Cu_6Sn_5 size before and after ageing

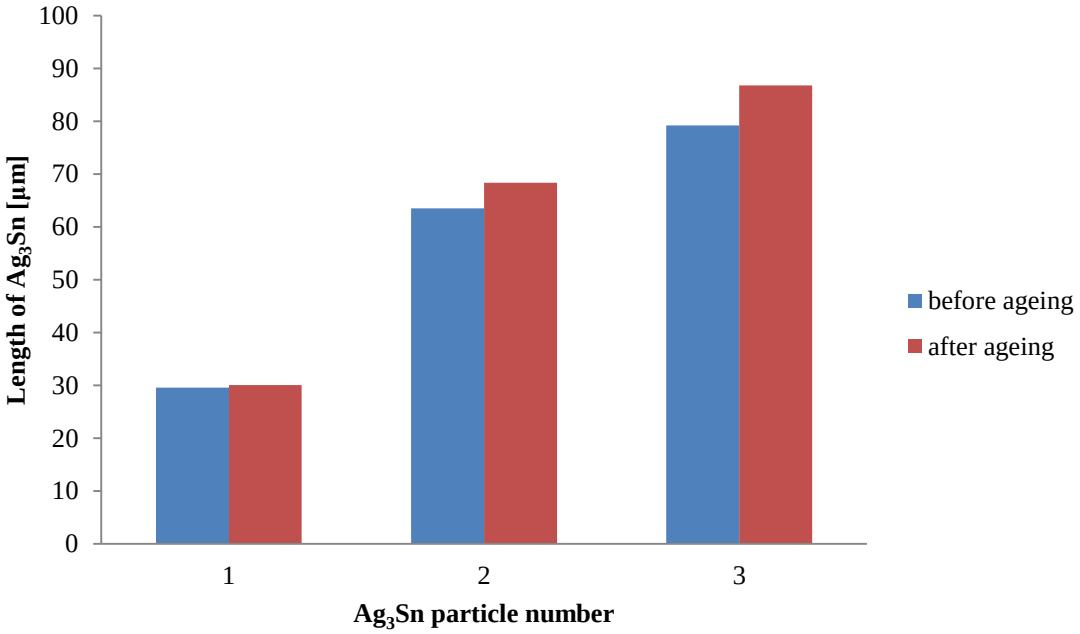

Figure 5.40: Comparison between Ag_3Sn size before and after ageing

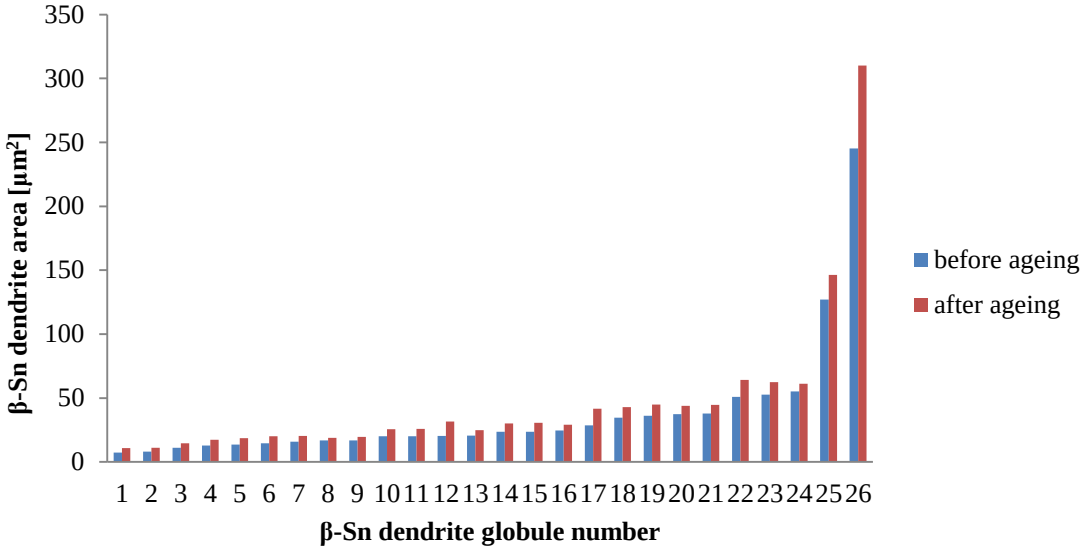

Figure 5.41: Comparison between β-Sn dendrite globule area before and after ageing

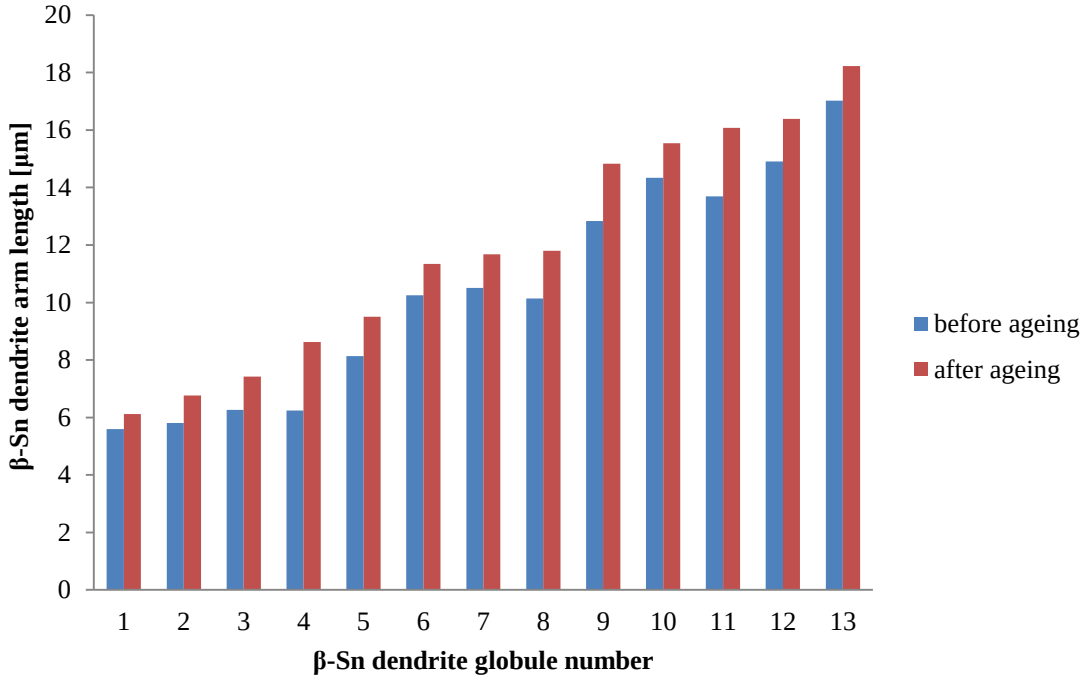

Figure 5.42: Comparison between β-Sn dendrite arm length before and after ageing

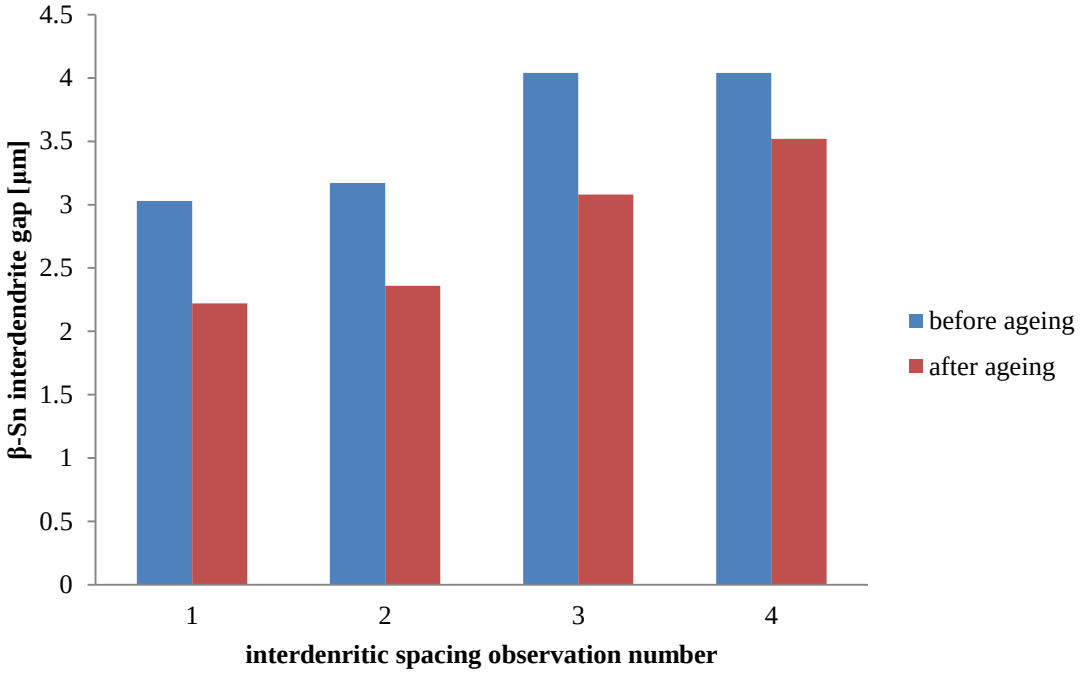

Figure 5.43: Comparison between β-Sn interdendritic gap before and after ageing

A selection of SEM micrographs of the reaction layer formed at the interface between the lead-free solder and the FR-4 copper substrate is shown in Figure 5.44. As can be seen, on more than one occasion, the substrate has acted as a nucleation site for primary Ag_3Sn needles. Such an effect could have a substantial influence on the durability of the solder joint, and can probably be influenced by varying the composition of the substrate, perhaps by use of thin coatings. The presence of primary Ag_3Sn needles can reduce the durability of the solder joint because very large particles will introduce brittle paths into the solder and lead to a higher chance of global and local brittle fracturing.

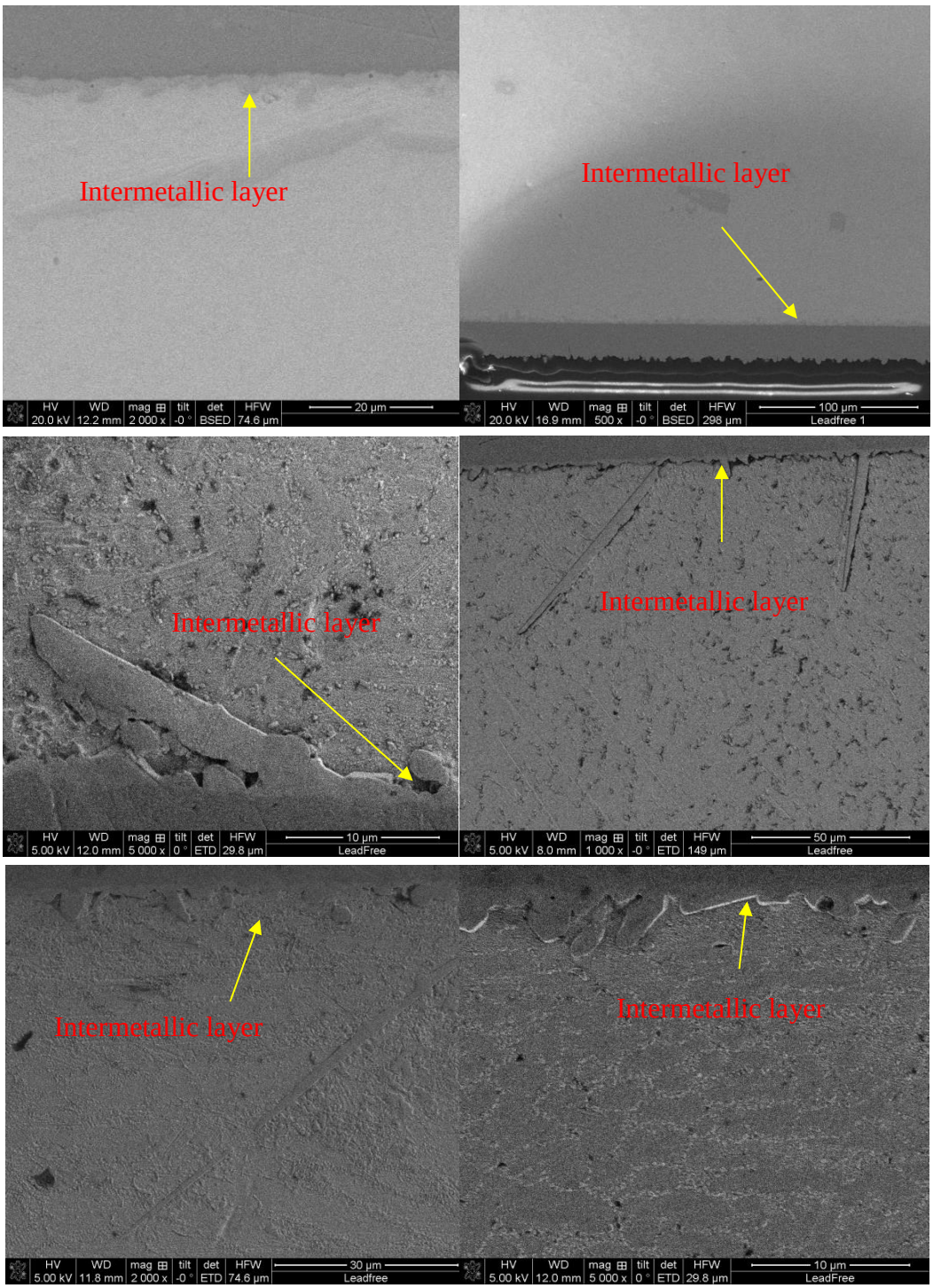

Figure 5.44: SEM micrographs using backscattered electronic imaging, showing intermetallic Cu substrate/lead-free solder interface

5.5 Summary

An analysis of optical and SEM micrographs of leaded eutectic solder alloy (Sn-37Pb) demonstrate a coarsening of the lead-phase grains after thermal ageing at 80°C for 10 hours. Increases of around 46% in the mean area (i.e. size) and 18% in the volume fraction of the lead phase were recorded and this is expected to be the reason for the drop in hardness. No systematic variations in size or volume fraction were observed across the solder balls in either the aged or unaged conditions, so the structures could be regarded as homogeneous.

By contrast, the lead free solder structures were rather inhomogeneous, particularly with regard to the presence of primary IMCs, which were large and isolated and, in places, were seen to be nucleated preferentially at the substrate solder interface. The sizes of both primary Cu_6Sn_5 and Ag_3Sn particles increased after ageing, although this was not expected to be the cause of the loss of hardness on ageing. The changes in the primary tin dendrite size and the interdendritic gap were, however, taken to be evidential of eutectic IMC coarsening, which would be expected to lead to a reduction in hardness on ageing.

Lastly, macroscopy of fractured and intact balls showed the presence of voids and stress concentrators at the failure plane (within top or bottom 10% of ball height). Although voids which help to increase durability through crack blunting, their presence also results in an increase in nominal stress at the plane in question. The stress concentration at the fracture plane was estimated to be about 2, and the increase in nominal stress due to the realised dimensions and the presence of voids was up to 3 (mm^2)%.

Chapter 6: Discussion

This chapter discusses the significance of the results in terms of alloy design for higher stress, higher temperature application, and the replacement of lead-based alloys.

The first part of the discussion focuses on the fatigue life as measured by the stress-life curves, firstly on the effect of microstructure and ageing on stress-life behaviour and, secondly, on a comparison of the findings of the current work with published fatigue data on the two alloys.

The second part of the discussion focuses on solder alloy constitutive behaviour, including elastic, plastic, stress cycling and creep behaviour. A key element of this aspect of the work is the measurement of the solder shear strain, so this part of the discussion commences with a comparison of strain assessment in this work with that of other published sources.

6.1 Stress-life behaviour

This section discusses the findings obtained from the fatigue testing of leaded and lead-free and solder joints. The S-N curves for isothermal testing at room temperature, 35°C, 75°C, as well and the nIP, IP and OoP tests. These results are discussed in the light of microstructural and property differences between the alloys and before and after ageing. They are also compared with like published data (i.e. other stress-life data), but the question of comparison with strain life data is deferred to the next section.

6.1.1 Fatigue life of Sn-37Pb solder alloy

From the S-N curves in Figure 4.15a and Table 4.2, it can be seen that the fatigue life decreases in an approximately exponential fashion with temperature throughout the range tested, corresponding to a roughly constant slope of the S-N curves. Figure 6.1 shows an Arrhenius plot of the time to failure at a fixed stress for each of the isothermal tests (including nIP) and, as can be seen, the Q/R value is about ($4000K^{-1}$).

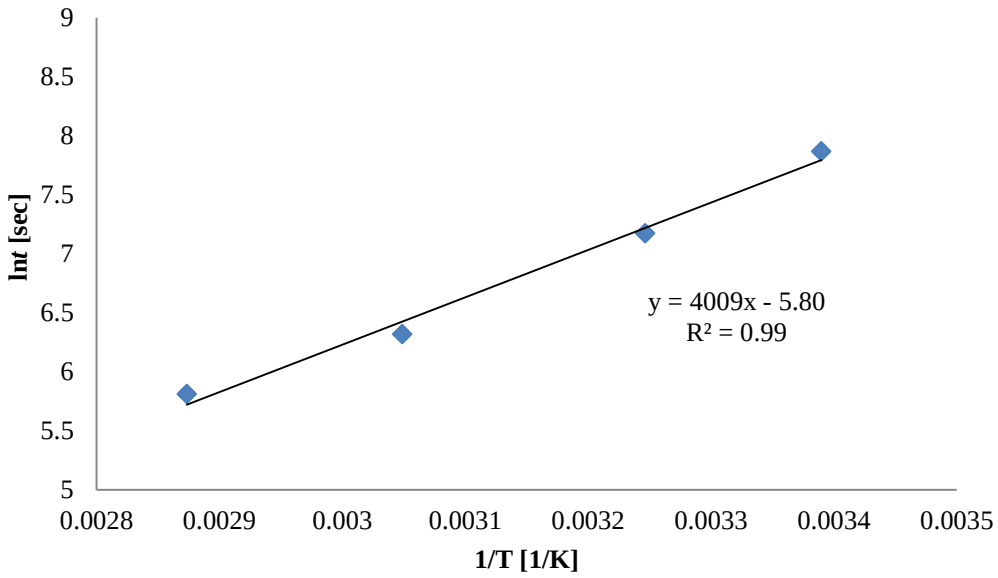

Figure 6.1: Arrhenius plot for time to failure against test temperature at a stress range of 14.3 MPa for Sn-37Pb

Also, as seen in Figure 5.13 and Table 5.2, there is a substantial effect of ageing on the microstructure of the Pb-Sn alloy, but a relatively modest effect on its room-temperature hardness. It might also be noted that ageing was carried out at 80°C (a little above the highest isothermal fatigue test temperature) for 10 hours, corresponding to between 3.5 and 7×10^4 HCF cycles and about 400 LCF cycles. Jung *et al*. [300] have measured an activation energy (expressed here as Q/R) of $4800K^{-1}$ for microstructural coarsening during static annealing of 60Sn-40Pb, and Vianco *et al*. [301] have measured values between 1900 and $4900K^{-1}$, depending on the starting microstructure, as varied by the cooling rate from the melt, finer microstructures leading to higher activation energies. It therefore seems likely that the same processes that govern particle coarsening (in this case, diffusion of lead in solid tin) are influencing the susceptibility to isothermal fatigue (including the nIP tests). It might also be noted that Ghosh [302] has cited an activation energy 1560 and $2045K^{-1}$ for thickening of an Ni_3Sn intermetallic layer formed during ageing of Sn-Pb solder on a copper substrate coated with a Ni-Pd composite layer.

For non-isothermal fatigue (i.e. the IP and OoP tests), the situation appears to be more complicated, since the fatigue life in both of these conditions is considerably shorter (about a factor of 5 for the IP and a factor of 10 for the OoP) than the extrapolated nIP

curve, out of all proportion to the small increase in average temperature. The life is considerably shorter than even the extrapolation of the 75°C isothermal test, so the effect, for the IP tests, still cannot be explained by the maximum stress always coinciding with the maximum temperature. Furthermore, such an explanation would still not account for the fatigue life being shorter for the OoP than the IP tests.

6.1.2 Fatigue life of Sn-3.8Ag-0.7Cu solder alloy

From Figure 4.15(b) and Table 4.2, it can be seen that the S-N curves behave in a broadly similar way between tests to the Sn-Pb alloy. The main difference is that the scatter on the lines is greater and the curves are less consistently parallel. Given the small number of points on each curve, it is not inconceivable that both effects are due to the greater microscopic heterogeneity of the lead-free alloy. As for the Pb-Sn alloy, an Arrhenius plot Figure 6.2 can be prepared for the effect of temperature on the fatigue life at fixed stress. Here, the activation energy (again expressed as Q/R) is higher at $5185K^{-1}$, although it might be noted that, because the curves converge at lower stress ranges, this activation energy will reduce with reducing stress range. This variation probably reflects the more complex microstructural changes going on the lead-free solder, where two phases (Cu_6Sn_5 and Ag_3Sn) are involved, with two distinct size distributions as primary and eutectic particles, respectively. The sensitivity of the phase diagram (Figure 3.2) to very small changes in composition is the most likely cause of the heterogeneity of the nature and occurrence of primary IMCs. As pointed out in Chapter 5, it is probably the coarsening of the eutectic that gives rise to the (more substantial than in Pb-Sn) change in hardness on ageing, although this may not be what affects the fatigue life.

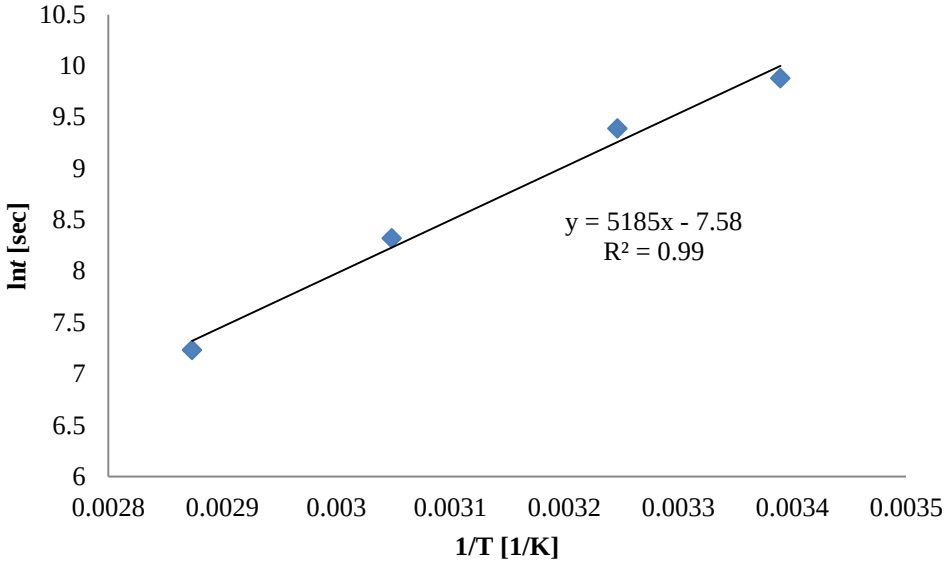

Figure 6.2: Arrhenius plot for time to failure against test temperature at a stress range of 12.4 MPa for Sn-3.8Ag-0.7Cu

Dutta *et al*. [238] have suggested that the coarsening of Ag_3Sn is related to the product of diffusion coefficient and solubility of Ag in Sn (both Arrhenius type activation processes) divided by temperature and also note that there is an additional factor caused by applied stress. Li *et al*. [303] have measured Cu_6Sn_5 growth at Sn-Ag-Cu/Cu interfaces to have a Q/R of around $1000K^{-1}$, whereas Tian *et al*. [304] estimate it to be around $8000K^{-1}$ for $(Cu,Ni)_6Sn_5$ and Cu_3Sn for the same alloy on Ni-plated Cu pads. This range of values, coupled with the multiple heterogeneity of the microstructure would seem to be enough evidence that the isothermal fatigue life of the Sn-Ag-Cu alloy is activated, which means there is a change in microstructure throughout the loading test in the same way as microstructural coarsening, possibly of large particles at the interface.

6.1.3 Comparison of stress- life of Sn-3.8Ag-0.7Cu and Pb-37Sn with other sources

There are only two studies of fatigue of solder joints where sufficient information is provided to plot stress-life data, and one other study on bulk solder.

Of these, Park and Lee [151] carried out strain-controlled, isothermal, reversing shear tests at room temperature on 9-ball arrays of Sn-37Pb and Sn-3.5Ag-0.75Cu mounted on Cu-FR4 substrates, very similar to the current work. They recorded a failure when the load in the array fell by a certain proportion, commencing at 50%, where it was clear

from resistance measurements that some of the joints had failed. They also published their cyclic load displacement data, so that it was possible (with a few linearising assumptions) to convert displacement range to stress range, and the resulting comparisons are shown in Figures 6.3 and 6.4 for the Sn-Pb and Sn-Ag-Cu alloys, respectively. On the other hand, Kim *et al*. [257] carried out shear vibration tests (essentially force-control) on complete PCB packages, again at room temperature, on Sn-36Pb-2Ag and Sn-1Ag-0.5Cu. They calculated the nominal shear stress in the solder using FEA and defined failure as a 10% increase in resistance across the package. The final published S-N curves for vibration frequencies of 15 Hz and 25 Hz could be used directly for comparison with the current work. Finally, Enke *et al*. [83] carried out wide-ranging tests on shear-lap bulk solder joints of Sn-40Pb under pure shear loading, again under force control at room temperature and Kanchanomai *et al*. [161] carried out strain-controlled tension LCF tests at R = -1 at room temperature on bulk specimens of Sn-3Ag-0.5Cu.

As can be seen from Figure 6.3, the stress ranges used by Park and Lee for the Sn-Pb alloy are much higher than those used in the current work for high-cycle fatigue, and are well into the plastic (low-cycle fatigue) range. At the one point of overlap, the life to 50% load drop is a factor of about 2 lower than the room temperature tests done here, although the slopes of the two S-N curves are very different, possibly due to the transition from high-cycle to low-cycle (elastic to plastic) fatigue. It is also possible that some of the difference is attributable to the microstructure of the alloy used by Park and Lee although it is not possible to assess this further from their micrographs. By contrast, the measurements of Kim *et al*. are well into the high-cycle fatigue range, and the slope is more consistent with those found in the current work, although fatigue lives are generally shorter than would be suggested by an extrapolation of the current RT isothermal S-N curve. Finally, the S-N curve of Kim *et al*. is more scattered, possibly due to the fact that failure of a proportion of multiple joints is used as the failure criterion. Overall, the picture is of isothermal S-N curves which are broadly consistent across the three studies at room temperature, with a steepening of the slope at higher stress ranges, presumably due to plasticity.

The bottom plot in Figure 6.3 includes data of Enke *et al*., measured on bulk samples, and it is plain that these data are well out of agreement with the other studies. One possible reason for this is that the lap shear tests lack any stress concentration, which was estimated to be around 2 in Chapter 5 of this thesis, and this factor alone would bring the data into considerably better agreement.

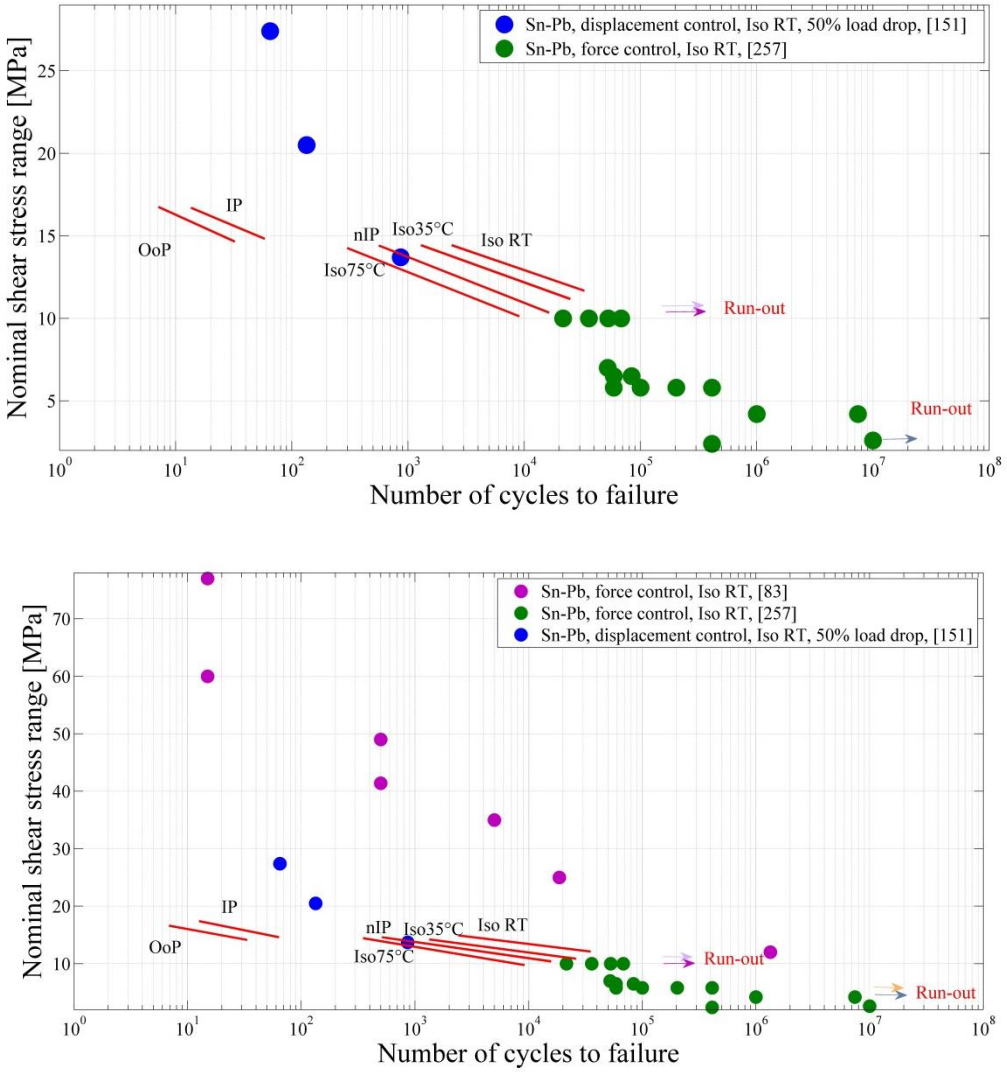

Figure 6.3: Comparison of the fatigue stress-life of Pb-Sn alloys from this work and other sources (top, BGA samples only, bottom BGA samples and bulk samples)

The comparison for the Sn-Ag-Cu alloys in Figure 6.4 show broadly the same effects as noted for the Sn-Pb alloys again with a general trend towards decreasing slope from LCF to HCF with the other published data indicating lower isothermal room temperature fatigue lives for a given stress range. Again, the bulk specimen data (this

time Kanchanomai *et al*. [161]) suggests considerably longer lives although, in this case conversion form tensile stress to maximum shear stress would result in a factor of two change in the stress which, along with the stress concentration effect noted above, would bring the curves more into line.

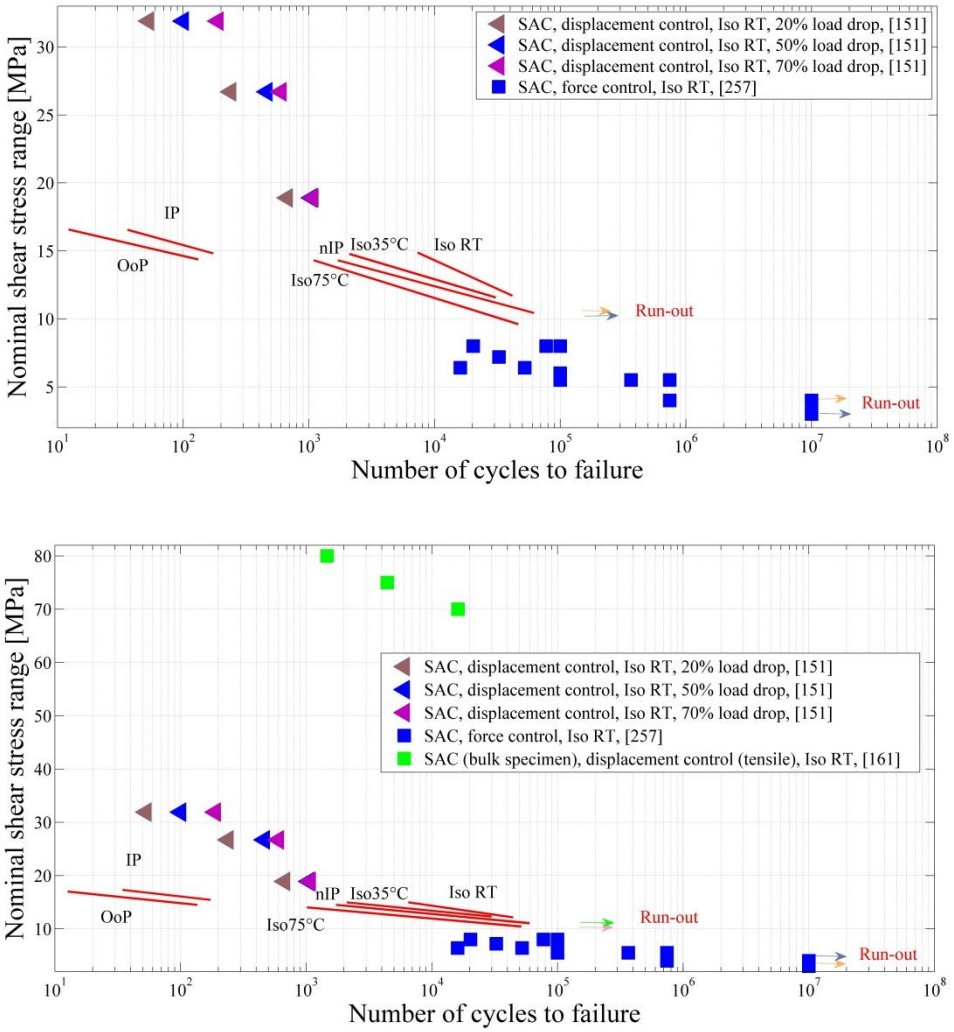

Figure 6.4: Comparison of the fatigue stress-life of SAC alloys from this work and other sources (top, BGA samples only, bottom BGA samples and bulk samples)

Of the data presented in Figures 6.3 and 6.4, only Kim *et al*. [257] found Sn-Ag-Cu alloys to be less resistant to fatigue than Sn-Pb at room temperature, although it must be noted that their Sn-Pb alloy also contained 2%Ag, whereas their Sn-Ag-Cu only contained 1%Ag. Thus, the observations are consistent with an improvement in fatigue life being associated with higher degree of particle strengthening, presumably due to interference with plastic crack growth. Andersson *et al.* [187], also found that the

fatigue life of lead-free solders (Sn-3.5Ag and Sn-4.0Ag-0.5Cu) and Wiese *et al.* [176], that life of Sn-4Ag-0.5Cu was better than Sn-37Pb at room temperature. Other alloys using IMC particle hardening, e.g. Sn-8Zn-3Bi studied by Peng *et al.* [180, 181], have also been found to have longer fatigue life than Sn-37Pb at room temperature. Solomon *et al.* [188, 189] found the isothermal fatigue resistance of both eutectic Sn-Ag and Sn-40Pb single lap joints to decrease with increasing temperature and the fatigue life of lead-free solder joints to be longer than leaded solder joints at both 35°C and 150°C.

As well as showing enhanced room temperature fatigue resistance, the current work also shows the IMC-strengthened alloy to be more resistant to isothermal fatigue at elevated temperature. This consistent with the work of Zhang *et al.* [178] who studied three levels of IMC strengthening; Sn-3.9Ag-0.6Cu, Sn-3.5Ag and Sn-0.7Cu, with only the third of these having poorer mechanical fatigue resistance than the eutectic Sn-37Pb at room temperature. However, at elevated temperatures, the fatigue resistance of all three lead-free solder alloys was better than Sn-37Pb.

Although a number of investigators, e.g. Kanchanomai *et al.* [182], for isothermal mechanical fatigue resistance of cast Sn-3.5Ag and Korhonen *et al.* [183] for isothermal mechanical fatigue resistance of dog-bone specimens of Sn-3.8Ag-0.7Cu, concur that durability decreases with increasing temperature, there are some researchers who have found that temperature has no effect on the fatigue life of solder. For example, Solomon *et al* [184] did not find any difference between the low cycle behaviour of 60Sn-40Pb at temperatures of -50, 35, and 125°C, and Vaynman *et al.* [185, 186] did not find any effect of temperature on the fatigue life of bulk cast Pb-3.5Sn and Sn-37Pb in the range 25 to 80°C. Furthermore, Duek *et al.* [152, 153] have suggested that the fatigue life of solder joints actually increases with increasing temperature. These observations are not necessarily at odds with the above discussion on stress-life behaviour, and may simply be due to the effect of plastic deformation as discussed in the following section.

Only one source, Eckert *et al.* [223, 224], has addressed the question of combined thermal cycling and vibration loading on solder joints, and theses authors showed that there was a clear interaction effect, the time to failure of BGA solder joints being

significantly shorter under combined loading than under temperature cycling or vibration alone at room temperature.

The low-cycle lives observed here certainly seem to suggest an interaction effect since lives are considerably shorter than an extrapolation of the equivalent isothermal curve (75ºC) would suggest. However, when expressed as stress-life at least, the relationship between the IP and OoP lives seem to be somewhat counter-intuitive. Since no other workers have studied the effect of phase on the TMF life of solders, it is necessary to look to studies on other alloys, which are also relatively scarce. In one study (Kliemt [305]) a cast aluminium alloy (AlSi6Cu4-T6) was tested under strain control, both IP and OoP, and a typical result is shown in Figure 6.5, where it can be seen that, at some strain ranges at least, the life is better under IP leading than it is under OoP loading. In an attempt to elucidate the rather complex stress-ageing phenomena involved in TMF of age-hardened aluminium alloys such as these, Toda *at al*. [306] applied a series of thermo-mechanical pre-treatments before assessing the IP TMF life. They found that OoP pre-treatments improved the subsequent IP fatigue life over the conventional T6 treatment, whereas IP pre-treatment reduced the subsequent fatigue life.

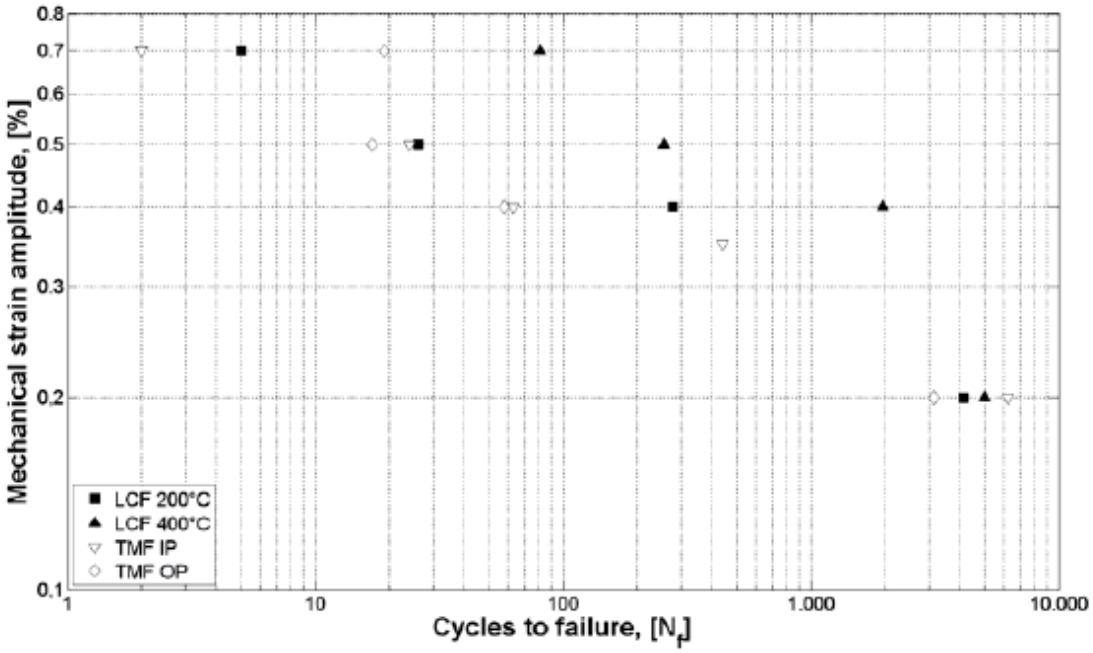

Figure 6.5: Mechanical strain amplitude vs. cycles to failure of AlSi6Cu4-T6 under low cycle fatigue and thermo-mechanical fatigue test conditions [305]

6.2 Constitutive behaviour of solder joints

As seen in the previous section, a complete understanding of fatigue behaviour and its comparison between tests depends not only on stress measurement and/or control, but also, potentially, on strain measurement and/or control. Before attempting this, it is necessary to ensure that comparisons of strain measurement are reliable, and this is particularly difficult in the case of BGA testing where it is often practice simply to record relative displacement between upper and lower substrate surfaces. Accordingly, this section is divided into four parts addressing, respectively; the relationship between displacement and strain, the cyclic behaviour, long-term deformation (creep) and, finally, strain-life behaviour.

6.2.1 Monotonic tests

The results of the monotonic tests on the lead-free specimen with copper substrate are shown in Figures 6.6 and 6.7 for room temperature and 75°C, respectively, expressed as nominal shear stress (using contact surface area) and nominal shear strain (shear displacement divided by height). The contribution to the displacement from the copper pillars was calculated from the known shear modulus, and was subtracted from the total shear displacement. The observed shear moduli at room temperature and 75°C are 7.4 GPa and 5.5 GPa, respectively. However, in the lead-free specimen with a FR-4 substrate at room temperature the apparent shear modulus is 2.2 GPa, as shown in Figure 6.8, so a significant proportion of the total shear displacement is associated with deformation of the substrate.

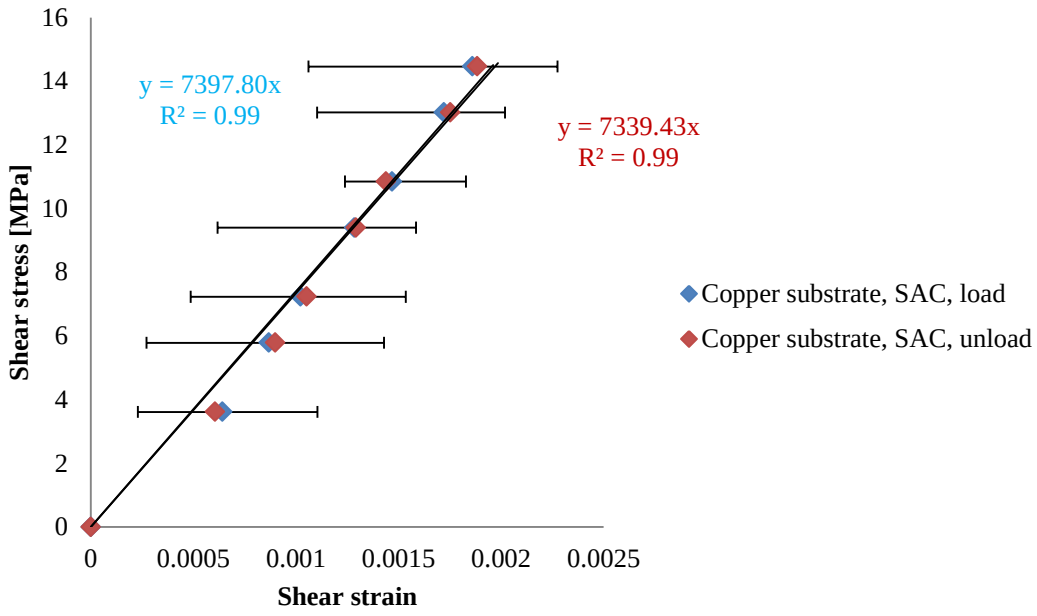

Figure 6.6: Lead-free solder shear stress-strain curves with copper substrate at room temperature

The value of the shear modulus of lead-free solder found here is similar to these measured on samples with copper substrates Table 2.2 [79, 80], the lower value given by the same authors (Table 2.2 [81]) being attributed to compliance of the test rig. Park and Lee [88] have also cited a lower value of shear modulus (2.54 GPa) using a 9-ball BGA, although this was in an elasto-plastic constitutive model: $\Delta\gamma = \frac{\Delta\tau}{G} + 2\left(\frac{\Delta\tau}{2K'}\right)^{\frac{1}{n'}}$.

where

τ: Shear stress

γ: Sum of elastic and plastic shear strain

G: Shear modulus

K': Cyclic-strength coefficient

n' : Cyclic strain- hardening

Table 6.1: Parameters for elasto-plastic constitutive model

	G [MPa]	***K' [MPa]***	***n'***
Value	2540	110.2	0.134

However, substituting $\Delta\tau = 10$ MPa, gives a value of $\Delta\gamma = 3.9 \times 10^{-3}$ which is still larger than the result in this current work ($\Delta\gamma = 1.35 \times 10^{-3}$). This discrepancy is possible due to displacements in the substrate, a matter that is discussed further in Section 6.2.4. Zhang *et al.* [87] have cited a value for *G* about a factor of 2 higher than found here, and was used in a simulation of cyclic behaviour, so is difficult to separate from their plastic and creep measurements. Even higher values of *G* are given by Pang *et al*. [74, 75], although the current authors were unable to verify the first of these from the published data (section 2.1.1) and, in any case, Pang *et al*. seem to have observed strains in both their tensile and shear tests a factor of around 100 higher than other authors.

One group [79, 80] have published Young's modulus as function of temperature:

E [GPa]=18.9 -0.044T [^{o}C] for Sn-37Pb

E [GPa] =18.6 -0.021T [^{o}C] for Sn-3.9Ag-0.6Cu

Using temperatures of 25°C and 75°C and a Poisson's ratio of 0.4, the values of shear modulus are in good agreement with those found here.

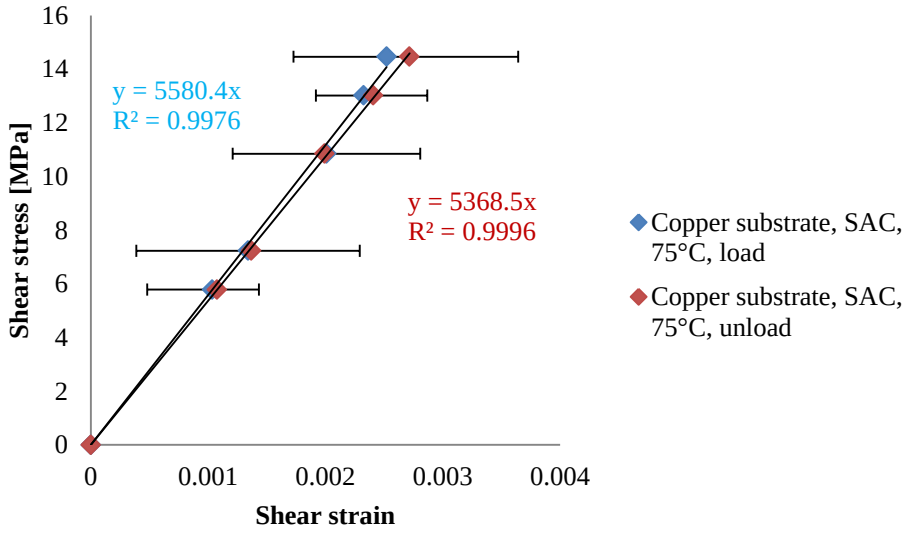

Figure 6.7: Lead-free solder shear stress-strain curves with copper substrate at 75°C

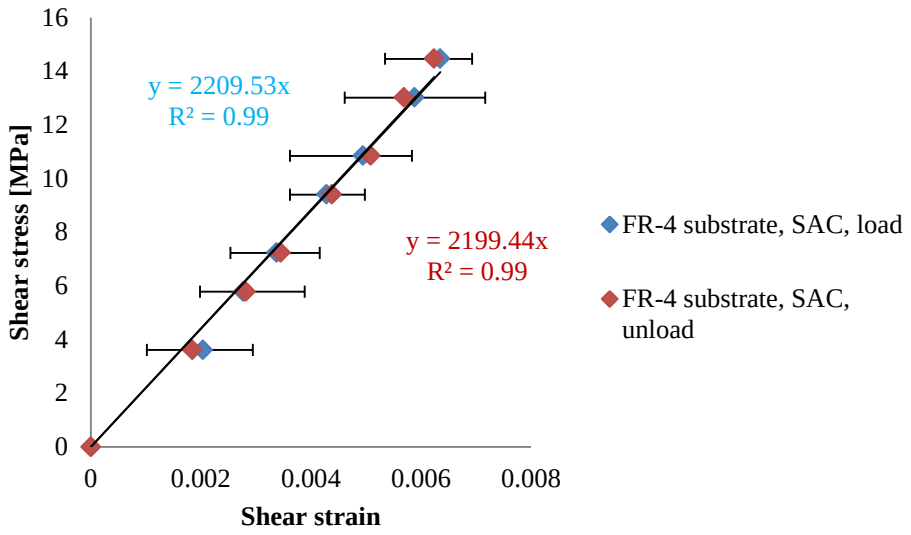

Figure 6.8: Lead-free shear stress-strain curves with FR-4 substrate at room temperature

Because the substrate and solder are under parallel loading, the shear strain in the FR-4 substrate can be calculated by using $\gamma_{\text{substrate}} = \tau\left(\frac{1}{2204.5} - \frac{1}{7368.6}\right)$ (Figures 6.6 and 6.8). The results from the leaded specimen with FR-4 with and without this correction at room temperature are shown in Figures 6.9 and 6.10, respectively, giving an estimated shear modulus for the Pb-Sn solder of (2.8-3.2 GPa). Published values of *G* for Pb-37Sn again very considerably although most are above the values found here. Of these, Shi *et al.* [73] and Haswell *et al.* [81] are closest, although these two sets of authors disagree about the effect of strain rate. The strain rate used in the current work is about 10^{-4} s^{-1} which is at the lower end of both sets of authors' ranges, and Shi *et al.* [73] had observed a considerable drop in *G* as the strain rate was reduced. The other authors cited in Table 2.2 all used somewhat higher strain rates than in the current work, so it seems that the values measured here are reasonably consistent with published work, especially given the uncertainties of grip effect, cooling rate, strain rate and Poisson's ratio.

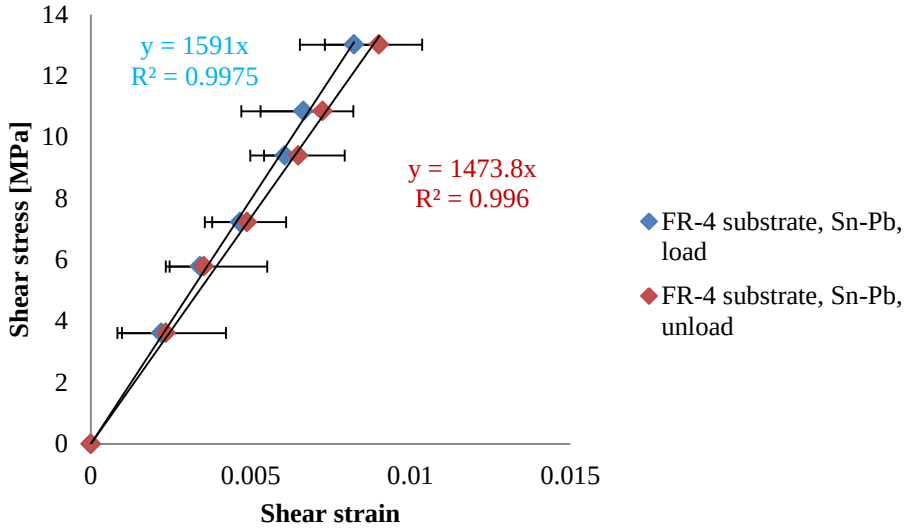

Figure 6.9: Leaded shear stress-strain curves with FR-4 substrate at room temperature

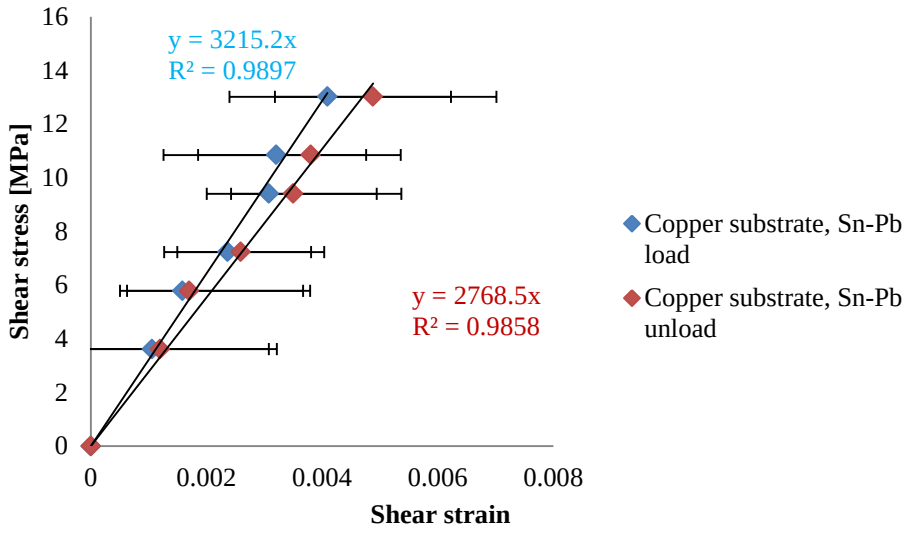

Figure 6.10: Leaded solder shear stress-strain curves corrected for effect of FR-4 at room temperature

6.2.2 Cyclic behaviour

As seen in Table 4.3, the Sn-Pb and Sn-Ag-Cu alloys behave in a fundamentally different way under isothermal room temperature fatigue, the Sn-Pb alloy showing an average overall cyclic hardening over the fatigue life and the Sn-Ag-Cu showing the opposite. In both cases the hardening/softening rate per cycle is of a similar magnitude and diminishes to zero as the stress range decreases, becoming negligible at a stress

range of 10.6 MPa, probably because the concentrated stress at the transition between solder and substrate drops below the yield stress of either alloy (Table 2.3).

As pointed out in the literature review, most researchers have observed cyclic softening in Sn-Pb alloys at room temperature [148-150]. However, Wen *et al*. [147] reported that 80% of their leaded samples exhibit cyclic hardening at room temperature, but that cyclic softening dominates at high temperature which is in agreement with the current work. All of the above authors carried out their tests on bulk specimens, although Wen *et al*. pointed out that cyclic period, strain range and stress level all affect softening/ hardening behaviour. In particular, they state that long cyclic periods lead to cyclic softening, which might account for the discrepancy.

Most investigators have reported cyclic softening in Sn-Ag-Cu alloys at room temperature [157, 159, 161, 162] in agreement with the current work. Others [151, 152] have observed that Sn-Ag-Cu exhibited initial cyclic hardening during fatigue test at room temperature, which is also observed in most of the tests at room temperature the current work.

6.2.3 Creep

As mentioned in section 4.4.3, the steady-state creep data did not follow Norton's law very well, although it should be pointed out the data and the tests were not configured to yield the parameters of a sinh law. Nevertheless, handbooks (e.g. [307]) do offer values for n of (6.3 for Sn-40Pb and 3.69 for Sn-3.8Ag-0.7Cu), comparable with the range observed here for Sn-Pb (4.2-13.6) but not for the Sn-Ag-Cu alloy (6.4-15.9). Others [308-310] have observed changes in with stress and temperature for a similar Sn-Ag-Cu alloy, although their reported values at 60°C and 80°C (around 8 to around 10) are still a bit lower than those observed here. However, Song *et al.* [309] have noted a change from low (n=4-6) to high (n=9-11) as the shear stress goes beyond a critical value (around 10 MPa depending a little on temperature) which is below those used here. Most authors agree that the anomalous creep behaviour of Sn-Ag-Cu alloys is associated with details of its microstructure and on interactions between coarsening and deformation.

There are many more observations of creep activation energy than stress exponent because all creep laws exhibit Arrhenius temperature dependence. The activation energies for leaded and lead-free solder alloys observed here were around 26 kJ/mol and 28 kJ/mol, respectively. As can be seen from Table 2.8, reported activation energies vary between 36 and 67 kJ/mol for Sn-37Pb, and 43 and 76 kJ/mol for Sn-Ag-Cu alloys of similar composition to those studied here. It also might be noted, as mentioned in sections 6.1.1 and 6.1.2, that the activation energy for the fatigue life is about 33 kJ/mol for Sn-37Pb and 43 kJ/mol for Sn-3.8Ag-0.7Cu. These higher values are more compatible with the lower bounds of the reported literature and since neither measure (stress-life or mean stress) is compatible with a specific creep test, it can be concluded that the processes influencing the fatigue life and the displacement drift are similar to the lower bound tests reported in the literature. Darveaux *et al.* [82] noted there is a relationship between the creep mechanism of solder alloys and stress regime. At low stress levels, Naborro-Herring and Coble are the main creep mechanisms. The latter of which is activated by grain boundary diffusion with a consequent low activation energy, which may explain the current results for Pb-Sn.

Table 6.2 shows the activation energy of Sn-Pb solder alloys for those studies reported in Table 2.8 for which the maximum stress was stated. In this work an activation energy of 33 kJ/mol was obtained at 14.2 MPa in shear (equivalent to 24-28MPa in tension) which is in agreement with the trends in Table 6.2.

Table 6.2: Variation of activation energy with maximum stress applied for Sn-Pb solder alloys

Maximum tensile stress applied [MPa]	***Q* [kJ/mol]**	**Reference**
20	35.74	[113]
30	44.9	[120]
70	54.1	[127]

Table 6.3 shows a similar selection of reported values of activation energy for Sn-Ag-Cu solder of similar composition to that used here. The corresponding activation energy in this work again at 14.2 MPa in shear (equivalent to 24-28MPa in tension) is again in agreement with the general trends, although there is a clearly anomalous value at 20

MPa [113], which may be attributable to the relatively high temperature range (20-150°C) compared with the current work (20-75°C) and consequent shift to Naborro-Herring creep.

Table 6.3: Variation of activation energy with maximum stress applied for Sn-Ag-Cu solder alloys

Maximum tensile stress applied [MPa]	***Q* [kJ/mol]**	**Reference**
20	76.13	[113]
30	43.13	[132]
70	62.3	[127]
100	65.3	[133]

6.2.4 Strain-life behaviour

As mentioned earlier, it is difficult to compare fatigue results in terms of stress-life behaviour when there is a significant amount of plastic deformation, whether by creep or time-independent plastic deformation. Equally, it has been shown that strain measurements on BGA and associated samples can include a significant contribution from deformation of the substrate. Figures 6.11 and 6.12 and Figures 6.13 and 6.14 highlight this difficulty for Pb-Sn and Sn-Ag-Cu alloys, respectively, compared with the work of Park and Lee discussed in Section 6.2.1.

In Figures 6.11 and 6.13, the stress range has been converted to strain range using the average displacement range over the life subtracting the known effects of FR-4 and using the nominal height of the solder ball, the maximum and minimum being shown as error bars. As can be seen, the effect of this conversion is to make the low-cycle results more congruent with the high-cycle results at 75°C, although there is still a certain amount of apparent mismatch in slope, particularly for the Pb-Sn alloy. Also, the differentiation between different temperatures in the isothermal tests is somewhat reduced in the strain-based presentation as is the scatter, particularly for the Sn-Ag-Cu alloy.

Figures 6.12 and 6.14 include the data reported by Park and Lee [151], where their displacement ranges have been converted to strain ranges using their published solder ball height. In order to see the effect more clearly, the strain range is shown in a logarithmic scale and, as can be seen, Park and Lee's data have a consistently higher slope and, more significantly; exhibited strain ranges which are typically a factor of 10 higher than in the current work. The second of these factors can be attributed largely to the observation in Section 6.2.1 that the effective shear modulus in this work is about 10 times that found by Park and Lee. The same point has been made by Fiedler [69]. Enk *et al.* [83] have also commented that load-controlled tests are less stable than displacement-controlled ones, although they acknowledge that defining the failure rate in terms of a load reduction of 50% gives similar results between displacement-controlled and load-controlled tests.

Although Park and Lee have reported that only BGA-based strain life curves, there are a number of studies based on bulk specimens. Figure 6.15 compares the current tests with a representative set of published strain-life data for Sn-Pb on bulk specimens, the line encompassing both load and displacement control. In Figure 6.16, the strains for Sn-Ag-Cu bulk specimens are tensile and this accounts for the factor of 2 offset. Clearly, however, the slopes for bulk specimen are higher than the current work, and are more like those measured by Park and Lee. This difference is likely to be due to the small stress range used in the current work, giving largely elastic strains.

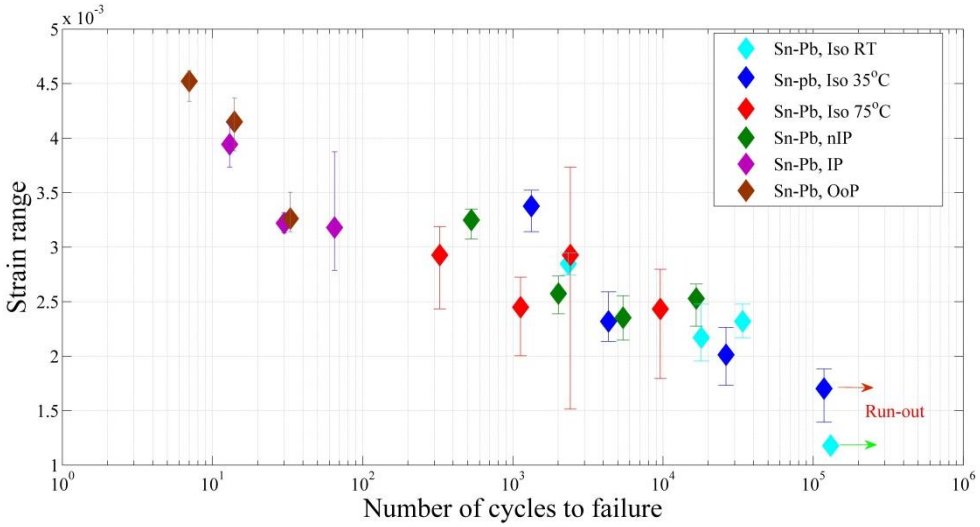

Figure 6.11: Strain-based fatigue life of Pb-Sn alloys (this work)

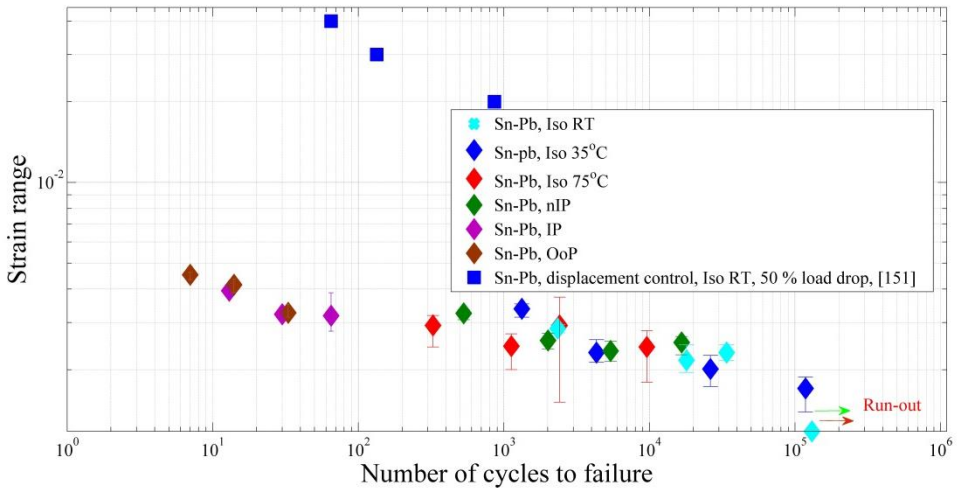

Figure 6.12: Comparison of strain-based fatigue life of Pb-Sn alloys between this work and Park and Lee [151] (BGA specimens)

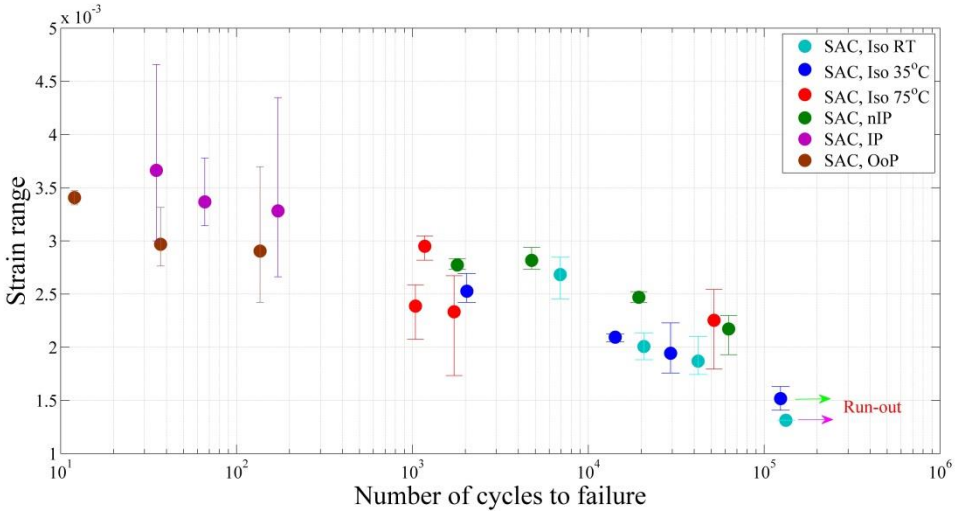

Figure 6.13: Strain-based fatigue life of SAC alloys (this work)

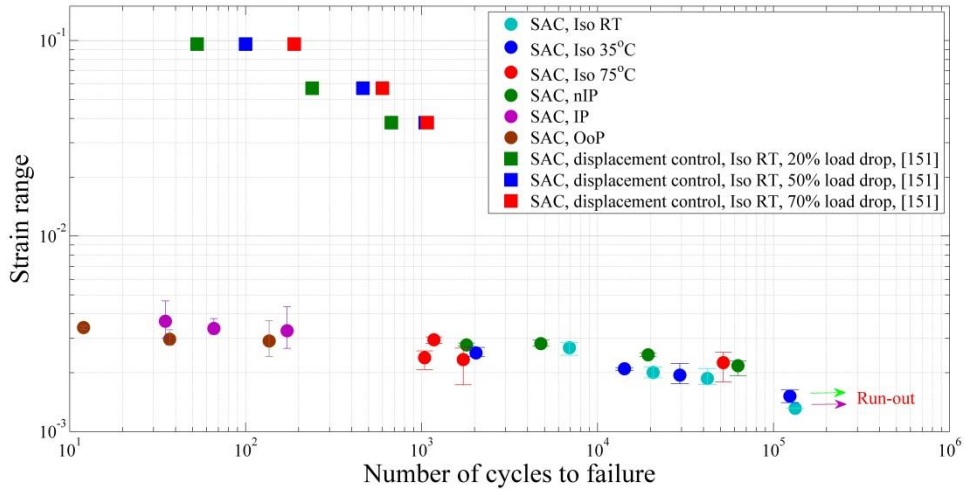

Figure 6.14: Comparison of strain-based fatigue life of SAC alloys between this work and Park and Lee [151] (BGA specimens)

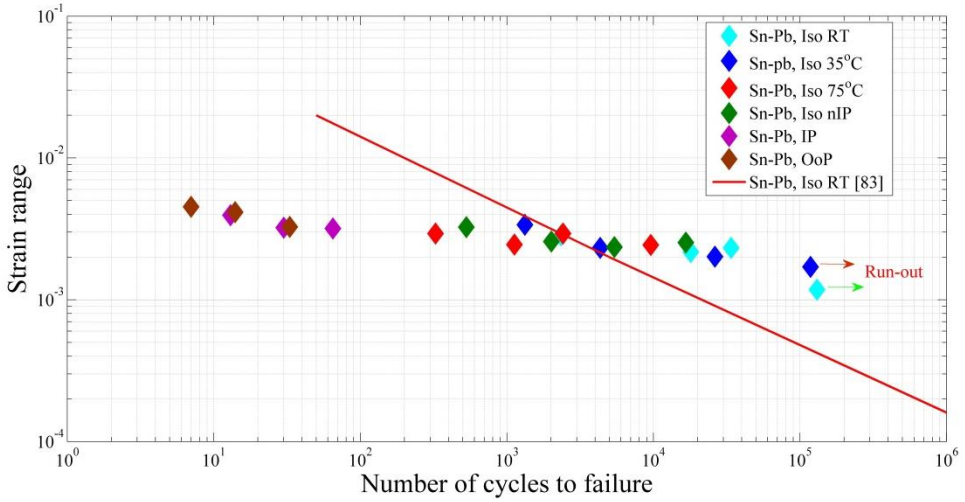

Figure 6.15: Comparison of strain-based fatigue life of Pb-Sn alloys between this work and other source [83] (bulk specimen)

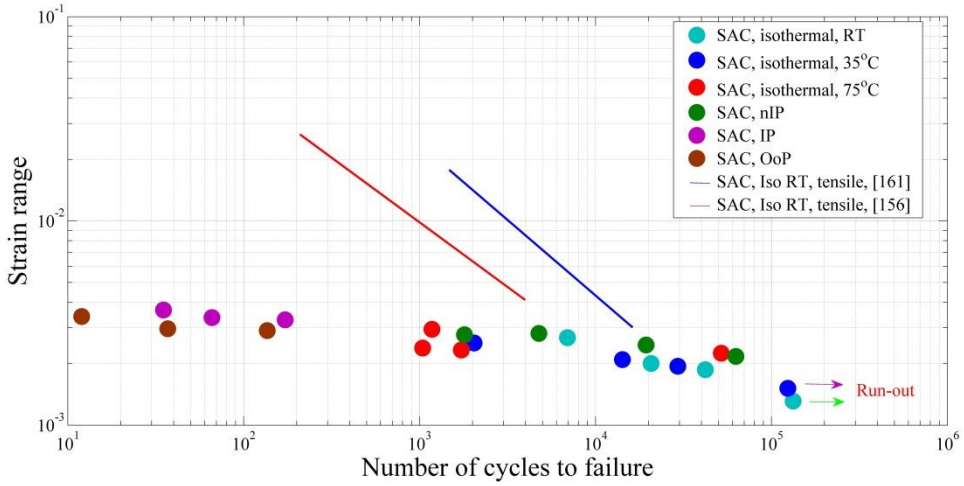

Figure 6.16: Comparison of strain-based fatigue life of SAC alloys between this work and other sources [156, 161] (bulk specimen)

Chapter 7: Conclusions and Future Work

This research set out to bring some coherence to the multitude of studies on the technical aspects of the replacement of lead-based solders. The approach was to compare the traditional Sn-Pb eutectic alloy with an exemplar replacement alloy, Sn-3.8Ag-0.7Cu. Although the focus was on TMF performance, a number of other closely associated issues were revealed in the course of the investigation on which conclusions can be drawn. Accordingly, the conclusions are presented in terms of; constitutive behaviour of solders, microstructure and microstructural evolution and, finally, fatigue performance.

7.1 Constitutive behaviour

There is considerable diversity in the reported properties of Sn-based solders. Much of this is due to their apparent sensitivity to temperature and strain rate, as well as their very low and variable yield stresses. Within the scope of this work, the following conclusions can be made about solder joint constitutive behaviour

- Although the measurement of load in the reported literature can be considered to be reliable, this cannot be said for displacement or strain measurements. Although this is less of an issue for bulk samples, these are significantly less representative of the configuration and condition involved in soldered joints. In view of this, it can be said that the current measurements are amongst the very few in which stress and strain in the solder have been measured unambiguously.
- The measured values of shear modulus for Sn-Pb solder (2.8-3.2 GPa) and for Sn-3.8Ag-0.7Cu solder (7.4 GPa at 25°C and 5.5 GPa at 75°C) are consistent with [73, 79-81].
- The creep data are difficult to compare with published tests which have been specifically designed to assess creep. However, from the values of stress exponent and the activation energies for strain drift and for fatigue life, it appears that significant creep is going on during tests, and Naborro-Herring and Coble are the creep mechanism which is consistent with the literature on Sn-Pb and Sn-Ag-Cu alloys [113, 132].

7.2 Effect of microstructure and constitution

Both alloys are essentially β-Sn with two distinct strengthening mechanisms. The Sn-Pb alloy has a dispersion of a weaker component (Pb) and so will rely on the reduction in

Sn grain size resulting from the eutectic solidification to bring about strengthening. The Sn-Ag-Cu alloy is dispersion strengthened by IMCs, the majority of which are very fine and are to be found in the interdendritic ternary eutectoid. Given this background, the following conclusions can be drawn about the effect of constitution on the observed properties:

- As mentioned by Kumar *et al*. [311], the elastic modulus of pure Sn is between 40 and 50 GPa, corresponding to a range in shear modulus from about 15 to 18 GPa, assuming Possion's ratio to be 0.36. Using a rule of mixtures, it might be expected that the shear modulus of Sn-Pb would be lower than this [67], whereas for Sn-Ag-Cu would be a little higher [311]. The current work is consistent with this in the relative values for the two alloys, but the absolute values are considerably lower. Some of the reason for this might be because of the relative areas at the middle of the solder ball compared with the contact surface.
- The lead-phase grains of the Pb-Sn alloy was found to coarsen over the period of fatigue testing, leading to a small, but significant, drop in hardness, in contrast to researchers who have not carried out a detailed analysis. The Sn-Ag-Cu alloy showed a larger difference in hardness, but this cannot be related to the size of the larger IMC particles, and was more likely due to coarsening of the eutectic IMC particles which could not be resolved in the current work.
- The primary IMC particles in the Sn-Ag-Cu alloy could occasionally be very large, sometimes up to 10% of the diameter of the solder ball. It is likely that this is the source of the scatter in mechanical behaviour of the Sn-Ag-Cu joints.

7.3 Fatigue performance

The fatigue tests in the current work covered a range from low-cycle to medium-high cycle fatigue and were carried out on BGAs under load control. In addition, a unique set of tests was carried out where temperature and stress cycling were in-phase and out-of-phase. Taken with the comments above on stress- and strain-measurement in solder joints, the following conclusions can be drawn:

7.3.1 Fatigue life based on stress range

- The Sn-Ag-Cu alloy showed better fatigue performance under all conditions tested, although the S-N curves exhibited greater scatter.

- As shown by the activation energy from the fatigue life, the lead-free solder was more resistant to degradation in durability as the temperature increases.
- Low-cycle fatigue lives are generally shorter than would be expected when extrapolating from the high-cycle fatigue range.
- Generally, the results are in agreement with other workers using load-control on BGA specimens. The lack of agreement with those using bulk specimens is attributed to stress-concentration at the fracture plane in BGAs.

7.3.2 Fatigue life based on strain range

- When expressed as strain-life, the differences between low-cycle and high-cycle and the effect of temperature are diminished. This is in agreement with some of the literatures.
- More surprisingly, the difference between the two alloys is increasingly less when expressed as strain-life, again in agreement with some researchers.
- Comparison of strain-life behaviour with the literature shows the current work to have a lower power dependent than workers either studying bulk or BGA specimens, attributable to the lack of plastic deformation in the current work.

7.4 Recommendations for future work

In terms of the holistic understanding of TMF in solder joints, the following issues remain to be resolved:

- The role of plastic deformation on TMF performance needs to be understood better for improved alloy selection. In particular, better models of the elastic, plastic, and creep behaviour need to be developed in terms of microstructure.
- For Sn-Ag-Cu alloys, it appears that most of the improved performance comes from the finely-dispersed IMSc and, indeed, the primary IMCs may have an adverse effect.
- There are clearly differences between measurements on BGAs and bulk specimens. Although some of these are associated with the difficulty in measuring the strain in BGAs, there is also as yet not fully understood, effect of BGA morphology and the detailed constitution of the interfacial area.

References

1. Manko, H.H., *Solders and soldering: materials, design, production, and analysis for reliable bonding*. 2001, New York: McGraw-Hill.
2. *Dudek, R.: Personal communication as part of the live project.*
3. Lee, N.C., *Introduction to surface mount technology*, in *Reflow Soldering Processes and Troubleshooting: SMT, BGA, CSP, and Flip Chip Technologies*. 2002, Newnes.
4. Lau, J.H., *Ball grid array technology*. 1995, New York: McGraw-Hill.
5. Primavera, A., *Influence of PCB parameters on chip scale package assembly and reliability (Part I).* Proceedings SMTA International Sept 12th, 1999.
6. Mawer, A., Cho, D., *Industry trends in ball grid array development.* IPC SMTA BGASymposiumProceedings, 1997.
7. Gilleo, K., *Area array packaging handbook*. 2002: McGraw-Hill.
8. Wassink, R.J.K., Verguld, M.M.F., *Manufacturing techniques for surface mounted assemblies*. 1995: Electrochemical Pub.
9. Judd, M., Brindley, K., *Soldering process*, in *Soldering in Electronics Assembly* 26 Mar 1999, Newnes. p. 11.
10. Plumbridge, W.J., Matela, R.J., Westwater, A., *Setting the scene*, in *Structural Integrity and Reliability in Electronics: Enhancing Performance in A Lead-Free Environment*. 2004, The Netherlands: Springer.
11. Judd, M., Brindley, K., *Soldering process*, in *Soldering in Electronics Assembly* 26 Mar 1999, Newnes. p. 51.
12. Minges, M.L. and Committee, A.I.H., *Electronic materials handbook: packaging*. 1989: ASM International.
13. Abtew, M., Selvaduray, G., *Lead-free solders in microelectronics.* Materials Science and Engineering R: Reports, 2000. **27**(5): p. 95-141.
14. Engelmaier, W., *Fatigue life of leadless chip carrier solder joints during power cycling.* Components, Hybrids, and Manufacturing Technology, IEEE Transactions on, 1983. **6**(3): p. 232-237.
15. Hall, P., *Forces, moments, and displacements during thermal chamber cycling of leadless ceramic chip carriers soldered to printed boards.* Components, Hybrids, and Manufacturing Technology, IEEE Transactions on, 1984. **7**(4): p. 314-327.
16. Hall, P., Dudderar, T.,Argyle, J., *Thermal deformations observed in leadless ceramic chip carriers surface mounted to printed wiring boards.* Components, Hybrids, and Manufacturing Technology, IEEE Transactions on, 1983. **6**(4): p. 544-552.
17. Scholand, A.J., Fulton, R. E., Bras, B., *Investigation of PWB layout by genetic algorithms to maximize fatigue life.* Journal of Electronic Packaging, Transactions of the ASME, 1999. **121**(1): p. 31-36.
18. Abe, K., Glaesemann, G. S., Gulati, S. T.,Hanson, T. A. , *Application of a phenomenological fatigue model to optical fibers.* Optical Engineering 1991. **30**(6).
19. Hall, P., *Creep and stress relaxation in solder joints of surface-mounted chip carriers.* Components, Hybrids, and Manufacturing Technology, IEEE Transactions on, 1987. **10**(4): p. 556-565.
20. Plumbridge, W.J., Matela, R.J., Westwater, A., *More complex mechanical behaviour*, in *Structural Integrity and Reliability in Electronics: Enhancing Performance in A Lead-Free Environment*. 2004, The Netherlands: Springer. p. 46.

21. Winterbottom, W.L., *Converting to lead-free solders: An automotive industry perspective.* JOM, July 1993. **45**(7): p. 20-24.
22. Korhonen, M.A., Brown, D. D.,Li, C. Y., *Mechanical properties of plated copper.* Proceedings of the Fall 1993 MRS Meeting, November 29, 1993 - December 3, 1993, 1994. **323**: p. 103-114.Publ by Materials Research Society.
23. Spearing, S.M., Tenhover, M. A., Lukco, D. B., Viswanathan, L., Hollen, D. K., *Models for the thermomechanical behavior of metal/ceramic laminates.* Proceedings of the Fall 1993 MRS Meeting, November 29, 1993 - December 3, 1993, 1994. **323**: p. 125-130.Publ by Materials Research Society.
24. Brandi S.D, L.S., Indacochea J.E, Xu R, *Brazeability and solderability of engineering materials*. 1993: ASM Handbook Volume 6, Welding, Brazing, and Soldering (ASM International).
25. Hwang, J.S., *Overview of Lead-Free Solders for Electronics & Microelectronics.* Proc. SMI'94, 1994: p. 405 - 421.
26. Tummala, R.R., Rymaszewski, Eugene. J.,Klopfenstein, Alan. G. . *Microelectronics packaging handbook*. 1989: Van Nostrand Reinhold.
27. Plumbridge, W.J., Matela, R.J., Westwater, A., *Introduction to the properties of materials*, in *Structural Integrity and Reliability in Electronics: Enhancing Performance in A Lead-Free Environment*. 2004, The Netherlands: Springer. p. 21.
28. Lau, J., Chang, C. , Lee ,R., Chen, T.-Y., Cheng, D. ,Tseng, T.J. , Lin, D., *thermal-fatigue life of solder bumped flip chip on micro via-in-pad (VIP) low cost substrates.* J. of Electronics Manufactruing, March 2000. **10**(1): p. 79.
29. Lee, N.C., Slattery, J. A.,Sovinsky, J. R.,Artaki, I.,Vianco, P.T., *Drop-in lead-free solder replacement.* Proceedings of the 1995 NEPCON West Technical Program. Part 2 (of 3), Febrary 26, 1995 - March 2, 1995, 1995. **2**: p. 1077-1086.Cahner Exposition Group.
30. Glazer, J., *Microstructure and mechanical properties of Pb-free solder alloys for low-cost electronic assembly: A review.* Journal of Electronic Materials, 1994. **23**(8): p. 693-700.
31. Schubert, A., Walter, H., Dudek, R., Michel, B., Lefranc, G., Otto, J., Mitic, G., *Thermo-mechanical properties and creep deformation of lead-containing and lead-free solders.* Proceedings,2001,International Symposium and Exhibition on Advanced Packaging Materials Processes, Properties and Interfaces, March 11, 2001 - March 14, 2001, 2001: p. 129-134.Institute of Electrical and Electronics Engineers Inc.
32. *http:// www.matweb.com. last accessed 15/7/2012*.
33. Puttlitz, K.J., *Overview of lead - free solder issues including selection*, in *Handbook of Lead-Free Solder Technology for Microelectronic Assemblies* K.J. Puttlitz, Stalter, K.A., Editor. 2004, Marcel Dekker Inc.
34. K.N.Subramanian, *High - temperature lead free solders with dispersoids*, in *Handbook of Lead-Free Solder Technology for Microelectronic Assemblies* K.J. Puttlitz, Stalter, K.A., Editor. 2004, Marcel Dekker Inc. p. 305.
35. Bradley, E., in *NEMI Pb-free interconnect task group report, IPC Work '99: An International Summit on Lead-Free Electronics Assemblies, Proceedings, Minneapolis, MN*. 1999.
36. Bath, J., Handwerker, C., and Bradley, E., *Research update: Lead-free solder alternatives, Circuits Assembly*. 2000. p.31–40.

37. *NCMS lead-free solder project final report, NCMS, National Center for Manufacturing Sciences, 3025 Boardwalk, Ann Arbor, Michigan 48108-3266, Report 0401RE96, August 1997, and CD-ROM database of complete dataset, including micrographs and raw data, August 1999. Information on how to order these can be obtained from http://www.ncms.org/.*
38. Artaki, I., Noctor, D.,Mather, J., Schroeder, S., Napp, D., Desantis, C., Desaulnier, W., Tsung-Yu, Pan., Felton, L., Palmer, M., Rosser, J., Felty, J., Vianco, P., Greaves, J., Whitten,G .,Yun, Zhu., Handwerker, C., *Research trends in lead-free soldering in the US: NCMS Lead-Free Solder Project.* Environmentally Conscious Design and Inverse Manufacturing, 1999. Proceedings. EcoDesign '99: First International Symposium On, 1999: p. 602-605.
39. Handwerker, C.A., *NCMS lead-free solder project: A summary of results, conclusions and recommendations, IPCWork '99: An International Summit on Lead-Free Electronics Assemblies, Proceedings, October 23–28, 1999; Minneapolis, MN.*
40. Handwerker, C.A., deKluizenaar, E.E., Suganuma, K. , Gayle, F.W., *Major international lead-free solder studies, in K. J. Puttlitz and K. A. Stalter, Eds., Issues and Implementation of Pb-free Technology in Microelectronics, McGraw-Hill, New York, .* 2004.
41. Moon, K., Boettinger, W., Kattner, U., Biancaniello, F., Handwerker, C., *The effect of Pb contamination on the solidification behavior of Sn-Bi solders.* Journal of Electronic Materials, 2001. **30**(1): p. 45-52.
42. Shangguan, D., Achari, A., *Evaluation of lead-free eutectic Sn-Ag solder for automotive electronics packaging applications.* Procedings Electronics Manufacturing Technology Symposium, 1994. 'Low-Cost Manufacturing Technologies for Tomorrow's Global Economy'. Proceedings 1994 IEMT Symposium., Sixteenth IEEE/CPMT International, 1994: p. 25-37 vol.1.
43. Arra, M., DongJi, X., Dongkai, S., *Performance of lead-free solder joints under dynamic mechanical loading.* Electronic Components and Technology Conference, 2002. Proceedings. 52nd, 2002: p. 1256-1262.
44. Plumbridge, W.J., Gagg, C.R., Peters, S., *The creep of lead-free solders at elevated temperatures.* Journal of Electronic Materials, 2001. **30**(9): p. 1178-83.
45. Harrison, M.R., Vincent, J. H. , *"IDEALS: Improved design life and environmentally aware manufacturing of electronics assemblies by lead-free soldering, Proc. IMAPS Europe'99 (Harrogate, GB), June 1999.*
46. *National Electronics Manufacturing Initiative (NEMI) Press Release, Jan. 24 2000, Information on how to order these can be obtained from http://www.nemi.org/newsroom/PR/2000/PR012400.html.*
47. Biglari, M.H., Oddy, M., Oud, M. A., Davis, P., De Kluizenaar, E. E., Langeveld, P., Schwarzbach D., *Pb-free solders based on SnAgCu, SnAgBi, SnAg, and SnCu, for wave soldering of electronic assemblies.* Proceedings, Electronics Goes Green 2000 plus a challenge for the next millnnium, 2000. **1**: p. 73-82.
48. Harrison, M.R., Vincent, J. H. , *Improved design life and environmentally aware manufacturing of electronic assemblies by lead-free soldering, http://www.lead-free.org/research/index.html.*

49. Richards, B., Levogne, C.L., Hunt, C.P., Nimmo, K. , Peters, S., Cusack, P., *Lead free soldering - an analysis of the current status of lead-free soldering*. 1999: DTI.
50. Kattner, U.R., Handwerker, C. A., *Calculation of phase equilibria in candidate solder alloys.* Zeitschrift fuer Metallkunde/Materials Research and Advanced Techniques, 2001. **92**(7): p. 740-746.
51. Kattner, U.R., *Phase diagrams for lead-free solder alloys.* JOM Journal of the Minerals, Metals and Materials Society, 2002. **54**(12): p. 45-51.
52. Puttlitz, K.J., Stalter, K.A., *Handbook of lead-free solder technology for microelectronic assemblies* 2004: Marcel Dekker Inc.
53. *Proprietary (patented) alloy ("Ecosol TSC") of Multicore Solders (special request).*
54. Ganesan, S., and Pecht, M, *Review of lead-free solder joint reliability*, in *Lead-Free Electronics*, E. Bradley, Handwerker, C.A., Bath, J., Editor. 2006, Wiley. p. 237.
55. Dasgupta , A., Huang, B., Lee, N.-C. , *Effect of lead-free alloys on voiding at microvia.* Apex , Anaheim, California, February 2004: p. 23-27.
56. Diepstraten, G., *Five steps to successful lead-free soldering: step 5.* Circuits Assembly (Magazine/Journal), August2001. **12**(8): p. 47-54.
57. Handwerker, C.A., deKluizenaar, E.E., Suganuma, K. , Gayle, F.W., *Major international lead (Pb) - free solder studies*, in *Handbook of Lead-Free Solder Technology for Microelectronic Assemblies* K.J. Puttlitz, Stalter, K.A., Editor. 2004, Marcel Dekker Inc. p. 698.
58. Kang, S.K. and Ference, T.G., *Nickel-alloyed tin-lead eutectic solder for surface mount technology.* Journal of Materials Research, 1993. **8**(5): p. 1033-1040.
59. Seelig, K. and Suraski, D., *Status of lead-free solder alloys.* 50th Electronic Components and Technology Conference, 2000: p. 1405-1409.
60. Database for Solder Properties with Emphasis on New Lead-Free Solders, R., Available:http://www.boulder.nist.gov/div853/lead−free/props01.html.
61. Hongtao, H., Jeffrey, S., *A review of mechanical properties of lead-free solders for electronic packaging.* Journal of Materials Science, 2009. **44**(5): p. 1141-1158.
62. Perkins, A.E. and Sitaraman, S.K., eds. *Solder joint reliability prediction for multiple environments*. 2010, Springer. 11.
63. Basaran, C. and Chandaroy, R., *Mechanics of Pb40/Sn60 near-eutectic solder alloys subjected to vibrations.* Applied Mathematical Modelling, 1998. **22**(8): p. 601-627.
64. Tang, H. and Basaran, C., *Influence of microstructure coarsening on thermomechanical fatigue behavior of Pb/Sn eutectic solder joints.* International Journal of Damage Mechanics, 2001. **10**(3): p. 235-255.
65. Kashyap, B.P. and Murty, G.S., *Experimental constitutive relations for the high temperature deformation of a Pb-Sn eutectic alloy.* Materials Science and Engineering, 1981. **50**(2): p. 205-213.
66. Kim, K.S., Huh, S.H., and Suganuma, K., *Effects of cooling speed on microstructure and tensile properties of Sn-Ag-Cu alloys.* Materials Science and Engineering A, 2002. **333**(1-2): p. 106-114.
67. Basaran, C. and Jiang, J., *Measuring intrinsic elastic modulus of Pb/Sn solder alloys.* Mechanics of Materials, 2002. **34**(6): p. 349-362.

68. Gomez, J. and Basaran, C., *Nanoindentation of Pb/Sn solder alloys; Experimental and finite element simulation results.* International Journal of Solids and Structures, 2006. **43**(6): p. 1505-1527.
69. Fiedler, B.A., *Fatigue failure kinetics and structural changes in lead-free interconnects due to mechanical and thermal cycling, PhD Thesis*. 2010, Northwestern University.
70. Mukai, M., Kawakami, T., Hiruta, Y., Takahashi, K., Kishimoto, K., and Shibuya, T., *Fatigue life estimation of solder joints in SMT-PGA packages.* Journal of Electronic Packaging, Transactions of the ASME, 1998. **120**(2): p. 207-212.
71. Sefton, D.E., Rist, M.A., and Gungor, S., *Rate-dependent deformation of Sn-3.5Ag lead-free solder.* Journal of Materials Science: Materials in Electronics, 2009. **20**(11): p. 1083-1089.
72. Bonnaud, E.L., *Issues on viscoplastic characterization of lead-free solder for drop test simulations.* Journal of Electronic Packaging, Transactions of the ASME, 2011. **133**(4).
73. Shi, X.Q., Zhou, W., Pang, H.L.J., and Wang, Z.P., *Effect of temperature and strain rate on mechanical properties of 63Sn/37Pb solder alloy.* Journal of Electronic Packaging, Transactions of the ASME, 1999. **121**(3): p. 179-185.
74. Schmetterer, C., *Cost 531 - Lead free solders: Handbook of properties of SAC solders and joints : ELFNET. Volume 2*. 2008, K-economy. p. 146.
75. Pang, J.H.L., Xiong, B.S., Neo, C.C., Zhang, X.R., and Low, T.H., *Bulk solder and solder joint properties for lead free 95.5Sn-3.8Ag-0.7Cu solder alloy.* 53rd Electronic Components and Technology Conference 2003, May 27, 2003 - May 30, 2003, 2003: p. 673-679.Institute of Electrical and Electronics Engineers Inc.
76. Pang, J.H.L. and Xiong, B.S., *Mechanical properties for 95.5Sn-3.8Ag-0.7Cu lead-free solder alloy.* Ieee Transactions on Components and Packaging Technologies, 2005. **28**(4): p. 830-840.
77. Enns, J.B., *Private communication of unpublished data. A&T Bell laboratories.* Whippany, New Jersey, 1983.
78. Engelmaier, W., *Test method considerations for SMT solder joint reliability.* Proceedings of the Technical Conference - IEPS, Fourth Annual International Electronics Packaging Conference., 1984: p. 360-369.Int Electronics Packaging Soc.
79. Zhang, Q., Dasgupta, A., and Haswell, P., *Viscoplastic constitutive properties and energy-partitioning model of lead-free Sn3.9Ag0.6Cu solder alloy.* 53rd Electronic Components and Technology Conference 2003, May 27, 2003 - May 30, 2003, 2003: p. 1862-1868.Institute of Electrical and Electronics Engineers Inc.
80. Zhang, Q., Dasgupta, A., and Haswell, P., *Partitioned viscoplastic-constitutive properties of the Pb-free Sn3.9Ag0.6Cu solder.* Nanostructured Magnetic Materials: Recent Progress in Magnetic Nanostructures, 2004. **33**: p. 1338-1349.Minerals, Metals and Materials Society.
81. Haswell, P. and Dasgupta, A., *Microthermomechanical analysis of lead-free SN-3.9AG-0.6CU alloys; Part I: Viscoplastic constitutive properties.* 2001 MRS Spring Meeting, April 16, 2001 - April 20, 2001, 2001. **682**: p. 26-32.Materials Research Society.

82. Darveaux, R. and Banerji, K., *Constitutive relations for tin-based solder joints.* IEEE transactions on components, hybrids, and manufacturing technology, 1992. **15**(6): p. 1013-1024.
83. Enke, N.F., Kilinski, T.J., Schroeder, S.A., and Lesniak, J.R., *Mechanical behaviors of 60/40 tin-lead solder lap joints.* Components, Hybrids, and Manufacturing Technology, IEEE Transactions on, 1989. **12**(4): p. 459-468.
84. Ren, W., Qian, Z., Lu, M., Liu, S., and Shangguan, D., *Thermal mechanical properties of two solder alloys.* Proceedings of the 1997 ASME International Mechanical Engineering Congress and Exposition, November 16, 1997 - November 21, 1997, 1997. **22**: p. 125-130.ASME.
85. Bjorndahl, W.D., Selk, K., and Chen, W., *Surface mount technology - capabilities and requirements.* Proceedings of the 1997 IEEE Aerospace Conference. Part 4 (of 4), February 1, 1997 - February 2, 1997, 1997. **4**: p. 285-291.
86. Larson, M.C. and Verges, M.A., *Extending the fatigue life of solder grid array (SGA) electronic packages.* Journal of Electronic Packaging, Transactions of the ASME, 2003. **125**(1): p. 18-23.
87. Zhang, Q., Dasgupta, A., Nelson, D., and Pallavicini, H., *Systematic study on thermo-mechanical durability of Pb-free assemblies: Experiments and FE analysis.* Journal of Electronic Packaging, Transactions of the ASME, 2005. **127**(4): p. 415-429.
88. Park, T.-S. and Lee, S.-B., *Cyclic stress –strain measurement tests of Sn3.5Ag0.75Cu solder joint.* Electronic Materials and Packaging, 2002, Proceedings of the 4th International Symposium, 2002: p. 317-323.Publ by IEEE.
89. Harada, M. and Satoh, R., *Mechanical characteristics of 96.5 Sn/3.5 Ag solder in micro-bonding.* Electronic Components and Technology Conference, 1990, 40th, 1990: p. 510-517 vol.1.
90. Pang, J.H.L., Xiong, B.S., and Low, T.H., *Low cycle fatigue study of lead free 99.3Sn-0.7Cu solder alloy.* International Journal of Fatigue, 2004. **26**(8): p. 865-872.
91. Lee, H.-T., Chen, M.-H., Jao, H.-M., and Liao, T.-L., *Influence of interfacial intermetallic compound on fracture behavior of solder joints.* Materials Science and Engineering A, 2003. **358**(1-2): p. 134-141.
92. Hu, J.M., Pecht, M., and Dasgupta, A., *Design of reliance die attach.* International Journal of Microcircuits and Electronic Packaging, 1993. **16**(1): p. 1-21.
93. Ohring, M., *Packaging materials, processes, and stresses*, in *Reliability and Failure of Electronic Materials and Devices*. 1998, Academic Press: San Diego. p. 417.
94. Hanna, C.E., Michaelides, S., Palaniappan, P., Baldwin, D.F., and Sitaraman, S.K., *Numerical and experimental study of the evolution of stresses in flip chip assemblies during assembly and thermal cycling.* Proceedings - Electronic Components and Technology Conference, 1999: p. 1001-1009.
95. Sitaraman, S.K., Raghunathan, R., and Hanna, C.E., *Development of virtual reliability methodology for area-array devices used in implantable and automotive applications.* Components and Packaging Technologies, IEEE Transactions on, 2000. **23**(3): p. 452-461.

96. Yang, Q.J., Shi, X.Q., Wang, Z.P., and Shi, Z.F., *Finite-element analysis of a PBGA assembly under isothermal/mechanical twisting loading.* Finite Elements in Analysis and Design, 2003. **39**(9): p. 819-833.
97. Mukai, M., Takahashi, H., Kawakami, T., Takahashi, K., Iwasaki, K., Kishimoto, K., and Shibuya, T., *Experimental and numerical verification of fatigue life estimation for solder bumps.* JSME International Journal, Series A: Solid Mechanics and Material Engineering, 2001. **44**(4): p. 567-572.
98. Xie, D.J., Chan, Y.C., Lai, J.K.L., and Hui, I.K., *Fatigue life estimation of surface mount solder joints.* Components, Packaging, and Manufacturing Technology, Part B: Advanced Packaging, IEEE Transactions on, 1996. **19**(3): p. 669-678.
99. Sun, Y. and Pang, J.H.L., *Digital image correlation for solder joint fatigue reliability in microelectronics packages.* Microelectronics Reliability, 2008. **48**(2): p. 310-318.
100. Schmidt, C.G., Simons, J.W., Kanazawa, C.H., and Erlich, D.C., *Thermal fatigue behavior of J-lead solder joints.* IEEE transactions on components, packaging, and manufacturing technology. Part A, 1995. **18**(3): p. 611-617.
101. de Kluizenaar, E.E., *Reliability of soldered joints. A description of the state of the art. Part 1.* Soldering and Surface Mount Technology, 1990(4): p. 27-38.
102. Jacques, S., Caldeira, A., Batut, N., Schellmanns, A., Leroy, R., and Gonthier, L., *A Coffin-Manson model to predict the TRIAC solder joints fatigue during power cycling.* 2011 14th European Conference on Power Electronics and Applications, EPE 2011, August 30, 2011 - September 1, 2011, 2011.IEEE Computer Society.
103. Bhate, D., Chan, D., Subbarayan, G., and Chiu, T.C., *Solder interconnection specimen design and test control procedure for valid constitutive modeling of solder alloys.* 10th Intersociety Conference on Thermal and Thermomechanical Phenomena and Emerging Technologies in Electronic Systems, ITherm 2006, May 30, 2006 - June 2, 2006, 2006. **2006**: p. 977-983.Institute of Electrical and Electronics Engineers Inc.
104. Poh, E.S.W., Zhu, W.H., Zhang, X.R., Wang, C.K., Sun, A.Y.S., and Tan, H.B., *Lead-free solder material characterization for thermo-mechanical modeling.* Thermal, Mechanical and Multi-Physics Simulation and Experiments in Microelectronics and Micro-Systems, 2008. EuroSimE 2008. International Conference on, 2008: p. 1-8.
105. Kariya, Y., Sato, K., Asari, S., and Kanda, Y., *Effect of joint size on low-cycle fatigue properties of Sn-Ag-Cu solder joint.* 2010 12th IEEE Intersociety Conference on Thermal and Thermomechanical Phenomena in Electronic Systems, ITherm 2010, June 2, 2010 - June 5, 2010, 2010.IEEE Computer Society.
106. Vianco, P., Rejent, J., and Martin, J., *The compression stress-strain behavior of Sn-Ag-Cu solder.* JOM, 2003. **55**(6): p. 50-55.
107. Qi, Y., Ghorbani, H.R., and Spelt, J.K., *Thermal fatigue of SnPb and SAC resistor joints: Analysis of stress-strain as a function of cycle parameters.* IEEE Transactions on Advanced Packaging, 2006. **29**(4): p. 690-700.
108. Kanda, Y. and Kariya, Y., *Influence of asymmetrical waveform on low-cycle fatigue life of micro solder joint.* Journal of Electronic Materials, 2010. **39**(2): p. 238-245.

109. Kok Ee, T., Xu, L., Pang, J.H.L., Lau, J.H., and Zhang, X.W., *Creep properties of Sn3wt%Ag0.5wt%Cu0.019wt%Ce (SACC) lead-free solder.* Electronics Packaging Technology Conference, 2008. EPTC 2008. 10th, 2008: p. 521-526.
110. Lu, H., Shi, H., and Zhou, M., *Thermally induced deformation of solder joints in real packages: Measurement and analysis.* Microelectronics Reliability, 2006. **46**(7): p. 1148-1159.
111. Suraski, D. and Seelig, K., *The current status of lead-free solder alloys.* IEEE Transactions on Electronics Packaging Manufacturing, 2001. **24**(4): p. 244-248.
112. Callister, W.D. and Rethwisch, D.G., in *Materials science and engineering: an introduction*. 2009, John Wiley and Sons. p. 265.
113. Ma, H., *Constitutive models of creep for lead-free solders.* Journal of Materials Science, 2009. **44**(14): p. 3841-3851.
114. Yifei, Z., Zijie, C., Mustafa, M., Suhling, J.C., Lall, P., and Bozack, M.J., *The influence of aging on the stress-strain and creep behavior of SAC solder alloys.* Thermal and Thermomechanical Phenomena in Electronic Systems (ITherm), 2010 12th IEEE Intersociety Conference on, 2010: p. 1-18.
115. Yifei, Z., Zijie, C., Suhling, J.C., Lall, P., and Bozack, M.J., *The effects of aging temperature on SAC solder joint material behavior and reliability.* Electronic Components and Technology Conference, 2008. ECTC 2008. 58th, 2008: p. 99-112.
116. Perkins, A.E. and Sitaraman, S.K., eds. Solder joint reliability prediction for multiple environments. 2010, Springer. 16.
117. Perkins, A.E. and Sitaraman, S.K., eds. Solder joint reliability prediction for multiple environments. 2010, Springer. 15.
118. Plumbridge, W.J., Matela, R.J., Westwater, A., in *Structural integrity and reliability in electronics: enhancing performance in a lead-free environment*. 2004, The Netherlands: Springer. p. 36.
119. Plumbridge, W.J., Matela, R.J., Westwater, A., in *Structural integrity and reliability in electronics: enhancing performance in a lead-free environment*. 2004, The Netherlands: Springer. p. 37.
120. Wiese, S., Schubert, A., Walter, H., Dukek, R., Feustel, F., Meusel, E., and Michel, B., *Constitutive behaviour of lead-free solders vs. lead-containing solders-experiments on bulk specimens and flip-chip joints.* Electronic Components and Technology Conference, 2001. Proceedings., 51st, 2001: p. 890-902.
121. Clech JP. Review and analysis of lead-free materials properties, N., Available at: http://www.metallurgy.nist.gov/solder/clech/Sn-Ag-Cu_Main.htm.
122. Zhang, L., Xue, S.-b., Gao, L.-l., Zeng, G., Chen, Y., Yu, S.-l., and Sheng, Z., *Creep behavior of SnAgCu solders with rare earth Ce doping.* Transactions of Nonferrous Metals Society of China, 2010. **20**(3): p. 412-417.
123. Zhang, G.S., Jing, H.Y., Xu, L.Y., Wei, J., and Han, Y.D., *Creep behavior of eutectic 80Au/20Sn solder alloy.* Journal of Alloys and Compounds, 2009. **476**(1-2): p. 138-141.
124. Schubert, A., Dudek, R., Auerswald, E., Gollbardt, A., Michel, B., and Reichl, H., *Fatigue life models for SnAgCu and SnPb solder joints evaluated by experiments and simulation.* Electronic Components and Technology Conference, 2003. Proceedings. 53rd, 2003: p. 603-610.

125. Xiao, Q. and Armstrong, W.D., *Tensile creep and microstructural characterization of bulk Sn3.9Ag0.6Cu lead-free solder.* Journal of Electronic Materials, 2005. **34**(2): p. 196-211.
126. Shi, X.Q., Wang, Z.P., Yang, Q.J., and Pang, H.L.J., *Creep behavior and deformation mechanism map of Sn-Pb eutectic solder alloy.* 2003. **125**: p. 81-88.American Society of Mechanical Engineers.
127. Qian, Z., Dasgupta, A., and Haswell, P., *Viscoplastic constitutive properties and energy-partitioning model of lead-free Sn3.9Ag0.6Cu solder alloy.* Electronic Components and Technology Conference, 2003. Proceedings. 53rd, 2003: p. 1862-1868.
128. Hannach, T., Worrack, H., Muller, W.H., and Hauck, T., *Creep in microelectronic solder joints: Finite element simulations versus semi-analytical methods.* 2009. **79**(6-7): p. 605-617.Springer Verlag.
129. Park, T.S., *A study on mechanical fatigue behaviors of ball grid array solder joints for electronic packaging*. 1986, DME 04041, KAIST (Daejeon, 2004).
130. Darveaux, R. and Banerji, K., *Constitutive relations for tin-based-solder joints.* Proceedings of the 42nd Electronic Components and Technology Conference, May 18, 1992 - May 20, 1992, 1992: p. 538-551.Publ by IEEE.
131. Darveaux R, B.K., Dody G., *Reliability of plastic ball grid array assembly*, in *Ball Grid Array Technology*, Lau. JL, Editor. 1995, McGraw-Hill: New York. p. 379.
132. Vianco PT. *Compression deformation response of 95.5Sn-3.9Ag-0.6Cu Solder, Available:http://www.seas.ucla.edu/eThinFilm/PbfreeWorkshop/pdf/vianco*.
133. Pang, J.H.L., Xiong, B.S., and Low, T.H., *Creep and fatigue characterization of lead free 95.5Sn-3.8Ag-0.7Cu solder.* 2004 Proceedings - 54th Electronic Components and Technology Conference, June 1, 2004 - June 4, 2004, 2004. **2**: p. 1333-1337.Institute of Electrical and Electronics Engineers Inc.
134. Wiese, S., Roellig, M., Mueller, M., Rzepka, S., Nocke, K., Luhmann, C., Kraemer, F., Meier, K., and Wolter, K.J., *The influence of size and composition on the creep of SnAgCu solder joints.* ESTC 2006 - 1st Electronics Systemintegration Technology Conference, September 5, 2006 - September 7, 2006, 2007. **2**: p. 912-925.Institute of Electrical and Electronics Engineers Inc.
135. Dudek, R., Nylen, M., Schubert, A., Michel, B., and Reichl, H., *An efficient approach to predict solder fatigue life and its application to SM- and area array components.* Electronic Components and Technology Conference, 1997. Proceedings., 47th, 1997: p. 462-471.
136. Shirley, D.R. and Spelt, J.K., *Primary creep in sn-3.8Ag-0.7Cu solder, part II: Constitutive creep model development and finite element analysis.* Journal of Electronic Materials, 2009. **38**(11): p. 2388-2397.
137. Pang, J.H.L. and Xiong, B.S., *Mechanical properties for 95.5Sn-3.8Ag-0.7Cu lead-free solder alloy.* Components and Packaging Technologies, IEEE Transactions on, 2005. **28**(4): p. 830-840.
138. Che, F.X., Zhu, W.H., Poh, E.S.W., Zhang, X.R., Zhang, X., Chai, T.C., and Gao, S., *Creep properties of Sn-1.0Ag-0.5Cu lead-free solder with Ni addition.* Journal of Electronic Materials, 2011. **40**(3): p. 344-354.
139. Wiese, S. and Wolter, K.J., *Creep of thermally aged SnAgCu-solder joints.* Microelectronics Reliability. **47**(2-3): p. 223-232.
140. Deplanque, S., Nuchter, W., Spraul, M., Wunderle, B., Dudek, R., and Michel, B., *Relevance of primary creep in thermo-mechanical cycling for life-time*

prediction in Sn-based solders. 6th International Conference on Thermal, Mechanical and Multi-Physics Simulation and Experiments in Micro-Electronics and Micro-Systems - EuroSimE 2005, April 18, 2005 - April 20, 2005, 2005. **2005**: p. 71-78.Institute of Electrical and Electronics Engineers Computer Society.

141. Anand, L., *Constitutive equation for the rate-dependent deformation of metals at elevated temperatures.* Journal of Engineering Materials and Technology, Transactions of the ASME, 1982. **104**(1): p. 12-17.
142. Chang, J., Wang, L., Dirk, J., and Xie, X., *Finite element modeling predicts the effects of voids on thermal shock reliability and thermal resistance of power device.* Welding Journal (Miami, Fla), 2006. **85**(3): p. 63-S-70-S.
143. Xu, C., Gang, C., and Sakane, M., *Prediction of stress-strain relationship with an improved Anand constitutive Model For lead-free solder Sn-3.5Ag.* Components and Packaging Technologies, IEEE Transactions on, 2005. **28**(1): p. 111-116.
144. Xu, C., Gang, C., and Sakane, M., *Modified Anand constitutive model for lead-free solder Sn-3.5Ag.* Thermal and Thermomechanical Phenomena in Electronic Systems, 2004. ITHERM '04. The Ninth Intersociety Conference on, 2004. **2**: p. 447-452 Vol.2.
145. Bhate, D., Chan, D., Subbarayan, G., Chiu, T.C., Edwards, D., and Gupta, V., *Constitutive behavior of Sn3.8Ag0.7Cu and Sn1.0Ag0.5Cu alloys at creep and low strain rate regimes.* ASME International Mechanical Engineering Congress and Exposition, IMECE 2007, November 11, 2007 - November 15, 2007, 2008. **5**: p. 183-196.American Society of Mechanical Engineers.
146. Clech, J.-p., *Review and analysis of lead-free solder material properties*, in *Lead-Free Electronics: iNEMI projects lead to successful manufacturing*, E. Bradley, Handwerker, C.A., Bath, J., Editor. 2007, Wiley.
147. Wen, S., Keer, L.M., Vaynman, S., and Lawson, L.R., *A constitutive model for a high lead solder.* Ieee Transactions on Components and Packaging Technologies, 2002. **25**(1): p. 23-31.
148. Chen, X., Yu, D.-H., and Kim, K.S., *Experimental study on ratcheting behavior of eutectic tin-lead solder under multiaxial loading.* Materials Science and Engineering A, 2005. **406**(1-2): p. 86-94.
149. Frear, D.R., *Thermomechanical fatigue of solder joints: A new comprehensive test method.* IEEE transactions on components, hybrids, and manufacturing technology, 1989. **12**(4): p. 492-501.
150. Hu, B., Zhou, P., Zhou, J., Yang, Y., and Wan, F. *The effect of temperature on low cycle fatigue of an eutectic solder*. in *2006 International Conference on Electronic Materials and Packaging, EMAP, December 11, 2006 - December 14, 2006*. 2006. Kowloon, China: Inst. of Elec. and Elec. Eng. Computer Society.
151. Park, T.-S. and Lee, S.-B., *Low cycle fatigue testing of ball grid array solder joints under mixed-mode loading conditions.* Journal of Electronic Packaging, 2005. **127**(3): p. 237-244.
152. Duek, M. and Hunt, C., *Low cycle isothermal fatigue properties of lead-free solders.* 9th Electronics Packaging Technology Conference, EPTC 2007, December 12, 2007 - December 12, 2007, 2007: p. 760-763.Institute of Electrical and Electronics Engineers Inc.

153. Duek, M. and Hunt, C., *Low cycle isothermal fatigue properties of lead-free solders.* Soldering and Surface Mount Technology, 2007. **19**(4): p. 25-32.
154. Subramanian, K.N., *Role of anisotropic behaviour of Sn on thermomechanical fatigue and fracture of Sn-based solder joints under thermal excursions.* Fatigue and Fracture of Engineering Materials and Structures, 2007. **30**(5): p. 420-431.
155. Liang, J., Gollhardt, N., Lee, P.S., Schroeder, S.A., and Morris, W.L., *Study of fatigue and creep behaviour of four high temperature solders.* Fatigue and Fracture of Engineering Materials and Structures, 1996. **19**(11): p. 1401-1409.
156. Zeng, Q.-L., Wang, Z.-G., Xian, A.I.P., and Shang, J.K., *Cyclic softening of the Sn-3.8Ag-0.7Cu lead-free solder alloy with equiaxed grain structure.* Journal of Electronic Materials, 2005. **34**(1): p. 62-67.
157. Shang, J.K., Zeng, Q.L., Zhang, L., and Zhu, Q.S., *Mechanical fatigue of Sn-rich Pb-free solder alloys.* Journal of Materials Science: Materials in Electronics, 2007. **18**(1-3): p. 211-227.
158. Yang, L., Yin, L., Roggeman, B., and Borgesen, P., *Effects of microstructure evolution on damage accumulation in lead-free solder joints.* 60th Electronic Components and Technology Conference, ECTC 2010, June 1, 2010 - June 4, 2010, 2010: p. 1518-1523.
159. Zhu, Q.S., Wang, Z.G., Zeng, Q.L., Wu, S.D., and Shang, J.K., *Rapid cycle-dependent softening of equal channel angularly pressed Sn-Ag-Cu alloy.* Journal of Materials Research, 2008. **23**(10): p. 2630-2638.
160. Kang, S.K., Lauro, P., Shih, D.-Y., Henderson, D.W., Gosselin, T., Bartelo, J., Cain, S.R., Goldsmith, C., Puttlitz, K.J., and Hwang, T.-K., *Evaluation of thermal fatigue life and failure mechanisms of Sn-Ag-Cu solder joints with reduced Ag contents.* 2004 Proceedings - 54th Electronic Components and Technology Conference, June 1, 2004 - June 4, 2004, 2004. **1**: p. 661-667.Institute of Electrical and Electronics Engineers Inc.
161. Kanchanomai, C., Miyashita, Y., and Mutoh, Y., *Low-cycle fatigue behavior of Sn-Ag, Sn-Ag-Cu, and Sn-Ag-Cu-Bi lead-free solders.* Journal of Electronic Materials, 2002. **31**(5): p. 456-465.
162. Kanchanomai, C., *Cyclic deformation behavior of Sn-Ag-Cu-Bi solder.* Proceedings of 41st Kasetsart University Annual Conference, February 3, 2003 - February 7, 2003, 2003: p. 359-366.
163. Cutiongco, E.C., Vaynman, S., Fine, M.E., and Jeannotte, D.A., *Isothermal fatigue of 63Sn-37Pb solder.* Journal of Electronic Packaging, Transactions of the ASME, 1990. **112**(2): p. 110-114.
164. Erinc, M., Schreurs, P.J.G., and Geers, M.G.D., *Integrated numerical–experimental analysis of interfacial fatigue fracture in SnAgCu solder joints.* International Journal of Solids and Structures, 2007. **44**(17): p. 5680-5694.
165. Erinc, M., Schreurs, P.J.G., and Geers, M.G.D. *A coupled numerical and experimental study on thermo-mechanical fatigue failure in SnAgCu solder joints*. in *Thermal, Mechanical and Multi-Physics Simulation Experiments in Microelectronics and Micro-Systems, 2007. EuroSime 2007. International Conference on*. 2007.
166. Di Maio, D., Murdoch, C., Thomas, O., and Hunt, C., *The degradation of solder joints under high current density and low-cycle fatigue.* Thermal, Mechanical and Multi-Physics Simulation, and Experiments in Microelectronics and Microsystems (EuroSimE), 2010 11th International Conference on, 2010: p. 1-6.

167. Basaran, C., Tang, H., and Nie, S., *Experimental damage mechanics of microelectronic solder joints under fatigue loading.* Mechanics of Materials, 2004. **36**(11): p. 1111-1121.
168. Kanchanomai, C. and Mutoh, Y., *Temperature effect on low cycle fatigue behavior of Sn-Pb eutectic solder.* Scripta Materialia, 2004. **50**(1): p. 83-88.
169. Di Maio, D., Thomas, O., Dusek, M., and Hunt, C., *Novel Testing Instrument for Lead-Free Solder Characterization.* Instrumentation and Measurement, IEEE Transactions on, 2011. **60**(10): p. 3444-3450.
170. Summers, T.S.E. and Morris Jr, J.W., *Isothermal fatigue behavior of Sn-Pb solder joints.* Journal of Electronic Packaging, Transactions of the ASME, 1990. **112**(2): p. 94-99.
171. Solomon, H.D., *Strain-life behavior in 60/40 solder.* Journal of Electronic Packaging, Transactions of the ASME, 1989. **111**(2): p. 75-82.
172. Vaynman, S., *Fatigue life prediction of solder material: Effect of ramp time, hold time and temperature.* 1990 Proceedings of the 40th Electronic Components and Technology Conference, May 20, 1990 - May 23, 1990, 1990. **1**: p. 505-509.Publ by IEEE.
173. Kanchanomai, C. and Mutoh, Y., *Low-cycle fatigue prediction model for Pb-free solder 96.5Sn-3.5Ag.* Journal of Electronic Materials, 2004. **33**(4): p. 329-333.
174. Pang, J.H.L., Xiong, B.S., and Low, T.H., *Low cycle fatigue study of lead free 99.3Sn–0.7Cu solder alloy.* International Journal of Fatigue, 2004. **26**(8): p. 865-872.
175. Kariya, Y. and Otsuka, M., *Mechanical fatigue characteristics of Sn-3.5Ag-X (x = Bi, Cu, Zn and In) solder alloys.* Journal of Electronic Materials, 1998. **27**(11): p. 1229-1235.
176. Wiese, S., Jakschik, S., Feustel, F., and Meusel, E., *Fracture behaviour of flip chip solder joints.* 51st Electronic Components and Technology Conference, May 29, 2001 - June 1, 2001, 2001: p. 1299-1306.Institute of Electrical and Electronics Engineers Inc.
177. Lee, K.O., Yu, J., Park, T.S., and Lee, S.B., *Low-cycle fatigue characteristics of Sn-based solder joints.* Journal of Electronic Materials, 2004. **33**(4): p. 249-257.
178. Zhang, Q., Dasgupta, A., and Haswell, P., *Isothermal mechanical durability of three selected PB-free solders: Sn3.9Ag0.6Cu, Sn3.5Ag, and Sn0.7Cu.* Journal of Electronic Packaging, Transactions of the ASME, 2005. **127**(4): p. 512-522.
179. Cuddalorepatta, G. and Dasgupta, A., *Effect of cyclic fatigue damage accumulation on the elastic-plastic properties of SAC305 solders.* Thermal, Mechanical and Multi-Physics simulation and Experiments in Microelectronics and Microsystems, 2009. EuroSimE 2009. 10th International Conference on, 2009: p. 1-7.
180. Peng, S., Andersson, C., Wei, X., Cheng, Z., Shangguan, D., and Liu, J., *Coffin-Manson constant determination for a Sn-8Zn-3Bi lead-free solder joint.* Soldering and Surface Mount Technology, 2006. **18**(2): p. 4-11.
181. Peng, S., Andersson, C., Zhaonian, C., Zonghe, L., Dongkai, S., and Liu, J., *Coffin-Manson equation determination for Sn-Zn based lead-free solder joints.* High Density Microsystem Design and Packaging and Component Failure Analysis, 2005 Conference on, 2005: p. 1-6.
182. Kanchanomai, C. and Mutoh, Y., *Effect of temperature on isothermal low cycle fatigue properties of Sn–Ag eutectic solder.* Materials Science and Engineering: A, 2004. **381**(1-2): p. 113-120.

183. Korhonen, T.-M., Lehman, L., Korhonen, M., and Henderson, D., *Isothermal Fatigue Behavior of the Near-Eutectic Sn-Ag-Cu Alloy between −25°C and 125°C.* Journal of Electronic Materials, 2007. **36**(2): p. 173-178.
184. Solomon, H., *Fatigue of 60/40 solder.* Components, Hybrids, and Manufacturing Technology, IEEE Transactions on, 1986. **9**(4): p. 423-432.
185. Vaynman, S., *Effect of temperature on isothermal fatigue of solders.* Components, Hybrids, and Manufacturing Technology, IEEE Transactions on, 1990. **13**(4): p. 909-913.
186. Vaynman, S., *Effect of temperature on isothermal fatigue of solders.* Proceedings of the 1990 Second Intersociety Conference on Thermal Phenomena in Electronic Systems - I-THERM II, May 23, 1990 - May 25, 1990, 1990: p. 16-20.Publ by IEEE.
187. Andersson, C., Lai, Z., Liu, J., Jiang, H., and Yu, Y., *Comparison of isothermal mechanical fatigue properties of lead-free solder joints and bulk solders.* Materials Science and Engineering: A, 2005. **394**(1-2): p. 20-27.
188. Solomon, H.D., *Low cycle fatigue of Sn96 solder with reference to eutectic solder and a high Pb solder.* Journal of Electronic Packaging, 1991. **113**(2): p. 102-108.
189. Solomon, H.D. *Low cycle fatigue of Sn96 solder with reference to eutectic solder and a high Pb solder*. in *Proceedings of the Winter Annual Meeting, November 25, 1990 - November 30, 1990*. 1990. Dallas, TX, USA: Publ by ASME.
190. Che, F.X., Pang, J.H.L., Xiong, B.S., Xu, L., and Low, T.H., *Lead free solder joint reliability characterization for PBGA, PQFP and TSSOP assemblies.* 55th Electronic Components and Technology Conference, ECTC, May 31, 2005 - June 4, 2005, 2005. **1**: p. 916-921.Institute of Electrical and Electronics Engineers Inc.
191. Xu, L., Pang, J.H.L., and Che, F.X., *Intermetallic growth and failure study for Sn-Ag-Cu/ENIG PBGA solder joints subject to thermal cycling.* 55th Electronic Components and Technology Conference, ECTC, May 31, 2005 - June 4, 2005, 2005. **1**: p. 682-686.Institute of Electrical and Electronics Engineers Inc.
192. Arulvanan, P., Zhong, Z., and Shi, X., *Effects of process conditions on reliability, microstructure evolution and failure modes of SnAgCu solder joints.* Microelectronics Reliability, 2006. **46**(2-4): p. 432-439.
193. Frear, D.R., Jang, J.W., Lin, J.K., and Zhang, C., *Pb-free solders for flip-chip interconnects.* JOM, 2001. **53**(6): p. 28-33.
194. Schubert, A., Dudek, R., Walter, H., Jung, E., Gollhardt, A., Michel, B., and Reichl, H., *Reliability assessment of flip-chip assemblies with lead-free solder joints.* 52nd Electronic Components and Technology Conference, May 28, 2002 - May 31, 2002, 2002: p. 1246-1255.Institute of Electrical and Electronics Engineers Inc.
195. Syed, A. *Reliability and Au embrittlement of lead free solders for BGA applications*. in *International Symposium and Exhibition on Advanced Packaging Materials Processes, Properties and Interfaces, March 11, 2001 - March 14, 2001*. 2001. Braselton, GA, United states: Institute of Electrical and Electronics Engineers Inc.
196. Syed, A., *Durability of lead-free solder connections for area-array packages.* IPC SMEMA Council APEX 2001: p. 2-7.

197. Suhling, J.C., Gale, H.S., Johnson, R.W., Islam, M.N., Shete, T., Lall, P., Bozack, M.J., Evans, J.L., Seto, P., Gupta, T., and Thompson, J.R., *Thermal cycling reliability of lead free solders for automotive applications.* ITherm 2004 - Ninth Intersociety Conference on Thermal and Thermomechanical Phenomena in Electronic Systems, June 1, 2004 - June 4, 2004, 2004. **2**: p. 350-357.Institute of Electrical and Electronics Engineers Inc.
198. Yang, C., Chan, Y.S., Lee, S.W.R., Ye, Y., and Liu, S., *Comparison of thermal fatigue reliability of SnPb and SAC solders under various stress range conditions.* 2009 International Conference on Electronic Packaging Technology and High Density Packaging, ICEPT-HDP 2009, August 10, 2009 - August 13, 2009, 2009: p. 1119-1123.IEEE Computer Society.
199. Barker, D., Vodzak, J., Dasgupta, A., and Pecht, M., *Combined vibrational and thermal solder joint fatigue. A generalized strain versus life approach.* Journal of Electronic Packaging, Transactions of the ASME, 1990. **112**(2): p. 129-134.
200. Barker, D.B., Dasgupta, A., and Pecht, M.G., *PWB solder joint life calculations under thermal and vibrational loading.* Journal of the IES, 1992. **35**(1): p. 17-25.
201. Barry, N., Jones, I.P., Hirst, T., Fox, I.M., and Robins, J., *High-cycle fatigue testing of Pb-free solder joints.* Soldering and Surface Mount Technology, 2007. **19**(2): p. 29-38.
202. Blanks, H.S., *Accelerated vibration fatigue life testing of leads and soldered joints* Microelectronics Reliability, 1976. **15**(3): p. 213-219.
203. Zhao, Y., Basaran, C., Cartwright, A., and Dishongh, T., *Thermomechanical behavior of micron scale solder joints under dynamic loads.* Mechanics of Materials, 2000. **32**(3): p. 161-173.
204. Zhao, Y., Basaran, C., Cartwright, A., and Dishongh, T., *Thermomechanical behavior of micron scale solder joints: An experimental observation.* Journal of the Mechanical Behavior of Materials, 1999. **10**(3): p. 135-146.
205. Darbha, K., Ling, S., and Dasgupta, A., *Stress analysis of surface-mount interconnections due to vibrational loading.* Journal of Electronic Packaging, Transactions of the ASME, 1997. **119**(3): p. 183-188.
206. Wang, H., Zhao, M., and Guo, Q., *Vibration fatigue experiments of SMT solder joint.* 2004. **44**(7): p. 1143-1156.Elsevier Ltd.
207. Plaza, G., Zhou, Y., Osterman, M., and Dasgupta, A., *SnAgCu (SAC) durability under vibration loading at different isothermal temperature conditions.* ASME Electronic and Photonics Packaging Division, July 8, 2007 - July 12, 2007, 2007. **1**: p. 515-521.American Society of Mechanical Engineers.
208. Chandaroy, R. and Basaran, C., *Damage mechanics of surface mount technology solder joints under concurrent thermal and dynamic loading.* Journal of Electronic Packaging, Transactions of the ASME, 1999. **121**(2): p. 61-68.
209. Zhao, Y., Basaran, C., Cartwright, A., and Dishongh, T., *Inelastic behavior of microelectronics solder joints under concurrent vibration and thermal cycling.* Thermomechanical Phenomena in Electronic Systems -Proceedings of the Intersociety Conference, 2000. **2**: p. 174-180.
210. Upadhyayula, K. and Dasgupta, A., *Incremental damage superposition approach for reliability of electronic interconnects under combined accelerated stresses.* Proceedings of the 1997 ASME International Mechanical Engineering Congress and amp; Exposition, November 16, 1997 - November 21, 1997, 1997.ASME.

211. Basaran, C., Cartwright, A., Zhao, Y., and Dishongh, T., *Reliability of BGA solder bumps.* Advanced Packaging, 2002. **11**(7): p. 47-56.
212. Basaran, C., Zhao, Y., Cartwright, A., and Dishongh, T., *Effects of thermodynamic loading.* Advanced Packaging, 2000. **9**(9).
213. Basaran, C., Cartwright, A., and Zhao, Y., *Experimental damage mechanics of microelectronics solder joints under concurrent vibration and thermal loading.* International Journal of Damage Mechanics, 2001. **10**(2): p. 153-170.
214. Steinberg, D.S., *Vibration analysis for electronic equipment*. 1988: Wiley.
215. Markstein, H.W., *Designing electronics for high vibration and shock.* Electronic Packaging and Production, 1987. **27**(4): p. 40-43.
216. Steinberg, D.S., *Stress screening with random vibration.* Proceedings, 27th Annual Technical Meeting - Institute of Environmental Sciences: Emerging Environmental Solutions for the Eighties. Volume 3: Contamination Control., 1981: p. 73-76.Inst of Environmental Sciences.
217. Basaran, C. and Chandaroy, R., *Thermomechanical analysis of solder joints under thermal and vibrational loading.* Journal of Electronic Packaging, Transactions of the ASME, 2002. **124**(1): p. 60-66.
218. McDowell, D.L., Miller, M.P., and Brooks, D.C. *Unified creep-plasticity theory for solder alloys*. in *Symposium on Fatigue of Electronic Materials, May 17, 1993 - May 17, 1993*. 1994. Atlanta, GA, USA: ASTM.
219. Busso, E.P., Kitano, M., and Kumazawa, T., *Visco-plastic constitutive model for 60/40 tin-lead solder used in IC package joints.* Journal of Engineering Materials and Technology, Transactions of the ASME, 1992. **114**(3): p. 331-337.
220. Qi, H., Osterman, M., and Pecht, M., *Plastic ball grid array solder joint reliability for avionics applications.* Ieee Transactions on Components and Packaging Technologies, 2007. **30**(2): p. 242-247.
221. Qi, H., Osterman, M., and Pecht, M., *Modeling of combined temperature cycling and vibration loading on PBGA solder joints using an incremental damage superposition approach.* IEEE Transactions on Advanced Packaging, 2008. **31**(3): p. 463-472.
222. Qi, H., Osterman, M., and Pecht, M., *A rapid life-prediction approach for PBGA solder joints under combined thermal cycling and vibration loading conditions.* Ieee Transactions on Components and Packaging Technologies, 2009. **32**(2): p. 283-292.
223. Eckert, T., Kruger, M., Muller, W.H., Nissen, N.F., and Reichl, H., *Investigation of the solder joint fatigue life in combined vibration and thermal cycling tests.* 60th Electronic Components and Technology Conference, ECTC 2010, June 1, 2010 - June 4, 2010, 2010: p. 1209-1216.Institute of Electrical and Electronics Engineers Inc.
224. Eckert, T., Muller, W.H., Nissen, N.F., and Reichl, H., *Modeling solder joint fatigue in combined environmental reliability tests with concurrent vibration and thermal cycling.* 2009 11th Electronic Packaging Technology Conference, EPTC 2009, December 9, 2009 - December 11, 2009, 2009: p. 712-718.Institute of Electrical and Electronics Engineers Inc.
225. Matin, M.A., Vellinga, W.P., and Geers, M.G.D., *Thermomechanical fatigue damage evolution in SAC solder joints.* Materials Science and Engineering: A, 2007. **445-446**(0): p. 73-85.

226. Iting, T., Li Jung, T., Yen, S.F., Chuang, T.H., Lo, R., Ku, T., and Enboa, W., *Identification of mechanical properties of intermetallic compounds on lead free solder*, in *Electronic Components and Technology Conference, 2005. Proceedings. 55th*. 2005. p. 687-691.
227. Fields, R.J., and Low, S. R, *Physical and mechanical properties of intermetallic compounds commonly found in solder joints.* The Metal Science of Joining, 1991: p. 165-174.
228. Kinyanjui, R., Lehman, L.P., Zavalij, L., and Cotts, E., *Effect of sample size on the solidification temperature and microstructure of SnAgCu near eutectic alloys.* Journal of Materials Research, 2005. **20**(11): p. 2914-2918.
229. Wu, C.M.L., Yu, D.Q., Law, C.M.T., and Wang, L., *Properties of lead-free solder alloys with rare earth element additions.* Materials Science and Engineering: R: Reports, 2004. **44**(1): p. 1-44.
230. Matin, M.A., Vellinga, W.P., and Geers, M.G.D., *Microstructure evolution in a Pb-free solder alloy during mechanical fatigue.* Materials Science and Engineering A, 2006. **431**(1-2): p. 166-174.
231. Moon, K.W., Boettinger, W.J., Kattner, U.R., Biancaniello, F.S., and Handwerker, C.A., *Experimental and thermodynamic assessment of Sn-Ag-Cu solder alloys.* Journal of Electronic Materials, 2000. **29**(10): p. 1122-1136.
232. De Castro, W.B.c., De Lucena Maia, M., Kiminami, C.S., and Bolfarini, C., *Microstructure of undercooled Pb–Sn alloys.* Materials Science and Engineering: A, 2001. **304-306**(0): p. 255-261.
233. Kang, H. and Yoon, W., *Microstructural morphology changes of the lead-tin eutectic alloy by different undercooling levels.* Materials Transactions, 2004. **45**(10): p. 2956-2959.
234. Arfaei, B., Tashtoush, T., Kim, N., Wentlent, L., Cotts, E., and Borgesen, P., *Dependence of SnAgCu solder joint properties on solder microstructure.* 2011 61st Electronic Components and Technology Conference, ECTC 2011, May 31, 2011 - June 3, 2011, 2011: p. 125-132.Institute of Electrical and Electronics Engineers Inc.
235. Ding, Y., Wang, C., Mingyu, L., and Han-Sur, B., *Aging effects on fracture behavior of 63Sn37Pb eutectic solder during tensile tests under the SEM.* Materials Science and Engineering A, 2004. **384**(1-2): p. 314-323.
236. Lampe, B.T., *Room temperature aging properties of some solder alloys* Welding Journal (Miami, Fla), 1976. **55**(10): p. 330s-340s.
237. Ding, Y., Wang, C., Tian, Y., and Li, M., *Influence of aging treatment on deformation behavior of 96.5Sn3.5Ag lead-free solder alloy during in situ tensile tests.* Journal of Alloys and Compounds, 2007. **428**(1-2): p. 274-285.
238. Dutta, I., Pan, D., Marks, R.A., and Jadhav, S.G., *Effect of thermo-mechanically induced microstructural coarsening on the evolution of creep response of SnAg-based microelectronic solders.* Materials Science and Engineering: A, 2005. **410–411**(0): p. 48-52.
239. Fix, A.R., Lopez, G.A., Brauer, I., Nuchter, W., and Mittemeijer, E.J., *Microstructural development of Sn-Ag-Cu solder joints.* Journal of Electronic Materials, 2005. **34**(2): p. 137-142.
240. Pang, J., Xu, L., Shi, X., Zhou, W., and Ngoh, S., *Intermetallic growth studies on Sn-Ag-Cu lead-free solder joints.* Journal of Electronic Materials, 2004. **33**(10): p. 1219-1226.

241. Long, X., Dutta, I., Sarihan, V., and Frear, D.R., *Deformation behavior of Sn-3.8Ag-0.7Cu solder at intermediate strain rates: Effect of microstructure and test conditions.* Journal of Electronic Materials, 2008. **37**(2): p. 189-200.
242. Snugovsky, L., Perovic, D.D., and Rutter, J.W., *Experiments on the aging of Sn-Ag-Cu solder alloys.* Powder Metallurgy, 2005. **48**(2): p. 193-198.
243. Dutta, I., *A constitutive model for creep of lead-free solders undergoing strain-enhanced microstructural coarsening: A first report.* Journal of Electronic Materials, 2003. **32**(4): p. 201-207.
244. Sayama, T., Takayanagi, T., Nagai, Y., Mori, T., and Yu, Q., *Evaluation of microstructural evolution and thermal fatigue crack initiation in SN-AG-CU solder joints.* 2003 International Electronic Packaging Technical Conference and Exhibition, July 6, 2003 - July 11, 2003, 2003. **1**: p. 749-756.American Society of Mechanical Engineers.
245. Gagliano, R.A., Fine, M.E., Vaynman, S., and Stolkarts, V., *Shear testing of solder joints: The effect of various parameters on the maximum shear stress of eutectic tin-lead solder.* Proceedings of the TMS Fall Meeting, 1999: p. 107-116.
246. Coyle, R.J., Solan, P.P., Serafino, A.J., and Gahr, S.A., *Influence of room temperature aging on ball shear strength and microstructure of area array solder balls.* 50th Electronic Components and Technology Conference, 2000: p. 160-169.IEEE.
247. Tsui, Y.K., Lee, S.W.R., and Xingjia, H., *Experimental investigation on the degradation of BGA solder ball shear strength due to room temperature aging.* Electronic Materials and Packaging, 2002. Proceedings of the 4th International Symposium on, 2002: p. 478-481.
248. Lee, S.W.R., Tsui, Y.-K., Hunag, X., and Yan, E.C.C., *Effects of room temperature storage time on the shear strength of PBGA solder balls.* 2002 ASME International Mechanical Engineering Congress and Exposition, November 17, 2002 - November 22, 2002, 2002. **2**: p. 259-262.American Society of Mechanical Engineers.
249. Ming, L., Lee, K.Y., Olsen, D.R., Chen, W.T., Tan, B.T.C., and Mhaisalkar, S., *Microstructure, joint strength and failure mechanisms of SnPb and Pb-free solders in BGA packages.* Electronics Packaging Manufacturing, IEEE Transactions on, 2002. **25**(3): p. 185-192.
250. Chou, G.J.S., *Microstructure evolution of SnPb and SnAg/Cu BGA solder joints during thermal aging.* Advanced Packaging Materials, 2002. Proceedings. 2002 8th International Symposium on, 2002: p. 39-46.
251. Law, C.M.T. and Wu, C.M.L., *Microstructure evolution and shear strength of Sn-3.5Ag-RE lead-free BGA solder balls.* High Density Microsystem Design and Packaging and Component Failure Analysis, 2004. HDP '04. Proceeding of the Sixth IEEE CPMT Conference on, 2004: p. 60-65.
252. Tz-Cheng, C., Kejun, Z., Stierman, R., Edwards, D., and Ano, K., *Effect of thermal aging on board level drop reliability for Pb-free BGA packages.* Electronic Components and Technology Conference, 2004. Proceedings. 54th, 2004. **2**: p. 1256-1262 Vol.2.
253. Zhang, Y., Kurumaddali, K., Suhling, J.C., Lall, P., and Bozack, M.J., *Analysis of the mechanical behavior, microstructure, and reliability of mixed formulation solder joints.* 2009 59th Electronic Components and Technology Conference,

ECTC 2009, May 26, 2009 - May 29, 2009, 2009: p. 759-770.Institute of Electrical and Electronics Engineers Inc.

254. Chiang, S.-Y., Chou, T.-L., Shih, Z.-H., Hong, H.-F., and Chiang, K.-N., *Life prediction of HCPV under thermal cycling test condition.* 2011. **88**: p. 785-790.Elsevier.
255. Borgesen, P. and Meilunas, M., *Effects of solder paste volume and reflow profiles on the thermal cycling performance of mixed SnAgCu/SnPb solder joints.* Components, Packaging and Manufacturing Technology, IEEE Transactions on, 2011. **1**(8): p. 1205-1213.
256. Nousiainen, O., Kangasvieri, T., Rautioaho, R., and Vahakangas, J., *Thermal fatigue endurance of Sn3Ag0.5Cu0.5In0.05Ni and Sn2.5Ag0.8Cu0.5Sb solders in composite solder joints of LTCC/PWB assemblies.* Soldering and Surface Mount Technology, 2011. **23**(1): p. 30-39.
257. Kim, Y., Noguchi, H., and Amagai, M., *Vibration fatigue reliability of BGA-IC package with Pb-free solder and Pb–Sn solder.* Microelectronics Reliability. **46**(2-4): p. 459-466.
258. Park, T.-S. and Lee, S.-B., *Isothermal low cycle fatigue tests of Sn/3.5 Ag/0.75 Cu and 63Sn/37Pb solder joints under mixed-mode loading cases.* 52nd Electronic Components and Technology Conference, May 28, 2002 - May 31, 2002, 2002: p. 979-984.Institute of Electrical and Electronics Engineers Inc.
259. Aluru, K., Wen, F.L., and Shen, Y.L., *Direct simulation of fatigue failure in solder joints during cyclic shear.* Materials & Design, 2011. **32**(4): p. 1940-1947.
260. Meier, K., Roellig, M., Schiessl, A., and Wolter, K.-J., *Life time prediction for lead-free solder joints under vibration loads.* 2011 12th Int. Conf. on Thermal, Mechanical and Multi-Physics Simulation and Experiments in Microelectronics and Microsystems, EuroSimE 2011, April 18, 2011 - April 20, 2011, 2011.IEEE Computer Society.
261. Wong, S.F., Malatkar, P., Rick, C., Kulkami, V., and Chin, I., *Vibration testing and analysis of ball grid array package solder joints.* 57th Electronic Components and Technology Conference 2007, ECTC '07, May 29, 2007 - June 1, 2007, 2007: p. 373-380.Institute of Electrical and Electronics Engineers Inc.
262. Chen, Y.S., Wang, C.S., and Yang, Y.J., *Combining vibration test with finite element analysis for the fatigue life estimation of PBGA components.* Microelectronics Reliability, 2008. **48**(4): p. 638-644.
263. Che, F.X. and Pang, J.H.L., *Vibration reliability test and finite element analysis for flip chip solder joints.* Microelectronics Reliability, 2009. **49**(7): p. 754-760.
264. Yu, D., Al-Yafawi, A., Nguyen, T.T., Park, S., and Chung, S., *High-cycle fatigue life prediction for Pb-free BGA under random vibration loading.* Microelectronics Reliability, 2011. **51**(3): p. 649-656.
265. Zhou, Y., Al-Bassyiouni, M., and Dasgupta, A., *Harmonic and random vibration durability of SAC305 and Sn37Pb solder alloys.* Ieee Transactions on Components and Packaging Technologies, 2010. **33**(2): p. 319-328.
266. Joo, J., Cho, S., and Han, B., *Characterization of flexural and thermo-mechanical behavior of plastic ball grid package assembly using moiré interferometry.* Microelectronics Reliability. **45**(3-4): p. 637-646.
267. Stout, E.A., Sottos, N.R., and Skipor, A.F., *Mechanical characterization of plastic ball grid array package flexure using Moire interferometry.* IEEE Transactions on Advanced Packaging, 2000. **23**(4): p. 637-645.

268. Jianjun, W., Minfu, L., Daqing, Z., and Sheng, L., *Investigation of interfacial fracture behavior of a flip-chip package under a constant concentrated load.* Components, Packaging, and Manufacturing Technology, Part B: Advanced Packaging, IEEE Transactions on, 1998. **21**(1): p. 79-86.
269. Park, T.-S., Baek, D.-C., and Lee, S.-B., *An experimental technique for the strain measurement of small structures using pattern recognition.* Sensors and Actuators A: Physical, 2004. **115**(1): p. 15-22.
270. Dishongh, T., Basaran, C., Cartwright, A.N., Ying, Z., and Heng, L., *Impact of temperature cycle profile on fatigue life of solder joints.* Advanced Packaging, IEEE Transactions on, 2002. **25**(3): p. 433-438.
271. Yang, S.Y., Kim, I., and Lee, S.-B., *A study on the thermal fatigue behavior of solder joints under power cycling conditions.* Ieee Transactions on Components and Packaging Technologies, 2008. **31**(1): p. 3-12.
272. Cho, S., Han, B., and Joo, J., *Temperature dependent deformation analysis of ceramic ball grid array package assembly under accelerated thermal cycling condition.* Journal of Electronic Packaging, Transactions of the ASME, 2004. **126**(1): p. 41-47.
273. Jinwon, J., Kihwan, O., Seungmin, C., and Bongtae, H., *Thermo-mechanical and flexural behavior of WB-PBGA package using moire interferometry.* Electronic Materials and Packaging, 2001. EMAP 2001. Advances in, 2001: p. 421-427.
274. Zhong, Z.W., *Thermal strain analysis of IC packages using various Moire methods.* Microelectronics International, 2004. **21**(3): p. 25-28.
275. Lee, B.-W., Jang, W., Kim, D.-W., Jeong, J.-h., Nah, J.-W., Paik, K.-W., and Kwon, D., *Application of electronic speckle-pattern interferometry to measure in-plane thermal displacement in flip-chip packages.* Materials Science and Engineering: A, 2004. **380**(1–2): p. 231-236.
276. Chandaroy, R. and Basaran, C., *Damage mechanics of surface mount packaging interconnects under concurrent thermal and dynamic loading.* Proceedings of the 1997 ASME International Mechanical Engineering Congress & Exposition, November 16, 1997 - November 21, 1997, 1997.ASME.
277. Hua, Y., Basaran, C., Hopkins, D.C., and Minghui, L., *Modeling deformation in microelectronics BGA solder joints under high current density. Part I. Simulation and testing.* Electronic Components and Technology Conference, 2005. Proceedings. 55th, 2005: p. 1437-1444 Vol. 2.
278. Ye, H., Hopkins, D.C., and Basaran, C., *Measurement of high electrical current density effects in solder joints.* Microelectronics Reliability, 2003. **43**(12): p. 2021-2029.
279. Ye, H., Basaran, C., and Hopkins, D.C., *Deformation of solder joint under current stressing and numerical simulation—II.* International Journal of Solids and Structures, 2004. **41**(18-19): p. 4959-4973.
280. Basaran, C. and Lin, M., *Electromigration induced strain field simulations for nanoelectronics lead-free solder joints.* International Journal of Solids and Structures, 2007. **44**(14-15): p. 4909-4924.
281. Massalski, T.B., Okamoto, H. , Subramanian, P. R.,Kacprzak, L., *Binary alloy phase diagram* ASM, Editor. 1990, ASM international, Materials p. 3014-3017.
282. Moon, K., Boettinger, W., Kattner, U., Biancaniello, F., Handwerker, C., *Experimental and thermodynamic assessment of Sn-Ag-Cu solder alloys.* Journal of Electronic Materials, 2000. **29**(10): p. 1122-1136.

283. http://media.digikey.com/pdf/Data%20Sheets/Injectorall%20PDFs/FR-4%20Spec's.pdf. last accessed 22/4/2013.
284. Graham, C., D , Ghaleeh, M., and Reuben, R.L., *Combined numerical-experimental study of a ball grid array solder connection.* work to be published.
285. Tien, J. and Davis, R., *Implementation of a PBGA into a high volume digital set-top box application.* In Pro. Of SMTA/IPC Electronics assembly Expo, Providence,RI, October 1998: p. S2-1,24-29.
286. http://www.mclennan.co.uk/datasheets/european/stepper/42dblseriesdla.pdf. last accessed 25/7/2014.
287. Incropera, F.P. and DeWitt, D.P., *Introduction*, in *Fundamentals of Heat and Mass Transfer*. 1996, Wiley. p. 8.
288. Carslaw, H.S. and Jaeger, J.C., *Conduction of heat in solids*. 1959: Clarendon Press.
289. Kim, D.C. and Choi, Y.D., *Analysis of conduction – natural convection conjugate heat transfer in the gap between concentric cylinders under solar irradiation.* International Journal of Thermal Sciences, 2009. **48**(6): p. 1247-1258.
290. Callister, W.D., *Mechanical properties of metals*, in *Materials Science And Engineering: An Introduction*. 2003, John Wiley and Sons. p. 118.
291. http://www.engineeringtoolbox.com/young-modulus-d_773.html. last accessed 1/5/2013.
292. http://www.3m.com/intl/kr/img/pdf_new/9882.pdf. Last accessed 1/5/2013.
293. Jousset, P. and Mohamed, R., *Elasto-plastic constitutive model for finite element simulation of structural adhesives.* Simulia Customer 2009: p. 1-15.
294. Mughrabi, H., *Dislocations and properties of real materials.* 1985(No.323): p. 244-262.the Insitutue of Metals.
295. Schubert , R. and bei, R., *Low cycle fatigue , PhD thesis*. 1989, Technische Universität Braunschweig.
296. Cramer, D.W., Allegany, N.Y., and Hoeppner, D.W., *Fatigue properties in engineering*, in *Fatigue and Fracture*. 1996, ASM International. Handbook Committee. p. 15.
297. Pilkey, W.D., *Formulas for stress, strain, and structural matrices*. 1994: Wiley.
298. Fine, M.E., Stolkarts, V., and Keer, L.M., *Fatigue crack nucleation assisted by thermal activation.* Materials Science and Engineering: A, 1999. **272**(1): p. 5-9.
299. Snugovsky, L., Snugovsky, P., Perovic, D.D., Sack, T., and Rutter, J.W., *Some aspects of nucleation and growth in Pb free Sn-Ag-Cu solder*. 2005. **21**: p. 53-60.Maney Publishing.
300. Jung, K. and Conrad, H., *Microstructure coarsening during static annealing of 60Sn40Pb solder joints: II eutectic coarsening kinetics.* Journal of Electronic Materials, 2001. **30**(10): p. 1303-1307.
301. Vianco, P., Rejent, J., Zender, G., and Kilgo, A., *Kinetics of Pb-rich phase particle coarsening in Sn-Pb solder under isothermal annealing-cooling rate dependence.* Journal of Materials Research, 2005. **20**(6): p. 1563-1573.
302. Ghosh, G., *Interfacial microstructure and the kinetics of interfacial reaction in diffusion couples between Sn-Pb solder and Cu/Ni/Pd metallization.* Acta Materialia, 2000. **48**(14): p. 3719-3738.
303. Li, X., Li, F., Guo, F., and Shi, Y., *Effect of isothermal aging and thermal cycling on interfacial IMC growth and fracture behavior of SnAgCu/Cu joints.* Journal of Electronic Materials, 2011. **40**(1): p. 51-61.

304. Tian, Y., Chow, J., Liu, X., Wu, Y.P., and Sitaraman, S.K., *Study of intermetallic growth and kinetics in fine-pitch lead-free solder bumps for next-generation flip-chip assemblies.* Journal of Electronic Materials, 2013. **42**(2): p. 230-239.
305. Kliemt, C., *Thermo-mechanical fatigue of cast aluminium alloys for engine applications under severe conditions*. 2012, Heriot-Watt University: Edinburgh.
306. Toda, H., Fukunaga, T., and Kobayashi, M., *Improvement of thermomechanical fatigue life in an age-hardened aluminum alloy.* Scripta Materialia, 2009. **60**(6): p. 385-387.
307. Kang, S.K., *Bi–Sn, Sn–Sb, Sn–Cu, Sn–Zn, and Sn–In solder-based systems and their properties*, in *Handbook of Lead-Free Solder Technology for Microelectronic Assemblies* K.J. Puttlitz, Stalter, K.A., Editor. 2004, Marcel Dekker Inc. p. 286.
308. Song, H.G., Morris, J.W., and Hua, F., *The creep properties of lead-free solder joints.* JOM, 2002. **54**(6): p. 30-32.
309. Song, H.G., Morris Jr, J.W., and Hua, F., *Anomalous creep in Sn-rich solder joints.* Materials Transactions, 2002. **43**(8): p. 1847-1853.
310. Xiao, Q., Nguyen, L., and Armstrong, W.D., *Aging and creep behavior of Sn3.9Ag0.6Cu solder alloy.* 2004 Proceedings - 54th Electronic Components and Technology Conference, June 1, 2004 - June 4, 2004, 2004. **2**: p. 1325-1332.Institute of Electrical and Electronics Engineers Inc.
311. Kumar, S., Jung, D., and Jung, J., *Wetting behavior and elastic properties of low alpha SAC105 and pure Sn solder.* Journal of Materials Science: Materials in Electronics, 2013. **24**(6): p. 1748-1757.